Hydrodynamic Interaction

Offshore Floating Structures

Second Edition

March, 2018

J.Koto, C.L.Siow, C.Guedes Soares,
H.Yasukawa, A.Maimun

Published By
Ocean & Aerospace Research Institute,
Indonesia

Preface

بسم الله الرحمن الرحيم

This book discuss on advanced hydrodynamic interaction theories and their application on offshore floating structures which consists of nine chapters. They are orderly challenge on hydrodynamic of floating structures in chapter-1, loading on offshore floating structures in chapter-2, review on hydrodynamic of offshore floating structures in chapter-3, hydrodynamic theories of floating structures in chapter-4, advanced hydrodynamic interaction theories of floating structures in chapter-5, Numerical solution of hydrodynamic of floating structures, experimental hydrodynamic interaction of FPSO-Shuttle tanker in chapter-7, simulation of hydrodynamic interaction of FPSO-Shuttle tanker in Chapter-8 and gad distance theories with application on semi-submersible-TLP as last chapter.

In the book, many pictures, derivation of equations and illustrations are enclosed to assist the readers' understanding.

2017 (First Edition)
BN: 20092016013

Published by OCEAN & AEROSPACE Research Institute

Authors

Jaswar Koto Dr

Professor on Offshore Engineering
President of Ocean & Aerospace Research Institute, Indonesia
Contract at Faculty of Mechanical Engineering, Universiti Teknologi Malaysia, Malaysia.
Email: jaswar@isomase.org or jaswar@utm.my

Siow Chee Loon, Dr

Lecturer on Offshore Engineering
Faculty of Mechanical Engineering, Universiti Teknologi Malaysia, Malaysia
Email: paulcloon@gmail.com

Carlos Guedes Soares, Dr

Professor on Offshore Engineering
Director of Center for Marine Technology and Engineering,
Technical University of Lisbon, Portugal
Email: c.guedes.soares@centec.tecnico.ulisboa.pt or c.guedes.soares@ist.utl.pt

Hironori Yasukawa, Dr

Professor on Hydrodynamic
Department of Transportation and Environmental Systems, Hiroshima University, Japan
Email: yasukawa@naoe.hiroshima-u.ac.jp

Adi Maimun, Dr

Professor on Naval Architecture
Head of Ship and Offshore Technology Research Group,
Faculty of Mechanical Engineering, Universiti Teknologi Malaysia,
Email: adi@utm.my

Acknowledgements

First and foremost, praises, thanks and syukur to Allah (S.W.T) to give the authors strength and ability to complete this book.

The authors would like to take this opportunity to express our highest appreciation to our colleagues in the Ocean and Aerospace Research Institute, Indonesia, Universiti Teknologi Malaysia, Center for Marine Technology and Engineering, Technical University of Lisbon, Hiroshima University and National Research Institute of Fisheries Engineering (NRIFE), Japan to provide proper guidance, encouragement, invaluable ideas, comment, recommendation, critics, suggestions and advice that to assist us for the successful completion of this book.

Also, the authors would like to thank Dr Hirata and the laboratory managers, Dr.Matsuda and Dr.Terada for the stimulating discussions on the experiment setup. The authors also thank fellow laboratory mates: Mr Khairuddin, Mr Matsumoto, Mr Zakiyama, Mr Hamasaki and Mr Yamashita and others who helped us in conducting the experiment and worked together to ensure the experiment is able to complete on time. Without they precious support, it would not be possible to conduct the research successfully.

To authors' families that always pray for our successful, all this things cannot pay for all what they all have done. Our special thanks also to our postgraduate students.

The authors are grateful to all colleagues, friends, institutions and parties for supporting this book.

List of Tables

List of Figures

List of Abbreviations

Abbreviation	Description
AC	Alternative Current
ANSYS	American Computer-aided engineering software
ANSYS AQWA	Diffraction Product of American Computer-aided engineering software
ANSYS CFX	Computational Fluid Dynamics software of American Computer-aided engineering software
CFD	Computational Fluid Dynamics
CLEAR-VOF	Computational Lagrangian-Eulerian Advection Remap-Volume of Fluid
DoF	Degree of Freedom
FLNG	Floating Liquefied Natural Gas
FPSO	Floating Production Storage and Offloading
HOBEM	Higher-Order Boundary Element Method
KVLCC2	Korean very large crude carrier 2
LNG	liquefied natural gas
NRIFE	National Research Institute of Fisheries Engineering, Japan
NWT	numerical wave tanks
RAO	Response Amplitude Of Operation
WAMIT	Wave Analysis frequency-domain, free-surface, radiation/diffraction code developed at Massachusetts Institute of Technology

List of Symbols

Symbol	Descriptions
A	Added mass
$\boldsymbol{A_{ij}}$	Added Mass in direction *i* due to motion in direction *j*
$\boldsymbol{A_{Proj}}$	Projected Area
$\boldsymbol{a_n, b_n, c_n}$	Constant of parabolic curve *n* used to represent curve of wave crest
$(\boldsymbol{\bar{a}, \bar{b}, \bar{c}})$	Coordinate
$\boldsymbol{A_w}$	Water plane area
$\boldsymbol{B}$	damping coefficient
$\boldsymbol{B_{ij}}$	Damping Coefficient in direction *i* due to motion in direction *j*
$\boldsymbol{b_p}$	Radiating damping coefficient
C	Restoring force
$\boldsymbol{C_a}$	Added mass coefficient
$\boldsymbol{C_D}$	Drag coefficient
$\boldsymbol{C_M}$	Mass coefficient
$\boldsymbol{C_{stP,n}}$	Intersection position between two connecting strip
D	Diameter
$\boldsymbol{Dd, D_{mn}}$	Normal dipole
$\boldsymbol{d_S}$	Distance the steal block shifted
$\boldsymbol{E_d}$	Dissipated Energy
$\boldsymbol{E_f}$	Energy flux
$\boldsymbol{E_W}$	Wave energy over a wave crest
$\boldsymbol{E_{W\ i,j}}$	Wave energy due to the motion *j* in *i*-direction
$\boldsymbol{F_D}$	Drag force
$\boldsymbol{F_j}$	Wave exciting force in direction *j*
$\boldsymbol{F_p}$	Diffracting force
$\boldsymbol{F^P_{i;n}}$	Radiating wave force acting on the structure *P* to induce motion in *i*-direction due to the motion of nearby structure in stage *n*

$F^{P}_{i;Tot}$	Total wave force due to incident wave force and interacting wave force acting on the floating structure *P* inducing the motion in direction *i*.
$F_{(P,i;Q,j)}$	Wave force acting on the structure *P* in direction *i* due to the radiating wave generated by structure *Q* in the motion direction *j*
$F^{S,n}_{(P,i;Q,j)}$	Wave force acting on structure *P* to induce the motion in direction *i* due to the motion of structure *Q* in direction *j* in stage *n*
$F(t)$	Periodic function
$F(f)$	Frequency series motion or wave data
f_j	Average distribution force in motion direction *j*
$f(t)$	Time series motion or wave data
$G(\overline{P};\overline{Q})$	Green Function
$\overline{GM_B}$	Distance of centre of gravity to centre of transverse direction moment
$\overline{GM_L}$	Distance of centre of gravity to centre of moment in longitudinal direction
$G_W(\overline{P}_m,\overline{Q}_n)$	Green surface wave
$\mathbf{g}$	Gravitational acceleration
h	Water depth
Im	Imaginary number
i	Complex number
J_n	First kind of Bessel function in order n
$\mathbf{K}$, $\mathbf{k}$	Wave number
KE	Kinetic Energy
k_{xx}	Radius of gyration in x direction
k_{yy}	Radius of gyration in y direction
K_{zz}	Radius of gyration for Z direction
L	Overall length of floating structure
l_{Crest}	Length between wave crest
l_{Nor}	The distance of the panel from origin of segment plane following the panel normal direction
$l_{mp,m}$	Position of the panel *m* projected to the segment plane
$l_{p0,n}$	The distance of the segment plane from origin following the plane normal

	direction
$\boldsymbol{l_{rad}}$	Distance propagate by radiating wave
$\boldsymbol{l_{st,n}}$	Length of the strip at the segment
$\boldsymbol{M_{i,j}}$	Moment due to motion *j* in direction *i*
$\boldsymbol{m_{Nor,n}}$	Normal direction of strip *n*
$\boldsymbol{m_{Tang,n}}$	Tangent direction of strip *n*
$\boldsymbol{m_{st,n}}$	Angle of strip *n*
N	Total number of element
n	Element number
$\boldsymbol{n_j}$	Unit Normal Vector respect to *j* direction
$\boldsymbol{n_{st,n}}$	Area normal vector of the strip *n*
$\boldsymbol{\vec{n}}$	Unit normal vector of area
$\boldsymbol{P_d}$	Dynamic pressure
$\boldsymbol{\bar{P}}$	Field Location
$\boldsymbol{PE}$	Potential Energy
$\boldsymbol{\bar{Q}}$	Source Location
$\boldsymbol{\mathcal{R}}$	Radius of wavelet
$\boldsymbol{r, R}$	Horizontal distance
$\boldsymbol{R_0}$	Real part of wave term
$\boldsymbol{R_1}$	Derivative of R_0
$\boldsymbol{Rt_{i,j}}$	Ratio of moment in direction *j* cause by the force in direction *i* to total moment in direction *j*
$\boldsymbol{Re}$	Real number
S	Surface Area
$\mathbf{S_B}$	Seabed surface
$\boldsymbol{S_{cST}}$	Total length of first radiating wave crest
$\boldsymbol{S_{cPT}}$	Total length of radiating wave crest at location *P*
$\boldsymbol{S_{cP,n}}$	Length of radiating wave crest represent by strip *n* at location *P*
$\boldsymbol{S_{cS,n}}$	Length of first radiating wave crest represent by strip *n*
$\boldsymbol{S_F}$	Free surface area

S_H	Wet surface area of floating structure
S_∞	Boundary located in the infinity distance
Ss, S_{mn}	Source
$\mathcal{T}$	Draught of floating structure
T	Period
t	Time
$u(t), u(x,t)$	Time dependent fluid particle velocity
$\dot{u}$	Horizontal fluid particle velocity
V_{max}	Magnitude of complex fluid particle velocity
W_S	Total weight of the model
w	Circular frequency of incident wave *(2π/T)*
$\dot{w}$	Vertical fluid particle velocity
w_B	weight of steel block
X_j	The motion of structure in direction *j*
$\dot{X}(t)$	Time dependent floating structure velocity
$\dot{X}_z$	Floating structure velocity in Z direction
$\ddot{X}_z$	Floating structure acceleration in Z direction
(x, y, z)	Coordinate
(x_P, y_P)	Field coordinate
(x_S, y_S)	Source coordinate
$(x_{st,n}, y_{st,n})$	The coordinate of the strip on the segment plane
$\bar{x}_{St,n}$	Area normal vector of the strip *n* in X-direction
$(\tilde{x}_G, \tilde{y}_G, \tilde{z}_G)$	Position of the center of gravity of model
$(\tilde{x}_p, \tilde{y}_p, \tilde{z}_p)$	Position of reflective optical tracking markers
$(x_{\psi S,n}, y_{\psi S,n})$	Connected coordinate of the strip segment plane
Y_n	Second kind of Bessel function in order n
$\bar{y}_{st,n}$	Area normal vector of the strip *n* in Y-direction
z_a	motion amplitude in stage *n*
α, ϵ	Leading Phase
β	Incident wave propagation direction

ε_a	Relative error
$\tilde{\gamma}$	Floating model initial heading angle
λ	Wavelength
λ/D_{FLNG}	Ratio of wavelength to Round Shape FLNG's diameter
∇	Displacement floating structure
Φ	Complex Wave Potential
ϕ	Complex time independent Wave Potential
ϕ_j	Complex time independent Radiation Wave Potential in direction of motion j
ϕ_I	Complex time independent Incident Wave Potential
ϕ_S	Complex time independent Scattering Wave Potential
ϕ_R	Complex time independent Radiation Wave Potential
ϕ_R^S	Diffracted interacting wave potential due to motion of nearby floating structure
$\dot{\phi}_Z$	Fluid particle velocity in Z direction
ϖ	Solid angle
ρ	Fluid density
ϑ	Wave propagation direction
θ_{In}	Angle the model inclines
$\theta_{mp,m}$	Normal angle of panel *m*
$\theta_{Pn,n}$	Normal angle for plane *n*
$\theta_{Pt,n}$	Tangent angle for plane *n*
θ_{rad}	Direction of propagation of the radiating wave
$\tilde{\theta}_1$	Time dependent roll angle
$\tilde{\theta}_2$	Time dependent pitch angle
$\tilde{\theta}_3$	Time dependent yaw angle
ζ, ς_a	Wave amplitude
$\zeta_{a,i}$	Radiating wave amplitude due to motion in direction *i*
$\zeta_{a\,i,j}$	The wave amplitude due to the motion *j* in direction *i*

Table of Contents

Chapter 1

1.0. Issue and Challenges of Floating Structures

1.1. Issues of Floating Structures

The floating structures are often used to explore natural resources in deep water area because fixed structures such as jacket structure is not applicable in deep water. Therefore, study on floating structure system is an important research topic in offshore industry. The floating structures are allowed to move freely within the design limit when the motion of structures is induced by external force such as wave force, drift force, wind force and current force. Besides, the motion characteristics of the floating structures are also easily influenced by the hulls design and the arrangement of structures on sea surface. These motion characteristics would be affected when the floating structures interact with each other on sea surface.

Interaction between floating structures becomes an important research topic especially on the study of the Floating Liquefied Natural Gas Storage (FLNG) offloading system design. This is because the gap between the FLNG with tanker ship is one of the important criteria to determine workability of the offloading system and the success of fluid transfer. To transfer liquefied natural gas (LNG), the distance between the storage tank and shuttle tanker should be as close as possible in order to reduce the amount of LNG boil off when the LNG is transferring from FLNG to the tanker ship. In recent development, it is suggested that the shuttle tanker has to be arranged side by side with the storage tank so that the pipe length can be minimised. Due to the close distance between floating structures, accurate prediction on the Response Amplitude Operator (RAO) of each structure in a multiple floating structures system are important to ascertain the safety of the structures' arrangement. In general, this study will concentrate on the dynamic motion interaction between floating structures which is used to extract natural gas in deep water area.

The environmental condition is one of the obstructions in limiting the arrangement of floating structures in the offshore system. Due to effect of wave, current and wind, motions of

the floating structures are difficult to predict. In this research, only the influence of first order wave forces to the motion of floating structure was studied because it is a significant factor in inducing the motion of floating structures. According to Ali et al. (2010), the external force acting on the single floating structure is only caused by incident wave in single floating structure system. However, the study of the wave load on the multiple floating structures becomes more complicated as the total wave force acted to the floating structures is the summation of the force from incident wave, the scattering wave from nearby structures and radiating wave due to the motion from nearby structures. This situation increases the complexity of the system and calls for a comprehensive study.

Previously, the studies on the interaction between floating structures focused on the wave drift force and motion response due to the interaction effect. From the research conducted by Ali et al. (2010), the outcomes showed that the interaction between multiple floating structures causes the motion response to become higher due to the extra radiating wave force transferred from one floating structure to the nearby floating structures. The observation was evaluated and proved by many researchers through their experimental studies or numerical simulation. However, there are still weaknesses from the numerical method used in the previous research. For example, some of the mathematical models to simulate the effect of hydrodynamic interaction are not applicable for the study of the structures arrange with a very small gap distance. This is because some of the proposed mathematical models applied Bessel function to simulate the wave propagation. Hence, if the condition could not satisfy the cylindrical coordinate function of Bessel function, the result gained may be incorrect. This problem was raised by Kashiwagi (2008); Kashiwagi and Shi (2010) in their research on comparing the wave interaction theory to their Higher-Order Boundary Element Method (HOBEM). The horizontal wave force they calculated using the theory shows consistent similarity with the result obtained from HOBEM. However, the different results were obtained from both of the theories for vertical wave force. To solve this problem, they applied the exact algebra method to their HOBEM method to allow their methodology works for multiple body interaction in very close gap.

Besides, most of the previous proposed methods were developed based on the potential theory. The diffraction potential theory executes the wave load on the floating structure by estimating the wave diffraction effect. In the potential theory, it is assumed that the viscous effect can be ignored in the calculation. This assumption causes the potential

theory to estimate a lower damping coefficient for the motion of floating structures. The damping coefficient of the floating structure is under-predicted, causing the RAO of floating structures prediction to become higher than the actual value in damping dominant region. This weakness of the potential theory was reported by Loken (1981) and Lu et al. (2011). Regarding this problem, over-prediction of RAO by the potential theory is negligible if the natural frequencies of the motions are not in the range of the wave frequency which exists in the structure operating environment. However, if the natural frequency of the motion is within the range of the favour wave frequency, then accurate estimation on the floating structure's RAO in the damping dominant region is required to ensure the safety of the floating structure.

Furthermore, the RAO of floating structures outside the damping dominant region can be predicted accurately as the diffraction potential theory is able to estimate the added mass and wave force of the floating structures correctly. From the motion equation, the motion of the floating structures in different wavelength depends on different factors as shown in Figure 1.1.

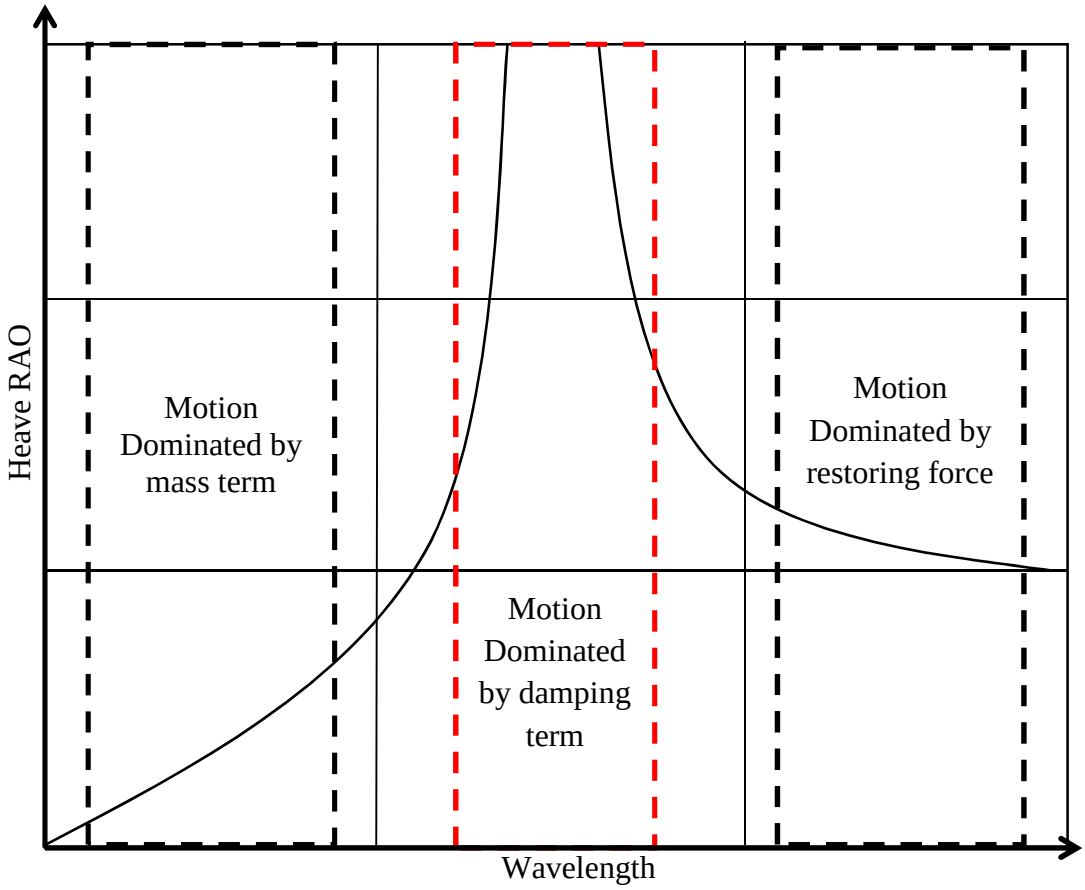

Figure 1.1: The dominant factor in influence the heave RAO of cylinder structure (Journee and Massie, 2001).

Figure 1.1 shows the example of the heave RAO tendency curve in different length of wavelength for the cylinder structure. When the wavelength is much shorter than the structure length, the motion of floating structure is more dominated by the mass term of the structure. On the other hand, in very long wavelength region, the motion of floating structure is more dominated by the restoring force of floating structure. Typically, the motion response amplitude operator, RAO is equal to one in the region if the wavelength is much longer than the structure length. In the region where the wave frequency is near to the natural frequency of the motion of floating structure, the RAO of the floating structure is more dominated by the damping term. In this region, high resonance effect would be existed. The RAO in the damping dominant region becomes the peak response in the RAO tendency curve.

In this book, the new generation of round shape FLNG was selected to be discussed. The advantage of round shape FLNG over the traditional ship-shape FLNG was studied by Lamport and Josefsson (2008). Their research includes the comparison of motion response, mooring system design, constructability and fabrication, operability, safety and costing between both the structures. The study conducted by Lamport and Josefsson (2008) and Arslan et al. (2011) obtained that this new design of FLNG has a better hydrodynamic behaviour as compared to ship shape structure. Besides, oil and gas companies prefer the FLNG design because it has larger storage volume and larger area for topside facilities. Lamport and Josefsson (2008) also found that the round shape FLNG performed better than ship shape FLNG in these two important factors. Moreover, the simple hull shape for the round shape FLNG also helps to reduce the construction cost as simple hull structures are easier to construct.

Due to the innovative design of a new generation of FLNG technology, there is more freedom to arrange other floating structures around the FLNG. For example, the structure arrangements in the previous design are typically placed in a side by side arrangement or in a tandem arrangement due to the shape of the FLNG. Also, the direction of tanker and FLNG arrangement are respected to the wave propagation direction and cannot be changed during the offloading process. According to Lamport and Josefsson (2008), the round FLNG increases the flexibility of structure arrangement. The relative direction of shuttle tanker to the

wave propagation direction is adjustable during the offloading process for a safer arrangement. To allow for horizontal rotations, the offloading system can be designed by utilizing an offloading reel station with the mooring hawser and hose attached on a pinned connection on a 90º trackline system at the periphery of the round shape FLNG. Therefore, the angle of arrangement for the Round Shape FLNG and shuttle tanker can be varied up to 180 degrees as shown in Figure 1.2. Hence, in this book, discussion on the RAO of the round shape FLNG only focuses on cases where the structure is alone and the interaction of FLNG with shuttle tanker due to the effect of gap distance between floating structures.

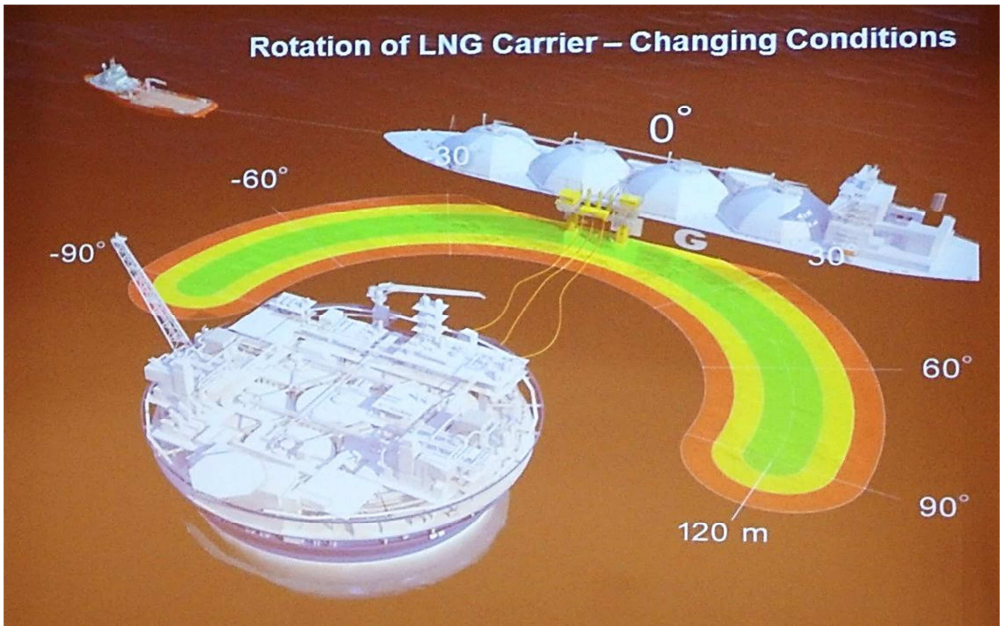

Figure 1.2: Allowance for the change of arrangement of LNG carrier during offloading process (Sevan Marine, 2014).

1.2. Challenges of Floating Structures

Offshore industry often requests for an accurate and efficient numerical model to predict the behaviour of the floating structure. The numerical model should be able to estimate the dynamic motion of floating structure accurately either the motion is dependent by the mass term, restoring force term or damping term. The amount of over-predict or under-predict in the prediction of motion of floating structure by the numerical model should be minimized to

avoid large difference in the motion of the floating structure observed during operating stage when compared to the numerical method result.

However, the current numerical model which has been developed based on the diffraction potential theory to estimate the damping coefficient of the floating structure also has its weakness. The theory ignores the viscous effect in estimating the hydrodynamic behaviour of floating structure, causing the under-estimation of damping coefficient predicted by the theory. This weakness causes the current numerical model to over-predict the motion of the floating structure significantly when the motion is dominant by the damping term. The over-estimation on the dynamic motion of floating structure in damping dominant region by diffraction potential theory causes the numerical model to be less accurate, and causes the hydrodynamic behaviour of floating structure difficult to predict by the numerical model in damping dominant region.

The inaccuracy of the current numerical model causes higher design cost and consumes longer time during floating structure design process. To predict the hydrodynamic behaviour of the floating structure in damping dominant region, model experiment test can be a good solution. However, the model experiment test is a costly and time consuming method to test the behaviour of floating structure. Therefore, the cost and time consumed to design the floating structure will increase because large amount of experiment test is required in estimating the motion of floating structure in damping dominant region. This is due to the weakness of the current numerical model in predicting the motion of floating structure in the damping dominant region.

According to Kvittem et al. (2012), the diffraction potential theory can predict the hydrodynamic behaviour of large floating structure accurately. This is because the effect of wave diffraction is significant when the incident wave interacts with large floating structure. When the motion of floating structure is dominant by the mass term or dominant by restoring force term, the motion of the floating structure estimated by the diffraction potential theory is close to the experiment result. However, the viscous effect is ignored by the diffraction potential theory, causing the motion predicted by the theory at damping dominant region to become over-estimated significantly. Based on the available literatures, the weakness of the diffraction potential theory as mentioned was also reported by Loken (1981) and Lu et al. (2011). Loken (1981) found that the diffraction potential theory would over predict the motion response of floating structure in damping dominant region due to under prediction of

radiation damping by the theory. Besides, Lu et al. (2011) reported similar finding in their research when comparing the potential theory and viscous theory. They found that the viscous theory mostly under-predicts the wave force in the calculation while the potential theory over predicts the motion when the viscous effect is ignored in the approach of potential theory.

Since the diffraction potential theory is accurate in most regions, except in the damping dominant region, this research proposed to develop the numerical model based on the theory. To improve the numerical model develop based on diffraction potential theory, the numerical model applies drag equation to predict the viscous effect acting on the floating structure because the viscous effect is ignored by the diffraction potential theory. The drag equation is modified, so, the additional viscous damping and linearize drag force calculated by using the modified drag equation can be combined with the radiation damping and radiating wave force estimated by using diffraction potential theory. The damping coefficients and the wave force estimated by both mathematical models are combined in the motion equation to calculate the dynamic motion of floating structure. Therefore, the motion of the floating structure when it is alone and when it is interacting with other structure was calculated by the new numerical model In this book to have a more accurate result regardless of the motion is dominant by mass term, restoring force term or damping term.

From the improvement made to the numerical model, offshore industry stands to benefit substantially from the new proposed numerical model which combines the diffraction potential theory with the drag equation to estimate the motion of floating structure. Through the improved the numerical model, the hydrodynamic behaviour of the floating structure can be predicted by numerical method with higher accuracy. As the motion of the floating structure in damping dominant region is important in designing the floating structure, the proposed numerical model is able to estimate the motion of floating structure with better accuracy. The amount of over-predict in the motion of floating structure can be reduced by the new proposed method. This proposed numerical model provides a better motion analysis method to the offshore industry and helps to reduce the cost and time consumed in designing a floating structure. This target can be achieved by reducing the amount of experiment test required to test the hydrodynamic behaviour of the floating structure.

Improving the accuracy of the numerical model to predict the hydrodynamic behaviour of floating structure is crucial to increase the reliability of the numerical solution to analyse the motion floating structure. The current numerical model is developed based on

diffraction potential theory, which is accurate in predicting the motion of floating structure in most regions except the damping dominant region. In this book, the alternative numerical model proposed includes the viscous effect which was ignored by diffraction potential theory in estimating the hydrodynamic behaviour of the floating structure. Through this improvement, the proposed numerical model is able to estimate the motion of floating structure in all the regions of motion regardless of the motion is dominant by mass term, restoring force term or damping term. This is because the under-estimation of the damping coefficient by the diffraction potential theory is improved by introducing the drag equation to predict the viscous damping which is ignored by the diffraction potential theory.

Chapter 2

2.0. Loading on Floating Structures

2.1. Components of Floating Structures

Floating offshore structures are used on open and ice seas, lakes, rivers, and oceans for a variety of activities, such as drilling and exploration of oil and gas and warfare. The floating offshore structures are constructed using the principles of naval architecture that require same structural components and their classification is based on their function. The floating offshore structures have huge structures with a number of components as an example shown in Figure.2.1. It consists of various parts that are bind together to make this huge structure resist a huge amount of forces that act upon it, during its life at the sea.

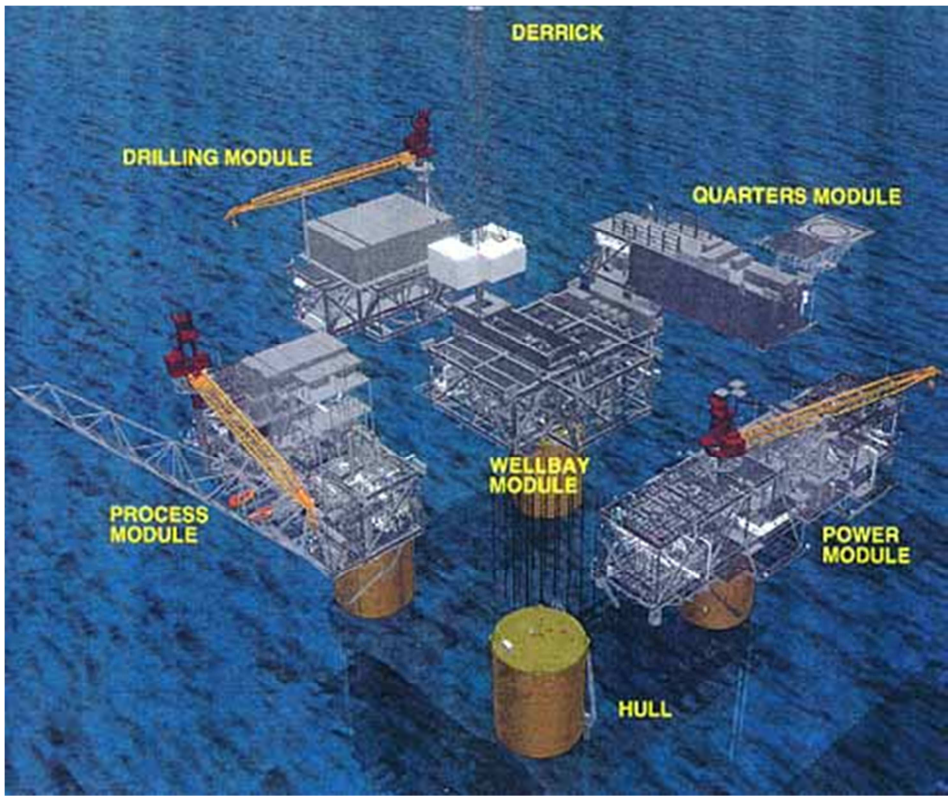

Figure.2.1: Components of an Offshore Rig [Drilling Info].

2.2. Types of Floating Structures

2.2.1. Floating Production System

Floating Production System (FPS) is equipped with production equipment. It is anchored in place with wire rope and chain, or can be dynamically positioned using rotating thrusters. Production from subsea wells is transported to the surface deck through production risers designed to accommodate platform motion.

Figure.2.2: Example of Floating Production System [SBS].

2.2.2. Floating Production Storage and Offloading

Floating Production, Storage and Offloading System (FPSO) consists of a large tanker type vessel moored to the seafloor. An FPSO is designed to process and stow production from nearby subsea wells and to periodically offload the stored oil to a smaller shuttle tanker. The shuttle tanker then transports the oil to an onshore facility for further processing. An FPSO may be suited for marginally economic fields located in remote deep-water areas where a pipeline infrastructure does not exist. Currently, there are no FPSO's approved for use in the Gulf of Mexico. However, there are over 70 of these systems being used elsewhere in the world.

Figure.2.3: Example of Floating Production, Storage and Offloading [Offshore Technology].

2.2.3. Single Point Anchor Reservoir

A Single Point Anchor Reservoir (SPAR) is a type of floating oil platform typically used in very deep waters, and is named for logs used as buoys in shipping that are moored in place vertically. Spar production platforms have been developed as an alternative to conventional platforms. The deep draft design of spars makes them less affected by wind, wave and currents and allows for both dry tree and subsea production. Spars are most prevalent in the US Gulf of Mexico; however, there are also spars located offshore Malaysia and Norway.

Figure.2.4: Truss SPAR DTU in Kikeh, Malaysia [Koto, 2017].

A spar platform consists of a large-diameter, single vertical cylinder supporting a deck. The cylinder is weighted at the bottom by a chamber filled with a material that is denser than water to lower the center of gravity of the platform and provide stability. Additionally, the spar hull is encircled by helical strakes to mitigate the effects of vortex-induced motion. Spars are permanently anchored to the seabed by way of a spread mooring system composed of either a chain-wire-chain or chain-polyester-chain configuration.

There are three primary types of spars; the classic spar, truss spar and cell spar. The classic spar consists of the cylindrical hull noted above, with heavy ballast tanks located at the bottom of the cylinder.

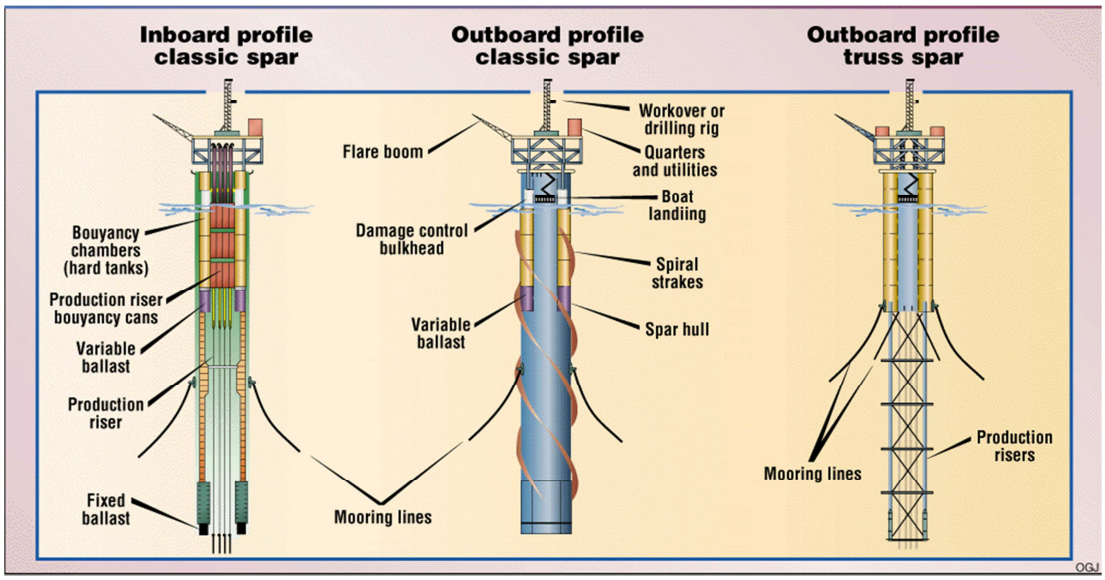

Figure.2.5: Three types of SPAR [Koto, 2017].

A truss spar has a shorter cylindrical "hard tank" than a classic spar and has a truss structure connected to the bottom of the hard tank. This truss structure consists of four large orthogonal "leg" members with X-braces between each of the legs and heave plates at intermediate depths to provide damping. At the bottom of the truss structure, there is a relatively small keel, or soft tank, that houses the heavy ballasting material. Soft tanks are typically rectangular in shape but have also been round to accommodate specific construction concerns. The majority of spars are of this type.

A third type of spar, the cell spar, has a large central cylinder surrounded by smaller cylinders of alternating lengths. At the bottom of the longer cylinders is the soft tank housing the heavy ballasting material, similar to a truss spar. The cell spar design was only ever used for one platform, the Red Hawk spar, which was decommissioned in 2014 under the Bureau of Safety and Environmental Enforcement's "Rigs-to-Reefs" program. At the time of its decommissioning it was the deepest floating platform to ever be decommissioned.

2.2.4. Semi-Submersible and Tension Leg Platform

Semi-Submersible and Tension Leg Platform are floating installations which rest on four or six pillar-like legs called columns with an equal weight distribution on each. These columns or legs are in turn attached to large basements called pontoons floating on the water surface. These pontoons may be ballasted or de-ballasted accordingly on and off operations. Often

these pontoons delve deeper under the water surface and maintain the buoyancy and position of the floating system. There is always a greater draft. Thereafter the operational deck is kept well aloof from the wave disturbance or the rough seas. However due to Small Water-plane Area the structure is sensitive to load variations and must be trimmed accordingly. They are by the virtue of their equivalent weight distribution and high draft and it has a greater stability than normal ships. The number of legs, pontoon design, the situation of the risers and drill equipment are decided at pre-design stage. They are generally instrumental in Ultra-deep waters where the fixed structures pose a problem. Their position is maintained generally by a catenary mooring system or sometimes in modern structures by Dynamic: Positioning System. These structures are gigantic and may be towed from one location to another by the virtue of a kind of ships called Heavy Lift Ships.

Figure.2.6: Typical of Tension Leg Platform for Malikai Project, Malaysia [Koto, 2017].

2.3. Loading on Floating Structures

Loads acting on ships and offshore structures are from gravity, environment and seismic. The gravity loads are arising from dead weight of structure and facilities either permanent or temporary. Seismic loads are arising from gravity loads which are a derived type. The environmental loads play a major role governing the design of offshore structures. Before starting the design of any structure, prediction of environmental loads accurately is important.

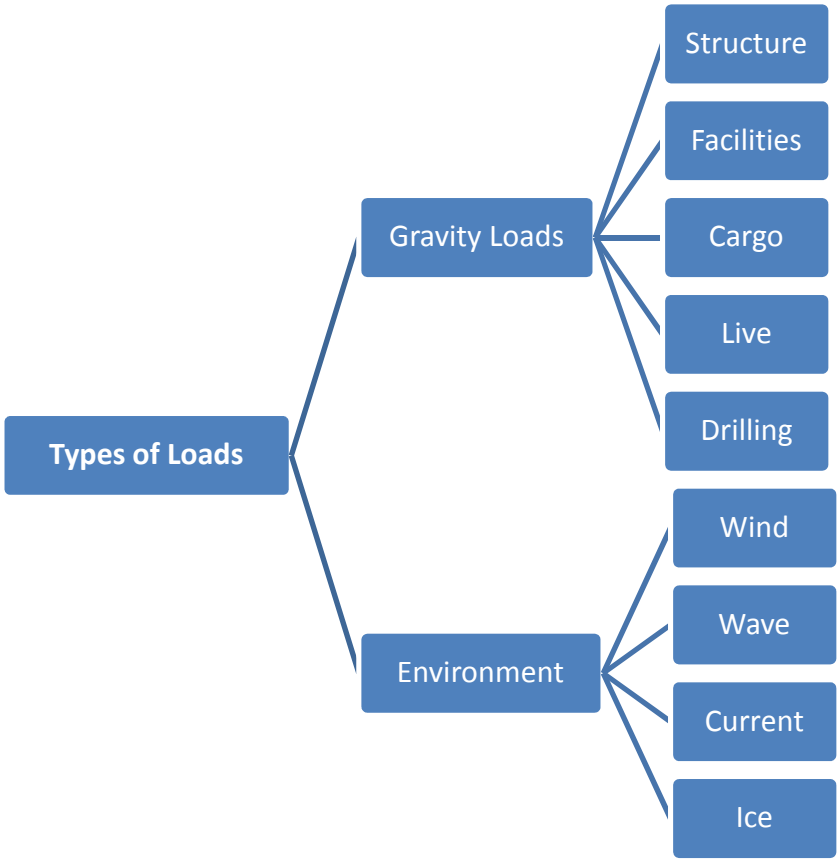

Figure.2.7: Loading on floating offshore structures.

Chapter 3

3.0. Hydrodynamic of Floating Structures

3.1. Research on Floating Structures

In the previous researches, many researchers have conducted a study on the phenomena of interaction between floating structures. Selected previous methods applied to study the interaction phenomena were reviewed in this chapter. From the available literature, most of the method proposed to analyse hydrodynamic interaction between multiple structures are based on the diffraction potential theory. The previous methods such as the exact interaction theory proposed by Kagemoto and Yue (1987), higher order boundary element method (HOBEM) proposed by Kashiwagi (2000) and exact algebraic method proposed by Siddorn and Taylor (2008) were developed based on the diffraction potential theory.

In the previous literature, the existing methods to predict the hydrodynamic interaction between floating structures show the capability of each method to predict the motion response of the floating structures due to interaction phenomena. The weaknesses of the existing method to predict the motion response of multiple structures system have been mentioned in the literature published by some scholars. The main weakness of the methods developed based on the potential theory is over predicting the motion response of the floating structures in resonance region. This weakness of the methods based on potential theory has been reported by Loken (1981). Besides, the similar problem of the potential theory in the study of hydrodynamic interaction also has been reported by Lu et al. (2011).

In addition, this chapter also reviews the design concept of non-ship shape Floating Liquefied Natural Gas Storage (FLNG). The design of non-ship shape FLNG is currently in the process of development to fulfil the requirement of offshore industry. One of the successful new types of FLNG is the cylinder shape floating structure which has been proposed by Sevan Marine ptd (Lamport et al., 2008). Currently, a few units of the cylinder shape floating structure designed by Sevan Marine are operating in open sea. The

performance of the cylinder type floating structure compared to traditional ship shape floating structure has been reviewed in the literature from this chapter before selecting the model as the FLNG model for this research.

The third part of this chapter presents the factors that would influence the motion data collected in the experiment test. The effect of the experiment setup on the floating structure motion data which can be collected in this study was reviewed in the literature before conducting the experiment. The aim of this research is to study the wave frequency motions of the selected model. From the literature reviewed, the wave frequency motion for large structure is not much influenced by the mooring system due to the size of the structure. The recommendations from the literatures are considered In this book when the collected experiment data is processed.

3.2. Hydrodynamic Interaction on Multiple Floating Structures

According to McIver (2002), he suggested that the concept of the hydrodynamic interaction which has been introduced by Kagemoto and Yue and then revised by Murai et al. and Kashiwagi, is the suitable numerical method used to study wave interaction with large arrays of floating bodies containing thousands of individual elements. Achievement of that numerical method leads to further development on approximation and asymptotic methods for the study of system consisting large arrays of interactions structures. Besides, Zhao et al. (2011) commented that hydrodynamic interaction study is also important in the design of FLNG in their research study. This is because the study of the multi-structures hydrodynamics interaction is an essential guiding to design a FLNG positioning system. Better understanding of hydrodynamics among the floating structures would help to improve the risk assessment and prevent collisions between vessels.

3.2.1. Basic Concept on Hydrodynamic Interaction Simulation

The study of interaction between multiple floating structures system has been started long time ago and a lot of concepts to predict the hydrodynamic interaction phenomena have been introduced. In 1974, a practical theory to analyse hydrodynamic forces on multiple cylinders in waves has been introduced by Ohkusu (1974). The concept proposed was considered as the hydrodynamic interaction effect in multiple cylinders system. In the study, he investigated the

hydrodynamic forces acting on the cylinders in two dimensional study. Besides, Ohkusu (1974) also found that the magnitude of the interaction effect between vertical cylinders is roughly inversely proportional to the square root of the spacing between the cylinders. In general, his research shows that the wave exciting force leads to the structures motion in waves which are able to influence the hydrodynamic interaction effect between the cylinders in the system.

Besides that, an exact interaction theory based on linear potential theory to study the hydrodynamic interaction among multiple 3-D floating bodies has been introduced by Kagemoto and Yue (1987). This concept became the essential concept for further development in the method for hydrodynamic interaction study by many researchers. In the research conducted by Kagemoto and Yue (1987), their proposed interaction concept has been applied in the study of interaction between two elastically connected cylinders. Aluminium strip was used to connect both the cylinders in model experiment. Their simulation result shows that the concept is able to predict the strong interaction effect which can influence the pitch and heave motion of cylinders. Besides, they found that the interaction effect also induce surge motion for the structures at beam sea condition.

3.2.2. Phenomena on Multiple Structure Interaction

A research on hydrodynamic interaction between two vertical cylinders in waves by using linearized potential theory has been conducted by Zhou et al. (1996). The method proposed by them calculates the velocity potential by using Graf's addition theorem. Graf's addition theorem is also known as a Neumann's addition theorem. In the research, Zhou et al. (1996) found that the magnitude of wave exciting forces acting on cylinders depend on the incident wave angle and the separation distance between the cylinders. In addition, they also found that the increase in size of the front cylinder in tandem arrangement causes the motion on the back cylinder to reduce due to larger wake of the front cylinder. Besides, their research was also found that the added mass for articulated cylinder becomes minimum value if the incident wave is propagated in beam sea direction. At the beam sea condition, the radiation damping for the cylinder becomes maximum value at this incident wave angle.

The interaction phenomenon was also observed by Sannasiraj et al. (2001) in their study related to diffraction and radiation problem on multiple floating structures in directional wave. Finite element method of two dimensional models was applied in that research to

evaluate hydrodynamic coefficients and forces in an oblique wave field. In the research, they found that the interference resonant frequencies are maintained the same regardless any incident wave angle.

Besides, the study related to hydrodynamic interaction has been carried out by Chakrabarti (2000). He conducted a research to investigate hydrodynamic forces acting on multi-module structures. In addition, motion response due to the interaction of moored structures also has been investigated by him. The wave forces on the structures were estimated by using an analytical approach. Chakrabarti (2000) found that the wave force is mostly depending on the progressive wave coefficients. Besides, the interaction effect is able to give significant influence to close spaced module and this effect is increased when the spacing is decreased. His comparison has shown that both the interaction technique and complete diffraction technique used in his research are good. Based on experimental result, the interaction technique is more efficient and faster to analyse the multiple structures cases.

The effect of waves heading on hydrodynamic interaction has been investigated by Kim et al. (2002). The motion program used in the study was developed based on three dimensional linearized potential theories and three dimensional source distribution techniques. Their proposed method was applied to study interaction between barge and ship model. In their case study, the size of barge model selected is larger than ship model. On the other hand, Inoue and Ali (2003) also applied the similar technique to investigate the motion behaviour and second order wave drift force on multiple floating structures system. The same study was also repeated by Ali et al. (2010) again to study the hydrodynamic interaction between two rectangular boxes with different sizes. Their numerical result shows that the hydrodynamic loads and structures' response is changed rapidly along the wave frequency due to hydrodynamic interaction phenomena. One of the observations obtained in the study is the motion response of the ship in side by side arrangement is smaller when the model is arranged on the lee side compare to the motion response of the ship model when it is arranged on the weather side due to the sheltering effect. Besides, they also observed that the peak frequency of ship motion response is shifted to a higher frequency zone if the gap is reduced and this behaviour is caused by the standing wave between the two floating structures.

A numerical method has been employed by Zhu et al. (2006) to study the effect of gap in multiple box shape structures system. In that study, the potential of incident wave and scattering wave were ignored and the motion of the structures was assumed only affected by

radiated wave. The numerical method was used to calculate the interaction effect between the multiple structures. The gap distance selected in the research ranged from 1% of breadth to 50% of breadth. The simulation result obtained showed the hydrodynamic interaction between floating structures can influence the surge, sway and heave motion. However, only sway motion showed a strong interaction effect on certain resonance wave number. Besides, their study obtained showed that the increase of gap width causes the resonance amplitude for adding mass and damping coefficients to decrease significantly. Also, the effect of hydrodynamic interaction due to the numbers of floating structures to the motion response of the structures has been also studied by Tajali and Shafieefar (2011). Their research results showed that the increase in the amount of pontoons can cause the peak frequency and peak amplitude of all direction of motion to increase.

In order to improve the safety of FLNG, the hydrodynamic interaction between FLNG vessel and LNG carrier which arranged in side by side arrangement has been studied by Zhao et al. (2012). A numerical modelling based on potential theory was developed by them to study the case. In their study, they separated all six types of motions into two groups. There is low frequency motion which involve surge, sway and yaw while the second group of motion was named as wave frequency motion which include heave, roll and pitch motion. In their simulation, they observed that the hydrodynamic interactions give more influence to the low frequency motion. In addition, they found that this phenomenon can affect the load on the structures connection systems.

3.2.3. Application of Higher Order Boundary Element Method (HOBEM) in Hydrodynamic Interaction Study

Hierarchical interaction theory in the framework of linear potential theory was introduced by Kashiwagi (2000). His theory was applied in the research on hydrodynamic interaction between a large numbers of columns supporting flexible structure. To further the study, Kashiwagi et al., (2005) conducted a research to investigate the wave drift force and moment on two side by side arranged ships by using Higher-Order Boundary Element method (HOBEM). The HOBEM method proposed by them was validated by comparing the generated result from their method with the result from previous available methods and experiment. Their research showed that the hydrodynamic interaction forces are more

dominant in the motion equation in the shorter wavelength region due to resonant phenomena. Finally, they concluded that the intensity of the interaction force depends on the ratio of the wavelength to the separation distance between two adjacent cylinders. They also highlighted that the second order steady force on each structure is large in both sway and heave motion if the hydrodynamic interaction effect is taken into consideration.

In addition, the similar HOBEM method also has been developed by Hong et al. (2005). In that study, the HOBEM is combined with a generalized model approach and later used to study the structure motion response and the drift force of side-by side moored structures. From the study, the hydrodynamic interaction between multiple structures systems can generate the sheltering effects and resonance of trapped water between two floating structures. At the same time, the radiation problem exists in the multiple structure system due to the nearer structures act as a wave maker to generate extra wave to influence another structure. Besides that, the research also found that the wave drift force is not significantly affected by roll resonance motion in side-by-side moored structures arrangement.

3.2.4. Comparison of Available Numerical model for Hydrodynamic Interaction Study

The applicability of wave interaction theory to study multiple floating bodies arranged in very small gap distance has been investigated by Kashiwagi (2008) and Kashiwagi and Shi (2010). The motion of four identical boxes-shaped structures has been simulated by using their developed numerical method. The studies obtained that the wave interaction theory is able to predict the motion accurately if the separation between the structures is satisfied with the addition theorem of Bessel functions. They also highlighted that the horizontal wave force calculated by the theory at a very small separation distance is good, agreed with the result obtained from HOBEM. However, both theories shows different results when use to predict the vertical wave force.

Comparison between the capability of potential theory and viscous fluid theory to predict the fluid characteristic in the narrow gaps between the floating bodies has been conducted by Lu et al. (2011). Their simulation results show that the viscous fluid theory is able to show the fluid characteristic but the predicted result is slightly smaller than the experimental result. However, the potential theory is over predicting the fluid resonance amplitude. The over prediction of wave force by potential theory can be reduced by

modifying the theory with included artificial damping term, μ equal to 0.4 to 0.5. This modification would enable the potential theory to calculate the fluid resonance more accurately. The research also obtained almost similar finding as previous research and new finding of this study is the two peak wave forces that can be observed in two different frequencies if three floating bodies are in the system.

Furthermore, the liquid resonant motion confined between two floating structures has been simulated by Wang et al. (2011) using fully nonlinear theory. The simulation result shows that resonant phenomena causes significant resonant motion effect to angular cylinder. They also found that the linear theory may overestimate the resonant effect if it is applied for flare or curvature body. Similar theory also applies by Yan (2011). He used the nonlinear theory to study the hydrodynamic interaction between two floating structures in the small gap arrangement. His research observed a strong fluid resonance phenomenon in the gap between structures and strong effect of hydrodynamic interaction between structures. The strong hydrodynamic interaction effect is able to change the motion response of structures if two structures are placed in small distance.

3.2.5. Alternative Solution in Hydrodynamic Interaction Study

Some researchers also introduced an approximation method applicable for the hydrodynamic interaction study. An iterative procedure to study diffraction of wave by a vertical cylinder with circular cross section has been proposed by Yilmaz (2004). The proposed iterative method was developed to solve the body boundary condition for each cylinder in the system with considering the scattering wave field due to another nearby cylinders. In the research, he also highlighted that the number of iterations taken by his method should be increased to obtain a better accuracy of prediction if the distance between cylinders is decreased. Besides, the iterative method is more efficient and faster to simulate the interaction cases if the number of structures is large.

A design oriented semi-analytical method to solve the radiation problem and evaluate the hydrodynamic and interaction coefficients has been proposed by Mavrakos (2004). In addition, analytical approach for a solution of hydrodynamic diffraction by arrays of elliptical cylinders has been also introduced by Chatjigeorgiou and Mavrakos (2010). The semi-analytical solution was developed using Mathieu function. To further the study, Chatjigeorgiou (2011) developed his previous analytic solution to enable it to analyse the

hydrodynamic interaction effect between elliptical and circular cylinders structures. In the research, he found that the variation of hydrodynamic loading on the interaction cases is relative to the wave heading angle. Besides, the interaction effect also depends on total number of structures and the structures' arrangement in the system.

In addition, Siddorn and Taylor (2008) have been tried to solve the radiation and diffraction problem for an array of truncated cylinders in the frequency domain by using exact algebraic method. In their method, the accuracy of the calculation depends on the number of evanescent modes and the evanescent modes can be increased to improve the accuracy. The research also found that closer space between cylinders can lead to larger free surface elevation and wave forces. They also highlighted that the observed phenomena mostly depend on the frequency of the incident wave and its direction. Besides that, they also commented that the radiation impedance matrix can be influenced by wave number.

3.2.6. Relative Motion and Intact Force between floating structures

Research on relative motion and wave elevation between two floating structures also has been simulated by Fang and Chen (2001) using the linear potential theory. The method they used is able to simulate three dimensional hydrodynamic interaction effects. From the research, they found that three dimensional method is able to predict the structures motion more accurately compared to two dimensional method because standing wave is considered not fully trap in three dimensional method. Besides, relative motion between two moored floating structures in side by side arrangement was also investigated by Koo and Kim (2005). In that research, the combined matrix method for hydrodynamic interaction problem has been proposed by them. The method proposed by them can solve for all hydrodynamic coefficients of all hulls simultaneously. Besides, the research also found that the wave elevation is smaller on the lee side of the models compared to the weather side due to the sheltering effect.

On the other hand, Feng (2009) tried to investigate the effect of structural interaction from another point of view. His research focused on the force act on two cables-connect floating structure. The numerical simulation method for contact phase was developed by him using random contact kinematics and dynamic method. By comparing the numerical result to experimental result, it is shown that the impact force obtained by the numerical method is always larger than experimental result.

3.2.7. Application of Numerical Software in Hydrodynamic Interaction Study

Due to the complexity of actual structures' hull form, the hydrodynamic response of an offshore spar structure which is linked to semi-submersible under regular waves has been investigate by Nallayarasu and Prasad (2012) using experimental and numerical method (ANSYS-AQWA). In their simulation, they included the viscous damping coefficient to predict the motion response using the AQWA software. The viscous damping coefficient they applied was estimated from the model decay experiment. From both the experimental and numerical result, it is obtained that the response of the spar is reduced after linking to semi-submersible due to the interaction of radiation wave generated by both the structures. However, the research also found that the motion response for unmoored semi-submersible is increased after linked to spar.

The ANSYS-AQWA commercial software has been used by Farid (2014) to simulate the phenomena of hydrodynamic interaction between floating structures. He used the ANSYS-AQWA to simulate the motion of large floating structure when the selected floating structure is alone, when the selected floating structure is interacting with another one floating structure and when the selected structure is interacting with another two floating structures. Besides, the research has been considered the effect of different gap distance between floating structures and effect of incident wave propagation direction to the motion of selected floating structure. His research showed that the ANSYS-AQWA commercial software able to predict the hydrodynamic behaviour of floating structure with acceptable result in the conditions when the floating structure is alone and when the floating structure is interacting with other floating structure.

Besides that, Yus-Farid (2015) also has been conducted a research to study the effect of main deck diameter to the motion response of his new designed X-round shape floating structure. In the design study, he used ANSYS-AQWA as the research tool to simulate the hydrodynamic behaviour of the X-round shape floating structure. Compared to the hydrodynamic behaviour of round shape floating structure, he found that the X-round shape floating structure have lower motion amplitude in heave direction and pitch direction. But, the surge RAO of round shape floating structure and X-round shape floating structure are same. From his simulation research, it was obtained that the X-round shape floating structure have lower motion amplitude compare to round shape floating structure because the radiation damping and added mass of the X-round shape floating structure is larger.

3.2.8. Summary of Multiple Floating Structures' Hydrodynamic Interaction

From the available literatures, the existing methods to predict the interaction between floating structures were mostly developed based on diffraction potential theory. The accuracy of the methods which developed from the diffraction potential theory was reviewed from the literatures. As commented by Loken (1981), it is predicted that the diffraction potential theory would over predict the motion response of floating structure in resonance wave frequency region due to under prediction of radiation damping by the diffraction potential theory. However, the diffraction potential theory can predict the motion response of floating structure accurately other than the resonance region.

3.3. Time Domain and Frequency Domain Analysis of Hydrodynamic Interaction

The hydrodynamic resonance phenomena of three dimensional multiple floating structures has been studied by Zhu et al. (2008) using a time domain method. The research found that the peak force response on floating structures at resonance frequency is the same between the result obtained from frequency domain technique and time domain technique. This finding showed that the time domain linear potential theory can be an alternative solution to solve the problem related to motion response due to hydrodynamic interaction between the floating structures in small gap.

3.4. Factors Influence the Motion Response and Numerical wave

The influence of water depth to the wave kinematics, wave force and sea keeping has been investigated by Clauss et al. (2009) using panel code WAMIT. In their research, the hydrodynamic coefficient of the structure such as damping, added mass and exciting force were also calculated by panel code WAMIT in their research. Besides using the diffraction potential theory, CFD software is an alternative tool used to study the effect of wave to structure motion. Capability of CFD to simulate the wave has been investigated by Finnegan and Goggins (2012) by studying several types of numerical techniques to model the numerical

wave tanks (NWT's). The ANSYS CFX software which applies the finite volume technique was used in his research to generate the numerical wave tanks. The research obtained that ANSYS CFX software is able to achieve the target to simulate the linear regular wave in the numerical wave tank.

Besides that, Sun and Kang (2012) also has been studied the method to simulate the wave and flow based on the Navier-Stokes equation and Computational Lagrangian-Eulerian Advection Remap-Volume of Fluid (CLEAR-VOF). The Navier-Stokes equation was discretized using three-step finite element method. The purpose of the research is to establish the wave and fluid flow in two dimensional numerical methods. The research obtained that CLEAR-VOF method is also suitable to simulate the wave in both structured and unstructured meshes since the finite element method is applied. Therefore, the simulation of wave for complex boundaries is possible to achieve by their proposed method.

3.5. Non-Ship-Shape Large Floating Structure Developments and Studies

A study to compare the advantages and disadvantage of round-fit shape floating structure to traditional ship shape floating structure has been conducted by Lamport and Josefsson (2008). After that, Arslan, Pettersen, and Andersson (2011) also performed a study on fluid flow around the round shape floating structure in side-by-side offloading condition. Both of the studies obtained that hydrodynamic behaviour for round shape floating structure is better than traditional ship shape floating structure. Besides that, Lamport and Josefsson (2008) found that the round-shape floating structure have better offloading benefits where it can provide significant shielding from waves, winds and current. They commented that the horizontal rotation between structures can be achieved by using an offloading reel station. By using this suggested offloading system, the offloading operation envelope can be as large as 270 degree.

In addition, a non-ship-shaped circular FPSO concept which has a capability for round-the-year drilling and production operation within an Arctic Frontier Region has been proposed by Srinivasan et al. (2008). Another type of non-ship shape FPSO was also designed by Wang, Zhang, and Liu (2012) and their designed floating structure has been named as inverted fillet quadrangular frustum pyramid-shaped structure (IQFP). Their study obtained that the IQFP has larger stability margin and better hydrodynamic performance compare to the ship-shaped floating structure.

3.6. Effect Mooring on Large Floating Structure Wave Frequency Motion

Typically, floating structures is fixed at the position using mooring system. Due to the extra weight contribute from the mooring system to the floating structures; the effect from the mooring cables may affect the motion characteristic of the floating structures. Recently, a study on the effect of mooring lines arrangement to the motion of spar platform has been conducted by Montasir et al. (2015). They studied the effect of the symmetric mooring configuration and asymmetric mooring configuration to the response of the selected truss spar model. Based on their study, the mooring system designed with different configurations do not cause any significant effect on horizontal type wave frequency motion and the effect of mooring to heave wave frequency motion is absolutely does not exist. However, the mooring system would give a significant effect on the initial offset of the truss spar model and influence the slow vary motion which is induced by drift force.

The floating structures on open sea experience two types of motions there are wave frequency motion and low frequency motion. According to Dercksen and Wichers (1992), the low frequency motion is induced by wind, current and wave drift force but the wave frequency motion is induced by first order wave force. In these two types of motions, only the low frequency motion corresponds to the mooring system's natural frequency. They commented that the low frequency motion is a type of resonance motion and is able to induce very large displacements and mooring force. Besides, Fitzgerald and Bergdahl (2007) also commented that the influence of mooring system to wave frequency motion response of large floating structure such as FPSO or FLNG is often negligible in the general offshore engineering practice. The similar opinion also mentioned by Cozijn and Bunnik (2004) in their study on the effect of coupled mooring effect to deep water calm buoy. They stated that the mooring coupling only affect the low frequency motion of large size floating structures but the wave frequency motion of the large structures would not be affected by the mooring coupling effect generally. In addition, another similar study has been conducted by Heurtier (2001) to study the effect of mooring coupled to the dynamic response of large floating structure. In his research, the effect of mooring to the response of floating structures was studied using time domain simulation method and his simulations were made for the conditions where the mooring system is coupled and the mooring system is uncoupled to the motion of large floating structure. From the simulation results, he observed that the response

amplitude operator of the selected large floating structure executed by coupled simulation and uncoupled simulation is almost similar. The mooring only have relatively small effect on the large floating structure surge dynamic motion and it does not have mooring effect on heave dynamic motion observed from his simulation.

In order to study the effect of mooring system to the motion of large floating structure in detail, Soares et al. (2005) has been conducted both experimental study and numerical study to estimate the motion of moored large floating structure in waves. In their experiment setup, the large floating structure was fixed in tank using six lines single point mooring system scaled to model size. In their numerical simulation, the motion of large floating structure was calculated by both the strip theory and panel method. The panel method program used for the calculation was WAMIT code. In their panel method, they made the calculation for the cases including the mooring force and without including the mooring force. In the comparison, the results from the panel method showed a very good prediction of the motion response of the floating structure in all directions of motion when compared to their experimental result. Besides, they also compared the panel method results which executed the motion response of large floating structure including mooring force and without including the mooring force in the calculation. In comparison, the panel method results showed that the effect of mooring system to the wave frequency oscillatory motion of the floating structure was very small hence they concluded that the mooring force have a negligible effect in calculating the wave frequency motions. Also, this shows that the panel method without including the mooring force in the estimation of the large size floating structure motion response amplitude is still able to provide good and accurate prediction.

From the literature reviewed, it is obtained that the mooring system would affect the low frequency motion of the large floating structure where the motion is induced by wind, current and wave drift force. However, the mooring system only has negligible effect to the wave frequency motion of the large floating structure where the motion is induced by first order wave force. This opinion is also similar with Yong et al. (2004). They commented that the mooring effect to the wave frequency motion of large size floating structure can be negligible when the wave amplitude is small because the inertial properties of the large floating structure have a higher order of magnitude compare to the mooring lines and riser. Therefore, the effect of the mooring system to the large floating structure wave frequency motion become relatively small and could be ignored directly in moderate sea state.

3.7. Effect of Regular and Irregular Wave on Motion of Floating structure

The dynamic motion of floating structure can be estimated by using regular and irregular wave simulation. The motion of floating structure in regular wave condition and irregular wave condition has been studied by Yu (1995). He conducted experiment test to simulate the motion of floating dock in regular wave and irregular wave condition so his research able to compare the different of response amplitude operate (RAO) of the moored floating dock simulated by both regular and irregular wave condition. From his experiment test, he obtained that the RAO of the floating dock simulated by regular and irregular wave condition are agreed between each other. Besides, he also found that the RAO of floating dock remains constant regardless of wave height selected in experiment test. His research concluded that the regular wave simulation is preferred if the maximum value of the motion is targeted in the research while irregular wave simulation is better for simulate the significant value of motion in wave.

In addition, Shen et al. (2004) has been conducted a research on ship motion using their proposed unsteady incompressible Reynolds-Average Navier-Stokes method (URANS). In their study, they simulated the ship motion in regular wave condition and irregular wave condition numerically in order to calculate the RAO of ship. The numerical result also compared to experiment result in purpose to verify their method. In their comparison, the simulation result calculated by regular wave condition and irregular wave condition are closely agree between each other. They commented that the existed small difference between the results is negligible. Besides that, both the simulation results generated by regular wave and irregular wave test shows good agree with experiments result.

On the other hand, a study to test the accuracy of DREA's strip theory based, linear frequency domain code (SHIPMO) has been conducted by Menon and Vienneau (1992). They compared the RAO of their model ship calculated by SHIPMO with the RAO of the ship obtained from regular wave experiment and irregular wave experiment. From their research, they found that the RAO calculated by SHIPMO is agreed with the RAO results from both the regular wave experiment and irregular wave experiment. However, the comparison shows that the RAO from SHIPMO is closer correlation with the RAO from regular wave experiment. Besides, Menon and Vienneau (1992) also commented that

experiment tests in irregular oblique waves may not return data suitable for correlation of the predicted RAO of ship in some cases. This is because in irregular wave test may include insufficient number of encounters, unavailability of phase data and degree of short crestedness in the case of data collect under natural conditions.

From the literature reviewed, it is found that the RAO of the floating structure can be estimated using the regular wave test or irregular wave test. This is because both the regular wave test and irregular wave test are able to predict the RAO of floating structure with the similar tendency. However, as mentioned by Yu (1995), regular wave test is more suitable to find the maximum value of RAO of floating structure due to the wave force. On the other hand, the irregular wave test will show more exact hydrodynamic behavior of the floating structure when the structure operate in the design operating condition.

3.8. Summary

This chapter presents the literature review about previous work done by other researchers. The phenomena of the hydrodynamic interaction between the multiple floating structures system were reviewed. Besides that, this chapter also reviews the limitation of simulation and capability of computer hardware to simulate the hydrodynamic fluid structure interaction cases. From this chapter, the factors that would influence the wave frequency motion of floating structure are also presented. From the literatures reviewed, the methodology of this research is designed and presented in Chapter Three.

Chapter 4

4.0. Basic Hydrodynamic Theories of Floating Structures

Motions and hydrodynamic coefficient of floating structures can be estimated using several theories. In this book, the diffraction potential theory was selected as the basic theory in predicting the motions of floating structures. In this chapter, the mathematical models discussed are diffraction potential theory and the method to solve the theory in numerical method. Besides, the drag equation is also presented in this chapter to describe the basic idea of this method in estimating the hydrodynamic force act on floating structures.

4.1. Diffraction Potential Theory

The floating structures float on the sea surface is forced to oscillate according to the frequency of wave. Typically, the fluid is assumed to be incompressible, irrational, in-viscid and negligible surface tension. If the motion is in steady state condition and the floating structure motion amplitude is relatively small, then the linear term of free surface condition, kinematic boundary condition and the Bernoulli equation can be ignored. In this condition, the hydrodynamic force or moment induce on the wetted surface of floating structures can be obtained by integrating the hydrodynamic pressure acting on the surface of floating structure which is obtained from the linear Bernoulli equation by using known velocity potentials in the desired direction.

In this book, the three dimension potential theory was applied to predict the motion of floating structures. The theory was applied to arbitrarily shape of floating structures and it was developed based on right-handed, earth-bound coordinated system origin at the mean water level and the Z-direction is positive downward. In this study, the water depth is assumed infinite depth condition.

4.1.1. 3-Dimension Diffraction Theory

In Figure 4.1, it shows the flow area, namely the wetted surface area of floating structure, S_H, the free surface area, S_F, the boundary located in the infinity distance, S_∞ and the seabed surface, S_B, will influence the hydrodynamic force. The mathematical model presented in this part are assumed that the wave attach angle is zero at positive X-axis and rotate toward positive Y-axis as shown in the Figure.4.1.

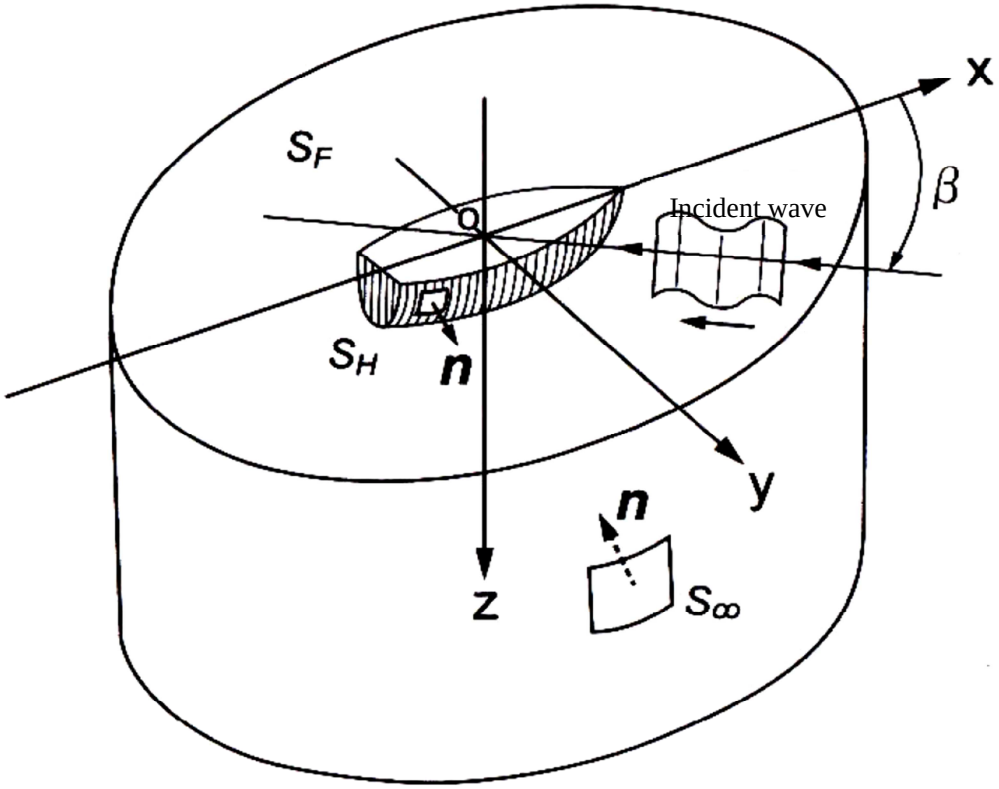

Figure 4.1: Definition of direction, coordinates and variables in diffraction potential theory (Kashiwagi et al., 2003).

The regular wave acts upon the floating structure can be described from the velocity potential. Based on the linear potential theory, the flow potential around the floating structures can be summed up by superposition theory where it involves superposition of undisturbed incident wave, ϕ_I, the wave diffracted from incident wave due the exist of floating structure, ϕ_S and the radiating wave potential, ϕ_R generated by the six degree motion of floating structure. The velocity potential equation is normally written in respective to the flow direction and the time is as shown below (Kashiwagi, 2008).

$$\Phi(x,y,z,t) = Re\left[\phi(x,y,z)e^{iwt}\right] = \frac{g\varsigma_a}{iw}\phi_D + \phi_R \qquad (4.1)$$

Where; g is gravity acceleration, ς_a is the incident wave amplitude, w is the circular frequency.

The first part of equation (4.1) is sum of the incidents-wave potential (ϕ_I) and the scattering wave potential (ϕ_S) which is referred as the total diffraction potential (ϕ_D) as expressed as in equation (4.2).

$$\phi_D = \underbrace{\{\phi_I(x,y,z) + \phi_S(x,y,z)\}}_{\text{Potential for diffraction wave}} \qquad (4.2)$$

Second part of the equation (4.1) represents the radiating potential (ϕ_R).

$$\phi_R = \underbrace{\sum_{j=1}^{6} iwX_j\phi_j(x,y,z)}_{\text{Potential for Radiation wave}} \qquad (4.3)$$

Where; X_j refer to motions amplitude which can be determined by solving the motion equation.

$\phi_j$is the radiation wave potential due to motions. In the radiating component, *j* refers to the *j*-th mode of motion, where *j*=1 is surge, *j*=2 is sway, *j*=3 is heave, *j*=4 is roll, *j*=5 is pitch, *j*=6 is yaw.

The equations above show the total wave potentials in the system which are contributed by the potential of incident wave, ϕ_I, scattering wave, ϕ_S and radiating wave, $\emptyset_R$. The phase and amplitude for both the incident wave and scattering wave are assumed to be the same. Radiating wave potential ($\emptyset_R$) is produced by the motion of the each single floating structure, whereas the total potential of radiating wave generated by each single structure is the summation of the radiating wave generated by each direction of the structures' motion.

The diffraction wave potential (ϕ_D) and radiating wave potential ($\emptyset_R$) must fulfil the conditions below (Kashiwagi, 2008).

i. Laplace equation

$$\nabla^2\phi_D = 0 \quad \text{and} \quad \nabla^2\phi_R = 0 \quad for\ 0 \le z \le h \tag{4.4}$$

ii. Free surface boundary condition

$$\frac{\partial\phi_D}{\partial z} + k\phi_D = 0 \quad \text{and} \quad \frac{\partial\phi_R}{\partial z} + k\phi_R = 0 \quad \text{at } z = 0 \tag{4.5}$$

iii. Sea bed boundary condition

$$\frac{\partial\phi_D}{\partial z} = 0 \quad \text{and} \quad \frac{\partial\phi_R}{\partial z} = 0 \quad \text{at } z = \infty \tag{4.6}$$

iv. Radiating Condition

The condition stated that the diffraction potential and the radiating potential would disappear when the distance from the floating structures is of great distance.

$$\phi_D \sim \frac{1}{\sqrt{r}} e^{-ik_0 r} \quad \text{and} \quad \phi_R \sim \frac{1}{\sqrt{r}} e^{-ik_0 r} \text{ should be 0 if } r\ \infty \tag{4.7}$$

v. Kinematic sea-surface condition

The condition is applied to submerge surface area of the floating structure in its mean position.

$$\frac{\partial\phi_D}{\partial\vec{n}} = 0 \quad \text{and} \quad \frac{\partial\phi_{R,j}}{\partial\vec{n}} = n_j \tag{4.8}$$

Where; n_j is the normal vector of the hull in direction j and it is positive into the fluid.

The velocity potential for the incident wave ($\emptyset_I$) is a type of surface wave, hence it is expressed in Euler form as shown as follow.

$$\phi_I = e^{-Kz+iK(x\cos\beta+y\sin\beta)} \tag{4.9}$$

Where; β is the coming angle of incident wave relative to the x-axis (Figure 6.1).

Besides, the radiated wave ($\emptyset_R$) is the wave potential related to the structure's motion. The velocity potential for the radiated wave is shown below.

$$\emptyset_R = \sum_{j=1}^{6} iwX_j\phi_j(x,y,z) \tag{4.10}$$

The wave potential (ϕ_j) due to the continuous surface of fluid can be explained by the following equation (Chakrabarti, 2000).

$$\phi_j(\bar{P}) = \iint_S \left\{\frac{\partial\phi_j(\bar{Q})}{\partial\vec{n}_{\bar{Q}}}G(\bar{P};\bar{Q}) - \phi_j(\bar{Q})\frac{\partial G(\bar{P};\bar{Q})}{\partial\vec{n}_{\bar{Q}}}\right\}dS(\bar{Q}) \tag{4.11}$$

From equation (4.11), the wave potential function at point *P* on the wetted floating structure surface due to the motion of the floating structure (*j*=1 to 6) and diffraction potential, (*j*=*D*) are represented by continuing distribution of wave sources over the mean wetted structure surface. $\phi_j(\bar{P})$ is the potential function on the wetted floating structure surface in a coordinate (x, y, z). In the diffraction case where (*j*=*D*), the potential is the diffraction potential. However, in the radiating case where (*j*=1 to 6), the potential is caused by the motion of the floating structure in the j^{th} direction. All potentials must fulfill all the boundary conditions.

In equation (4.11), $\phi_j(\bar{Q})$ represents the source strength on the surface area located at a coordinate$(\bar{a}, \bar{b}, \bar{c})$. The source strength is from the motion of the floating structure in the j^{th} direction. $G(\bar{P}; \bar{Q})$ in the equation (4.11) is the Green function of the pulsating source $\phi_j(\bar{Q})$ in the coordinate $(\bar{a}, \bar{b}, \bar{c})$ and on the potential located at (x, y, z). The Green function also fulfils the Laplace equation, free surface boundary condition, sea bed boundary condition and radiation condition. The surface $S(\bar{Q})$ in the equation (4.11) consists of wetted surface area of floating structure, free surface area, the boundary located in the infinity distance and the seabed surface.

Since the study focuses on the flow around the floating structure, the surface integration should focus on the wetted surface area of floating structure, S_H. In the case of structure floating on free surface, the surface integration can be written as follow (Kashiwagi et al., 2003).

$$\frac{1}{2}\phi_j(\bar{P}) = \iint_{S_H} \left\{ \frac{\partial \phi_j(\bar{Q})}{\partial \vec{n}_{\bar{Q}}} - \phi_j(\bar{Q}) \frac{\partial}{\partial \vec{n}_{\bar{Q}}} \right\} G(\bar{P}; \bar{Q}) dS(\bar{Q}) \qquad (4.12)$$

In radiating case, the kinematic sea-surface condition as shown in equation (4.8) is applied in equation (4.12). The surface integration equation in equation (4.12) can be rewritten as follow.

$$\frac{1}{2}\phi_j(\bar{P}) = -\iint_{S_H} \phi_j(\bar{Q}) \frac{\partial}{\partial \vec{n}_{\bar{Q}}} G(\bar{P}; \bar{Q}) dS(\bar{Q}) + \iint_{S_H} n_j G(\bar{P}; \bar{Q}) dS(\bar{Q}) \qquad (4.13)$$

Where in equation (4.13), j=1 to 6.

In diffraction case, the diffraction wave potential refers to the total of incident wave potential and scattering wave potential as shown in equation (4.2), $\phi_D = \phi_I + \phi_S$. According to radiating boundary condition, the scattering wave disappeared when the distance from the floating structure is far enough. Therefore, surface integration in the boundary surface located at the infinity distance from the floating structure only need to consider the incident wave potential. Besides, the kinematic sea-surface condition as shown in equation (4.8) for diffraction case state that differentiation of the diffraction potential to surface normal

direction at wetted surface of floating structure is zero, $\partial\phi_D/\partial\vec{n} = 0$. Thus, equation (4.11) for diffraction case can be written as follow.

$$\frac{1}{2}\phi_D(\bar{P}) = -\iint_{S_H} \phi_D(\bar{Q})\frac{\partial}{\partial\vec{n}_{\bar{Q}}}G(\bar{P};\bar{Q})dS(\bar{Q}) + \iint_{S_\infty}\left\{\frac{\partial\phi_I(\bar{Q})}{\partial\vec{n}_{\bar{Q}}} - \phi_I(\bar{Q})\frac{\partial}{\partial\vec{n}_{\bar{Q}}}\right\}G(\bar{P};\bar{Q})dS(\bar{Q}) \quad (4.14)$$

Integration of variable $\phi_I(\bar{Q})$ and $G(\bar{P};\bar{Q})$ in the second term on the right side of equation (4.14) to the boundary surface located at the infinity distance from the floating structure using Green Equation can obtain the undisturbed incident wave potential function on the wetted floating structure, $\phi_I(\bar{P})$. Therefore, equation (4.14) is rewritten as follow.

$$\frac{1}{2}\phi_D(\bar{P}) = -\iint_{S_H} \phi_D(\bar{Q})\frac{\partial}{\partial\vec{n}_{\bar{Q}}}G(\bar{P};\bar{Q})dS(\bar{Q}) + \phi_I(\bar{P}) \quad (4.15)$$

By rearranging equation (4.13) and equation (4.16) with all the collected unknown variables to the left and the known variables to the right, the equation can be written as in equation (4.16).

$$\frac{1}{2}\phi_j(\bar{P}) + \iint_{S_H} \phi_j(\bar{Q})\frac{\partial}{\partial\vec{n}_{\bar{Q}}}G(\bar{P};\bar{Q})dS(\bar{Q}) = \begin{cases} \iint_{S_H} n_j(\bar{Q})G(\bar{P};\bar{Q})dS(\bar{Q}) & \text{if} \quad j = 1 \text{ to } 6 \\ \phi_I(\bar{P}) & \text{if} \quad j = D \end{cases} \quad (4.16)$$

From equation (4.11) to equation (4.16),

$$G(\bar{P};\bar{Q}) = \frac{1}{4\pi}\left[-\left(\frac{1}{r}+\frac{1}{r_1}\right)+G_W(X,Y)\right] \tag{4.17}$$

And

$$\left.\begin{matrix} r \\ r_2 \end{matrix}\right\} = \sqrt{(x-\bar{a})^2+(y-\bar{b})^2+(z\mp\bar{c})^2} \tag{4.18}$$

$$X = K\sqrt{(x-\bar{a})^2+(y-\bar{b})^2}\,, \qquad Y = K(z+\bar{c}) \tag{4.19}$$

In equation (4.18) and equation (4.19), $G_W(X,Y)$ represents the Green surface wave function. The coordinate *P*(x, y, z) is the point of potential function while $Q(\bar{a},\bar{b},\bar{c})$ is the point of the source.

4.1.2. Constant Panel Method on Solving 3-Dimension Diffraction potential Theory

The equation (4.16) is required to solve by numerical solution especially the equation is applied to predict the hydrodynamic pressure on complex floating structure. Typically, the potential function in equation (4.16) is solved using constant panel method. Using this method, immerge area of the floating structure is subdivided into a number of panels, *N*. The normal vector, n_j and the incident wave potential, $\phi_I(P)$ on each panel can be calculated by direct mathematical equation. Hence, all the variables on the right side of equation (4.16) are known.

The numerical equation of equation (4.16) after equation (4.17) is inserted is shown as follow.

$$\frac{1}{2}\phi_j(\bar{P}_m)+\frac{1}{4\pi}\sum_{n=1}^{N}\phi_j(\bar{Q}_n)\left[\left\{-\frac{\partial}{\partial\vec{n}_{\bar{Q}}}\left(\frac{1}{r}+\frac{1}{r_1}\right)+\frac{\partial}{\partial\vec{n}_{\bar{Q}}}G_W(\bar{P}_m,\bar{Q}_n)\right\}\Delta S_n\right]$$

$$=\frac{1}{4\pi}\sum_{n=1}^{N}n_j(\bar{Q}_n)\left[\left\{\left(\frac{1}{r}+\frac{1}{r_1}\right)+G_W(\bar{P}_m,\bar{Q}_n)\right\}\Delta S_n\right]$$

$$= \phi_I(\bar{P}_m) \quad ; \ m = 1 \text{ to } N \tag{4.20}$$

To simplify equation (4.20), the whole equation can be multiplied by 4π and rewritten in the following form.

$$2\pi\phi_j(\bar{P}_m) + \sum_{n=1}^{N} \phi_j(\bar{Q}_n)\left[-D_{mn} + \left\{\frac{\partial}{\partial n_Q} G_W(\bar{P}_m, \bar{Q}_n)\right\}\Delta S_n\right]$$
$$= \sum_{n=1}^{N} n_j(\bar{Q}_n)[-S_{mn} + \{G_W(\bar{P}_m, \bar{Q}_n)\}\Delta S_n]$$
$$= 4\pi\phi_I(\bar{P}_m) \quad ; \ m = 1 \text{ to } N \tag{4.21}$$

Where the unknown D_{mn} and S_{mn} are the normal dipoles over a quadrilateral panel and source over a quadrilateral panel.

$$D_{mn} = \iint_{S_n} \frac{\partial}{\partial n_{\bar{Q}}}\left(\frac{1}{r} + \frac{1}{r_1}\right) dS(\bar{Q}) \tag{4.22}$$

$$S_{mn} = \iint_{S_n} \left(\frac{1}{r} + \frac{1}{r_1}\right) dS(\bar{Q}) \tag{4.23}$$

The solution of distribution of normal dipoles, D_{mn} and source, S_{mn} over a quadrilateral panel can be solved using the Newman method (Newman, 1986). In this case, only the wetted surface area of floating structure has to be considered in obtaining the normal dipole and source.

The general solution for green surface wave, $G_W(\bar{P}_m, \bar{Q}_n)$ in equation (4.20) and equation (4.21) is shown as follow.

$$G_W(\bar{P}, \bar{Q}) = -2K\hat{G}(X, Y) \tag{4.24}$$

$$\frac{\partial}{\partial \vec{n}_{\bar{Q}}} G_W(\bar{P}, \bar{Q}) = -2K^2 \left[\frac{n_x(\bar{a} - x) + n_y(\bar{b} - y)}{R} \frac{\partial \hat{G}}{\partial X} + n_z \frac{\partial \hat{G}}{\partial Y} \right] \tag{4.25}$$

$$\hat{G}(X, Y) = R_0(X, Y) - i\pi e^{-Y} \boldsymbol{J_0}(X) \tag{4.26}$$

$$\frac{\partial \hat{G}}{\partial X} = R_1(X, Y) + i\pi e^{-Y} \boldsymbol{J_1}(X) \tag{4.27}$$

$$\frac{\partial \hat{G}}{\partial Y} = -\frac{1}{\sqrt{X^2 + Y^2}} - \hat{G}(X, Y) \tag{4.28}$$

From equation (4.24) to equation (4.28), variables X, Y are the same as equation (4.19). The coordinate $\bar{P}$(x, y, z) is the point of potential function while $Q(\bar{a}, \bar{b}, \bar{c})$ is the point of the source.

Where n_x is the normal vector of the panel in x-direction, n_y is the normal vector of the panel in y-direction, n_z is the normal vector of the panel in z-direction, $\boldsymbol{J_0}$ is the first kind of Bessel function in order 0, $\boldsymbol{J_1}$ is the first kind of Bessel function in order 1, R_0 is the real part of the wave term, R_1 is the derivative of R_0 with respect to X.

In diffraction cases, the right side of integration equation (4.20), $\phi_I(\bar{P}_m)$ can be estimated using wave equation (4.9). The wave potential in X direction and Y direction is related to the combination of trigonometry functions expend from wave equation (4.9). By applying Euler's theorem, equation (4.9) can be rewritten as follow.

$$\begin{aligned} \phi_I = \; & e^{-Kz} \\ & \cdot \{\cos[k(x \cdot cos\beta + y \cdot sin\beta)] \\ & + i \sin[k(x \cdot cos\beta + y \cdot sin\beta)]\} \end{aligned} \tag{4.29}$$

Equation (4.29) can be expended using trigonometry theory to obtain the final solution as follow.

$$\phi_I = e^{-Kz} \cdot \{\cos kx \cos\beta \cos ky \sin\beta - \sin kx \cos\beta \sin ky \sin\beta + i \cdot [\sin kx \cos\beta \cos ky \sin\beta + \cos kx \cos\beta \sin ky \sin\beta]\} \quad (4.30)$$

From equation (4.30), it is obtained that the incident wave potential can be divided into four terms and each term represents the incident wave potential in each respected direction. The four terms of wave potential divided from equation (4.30) are X direction, Y direction, Z direction and N direction which represent the yaw direction. To select the incident wave term for X, Y, Z, N direction, the following trigonometry theory are applied (Kashiwagi et al., 2003).

i. Flow velocity in X direction:
   The maximum velocity obtained when wave angle, β is zero degree and the zero velocity at wave angle, β is 90 degree.

ii. Flow velocity in Y direction:
   The maximum velocity obtained when wave angle, β is 90 degree and the zero velocity at wave angle, β is zero degree.

iii. Flow velocity in Z direction:
   The wave velocity should not equal to zero at any wave angle, β.

iv. Flow velocity in N direction:
   The wave velocity become zero when wave angle, β equal to zero degree and 90 degree.

Hence, the wave potential in the direction X, Y, Z, N can be obtained from equation (4.30) based on the stated assumptions above. Where,

$$\left.\begin{aligned}\phi_I^X &= e^{-Kz}\cdot \sin kx \cos\beta \cos ky \sin\beta \\ \phi_I^Y &= e^{-Kz}\cdot \cos kx \cos\beta \sin ky \sin\beta \\ \phi_I^Z &= e^{-Kz}\cdot \cos kx \cos\beta \cos ky \sin\beta \\ \phi_I^N &= -e^{-Kz}\cdot \sin kx \cos\beta \sin ky \sin\beta \end{aligned}\right\} \quad (4.31)$$

By considering the floating structure is symmetry in Y –axis, the radiating wave generated by each type of motion is related to the normal vector on the wetted surface and incident wave potential can be separated into four main types as presented in equation (4.31), then wave exciting force or moment induce the motions of floating body can be grouped as follow.

i. Flow velocity in X direction:
   Surge motion (j=1) and pitch motion (j=5)
ii. Flow velocity in Y direction:
   Sway motion (j=2) and Roll motion (j=4)
iii. Flow velocity in Z direction:
   Heave motion (j=3)
iv. Flow velocity in N direction:
   Yaw motion (j=6)

Finally, assumption is made that immerge area of the floating structure is subdivided into a number of panels, N. Therefore, equation (4.21) can be transformed into N set of simultaneous linear equation with N unknown complex source strength as shown in the following matrix.

$$\begin{pmatrix} A_{1,1} & \cdots & A_{1,N} \\ \vdots & \ddots & \vdots \\ A_{N,1} & \cdots & A_{N,N} \end{pmatrix} \cdot \begin{pmatrix} \phi_{j,1} \\ \vdots \\ \phi_{j,N} \end{pmatrix} = \begin{pmatrix} B_{j,1} \\ \vdots \\ B_{j,N} \end{pmatrix} \quad (4.32)$$

Where, j=1 to 6 in radiation case and j=D in diffraction case.

$$A_{n,n} = 2\pi \quad (4.33)$$

$$A_{n,m} = \left[-D_{mn} + \left\{ \frac{\partial}{\partial \vec{n}_{\bar{Q}}} G_W(\bar{P}_m, \bar{Q}_n) \right\} \Delta S_n \right] \quad (4.34)$$

$$B_{j,m} = \sum_{n=1}^{N} n_j(\bar{Q}_n)[-S_{mn} + \{G_W(\bar{P}_m, \bar{Q}_n)\}\Delta S_n] \quad \text{in radiating case} \quad (4.35)$$

$$B_{j,m} = 4\pi\phi_I(\bar{P}_m) \quad \text{in diffraction case} \quad (4.36)$$

The matrix equation (4.32) represents the total N number of unknowns and N number of simultaneous linear equations. Therefore, the matrix equation (4.32) can be solved using direct solution method. Once the matrix equation (4.32) is solved, the diffraction wave potential and radiating wave potential on each panel located on the wetted surface of floating structures are obtained. In this book, the direct solution method applied in solving the complex matrix equation (4.32) is Gauss's elimination method using pivoting technique.

4.1.3. Solution of Source and Normal Dipoles over a Quadrilateral Panel

Equation (4.21) has shown the numerical solution to solve the boundary condition integration equation. In the equation, the wetted surface of floating structure is divided into N number of panels. In order to solve equation (4.21), the source, *Ss* and normal dipole, *Dd* over a quadrilateral panel have to be computed accurately on each panel. The equations to calculate the normal dipole and source are shown in equation (4.22) and (4.23) respectively. In this book, assumption is made that the wetted surface is covered by N number of rectangle panels. The solution to solve equation (4.22) and equation (4.23) was explained by Newman (Newman, 1986).

By considering the field point coordinate, $\bar{P}$ as (x, y, z), the flat quadrilateral panel is in the plane z=0 with vertices at the point $x = \xi_n$and $y = \eta_n$ and n=1 to 4 as it is a rectangle panel. The potential at coordinate $\bar{P}$ due to the distribution of normal dipoles, *Dd* and source distribution, *Ss* with the constant strength of -4π over the panel is written as follow.

$$Dd = \iint \left[\frac{\partial}{\partial \zeta} \left(\frac{1}{r} \right) \right]_{\zeta=0} d\xi \, d\eta = - \iint \left[\frac{\partial}{\partial z} \left(\frac{1}{r} \right) \right]_{\zeta=0} d\xi \, d\eta \quad (4.37)$$

$$Ss = \iint \left[\left(\frac{1}{r}\right)\right]_{\zeta=0} d\xi\, d\eta = \int_z^{\infty} Dd\, dz = -\int_z^{\infty} z\, dDd - zDd \qquad (4.38)$$

Equation (4.37) is the surface integrals over the domain of the panel. The value of *Dd* in equation (4.37) is equal to the panel's solid angle viewed from the field point $\bar{P}$. The solid angle also has similar algebraic convention sign as *z*. The solid angle can be defined from elementary plane geometry and it is related to independent properties of each vertex.

The solid angle covered by a surface is defined as the surface area of a unit sphere covered by the surface's projection onto the sphere and the equation can be written as follow.

$$\varpi = \iint_S \frac{\vec{n} \cdot r}{r^2} \Delta S = \iint_S \frac{\partial}{\partial \vec{n}_{\bar{Q}}} \left(\frac{1}{r}\right) dS \qquad (4.39)$$

Where $\vec{n}$ is the unit vector from the origin, $\bar{P}$, dS is the differential area of the surface and r is the distance from the origin to the surface, *dS*. The solid angle is measured in steradians. If the surface is covered by the whole sphere then the number of steradians is 4π. By comparing equation (4.39) to equation (4.22), the solution for equation (4.22) can be obtained if the solid angle between field point, P with vertex can be executed.

According to Newman (1986), equation (4.37) and equation (4.38) can be transformed to direct numerical solution. The numerical solution for both the equations provided by Newman (1986) is shown in equation (4.40) and (4.41).

First, the execution should be conducted in local coordinate system and the panel surface is assumed at *z*=0. In Figure 4.2, local coordinate of each vertex is $x = \xi_n, y = \eta_n$ and *n*=1 to 4. The length of each side of the square panel is s_n and *n*=1 to 4. Therefore, the normal dipole and source at coordinate $\bar{P}$(x, y, z) due to vertex at $\bar{Q}(\xi_n, \eta_n, 0)$ can be calculated by equation (4.40) and (4.41).

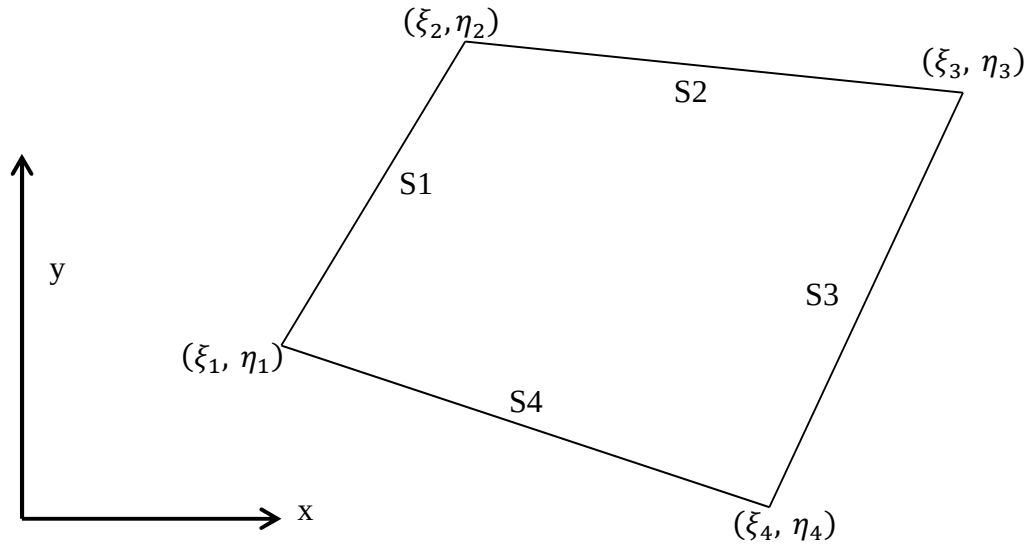

Figure 4.2: Local coordinate of each vertex in plan view

$$Dd = \sum_{n=1}^{4} \left\{ \tan^{-1} \frac{\delta\eta_n[(x-\xi_n)^2 + z^2] - \delta\xi_n(x-\xi_n)(y-\eta_n)}{R_n z \delta\xi_n} - \tan^{-1} \frac{\delta\eta_n[(x-\xi_{n+1})^2 + z^2] - \delta\xi_n(x-\xi_{n+1})(y-\eta_{n+1})}{R_{n+1} z \delta\xi_{n+1}} \right\} \quad (4.40)$$

$$Ss = \sum_{n=1}^{4} [(x-\xi_n)\sin\theta_n - (y-\eta_n)\cos\theta_n] \log \frac{R_n + R_{n+1} + s_n}{R_n + R_{n+1} - s_n} - zD \quad (4.41)$$

Where,

$$\delta\xi_n = \xi_{n+1} - \xi_n \quad (4.42)$$

$$\delta\eta_n = \eta_{n+1} - \eta_n \quad (4.43)$$

$$R_n = \sqrt{(x-\xi_n)^2 + (y-\eta_n)^2 + z^2} \quad (4.44)$$

$$R_{n+1} = \sqrt{(x-\xi_{n+1})^2 + (y-\eta_{n+1})^2 + z^2} \quad (4.45)$$

$$\theta_n = \tan^{-1}\frac{\delta\eta_n}{\delta\xi_n} \tag{4.46}$$

4.1.4. Solution for Real Part of Wave Term of Three Dimension Green Function

The solution for green surface wave, $G_W(\bar{P}_m, \bar{Q}_n)$ is shown from equation (4.24) to equation (4.28). In these equations, $\boldsymbol{J_0}$ and $\boldsymbol{J_1}$ are the Bessel function of First Kind in order 0 and 1 respectively. While, the R_0 and R_1 are the real part of the wave term and derivative of R_0. To obtain the value of $\boldsymbol{J_0}, \boldsymbol{J_1}$, R_0 and R_1 which are required in calculating the green surface wave $G_W(\bar{P}_m, \bar{Q}_n)$ in equation (4.24), this book used the subroutine provided by Prof Takagi Ken from Tokyo University (Kashiwagi et al., 2003). The subroutine solves the variables in non-dimensional form. To apply the subroutine in execution, it is assumed that variable P_m in equation (4.24) is the coordinate of field point and it is labelled as coordinate $\bar{P}_m(x, y, z)$. Variable Q_n in equation (4.24) is the coordinate of source point where the coordinate is labelled as $\bar{Q}_n(a, b, c)$. In equation (4.24), the variable X is the non-dimensional distance in horizontal plane and variable Y is the non-dimensional distance in vertical plane and the solutions of X and Y are as follow.

$$X = L \cdot K\sqrt{(x-\bar{a})^2 + \left(y-\bar{b}\right)^2} \tag{4.47}$$

$$Y = L \cdot K(z+\bar{c}) \tag{4.48}$$

Where; L is the overall length of the floating structure, K is the wave number, $K = 2\pi/\lambda$, and λ is wavelength.

The real part of wave term, R_0 in equation (4.26) and the derivative of R_0 with respect to X in equation (4.27) can be calculated based on the horizontal and vertical distance between source point and field point. In the subroutine provided by Prof. Takagi Ken, the conditions applied to execute R_0 and R_1 can be separated into six conditions as shown below (Kashiwagi et al., 2003).

i. If horizontal place distance is equal to zero, X=0

ii. If vertical plane distance is equal to zero, Y=0

iii. If the horizontal place distance is small, $Y > 1.7X$ and $X < 7.5$

iv. If horizontal plane distance and vertical plane distance is large, $\sqrt{X^2 + Y^2} > 14$

v. If horizontal plane distance and vertical plane distance is small, $Y > 0.25X$

vi. If the vertical place distance is small.

The equations applied to execute R_0 and R_1in the six mentioned conditions are as follow:

I. If horizontal place distance is equal to zero, X=0 (Kashiwagi et al., 2003).

$$R_0(0,Y) = \oint_0^\infty \frac{e^{-KY}}{K-1} dk = e^{-Y} \int_{-Y}^\infty \frac{e^{-t}}{t} dt - i\pi e^{-Y}$$
$$= e^{-Y}\{E_1(-Y - i0) - i\pi\}$$
$$= e^{-Y} Re[E_1(-Y)] \quad (4.49)$$

$$R_1(0,Y) = 0 \quad (4.50)$$

Where,

$$e^Y E_1(Y) = \frac{1}{Y} \sum_{n=0}^{\infty} \frac{n!}{(-Y)^n} \quad (4.51)$$

II. If vertical plane distance is equal to zero, Y=0 (Kashiwagi et al., 2003).

$$R_0(X,0) = -\frac{\pi}{2}\{H_0(X) + \boldsymbol{Y_0}(X)\} \quad (4.52)$$

$$R_1(X,0) = \frac{\pi}{2}\{H_1(X) + \boldsymbol{Y_1}(X)\} - 1 \quad (4.53)$$

Where,

$$\left.\begin{aligned} H_0(X) &= \frac{2}{\pi}\sum_{n=0}^{\infty}\frac{(-1)^n\, x^{2n+1}}{[(2n+1)!!]^2} \\ H_1(X) &= \frac{2}{\pi}\sum_{n=0}^{\infty}\frac{(-1)^n\, x^{2n+2}}{(2n+1)!!\,(2n+3)!!} \end{aligned}\right\} \quad \text{if } X < 25 \qquad (4.54)$$

$$\left.\begin{aligned} H_0(X) &= Y_0(x) + \frac{2}{\pi}\sum_{n=0}^{\infty}\frac{(-1)^n}{x^{2n+1}}[(2n-1)!!]^2 \\ H_1(X) &= Y_1(x) + \frac{2}{\pi}\left[1 + \sum_{n=0}^{\infty}\frac{(-1)^n}{x^{2n+2}}(2n-1)!!\,(2n+1)!!\right] \end{aligned}\right\}$$

$$\text{if } X \geq 25 \qquad (4.55)$$

$\boldsymbol{Y_0}$ and $\boldsymbol{Y_1}$ is second kind of Bessel function in order 0 and order 1 respectively.

III. If the horizontal place distance is small, $Y > 1.7X$ and $X < 7.5$ (Newman, 1984).

$$R_0(X,Y) = \sum_{n=0}^{\infty}\frac{\left(-\frac{X^2}{4}\right)^n}{(n!)^2}[F_n(Y) + e^{-Y}\,E_1(-Y)] \qquad (4.56)$$

$$R_1(X,Y) = \frac{2}{X}\sum_{n=0}^{\infty}\frac{\left(-\frac{X^2}{4}\right)^n}{n!\,(n-1)!}\,[F_n(Y) + e^{-Y}E_1(-Y)] \qquad (4.57)$$

Where,

$$\left.\begin{aligned} F_0(Y) &= 0 \\ F_1(Y) &= \frac{1}{Y} + \frac{1}{Y^2} \\ F_n(Y) &= F_{n-1} + \frac{(2n-2)!}{Y^{2n-1}} + \frac{(2n-1)!}{Y^{2n}} \quad (n \geq 2) \end{aligned}\right\} \qquad (4.58)$$

Solution of $E_1(Y)$ is similar to equation (4.51)

IV. If horizontal plane distance and vertical plane distance is large, $\sqrt{X^2+Y^2} > 14$ (Noblesse, 1982)

$$R_0(X,Y) = -\sum_{n=0}^{\infty} \frac{1}{r_1^{n+1}} P_n\left(\frac{Y}{r_1}\right) - \pi e^{-Y} \boldsymbol{Y_0}(X) \tag{4.59}$$

$$R_1(X,Y) = X\sum_{n=0}^{\infty} \frac{1}{r_1^{n+3}} Q_n\left(\frac{Y}{r_1}\right) + \pi e^{-Y} \boldsymbol{Y_1}(X) \tag{4.60}$$

Where,

$$r_1 = \sqrt{X^2+Y^2} \tag{4.61}$$

$$\left.\begin{aligned} P_0\left(\frac{Y}{r_1}\right) &= 1 \\ P_1\left(\frac{Y}{r_1}\right) &= \left(\frac{Y}{r_1}\right) \\ P_n\left(\frac{Y}{r_1}\right) &= (2n-1)\left(\frac{Y}{r_1}\right)\cdot P_{n-1}\left(\frac{Y}{r_1}\right) - (n-1)^2 P_{n-2}\left(\frac{Y}{r_1}\right) \end{aligned}\right\} \tag{4.62}$$

$$\left.\begin{aligned} Q_0\left(\frac{Y}{r_1}\right) &= 1 \\ Q_1\left(\frac{Y}{r_1}\right) &= 3\left(\frac{Y}{r_1}\right) \\ Q_n\left(\frac{Y}{r_1}\right) &= (2n+1)\left(\frac{Y}{r_1}\right)\cdot Q_{n-1}\left(\frac{Y}{r_1}\right) - (n^2-1) Q_{n-2}\left(\frac{Y}{r_1}\right) \end{aligned}\right\} \tag{4.63}$$

$\boldsymbol{Y_0}$ and $\boldsymbol{Y_1}$ is second kind of Bessel function in order 0 and order 1 respectively

V. If horizontal plane distance and vertical plane distance is small, $Y > 0.25X$ (Newman, 1984).

$$R_0(X,Y) = -e^{-Y}\left[\frac{\pi}{2}\boldsymbol{Y_0}(X) + \boldsymbol{J_0}(X)\log\left(\frac{Y+r_1}{X}\right) + \frac{\pi}{2}H_0(X)\frac{r_1}{X} + \sum_{n=1}^{\infty}\left\{\frac{1}{(2n)!}U_{2n}(X,Y) + \frac{1}{(2n+1)!}U_{2n+1}(X,Y)\right\}\right] \quad (4.64)$$

$$R_1(X,Y) = -e^{-Y}\left[-\frac{\pi}{2}\boldsymbol{Y_1}(X) - \boldsymbol{J_1}(X)\log\left(\frac{Y+r_1}{X}\right) - \boldsymbol{J_0}\left(\frac{Y}{Xr_1}\right) - \frac{\pi}{2}H_0(X)\frac{Y^2}{X^2 r_1} + \left\{1 - \frac{\pi}{2}H_1(X)\right\}\frac{r_1}{X} + \sum_{n=1}^{\infty}\left\{\frac{1}{(2n)!}V_{2n}(X,Y) + \frac{1}{(2n+1)!}V_{2n+1}(X,Y)\right\}\right] \quad (4.65)$$

Where,

$$\left.\begin{aligned} U_2(X,Y) &= \frac{Y}{2}r_1 \\ U_{2n}(X,Y) &= -\frac{2n-1}{2n}X^2\,U_{2n-2}(X,Y) + \frac{Y^{2n-1}}{2n}r_1 \\ U_3(X,Y) &= \frac{Y^2}{3}r_1 \\ U_{2n+1}(X,Y) &= -\frac{2n}{2n+1}X^2\,U_{2n-1}(X,Y) + \frac{Y^{2n}}{2n+1}r_1 \end{aligned}\right\} \quad (4.66)$$

$$\left.\begin{aligned} V_2(X,Y) &= \frac{XY}{2r_1} \\ V_{2n}(X,Y) &= -\frac{2n-1}{2n}\left(X^2\, V_{2n-2}(X,Y) + 2X\, U_{2n-2}(X,Y)\right) + \frac{Y^{2n-1}}{2n}\frac{X}{r_1} \\ V_3(X,Y) &= \frac{XY^2}{3r_1} \\ V_{2n+1}(X,Y) &= -\frac{2n}{2n+1}\left(X^2\, V_{2n-2}(X,Y) + 2X\, U_{2n-1}(X,Y)\right) + \frac{Y^{2n}}{2n+1}\frac{X}{r_1} \end{aligned}\right\} \quad (4.67)$$

Where $\boldsymbol{J_0}$ and $\boldsymbol{J_1}$ are the first kind of Bessel function in order 0 and order 1 respectively, $\boldsymbol{Y_0}$ and $\boldsymbol{Y_1}$ are the second kind of Bessel function in order 0 and order 1 respectively, solution for $H_0(X)$ and $H_1(X)$ are similar to equation (4.54) and equation (4.55).

VI. If the vertical place distance is small (Newman, 1984).

$$R_0(X,Y) = -e^{-Y}\left[\sum_{n=1}^{\infty}\frac{Y^n}{n!}I_n\left(\frac{X}{Y}\right) + \frac{\pi}{2}\{H_0(X) + \boldsymbol{Y_0}(X)\}\right] \quad (4.68)$$

$$R_1(X,Y) = -e^{-Y}\left[\sum_{n=1}^{\infty}\frac{Y^{n-1}}{n!}I'_n\left(\frac{X}{Y}\right) - \frac{\pi}{2}\{H_1(X) + \boldsymbol{Y_1}(X)\} + 1\right] \quad (4.69)$$

Where,

$$\left.\begin{aligned} I_0\left(\frac{X}{Y}\right) &= \log\left(\frac{1+\sqrt{\left(\frac{X}{Y}\right)^2+1}}{\left(\frac{X}{Y}\right)}\right) \\ I_1\left(\frac{X}{Y}\right) &= \sqrt{\left(\frac{X}{Y}\right)^2+1} - \left(\frac{X}{Y}\right) \\ I_n\left(\frac{X}{Y}\right) &= \frac{\sqrt{\left(\frac{X}{Y}\right)^2+1}\left(\frac{X}{Y}\right)^2 (n-1)\, I_{n-2}\left(\frac{X}{Y}\right)}{n} \end{aligned}\right\} \quad (4.70)$$

$$\left.\begin{aligned} I_0'\left(\frac{X}{Y}\right) &= -\frac{1}{\frac{X}{Y}\sqrt{\left(\frac{X}{Y}\right)^2+1}} \\ I_1'\left(\frac{X}{Y}\right) &= \frac{\left(\frac{X}{Y}\right)}{\sqrt{\left(\frac{X}{Y}\right)^2+1}} - 1 \\ I_n'\left(\frac{X}{Y}\right) &= \frac{\frac{\left(\frac{X}{Y}\right)}{\sqrt{\left(\frac{X}{Y}\right)^2+1}} - \left(\frac{X}{Y}\right)(n-1)\left\{2I_{n-2}\left(\frac{X}{Y}\right) + \left(\frac{X}{Y}\right)I_{n-2}'\left(\frac{X}{Y}\right)\right\}}{n} \end{aligned}\right\} \quad (4.71)$$

Where; $\boldsymbol{Y_0}$ and $\boldsymbol{Y_1}$ are the second kind of Bessel function in order 0 and order 1 respectively.

To obtain the real part of the wave term and derivation of the wave term, Bessel Function is applied in the calculation. The Bessel function is typically used to describe the particle motions. The Bessel function is always applied as the solution to solve second order differential equation as in the form below (Niedziela, 2008).

$$x^2y'' + xy' + (x^2 - v^2)y = 0 \quad (4.72)$$

Equation (4.72) can be rearranged into the following form.

$$x(xy')' + (x^2 - v^2)y = 0 \quad (4.73)$$

Hence, the Bessel function is the solution for equation (4.73) and it is written in the power series as follow (Niedziela, 2008).

$$y = \boldsymbol{J_v}(x) = \sum_{n=0}^{\infty} \frac{(-1)^n}{n!\,(v+n)!}\left(\frac{x}{2}\right)^{2n+v} \quad (4.74)$$

Equation (4.74) is the Bessel function of the first kind. The variable *v* is the order of the Bessel function.

The Bessel function of the second kind also known as Neumann function and it is singular at the origin. The second kind of Bessel function was developed as a linear combination of the Bessel function of the first order as shown below (Niedziela, 2008).

$$\boldsymbol{Y}_v(x) = \frac{\boldsymbol{J}_v(x)\cos v\pi - \boldsymbol{J}_{-v}(x)}{\sin v\pi} \tag{4.75}$$

4.1.5 Execution of Hydrodynamic Force and Hydrodynamic Coefficient

i. Hydrodynamic Force

Summation of the diffraction wave potential, $\emptyset_D$ and the radiating wave potential, $\emptyset_R$ give the total wave potential. The linear wave theory can be used to compute the dynamic pressure (Journee and Massie, 2001).

$$P_d = -\rho\frac{\partial \Phi}{\partial t} \tag{4.76}$$

Therefore the wave excitation forces and moments of all six directions of motion can be obtained by the equation below (Journee and Massie, 2001).

$$\begin{aligned} F_j &= -\iint_{S_B} P_d n_j dS_B \\ &= -\rho w^2 \zeta_0 e^{-iwt} \iint_{S_B} (\phi_I + \phi_S) n_j dS_B \end{aligned} \tag{4.77}$$

Where, j=1, 2, … 6 represent the six directions of motion for the structure, $S_B$is the wetted surface area of the structure, ρ is the fluid density, t is time, ζ_0 is incident wave amplitude, n_j is the normal vector on the structure surface and F_j is the force or moment acted in the direction of motion j. The motion of the structure can be estimated if the external force or moment acted to the structure due to the wave force is known.

ii. Added Mass, Damping coefficient and Restoring force

To predict the added mass and damping coefficients at the equation above, the equation (4.78) and equation (4.79) can be used (Kashiwagi et al., 2003).

$$\text{Added Mass}, A_{ij} = -\rho \iint_{S_H} Re\left[\phi_j(x,y,z)\right] n_i dS \tag{4.78}$$

$$\text{Damping}, B_{ij} = \rho w \iint_{S_H} Im\left[\phi_j(x,y,z)\right] n_i dS \tag{4.79}$$

Where ρ is the density of fluid, $\phi_j(x,y,z)$ is radiation wave potential due to motion in direction j, n_i is unit normal vector of structure, $j = 1,2,3,\ldots,6$ represent 6 direction of structure motions, and i is the direction of normal vector.

From the equation above, the added mass for the motion in each direction is the real part of radiating wave potential while the damping coefficient is the imaginary part of radiating wave potential.

4.1.6 General Floating Body Motion Formulation

The motions of floating bodies can be categorised into linear motion or rotational motion and oscillation motion or non-oscillation motion. For rotational motion it involves the motion of roll, pitch and yaw while linear motion involves the motion of surge, sway and heave. Besides, in this book all six types of motion are considered as oscillation motion.

After all coefficients of these six types of motions are determined, the motion amplitude due to the wave loading can be calculated. The motions amplitude is calculated based on coupling motion equation. The equations developed by Kashiwagi et al. (2003) were used in this book to calculate the motion response of floating structure.

4.1.6.1. Surge - Pitch Coupling Motion

Equation of coupling motion between surge and pitch motion are given by Kashiwagi et al. (2003) by referring to the force, added mass and damping to the centre of gravity of the structure as shown follow.

$$[-w^2(\rho\nabla + A_{11}) + iwB_{11}]X_1 + [-w^2A_{15} + iwB_{15}]X_5 = F_1 \tag{4.80}$$

$$[-w^2(\rho\nabla + A_{51}) + iwB_{51}]X_1 + \left[-w^2\left(\rho\nabla k_{yy}^2 + A_{55}\right) + iwB_{55} + \rho g\nabla\overline{GM_L}\right]X_5 = F_5 \quad (4.81)$$

Where; w is the circular frequency, ρ is the fluid density, ∇ is displacement of the structure, k_{yy} is radius of gyration in y direction, $\overline{GM_L}$ is distance of centre of gravity to centre of moment in longitudinal direction, X_1 is surge motion amplitude, X_5 is pitch motion amplitude, $F_1$is surge force and F_5 is pitch moment, A_{ij} is added mass of *i* direction by due to motion in *i* direction where *i, j* =1, 5 and B_{ij} is damping of j direction due to motion in i direction where *i, j* =1, 5.

In equation (4.80) and equation (4.81), the variables needed to solve are the surge motion amplitude, X_1 and pitch motion amplitude (X_5). The equation (4.80) and (4.81) can be solved by the following way in order to obtain the surge and pitch motion amplitude.

The following assumptions are made,

$$a = -w^2(\rho\nabla + A_{11}) + iwB_{11}$$
$$b = -w^2A_{15} + iwB_{15}$$
$$c = -w^2(\rho\nabla + A_{51}) + iwB_{51}$$
$$d = -w^2\left(\rho\nabla k_{yy}^2 + A_{55}\right) + iwB_{55} + \rho g\nabla\overline{GM_L}$$

Hence, equations (4.80) and (4.81) can be simplified as below,

$$aX_1 + bX_5 = F_1 \quad (4.82\text{ (i)})$$
$$cX_1 + dX_5 = F_5 \quad (4.82\text{ (ii)})$$

Re-structure equations 4.82(i) and 4.82(ii)

$$X_1 = \frac{F_1 - bX_5}{a} \quad (4.82\text{ (iii)})$$
$$X_5 = \frac{F_5 - cX_1}{d} \quad (4.82\text{ (iv)})$$

By replacing equation 4.82(iv) into equation 4.82(iii), it is obtained that,

$$X_1 = \frac{F_1}{a} - \frac{b}{a}\left(\frac{F_5 - cX_1}{d}\right) \qquad (4.82\ (v))$$

By solving equation 4.82 (v), the surge motion amplitude is obtained as follow.

$$\text{Surge motion amplitude, } X_1 = \frac{dF_1 - bF_5}{ad - cb} \qquad (4.83)$$

By replacing equation (4.81) into equation 4.82(iv), the pitch motion amplitude is obtained as follow.

$$\text{Pitch motion amplitude, } X_5 = \frac{F_5}{d} - \frac{c}{d}\left(\frac{dF_1 - bF_5}{ad - cb}\right) \qquad (4.84)$$

4.1.6.2. Sway - Roll Coupling Motion

Same as surge – pitch motion equation, the sway – roll coupling motion equation were also provided by Kashiwagi et al. (2003) as mentioned in the book. The equation for sway – roll coupling motion by refer the force, added mass and damping to the centre of gravity of the structure is shown as follow.

$$[-w^2(\rho\nabla + A_{22}) + iwB_{22}]X_2 + [-w^2A_{24} + iwB_{24}]X_4 = F_2 \qquad (4.85)$$

$$[-w^2A_{42} + iwB_{42}]X_2 + [-w^2(\rho\nabla k_{xx}^2 + A_{44}) + iwB_{44} + \rho g\nabla\overline{GM_B}]X_4 = F_4 \qquad (4.86)$$

Where w is the circular frequency, ρ is the fluid density, ∇ is displacement floating structure, k_{xx} is radius of gyration in x direction, $\overline{GM_B}$ is distance of centre of gravity to centre of transverse direction moment, X_2 is sway motion amplitude, X_4 is roll motion amplitude, F_2 is sway force, F_4 is roll moment, A_{ij} is added mass of j direction due to motion in i direction and i, j =2, 4, B_{ij} is damping of j direction due to motion in i direction where i, j =2, 4.

So, assumptions are made that,

$$a = -w^2(\rho\nabla + A_{22}) + iwB_{22}$$
$$b = -w^2A_{24} + iwB_{24}$$
$$c = -w^2(\rho\nabla + A_{51}) + iwB_{51}$$
$$d = -w^2\left(\rho\nabla k_{yy}^2 + A_{55}\right) + iwB_{55} + \rho g\nabla\overline{GM_L}$$

After that, the motion amplitude for the sway and roll motion can be calculated by the following equations.

$$\text{Sway motion amplitude}, X_2 = \frac{dF_2 - bF_4}{ad - cb} \quad (4.87)$$

$$\text{Roll motion amplitude}, X_4 = \frac{F_4}{d} - \frac{c}{d}\left(\frac{dF_4 - bF_1}{ad - cb}\right) \quad (4.88)$$

4.1.6.3. Heave Motion

The uncoupling heave motion equation given by Kashiwagi et al. (2003) in the book is presented at equation (4.89). The equation of motion refers to the force, added mass and damping to the structure's centre of gravity.

$$\left[-(1 + A_{33}) + iB_{33} + \frac{A_w}{K\nabla}\right]\frac{X_3}{\varsigma} = \frac{A_w}{K\nabla}F_3 \quad (4.89)$$

Where; A_{33} is added mass of heave motion, B_{33} is damping of heave motion, F_3 is heave force, X_3 is heave motion amplitude, A_w is water plane area, K is wave number, ∇ is displacement of floating structure and ς is wave amplitude.

4.1.6.4. Yaw Motion

Besides, the uncoupling yaw motion equation which was given by Kashiwagi et al. (2003) in the same book is presented at equation (4.90). The equation of yaw motion refers to the force, added mass and damping to the structure's centre of gravity.

$$\left[-\left\{\left(\frac{K_{zz}}{L}\right)^2 + A_{66}\right\} + iB_{66}\right]\frac{X_6 L}{\varsigma} = \frac{A_w}{K\nabla}F_6 \qquad (4.90)$$

Where; A_{66} is added mass of yaw motion, B_{66} is damping of yaw motion, F_6 is yaw moment, X_6 is yaw motion amplitude, K_{zz} is radius of gyration for Z direction, K is wave number, L is length of floating body, ∇ is displacement of floating structure, and ς is wave amplitude.

4.2. Drag Force on an Oscillating Structure in Wave

The adapted quadratic drag force equation can be used to estimate the drag force by considering the effect of fluid in non-steady motion condition. When the fluid particle past through a structure in a non-steady condition, the motion of fluid particle around the structure will produce a force component. In this sub-chapter, let assume that the structure is a uniform slender cylinder with diameter equal to *D*, and then the force per unit length calculate by drag equation can be obtained from the equation below (Journee and Massie, 2001).

$$dF_D(t) = \frac{1}{2}\rho C_D D \cdot u(t)|u(t)| \qquad (4.91)$$

Where; $dF_D(t)$ is the total drag force per unit length, ρ is fluid density, D is the diameter of pile, C_D is drag coefficient and $u(t)$ is fluid particle velocity.

In equation (4.91), the drag coefficient in equation (4.91) can be predicted by experimental method. The drag coefficient is included the frictional drag due to the dynamic effect of fluid and the disturbance fluid around structure surface. If the fluid motion around the structure is due to oscillatory wave, then the flow field with respect to time in submerged structure is in a non-uniform condition. To obtain the total drag force acted on the structure at

any instant of time by drag equation, the flow velocity along the length of the structure must be calculated first and then the total drag force can be calculated by integrating equation (4.91) over the total submerged structure length. Therefore, equation (4.91) can be rewritten as follow to get the total drag force acted on the structure. (Journee and Massie, 2001).

$$F_D(t) = \int_{x=0}^{L} \left[\frac{1}{2}\rho C_D D \cdot u(x,t)|u(x,t)|\right] dx \qquad (4.92)$$

Where; $F_D(t)$ is the total drag force at any instant of time, ρ is fluid density, D is the diameter of pile, C_D is drag coefficient, $u(x,t)$ is fluid particle velocity at location x and at instant of time, t.

To continue, if the structure is free to move and oscillate due to the fluid flow, the calculation must then considers the factors where the exerted force by the structure due to the water particle motion around its wetted surface and the force to induce the structure to oscillate. To solve the drag equation for the case where structure is free to move in wave, the drag force acted on the structure is considered causes by the flow disturbance and the wake near the structure.

4.2.1. Drag Force Act on an Oscillating Structure in Wave

The drag force is complicated to evaluate in the case where the flow is oscillating and the structure is free to move. This is because the drag force acted on the structure is due to the disturbance of structure to fluid particle motion and the wake near to the structure. Therefore, both the fluid particle motion and structure motion must be taken into consideration in evaluating the drag force as shown in equation (4.93) (Journee and Massie, 2001).

$$B\dot{X}(t) \equiv \frac{1}{2}\rho C_D D \left(u_p(t) - \dot{X}(t)\right)\left|u_p(t) - \dot{X}(t)\right| \qquad (4.93)$$

Where; $\dot{b}$ is the damping coefficient (N.s/m), $u_p(t)$ is the time-dependent fluid particle velocity (m/s) and, $\dot{X}(t)$ is the time-dependent structure velocity (m/s).

There are two available methods to solve equation (4.93). First, the relative velocity approach method can be used to solve the drag equation. In this approach, it is assumed that the wake near to the structure is dependent on the relative velocity of fluid particle to the structure velocity, $\left(u_p(t) - \dot{X}(t)\right)$. The drag force acted on the structure is in the relation of square to the relative velocity between fluid particle velocities with respect to the structure velocity. In this approach, the unknown structure velocity is not able to be separated from the undisturbed fluid particle velocities when executing the drag force acted on the structure. Therefore, this approach does not allow the time dependent drag force to execute separately without considering the response of the structure. To solve the drag equation by this approach, simultaneous solution of the differential motion equation with iterative loop is required to perform in each time step until approximate result of structure velocity is obtained in each time step (Journee and Massie, 2001).

Secondly, the drag equation also can be evaluated by absolute velocity approach. This approach applies the superposition principle to solve the drag equation. The structure motion and the fluid particle motion are treated as the independent phenomena in this approach. The right side of equation (4.93) can be expanded as shown in equation (4.94). In this approach, it is assumed that the drag force is the summation of the waves force on a stationary structure which is in the relationship to $u_p(t)\left|u_p(t)\right|$ and the force exerted on the structure motion in still water with the relationship to $\dot{X}^2$. In addition, this approach also assumes that the structure velocity is relatively smaller as compared to the fluid particle velocity and this also means that the drag force is mostly contributed by the $u_p(t)\left|u_p(t)\right|$ term. Assumption is made that the relative small magnitude of $\dot{X}^2$in the drag equation can be linearized and moved to the left side of the motion equation. And then, the linearized drag force is assumed as a linear damping and the effect causes the increase of the structure's damping. In this approach, the differential motion equation involved the nonlinear drag force calculation is linearized and the wave exciting force acted on the structure is assumed to have no influence from the structure motion. Therefore, the execution of the structure motion and wave drag force by this method is simpler and more straightforward as compared to relative velocity approach (Journee and Massie, 2001).

$$B\dot{X}(t) \equiv \frac{1}{2}\rho C_D D\left\{u_p(t)\left|u_p(t)\right| - 2u_p(t)\dot{X}(t) + \dot{X}(t)\left|\dot{X}(t)\right|\right\} \qquad (4.94)$$

4.3. Wave Energy in Regular Wave Condition

The wave energy is formed from the kinetic energy which is related to the motion of wave particle motion and the potential energy which is in relationship with elevation of wave amplitude. The total wave energy on the ocean surface is obtained by summing up the potential energy and kinetic energy.

Assumption is made that wave potential in equation (4.9) can be rewritten in two dimension form and the distance coordinate and time dependent term are considered. The real part of two dimension wave potential in general case is shown in equation (4.95) (Journee and Massie, 2001).

$$\phi_I = \frac{\zeta_a g}{w} \cdot \frac{\cosh k(h+z)}{\cosh kh} \cdot \sin(kx - wt) \qquad (4.95)$$

Where; ϕ_I is incident wave potential, ζ_a is wave amplitude, h is water deep, g is gravity acceleration, w is wave velocity in $2\pi/(Wave\ Period, T)$, k is wave number, $2\pi/(wavelength, \lambda)$, x is the horizontal distance from origin, z is the vertical distance from origin, and t is time.

The wave kinetic energy can be obtained by integrating the wave particle velocity in horizontal plane and vertical plane in the proportional of square over a wavelength and the length from seabed to sea surface. The equation of kinetic energy is shown as follow (Journee and Massie, 2001):

$$KE = \frac{1}{2}\rho \int_0^{\lambda} \int_{\zeta}^{h} (\dot{u}^2 + \dot{w}^2) \cdot dz \cdot dx$$

$$= \frac{1}{2}\rho \int_0^{\lambda} \int_0^{h} (\dot{u}^2 + \dot{w}^2) \cdot dz \cdot dx + \frac{1}{2}\rho \int_0^{\lambda} \int_{\zeta}^{0} (\dot{u}^2 + \dot{w}^2) \cdot dz \cdot dx \quad (4.96)$$

Where; h is water deep, ρ is fluid density, λ is wavelength, ζ is wave elevation, u is horizontal wave particle velocity, w is vertical wave particle velocity.

In the equation (4.96), the second term is in approximate to

$$\frac{1}{2}\rho\int_0^{\lambda}\int_{\zeta}^{0}(\dot{u}^2+\dot{w}^2)\cdot dz\cdot dx \cong \frac{1}{2}\rho\int_0^{\lambda}\left\{\int_{\zeta}^{0}\cdot dz\right\}(\dot{u}^2+\dot{w}^2)\cdot dx$$
$$= -\frac{1}{2}\rho\zeta\int_0^{\lambda}(\dot{u}^2+\dot{w}^2)\cdot dx \qquad (4.97)$$

The equation (4.97) is a nonlinear equation, to linearize the kinetic wave energy' equation, assumption is made that the second part of equation (4.96) can be ignored. Therefore, the evaluation of kinetic energy only requires the region from seabed to sea surface in vertical direction. The wave particle velocity in horizontal direction and vertical direction can be obtained by differentiate the wave potential equation (4.95) in the respective direction as shown below.

$$\dot{u} = \frac{\partial\phi_I}{\partial x} = \zeta_a\frac{kg}{w}\cdot\frac{\cosh k(h+z)}{\cosh kh}\cdot\cos(kx-wt)$$
$$= \zeta_a w\cdot\frac{\cosh k(h+z)}{\sinh kh}\cdot\cos(kx-wt) \qquad (4.98)$$

$$\dot{w} = \frac{\partial\phi_I}{\partial z} = -\zeta_a\frac{kg}{w}\cdot\frac{\sinh k(h+z)}{\cosh kh}\cdot\sin(kx-wt)$$
$$= -\zeta_a w\cdot\frac{\sinh k(h+z)}{\sinh kh}\cdot\sin(kx-wt) \qquad (4.99)$$

Where $kg = \dfrac{w^2}{\tanh kh}$

By ignoring the second part of equation (4.96) and inserting equation (4.98) and (4.99) into equation (4.96), the following equation (4.100) is obtained.

$$KE = \frac{1}{2}\rho\int_0^{\lambda}\int_0^{h}\left[\left(\zeta_a w\cdot\frac{\cosh k(h+z)}{\sinh kh}\cdot\cos(kx-wt)\right)^2\right.$$
$$\left.+\left(-\zeta_a w\cdot\frac{\sinh k(h+z)}{\sinh kh}\cdot\sin(kx-wt)\right)^2\right]\cdot dz\cdot dx \quad (4.100)$$

Equation (4.100) is integrated and simplified by using trigonometry relationship and dispersion relationship to estimate wave kinetic energy per unit wave crest length. The equation obtained can be written as follow:

$$KE = \frac{1}{4}\rho g\zeta_a^2 \cdot \lambda \tag{4.101}$$

On the other hand, the wave potential energy is also contributed by the change of wave elevation, ζ. By considering the wave amplitude, the equation of wave potential energy can be written as follow:

$$PE = \frac{1}{2}\int_0^{\lambda} \rho g\zeta^2 \cdot dx \tag{4.102}$$

Where; ζ is wave elevation, $\zeta = \zeta_a \cos(kx - wt)$, g is gravity acceleration, w is wave velocity in $2\pi/(Wave\ Period, T)$, k is wave number, $2\pi/(wave\ length, \lambda)$, x is horizontal distance from origin, and t is time.

The wave elevation at any distance from the origin and at any time can be calculated using equation $\zeta = \zeta_a \cos(kx - wt)$. By inserting the wave elevation equation into equation (4.102), equation (4.103) is obtained. After that, the wave potential energy can be evaluated by integrating equation (4.103) over a wavelength.

$$PE = \frac{1}{2}\rho g\zeta_a^2 \int_0^{\lambda} \cos^2(kx - wt) \cdot dx \tag{4.103}$$

By solving equation (4.103), the wave potential energy per unit length of wave crest can be calculated using the equation (4.104).

$$PE = \frac{1}{4}\rho g\zeta_a^2 \cdot \lambda \tag{4.104}$$

Trigonometry relationship applied to simplify equation (4.100) and equation (4.103) is listed in equation (4.105).

$$\int_0^h \sinh^2 k(h+z) \cdot dz = \frac{1}{4k}\sinh 2kh + \frac{1}{2}h \qquad (4.105a)$$

$$\int_0^h \cosh^2 k(h+z) \cdot dz = \frac{1}{4k}\sinh 2kh - \frac{1}{2}h \qquad (4.105b)$$

$$\int_0^\lambda \sin^2(kx - wt) \cdot dx = \frac{1}{2}\lambda \qquad (4.105c)$$

$$\int_0^\lambda \cos^2(kx - wt) \cdot dx = \frac{1}{2}\lambda \qquad (4.105d)$$

As mentioned in the beginning of this sub-chapter, total wave energy, E_W on the ocean surface is obtained from the sum of the potential energy and kinetic energy. Then, equation (4.101) and equation (4.104) are combined to estimate the total wave energy per length of crest which is as shown in equation (4.106).

$$E_W = KE + PE = \frac{1}{4}\rho g \zeta_a^2 \cdot \lambda + \frac{1}{4}\rho g \zeta_a^2 \cdot \lambda$$
$$= \frac{1}{2}\rho g \zeta_a^2 \cdot \lambda \qquad (4.106)$$

4.4. Dynamic of Rigid Structure and Its Energy Relations

The motion of floating structure is often described by a single linear mass-spring system. To explain the energy and motion relationship, assumption is made that the structure would experience uncouple harmonic oscillation motion in vertical direction. In equation (4.107), the motion equation describes the vertical motion of structure with decaying motion in still water condition without any external force (Journee and Massie, 2001).

$$(m + A)\ddot{z} + B\dot{z} + Cz = 0 \qquad (4.107)$$

Where; m is the mass of structure, A is added mass, B is damping, C is restoring force, $\ddot{z}$, $\dot{z}$ and z is the structure vertical acceleration, vertical velocity and vertical distance from origin.

In the equation (4.107), the structure distance from origin can be written in following equation.

$$z = z_a \sin wt \tag{4.108}$$

Where, z_a is the amplitude of structure vertical motion, w is the motion frequency, t is time.

By differentiate equation (4.108) with respect to time, motion velocity and motion acceleration, the motion velocity and motion acceleration equations obtained are as shown in equation (4.109) and equation (4.110).

$$\dot{z} = \frac{dz}{dt} = w \cdot z_a \cos wt \tag{4.109}$$

$$\ddot{z} = \frac{d\dot{z}}{dt} = -w^2 \cdot z_a \sin wt \tag{4.110}$$

The motion equation which represents the structure motion in vertical direction and still water condition is shown in equation (4.107). From the three terms in the motion equation, it is shown that the work can be done in mass, damping and restoring force components. To obtain the work done by each component in the oscillation motion, each component involved in the motion equation can be integrated over a period of motion, T (Journee and Massie, 2001).

The work done by mass term in motion equation in unit of time is shown in equation (4.111).

$$\frac{1}{T}\int_0^T \{(m+A)\cdot \ddot{z}\}\cdot\{\dot{z}\cdot dt\} = \frac{-{z_a}^2(m+A)w^3}{T}\int_0^T \sin wt \cdot \cos wt \cdot dt$$
$$= 0 \tag{4.111}$$

The work done by the damping term in motion equation in unit of time is shown in equation (4.112).

$$\frac{1}{T}\int_0^T \{B \cdot \dot{z}\} \cdot \{\dot{z} \cdot dt\} = \frac{{z_a}^2 B\, w^2}{T}\int_0^T \cos^2 wt \cdot dt$$

$$= \frac{1}{2} B\, w^2 {z_a}^2 \qquad (4.112)$$

The work done by the restoring force term in motion equation in unit of time is as shown in equation (4.113).

$$\frac{1}{T}\int_0^T \{C \cdot z\} \cdot \{\dot{z} \cdot dt\} = \frac{{z_a}^2 C\, w}{T}\int_0^T \sin wt \cdot \cos wt \cdot dt$$

$$= 0 \qquad (4.113)$$

From the equation (4.111) to equation (4.113), it is shown that the mass term and the restoring force term in the motion equation do not dissipate energy in motion. The energy can only be dissipated from the motion to water and wave is generated through damping effect. Therefore, the energy dissipate, E_d from the structure motion can be calculated by integrating the damping force of structures $b \cdot \dot{z}$ times the distance the structure travel $\dot{z} \cdot dt$ and then divided by motion period T (Journee and Massie, 2001).

$$E_d = \frac{1}{2} B\, w^2 {z_a}^2 \qquad (4.114)$$

In equation (4.114), the dissipate energy evaluated is in unit of work done per unit of time. The dissipate energy calculated by equation (4.114) is also equal to the energy dissipated to generate radiating wave by the motion of floating structure. This approach to estimate dissipates energy from motion is suitable for all six directions of oscillation motion.

4.5. Quadratic Splines for Curve Fitting

The quadratic splines technique is used to define a second order quadratic curve for each interval between two data points. This technique would link the two data point using polynomial equation as shown in equation (4.115) (Chapra and Canale, 2010).

$$f_n(x) = a_n x^2 + b_n x + c_n \qquad (4.115)$$

Where; a_n, b_n, c_n is the constant of the polynomial equation defined by quadratic splines technique and n is the number of interval between two data points.

From Figure 4.3, if the total interval available is N, then the total number of data required is N + 1, therefore, the subscript n = 1, 2, 3, …, N+1. Besides, equation (4.115) also shows that three unknowns are required to define the quadratic equation which represents the curve of the interval. So, a total of 3 × N equations must be identified to solve all the unknowns.

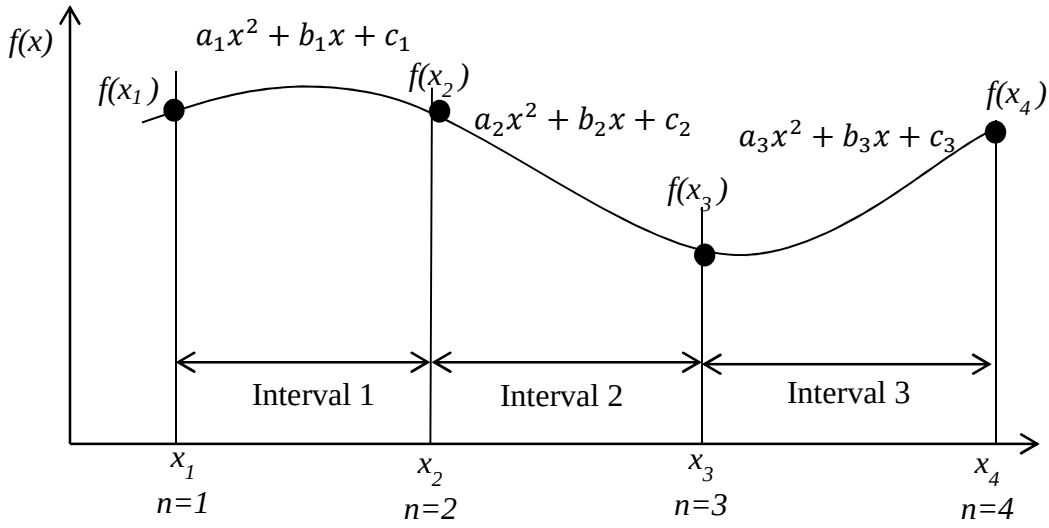

Figure 4.3: The notation used to define the quadratic spline curve.

To obtain a total of 3 × N equations from the available N + 1 data points, four conditions is stated in quadratic spline techniques.

i. At the data point n = 2, 3, 4, …, N, the function of the adjacent polynomials must be equal. This means that at these data points, a total of two equations can be obtained at each data point.

$$a_{n-1}x_n^2 + b_{n-1}x_n + c_{n-1} = f(x_n) \qquad (4.116)$$

$$a_n x_n^2 + b_n x_n + c_n = f(x_n) \qquad (4.117)$$

ii. The first function must pass through the point $(x_1, f(x_1))$ while the last function must pass through the point $(x_{N+1}, f(x_{N+1}))$.

$$a_1 x_1^2 + b_1 x_1 + c_1 = f(x_1) \quad (4.118)$$

$$a_N x_{N+1}^2 + b_N x_{N+1} + c_N = f(x_{N+1}) \quad (4.119)$$

iii. At the data point n = 2, 3, 4, …, N, the first derivatives between the function $f'(x_{n-1})$ and function $f'(x_n)$ must be equal.

$$f'_{n-1}(x_i) = f'_n(x_n)$$

Where,

$$f'_{n-1}(x_i) = 2a_{n-1}x_n + b_{n-1}x_n \quad (4.120)$$

$$f'_n(x_n) = 2a_n x_n + b_n x_n \quad (4.121)$$

iv. Let the second derivative of the first function at first data point equal to zero.

$$2a_1 = 0 \quad (4.122)$$

By solving the available equations simultaneously, the unknown a_n, b_n, c_n in each function $f_n(x)$ are evaluated.

4.6. Huygens Principle for Wave Propagation

According to Renato et al. (2015) and Kagawa (1999), the Huygens Principle state that all the points at the wave front can be considered as a centre position of the secondary source given

rise to spherical wavelet; the new wave front is considered as an envelope for all the wavelet from the secondary source as shown in Figure 4.4 and Figure 4.5.

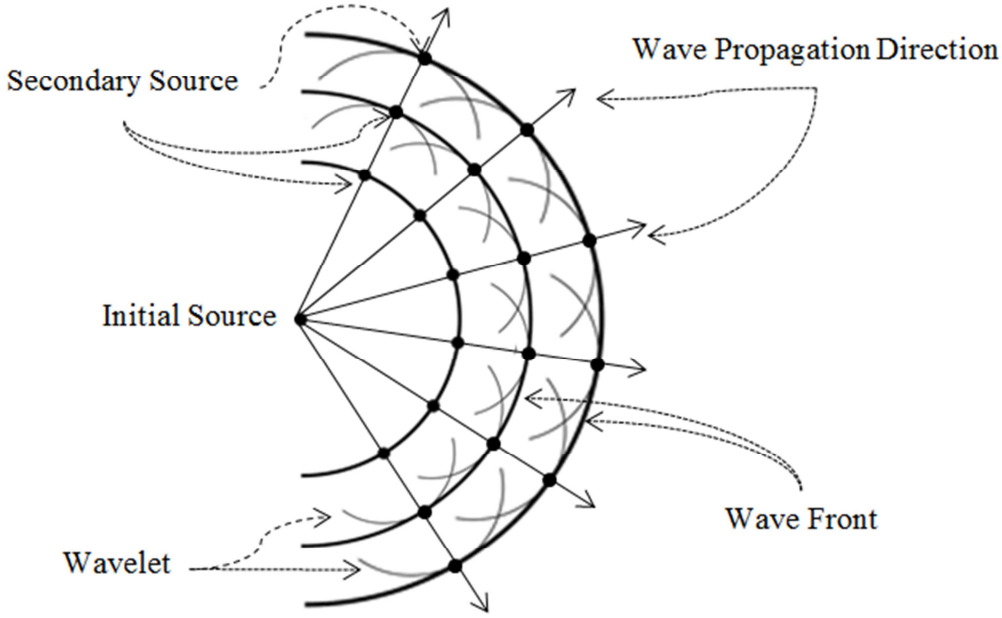

Figure 4.4: Prediction of spherical Wave propagation by Huygens Principle.

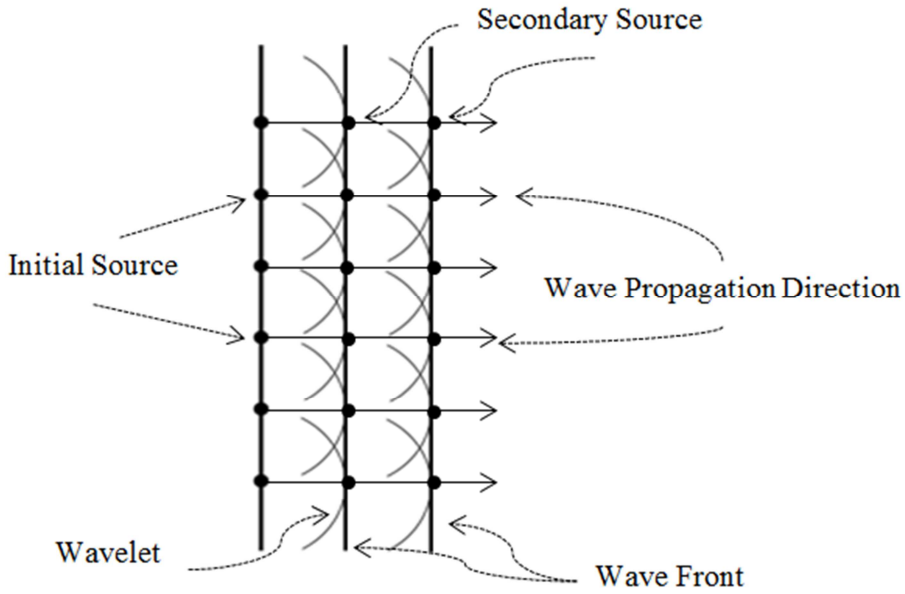

Figure 4.5: Prediction of Plane Wave propagation by Huygens Principle.

Based on the prediction by Huygens Principle, the spherical wave fronts will remain as spherical wave fronts even when it propagates away from its initial source point as shown in Figure 4.4. Similar to the propagation of the plane wave fronts as shown in Figure 4.5, the plane wave fronts still remains as plane wave fronts when it propagates from its initial source. Therefore, it is observed that the direction of wave propagation is always in normal direction to the wave fronts.

4.6.1. Application of Huygens Principle in Generating Oblique Wave

This part of the study assumes that wave is generated by the paddles type wave generator. The oblique wave generates and then propagates in the direction of certain angle according to the normal direction of the wave generator. This condition can be achieved by determining the delay time between the wave paddles. The amount of delay time required between the neighbouring waves paddled can be calculated using the equations follow (Frigaard et al., 1993).

$$\alpha = l_p \cdot \frac{2\pi \sin \vartheta}{\lambda} \tag{4.123}$$

Where, α is the delay time required between the neighbouring waves paddled, l_p is the length of wave paddle, ϑ is the angle of wave propagation direction with respect to the normal direction of the wave generator, λ is wavelength.

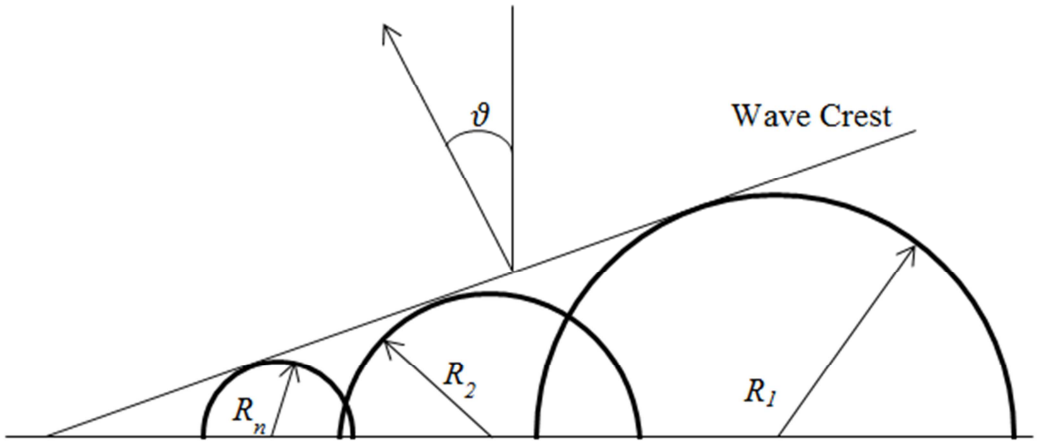

Figure 4.6: Predicting of direction of wave propagation by Huygens Principle.

In Figure 4.6, the wave crest of the oblique wave generated by wave generator is predicted by Huygens principle. The generated wave propagated in the angle of ϑ with respect to the normal direction of wave generator, assuming that the wave generator is built by N number of wave paddles. The wavelet with the radius $\mathcal{R}_n$ is generated by wave paddles *n* and the radius $\mathcal{R}_n$ can be calculated by the equation below.

$$\mathcal{R}_n = \lambda \cdot \frac{\alpha \cdot (n-1)}{2\pi} \tag{4.124}$$

Also, the energy flux, E_f in the generated oblique wave over the total crest length can be calculated by the following equation (Frigaard et al., 1993).

$$E_f \sim \zeta^2 w \, l_{Crest} \cos\vartheta \tag{4.125}$$

Where ζ is the wave amplitude, w is the wave speed, l_{Crest} is the length of wave crest, ϑ is the angle of wave propagation direction with respect to the normal direction of the wave generator.

The energy flux, E_f in equation (4.125) also can be evaluated by estimating the amount of energy from the wave generator absorbed by fluid to generate the oblique wave.

4.7. Bisection Method to Solve the Root of Equation

To apply the bisection method, the interval from x_l to x_u which must consist the value of $f(x_l)$ and $f(x_u)$ in opposite sign. Bisection method is categorised as incensement search method. This method divides the interval into half if the interval consists of the root. This method assumes that the root is located at the middle point of the subinterval which made the function to change the sign. The method evaluates the function value at the middle point if the function changed sign over the interval. This process is repeated until relative error has achieved the required percentage. The procedure to find the root by using bisection method is explained as follow (Chapra and Canale, 2010).

i. Select the lower x_l and upper x_u and then check the selected interval either the function would change sign.

$$f(x_l) \cdot f(x_u) < 0 \tag{4.126}$$

ii. Estimate the root, x_r by obtained the middle point of the interval

$$x_r = \frac{x_l + x_u}{2} \tag{4.127}$$

iii. Search the subinterval which causes the function change sign by following rules.

a. If $f(x_l) \cdot f(x_u) < 0$ then this means the root is lies in the lower interval. Therefore, set the value $x_r = x_l$.
b. If $f(x_l) \cdot f(x_u) > 0$ then this means the root is lies in the upper interval. Therefore, set the value $x_r = x_u$.
c. If $f(x_l) \cdot f(x_u) = 0$ then this means the root is obtained and equal to x_r, the process to find the root has ended.

iv. Evaluate an approximate percentage relative error, ε_a, if the relative error falls below the minimum error required, then terminate the process and assume the root is equal to x_r. Else, repeat step ii to step iv. The approximate percentage relative error, ε_a can be calculated using the equation below.

$$\varepsilon_a = \left| \frac{x_r^{new} - x_r^{old}}{x_r^{new}} \right| \times 100\% \tag{4.128}$$

4.8. Fast Fourier Linearization Series

Fourier series linearization is used in the research to linearize the second order drag equation to calculate the linearized drag force. Based on the method, the expansion of a time dependent periodic function *F(t)* in terms of an infinite sum of sines and cosines can be described by

Fourier series. The Fourier series provide a method to simplify an arbitrary periodic function into a few simple terms so the Fourier series is able to solve each term individually and recombine to obtain the solution to the original equation. Typically, the Fourier series is represented by the following equation (Journee and Massie, 2001).

$$F(t) = a_0 + \sum_{n=1}^{\infty} [a_n \cos(nwt) + b_n \sin(nwt)] \tag{4.129}$$

Where $F(t)$ is the periodic function for a time series, a_n is the coefficient and n=0, 1, 2, 3, …, b_n is the coefficient and n=1, 2, 3, …, n is the integer, t is time, w is the frequency in radian, $2\pi/T$ and T is the period of the function.

Besides, the coefficient a_n and b_n can be solved by the following equations.

$$\begin{aligned} a_0 &= \frac{1}{T}\int_0^T F(t)dt \\ a_n &= \frac{2}{T}\int_0^T F(t)\cdot\cos(nwt)\,dt, \qquad when\ n > 1 \end{aligned} \tag{4.130}$$

$$b_n = \frac{2}{T}\int_0^T F(t)\cdot\sin(nwt)\,dt \tag{4.131}$$

The periodic function represented by the Fourier series can be linearized. In engineering application, the quadratic function such as the drag equation which represented in the periodic series function typically can be written as in equation (4.132).

$$F(t) = A\cos(nwt)\cdot|\cos(nwt)| \tag{4.132}$$

Equation (4.132) can be linearized by the Fourier series Linearization method so the linearized force can be used for further study. Based on the Fourier series, the coefficient a_n and b_n for the equation (4.132) is listed as follow:

$$a_0 = 0$$

$$a_1 = \frac{8}{3\pi}$$

$$a_3 = \frac{8}{15\pi}$$

$$a_5 = \frac{8}{105\pi}$$

$$a_n = 0 \quad if\ n = 2, 4, 6, 8, \ldots$$

$$b_n = 0, \quad n = 1, 2, 3, \ldots$$

From the Fourier series linearization method, the linear equivalent value for the equation (4.132) after linearized should be equal to a_1. However, even though the second coefficient a_2 is equal to zero, the coefficient a_3 still represents the 20% of amplitude compared to coefficient a_1. Therefore, it is unavoidable that the signal is missing when linearization the quadratic function by Fourier series linearization method (Journee and Massie, 2001).

4.9. Summary

This chapter discusses the basic theory used in developing the proposed method. The diffraction potential theory is discussed in detail and the equations applied in developing the proposed method is presented in this chapter. Besides, the drag equation, Huygens Principle and motion dissipate energy concepts are also discussed in this chapter. The presented concepts in this chapter were used to further improve the proposed method to estimate the RAO of floating structure more accurately and to estimate the interaction effect of between floating structures. The application of the available concepts to further develop the proposed method is discussed in Chapter 5.

Chapter 5

5.0. Hydrodynamic Interaction Theories of Floating Structures

5.1. Diffraction Potential Theory with Drag Equation Correction Method

In theoretical point of view, the diffraction potential theory solves the hydrodynamic coefficient and force acting on floating structure in frequency domain and this theory is a type of linear theory. However, the drag equation is a time domain non-linear theory. The drag equation estimates the wave force acting on the floating structure in two dimensional forms.

A research conducted by Harnois et al. (2015) obtained that the diffraction potential theory is an efficient and established method to solve wave induced motion problem. The method is quite accurate in obtaining the motion amplitude of large floating structure because the wave diffraction effect is quite strong for the large structure. However, the diffraction potential theory is not considered as the viscous effect in the calculation and this causes the method fail to perform well in predicting the structure RAO at damping dominant region.

On the other hand, the drag equation calculate the drag force by includes the viscous effect due to the interaction between structure wetted surfaces with fluid. Therefore, in this research, the drag equation was selected to be modified and was involved in the estimation of the heave motion of floating structure together with diffraction potential theory in order to improve the accuracy of the heave RAO of floating structure predicted by the proposed method. This is because the diffraction potential theory could not predict the viscous effect in the calculation and lead to over prediction of heave RAO in damping dominant region. The procedure explained below is called *Jaswar-Siow Drag Damping Correction Method*.

5.1.1. Combination of Diffraction Potential Theory with Drag Equation

The general drag equation is discussed in sub-chapter 4.2 and written in equation (4.91). In the method, the drag force due to the wave effect on submerge model is calculated using drag force equation as shown in equation (5.1).

$$F_D = \frac{1}{2}\rho A_{Proj} C_D \left|\dot{\phi}_Z - \dot{X}_z\right|\left(\dot{\phi}_Z - \dot{X}_z\right) \tag{5.1}$$

Where; ρ is fluid density, A_{Proj} is projected area in Z direction, C_D is drag coefficient in wave particular motion direction, $\dot{\phi}_Z$ is velocity of particle motion in Z-direction in complex form, $\dot{X}_z$ is structure velocity in Z-direction.

In order to simplify the calculation, the calculation is conducted based on the absolute velocity approach as presented in Chapter 4.2.1. The floating structure dominant term is ignored in the calculation because it is assumed that the fluid particular velocity is much higher compared to structure velocity. Expansion of the equation (5.1) is shown as follows.

$$F_D = \frac{1}{2}\rho A_{Proj} C_D \left|\dot{\phi}_Z\right|\left(\dot{\phi}_Z\right) - \frac{1}{2}\rho A_{Proj} C_D \left|\dot{\phi}_Z\right|\dot{X}_z - \frac{1}{2}\rho A_{Proj} C_D \left|\dot{X}_z\right|\dot{\phi}_Z + \frac{1}{2}\rho A_{Proj} C_D \left|\dot{X}_z\right|\dot{X}_z \tag{5.2}$$

By ignoring all the terms consisting of $\left|\dot{X}_z\right|$, the equation (5.2) can be reduced to the following format.

$$F_D = \frac{1}{2}\rho A_{Proj} C_D \left|\dot{\phi}_Z\right|\left(\dot{\phi}_Z\right) - \frac{1}{2}\rho A_{Proj} C_D \left|\dot{\phi}_Z\right|\dot{X}_z \tag{5.3}$$

The above equation (5.3) is still highly nonlinear and this is impossible to combine with the linear analysis based on diffraction potential theory. To enable the drag force to combine with the diffraction force calculated by diffraction potential theory, the nonlinear drag term can be expanded in Fourier series. By using the Fourier series linearization method as presented in sub-chapter 4.8, equation (5.3) is written in the linear form as follow.

$$F_D = \frac{1}{2}\rho A_{Proj} C_D \frac{8}{3\pi} V_{max}(\dot{\phi}_Z) - \frac{1}{2}\rho A_{Proj} C_D \frac{8}{3\pi} V_{max} \dot{X}_z \qquad (5.4)$$

Where V_{max} in equation (5.4) is the magnitude of complex fluid particle velocity in Z direction. From the equation (5.4), it is summarized that the first term is linearize drag force due to wave and the second term is the viscous damping force due to the drag effect.

According to Sjöbris (2012), the linearize term $\frac{8}{3\pi} V_{max}$ in the equation (5.4) is the standard result which can be obtained if the work of floating structure performance at resonance is assumed equal between nonlinear and linearized damping term.

Next, the linearized drag equation as shown in equation (5.4) and the diffraction term which is calculated by diffraction potential theory is combined in motion equation. The modified motion equation is shown in equation (5.5).

$$(m + A)\ddot{X}_z + \left(b_p + \frac{1}{2}\rho A_{Proj} C_D \frac{8}{3\pi} V_{max}\right)\dot{X}_z + kX_z = F_p + \frac{1}{2}\rho A_{Proj} C_D \frac{8}{3\pi} V_{max}(\dot{\phi}_Z) \qquad (5.5)$$

Where; m is structure mass, k is restoring force, A, b_p, F_p is heave added mass, heave diffraction damping coefficient and heave diffraction force calculated from diffraction potential method respectively, $\frac{1}{2}\rho A_{Proj} C_D \frac{8}{3\pi} V_{max}$ is the viscous damping, $\frac{1}{2}\rho A_{Proj} C_D \frac{8}{3\pi} V_{max}(\dot{\phi}_Z)$ is the drag force defined from the drag equation.

5.1.2. Solution of Water Particle Velocity to Predict Drag Force

To obtain the drag force contributed to heave motion, the wave particle velocity in heave direction must be obtained. This water particle motion can be estimated from the linear wave potential equation. From the theory, the speed of water particle motion in the Z-direction can be calculated by using differential wave potential motion in Z-direction.

As mentioned, the drag force calculated by using the drag equation is in the function of time; therefore, the time and space dependent wave potential in the complex form should be used here. The wave potential in Euler form as follows.

$$\phi(x,y,z) = \frac{\varsigma g}{w} e^{-Kz+iKR+i\alpha} \tag{5.6}$$

Equation (5.6) is expanded and the following equation is obtained.

$$\phi(x,y,z) = \frac{\varsigma g}{w} e^{-Kz} \cdot [\cos(KR) + i\sin(KR)] \cdot [\cos\alpha + i\sin\alpha] \tag{5.7}$$

Rearrange the equation (5.7), the simplify equation is shows in equation (5.8).

$$\phi(x,y,z) = \frac{\varsigma g}{w} e^{-Kz} \cdot [\cos(KR+\alpha) + i\sin(KR+\alpha)] \tag{5.8}$$

Differentiate the equation (5.8) to the Z-direction, the water particle velocity at Z-direction is shown in equation (5.9).

$$\dot{\phi}_Z(x,y,z) = \frac{\varsigma g}{w} (-K) e^{-Kz} \cdot [\cos(KR+\alpha) + i\sin(KR+\alpha)] \tag{5.9}$$

Since this numerical model is built for deep water condition, hence based on dispersion equation, the wave speed, w in equation (5.9) can be replaced by $Kg = w^2$ and rewritten as in equation (5.10).

$$\dot{\phi}_Z(x,y,z) = \varsigma w e^{-Kz} \cdot [\cos(KR+\alpha) + i\sin(KR+\alpha)] \tag{5.10}$$

Whereas in the equations (5.6) to (5.10), ς is the wave amplitude, g is the gravity acceleration, w is the wave speed, K is wave number, R is the horizontal distance referring to zero coordinate, α is the time dependent variable.

The horizontal distance, R and the time dependent variable, α can be calculated by the following equation (5.11) and equation (5.12).

$$R = Kx\cos\beta + Ky\sin\beta \tag{5.11}$$

$$\alpha = wt + \epsilon \tag{5.12}$$

Where in equation (5.11) and equation (5.12), β is wave heading angle, ϵ is the leading phase of the wave particle velocity at the Z-direction and t is time.

To calculate the drag forces by using the drag equation, equation (5.10) can be modified by the following assumptions.

First, since the drag equation is a two dimensional method, therefore the wetted surface area in Z-direction is all projected to the bottom of structure.

Second, as mentioned in the previous part, this method applies the absolute velocity method and the heave motion of model is considered very small and can be neglected. Therefore, the change of displacement in Z-direction is neglected.

From the first and second assumptions, the variable z in equation (5.10) is not affected by time. The variable z is a constant and equal to the draught of the structure. By ignoring the time series term, the equation (5.10) can be rewritten in equation (5.13).

$$\dot{\phi}_Z(x,y,z) = \varsigma w e^{-Kz} \cdot [\mathrm{Cos}(KR) + i\,\mathrm{Sin}(KR)] \qquad (5.13)$$

The above equation (5.13) is used in this research to calculate the water particle velocity which is required to estimate the drag force by using the drag equation as shown in equation (5.4).

5.1.3. Execution of Projected Area

As shown in the drag equation, the drag force calculated by drag equation is proportional to the projected area in the desire direction. In this research, the drag equation is only applied to improve the heave motion prediction by diffraction potential theory. Therefore, the surface area of the whole structure should be projected into X-Y plane at the bottom of structure.

To obtain the projected area in X-Y plane, the integration can be made by integrating from the wetted surface of structure to the normal vector of structure. The projected area is calculated by the equation (5.14).

$$A_{Proj} = \iint_{S_B} n_3 dS_B \qquad (5.14)$$

In diffraction potential theory, the integration equation is solved by constant panel method. The constant panel method divides the wetted surface of floating structure into number of panels and the total force acting on the structure can be obtained by summing up the force acting on each panel in vector form. The similar approach also can be applied to calculate the projected area and drag force using the drag equation. Since the information of each panel such as the unit normal vector of area, centre point of panel and surface area of panel are known and calculated in the part of diffraction potential theory, then the same information is used to estimate the drag force.

The equation (5.4) can be calculated using the panel data generated in diffraction potential theory where the $A_{Proj}(\dot{\phi}_Z) = \sum_{n=1}^{N} n_{3,n} S_{s,n}(\dot{\phi}_{Z,n})$ and n is the panel number. The total force acting on the structure wetted surface can be calculated by summing up the force acting on each panel. The numerical solution for equation (5.4) is shown in equation (5.15).

$$F_D = \frac{1}{2}\rho C_D \frac{8}{3\pi} V_{max} \sum_{n=1}^{N} n_{3,n} S_{s,n}(\dot{\phi}_{Z,n}) - \frac{1}{2}\rho C_D \frac{8}{3\pi} V_{max} \dot{X}_Z \sum_{n=1}^{N} n_{3,n} S_{s,n} \quad (5.15)$$

Where V_{max} is the amplitude of complex fluid particle velocity in Z direction, $n_{3,n}$ is the area normal vector in Z direction for panel n, $S_{s,n}$ is the area of panel n, $\dot{\phi}_{Z,n}$ is the Z direction of wave velocity for panel n and it is calculated using equation (5.10), ρ is fluid density, C_D is drag coefficient in wave particular motion direction.

Besides, the wave velocity potential at each panel can be calculated by equation (5.10) if the centre point position of each panel and wave attached angle are known.

5.1.4. Determination of Drag Coefficient

Typically the drag coefficient can be identified from experimental results. In this study, the drag coefficient is determined based on previous empirical data. To enable the previous empirical to be used in this study, the round shape FLNG is assumed as a vertical cylinder. Second, the laminar flow condition is applied to calculate the drag damping and drag force so

that it is matched with the assumption applied in diffraction potential theory. In this research, the drag coefficient applied is listed in Table 5.1. The variable L and variable D which need to select the suitable drag coefficient is shown in the Figure 5.1.

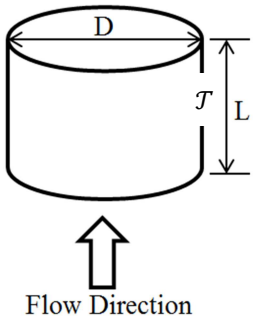

Figure 5.1: Dimension of Vertical Cylinder and flow direction

Table 5.1: Drag Coefficient C_D in the function of L/D (Cengel and Cimbala, 2010)

$\mathcal{T}$/D	C_D
0.5	1.1
1	0.9
2	0.9
4	0.9
8	1.0

In the Table 5.1, the variable $\mathcal{T}$ is the draught of the floating structure and D is the diameter of the floating structure. The drag coefficient listed in Table 5.1 is only suitable for vertical cylinder type structure such spar and round shape FLNG.

5.2. Progressive Radiating Wave Generated by Free Moving Floating Structure

The radiating wave can be generated by the motion of floating structure. The radiating wave is generated due to dissipation of energy from the motion of floating structure. In this condition, the floating structure is treated as a wave generator. Due to the complex shape of the floating structure, the wave generated by the floating structure requires detail

consideration on the shape of the wetted surface. In this sub-chapter, a mathematical model is proposed to obtain the curve to represent the radiating wave crest on sea surface. *Jaswar-Siow Interacting Method*

5.2.1. Curve of Wave Crest for Progressive Radiating Wave

To predict the curve of the radiating wave crest, the floating structure is divided into four quarter in this method as shown in Figure 5.2. The propsed method to predict the curve of radiating wave crest in this research is applicable for any monohull floating structure.

In Figure 5.2, the general floating structure is divided into four segments by two straight lines. One line connects the forward point perpendicular to aft-ward point perpendicular of the structure and another line connects the port-side to starboard side. Four planes are created in each quarter of segment and the length of the planes, $l_{p0,n}$ (n = 1 to 4) can be calculated if the coordinates (FA,0), (0,BD), (AA,0), (0,-BD) are known. Where, (FA,0) is the most forward coordinate of the structure from origin coordinate, (AA,0) is the most aft-ward coordinate of the structure from origin coordinate. BD is half breadth of the structure. Therefore, the length of the planes, $l_{p0,n}$ (n = 1 to 4) can be calculated by equation (5.16).

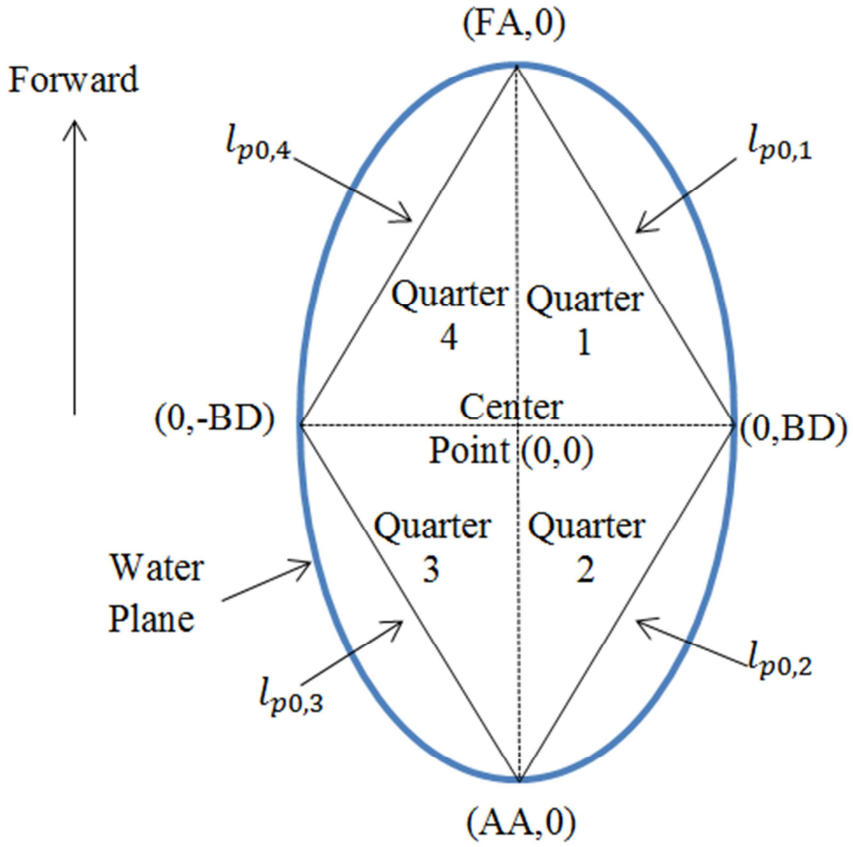

Figure 5.2: The label of segment of floating structure in plan view

$$
\begin{aligned}
l_{p0,1} &= \sqrt{FA^2 + BD^2} \\
l_{p0,2} &= \sqrt{AA^2 + BD^2} \\
l_{p0,3} &= \sqrt{AA^2 + (-BD)^2} \\
l_{p0,4} &= \sqrt{FA^2 + (-BD)^2}
\end{aligned}
\tag{5.16}
$$

Since the floating structure is always symmetrical between port side and starboard side, the length of plane $l_{p0,1} = l_{p0,4}$and $l_{p0,2} = l_{p0,3}$. Besides, the tangent direction, $\theta_{Pt,n}$ of each plane, $l_{p0,n}$ (n = 1 to 4) can be calculated by the equation (5.17).

$$\begin{aligned}\theta_{Pt,1} &= \tan^{-1}\left(\frac{BD}{-FA}\right)\\ \theta_{Pt,2} &= \tan^{-1}\left(\frac{BD}{-AA}\right)\\ \theta_{Pt,3} &= \tan^{-1}\left(\frac{-BD}{-AA}\right)\\ \theta_{Pt,4} &= \tan^{-1}\left(\frac{-BD}{FA}\right)\end{aligned} \tag{5.17}$$

In equation (5.17), the angle of tangent direction, $\theta_{Pt,n}$ calculated is zero at x=0 as show in Figure 5.3. The angle of the normal direction, $\theta_{Pn,n}$ to angle of tangent direction, $\theta_{Pt,n}$ is always different by $\pi/2$. The normal direction should be pointing outward from the center coordinate. Therefore, the normal direction of each plane, $\theta_{Pn,n}$ can be calculated by the equation (5.18).

$$\begin{aligned}\theta_{Pn,1} &= \theta_{Pt,1} - \left(\pi/2\right)\\ \theta_{Pn,2} &= \theta_{Pt,2} + \left(\pi/2\right)\\ \theta_{Pn,3} &= \theta_{Pt,3} - \left(\pi/2\right)\\ \theta_{Pn,4} &= \theta_{Pt,4} + \left(\pi/2\right)\end{aligned} \tag{5.18}$$

The distance of the segment plane, $l_{p0,n}$ (n = 1 to 4) from origin following the normal direction of the plane $\theta_{Pn,n}$ is calculated after the angle of normal plane direction is known. The equation used to estimate the distance of the segment plane from origin that follows the normal direction of the plane, $l_{p0n,n}$ (n = 1 to 4) is shown in equation (5.19).

$$\begin{aligned}l_{p0n,1} &= BD \cdot \sin\theta_{Pn,1}\\ l_{p0n,2} &= BD \cdot \sin\theta_{Pn,2}\\ l_{p0n,3} &= -BD \cdot \sin\theta_{Pn,3}\\ l_{p0n,4} &= -BD \cdot \sin\theta_{Pn,4}\end{aligned} \tag{5.19}$$

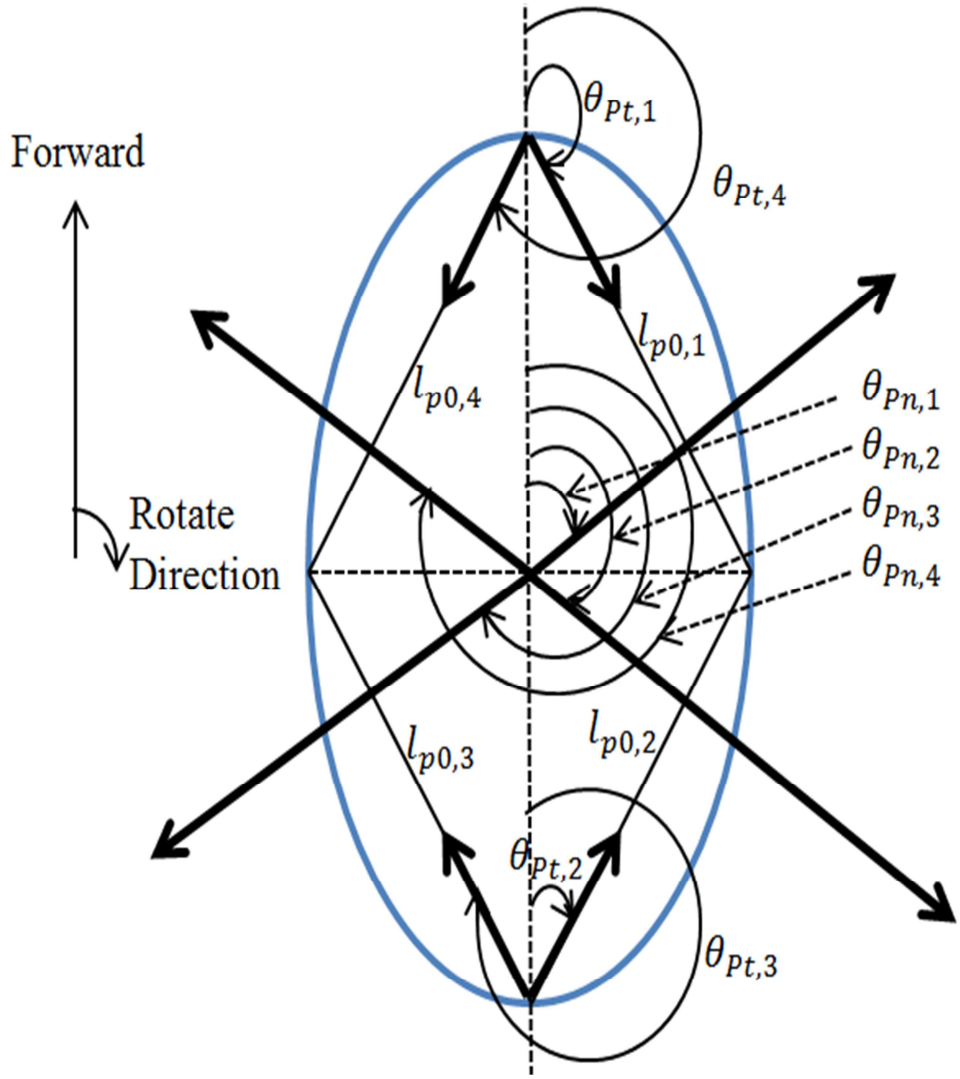

Figure 5.3: Tangent direction and normal direction of each segment plane

The distance of the segment plane from origin following the normal direction of the plane can be calculated using the equation (5.19) and it was developed using the geometry rule as shown in Figure 5.4.

From the Figure 5.4, the angle of *a*, *b* can be calculated by using the the equation (5.20) and the equation (5.21).

$$a = {}^{\pi}/_{2} - \theta_{Pn,1} \tag{5.20}$$

$$b = \pi - {}^{\pi}/_{2} - a = {}^{\pi}/_{2} - \left({}^{\pi}/_{2} - \theta_{Pn,1}\right)$$
$$= \theta_{Pn,1} \tag{5.21}$$

Using the trigonometry theorem, the equation for distance $l_{p0n,n}$ (n =1 to 4) as shown in equation (5.19) is obtained.

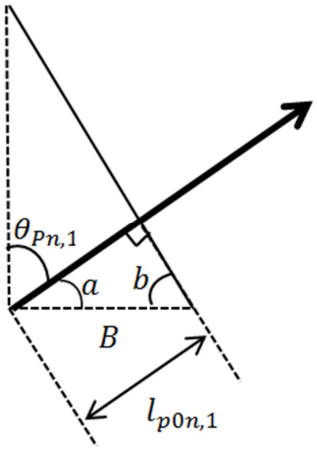

Figure 5.4: Calculation of distance between the segment planes number one from origin follows the normal direction

Typically, the wave-front of the radiating wave generated would take the shape of the structure generating the wave and the generated wave always propagates outward in all directions from the center position of the structure. This research assume that the radiating wave generated by the motion of floating structure would propagate outward following the normal direction of the structure's wetted surface generating the wave. At the same time, the crest length of the radiating wave is expanded following the tangent direction of the wave crest. The generated radiating wave will disappeare after it propagates in a long distance away from the structure. This is because the amount of wave energy in one wave crest is always constant and every single unit of wave crest would share the same amount of energy. When the radiating wave propagates outward from the center of structure, the wave crest expands. This means that, the available wave energy in each single unit of length of wave crest is reduced since the amount of wave energy in the total length of wave crest remains the same. Therefore, when the radiating wave propagates far from the structure, the crest length becomes longer and causes the available radiating wave energy obtain by each unit area on the sea surface to become very small and finally can be ignored. This observation is similar to the radiating wave boundary condition which is explained at equation (4.7).

As mentioned, the radiating wave length is assumed to take the shape of floating structure, progressing outward in normal direction of structure surface and the wave expands in tangential direction of wave-front. If the floating structure is an inverted pyramid shape, then the generated radiating wave in heave motion and the pattern of wave crest is assumed as shown in Figure 5.5.

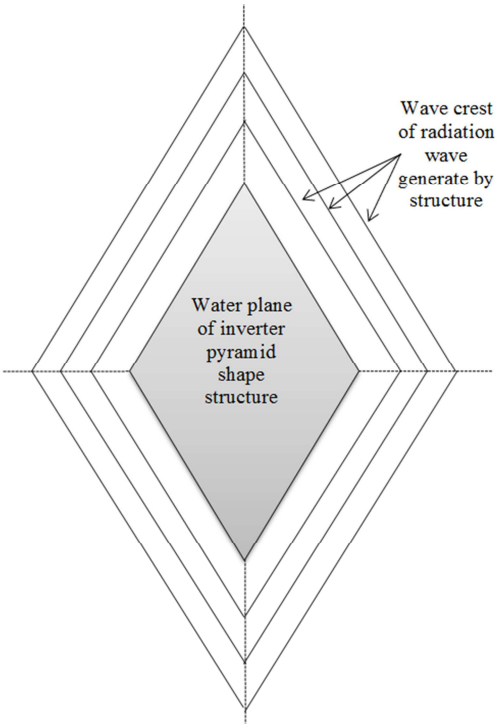

Figure 5.5: The radiating wave generated by inverted pyramid shape structure

However, the floating structures have more complex shape especially the ship shape floating structure. Therefore, a mathematical model to represent the curve of the wave-front for the radiating wave generated by floating structure is required. In Chapter Four, the progressive wave is represented by the wave potential. The wave force acting on the structure surface can be calculated by integrating the wave potential over the surface in the normal direction of the surface as shown in equation (4.77). Therefore, it is obtained that the wave force acting on the surface is in the function of normal direction of structure surface. According to the equation (4.77), the relationship between wave forces acting on the structure with the surface normal direction can be written as in the equation (5.22):

$$F_j \propto \iint_{S_B} n_j dS_B \tag{5.22}$$

Where F_j is the wave force in each direction of motion, j = 1 to 6, n_j is the surface normal vector in each direction of motion, j = 1 to 6, S_B is the wetted structure surface.

Since the wave force acting on the structure is related to the surface normal vector, hence, it is logically accepted that the radiating wave generated by the motion of structure is also in relationship with the surface normal vector. However, the surface wave is progressing outward in horizontal plane, so only surface normal vector in X-direction and Y-direction is considered here to predict the curve of the wave-front for radiating wave generated by structure motion.

Besides, the constant panel method as explain in Chapter Four is used to solve the diffraction potential theory. The constant panel method divides the wetted structure surface to a number of panels. Each panel on the wetted surface represent a small portion of wetted surface area. In the Figure 5.2, the floating structure is divided into four segments and a segment plane can be created in each segment to connect the most forward point or aft-ward point with the half-breadth point of the structure. To obtain the distribution of area normal vector on the segment plane, all panels representing the structure wetted surface is projected to the segment plane as shown in Figure 5.6.

The Figure 5.6 shows the projection of panel representing the wetted surface area of structure to the segment plane. In the figure, $l_{p0n,1}$ is the distance of the segment plane from center point following the normal direction of the plane and it is calculated by equation (5.19). $\theta_{Pn,1}$ is the normal direction of the segment plane.

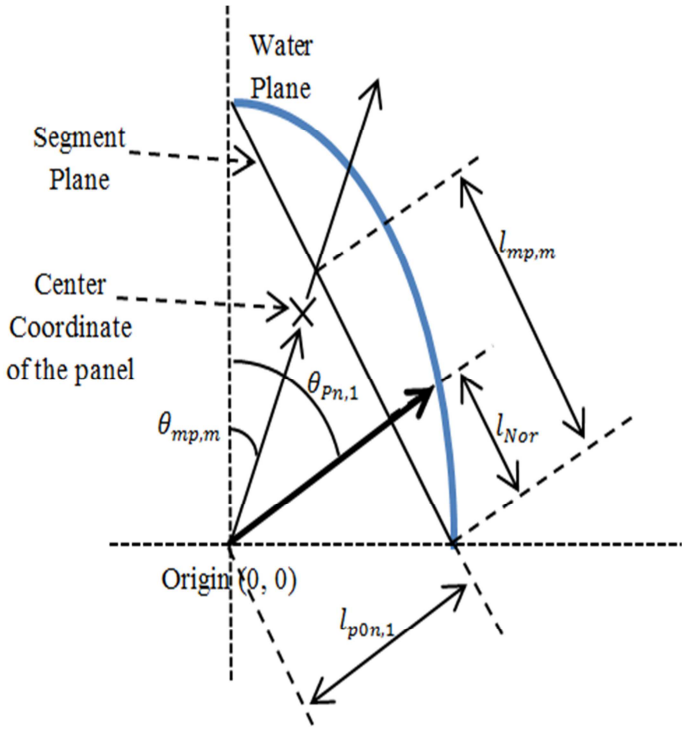

Figure 5.6: Parameter required for projection the panels of structure surface to segment plane

The position of the panel projected to the segment plane, $l_{mp,m}$ (m = 1 to Total number of panel, M) can be evaluated by considering the location of the panel and calculated by using the equation (5.23) to equation (5.25).

$$\theta_{mp,m} = \tan^{-1}\frac{y_m}{x_m} \tag{5.23}$$

Where y_m is the y coordinate of the panel m, x_m is the x coordinate of the panel m.

$$l_{Nor} = l_{p0n,1} \cdot \tan\left({}^{\pi}/_{2} - \theta_{Pn,1}\right) \tag{5.24}$$

$$l_{mp,m} = l_{Nor} + l_{p0n,1} \cdot \tan\left(\theta_{Pn,1} - \theta_{mp,m}\right) \tag{5.25}$$

Repeating from equation (5.23) to equation (5.25) for all panels, the projected position of each panel to the segment plane, $l_{mp,m}$ (m = 1 to Total number of panel, M) is evaluated.

In the next step, the segment panel is divided into a number of strips as shown in Figure 5.7. Each strip on the segment panel is assumed to have the same function as a paddle of wave maker which is able to generate wave when the strip oscillates.

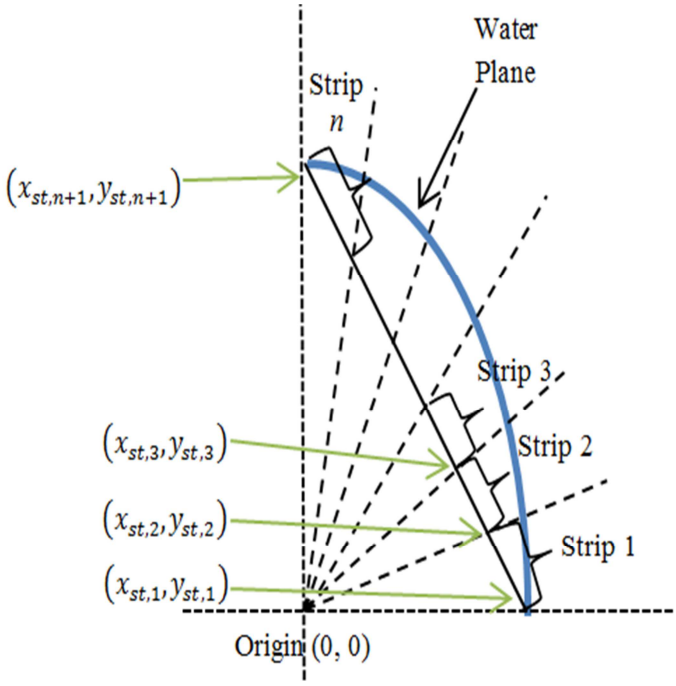

Figure 5.7: Divide the segment plane into *n* number of strips

As shown in the Figure 5.7, the $(x_{st,n}, y_{st,n})$ is the coordinate of the strips on the segment plane. If the total number of strips is equal to N, then the total number of coordinates available is equal to (N+ 1).

The length of strip l_{st} is depending on the length of the segment plane and the number of strip divided. In general, the number of strip that should be divided is depending on the complication of hull. More strips are required to make each segment plane for more complicated hull. The length of the strip at the segment can be calculated by the equation (5.26).

$$l_{st,1} = \frac{l_{p0,1}}{n} \tag{5.26}$$

Where $l_{p0,1}$ is the length of the segment plane one, *n* is the number of strips in the segment.

The coordinate $(x_{st,1}, y_{st,1})$ can be calculated by the following equation after the length of strip is known. The variable required to calculate the coordinate is shown in Figure 5.8.

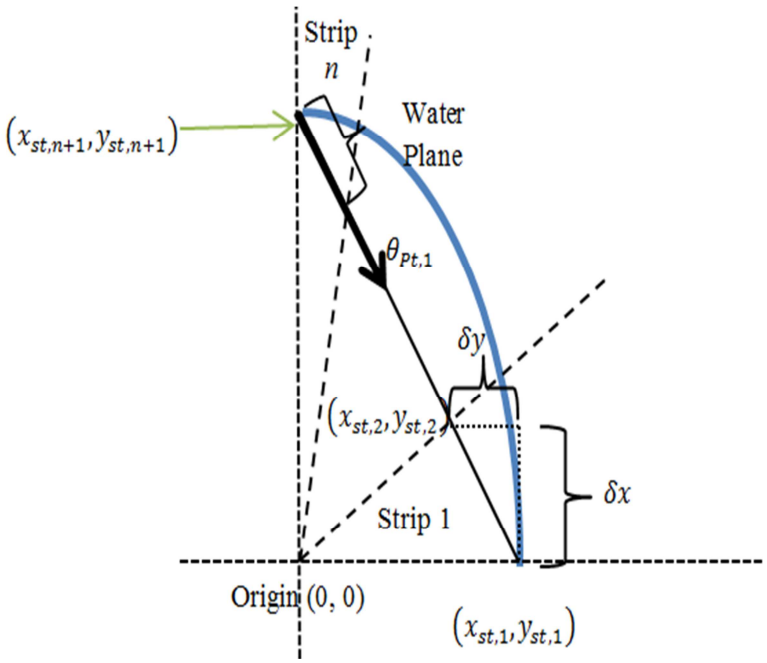

Figure 5.8: Define the coordinate of strip cut on segment plane

In the Figure 5.8, δx and δy are the length of strip in x-direction and y-direction. The angle of tangent direction of the segment plane one, $\theta_{Pt,1}$ is calculated in equation (5.18). To obtain δx and δy, the equation (5.31) and equation (5.32) are applied.

$$\delta x^2 + \delta y^2 = {l_{st,1}}^2 \tag{5.27}$$

By dividing the whole equation (5.27) with δx^2 we can obtain,

$$1 + \frac{\delta y^2}{\delta x^2} = \frac{{l_{st,1}}^2}{\delta x^2} \tag{5.28}$$

Where the slope of the plane is,

$$m = \frac{\delta y}{\delta x} = \tan \theta_{Pt,1} \tag{5.29}$$

And then, the equation (5.28) can be rewritten in following form,

$$1 + m^2 = \frac{{l_{st,1}}^2}{\delta x^2} \tag{5.30}$$

By rearranging the equation (5.30) and inserting the equation (5.29) into equation (5.30), the variable δx and δy can be calculated in equation (5.31) and equation (5.32) respectively.

$$\delta x = \sqrt{\frac{{l_{st,1}}^2}{1 + \tan^2 \theta_{Pt,1}}} \tag{5.31}$$

$$\delta y = \delta x \cdot m = \delta x \cdot \tan \theta_{Pt,1} \tag{5.32}$$

In segment one, the segment plane has the angle of segment plane larger than $\pi/2$. Therefore, the calculated δy in segment 1 should be in negative sign. After that, the coordinate of each strip can be calculated by equation (5.33) and (5.34).

$$x_{st,n} = \delta x \cdot (n - 1) \tag{5.33}$$

$$y_{st,n} = BD + \delta y \cdot (n - 1) \tag{5.34}$$

In the equation (5.34), the variable *BD* is the length of half-breadth of the structure.

Since the plane is created to represent the surface of the floating structure, therefore each strip on the segment plane should have different normal vector in X-direction and Y-direction according to the normal vector of the panel on the structure surface project to the plane. As reminded, the equation to predict the location of the panel project to the segment

plane surface is calculated by equation (5.25). Assuming the panel has area normal vector in X, Y direction $n_{mp,m} = \bar{x}_m i + \bar{y}_m j$ and *m* is the panel number, the area normal vector of the strip can be calculated by summing up the normal vector of each panel projected to the strip.

Let the area normal vector of the strip *n* is ($n_{st,n} = \bar{x}_{St,n}\, i + \bar{y}_{st,n}\, j$), then the variable $\bar{x}_{St,n}$ and $\bar{y}_{st,n}$ can be calculated by the equation (5.35) and the equation (5.36).

$$\bar{x}_{St,n} = \sum_{m=1}^{M} \bar{x}_m \qquad Where\ n = 1\ to\ \ Total\ strip, N \qquad (5.35)$$

$$\bar{y}_{St,n} = \sum_{m=1}^{M} \bar{y}_m \qquad Where\ n = 1\ to\ \ Total\ strip, N \qquad (5.36)$$

Whereas in the equation (5.35) and (5.36), m is the number of panel projected to the strip *n* and *M* is the total number of panels projected to the surface of strip *n*.

As shown in Figure 5.9 (a), the strip is not jointed to each other on segment plane due to the area normal vector of each strip is not same. To make the strip to be jointed to each other; the strip position is required to be adjusted according to its area normal vector and the area normal vector of another strip near to it.

In the Figure 5.9, it shows the concept to adjust the strip position according to the strip area normal vector direction so that each strip can be connected to each other to form a continuous line to represent the hull form. In Figure (5.9b), the original coordinate of strip n,$(x_{st,n}, y_{st,n})$ is calculated by equation (5.33) and equation (5.34). The new coordinate of strip *n*, $(x_{\psi S,n}, y_{\psi S,n})$ can be calculated by finding the intersection point between the strip surface and the strip boundary. The equation to calculate the new coordinate of strip *n* is shown as follow.

Let the first coordinate of $(x_{\psi S,n}, y_{\psi S,n})$ to be the same as the original coordinate of strip *n* $(x_{st,n}, y_{st,n})$, where

$$x_{\psi S,1} = x_{st,1} \qquad (5.37)$$

$$y_{\psi S,1} = y_{st,1} \qquad (5.38)$$

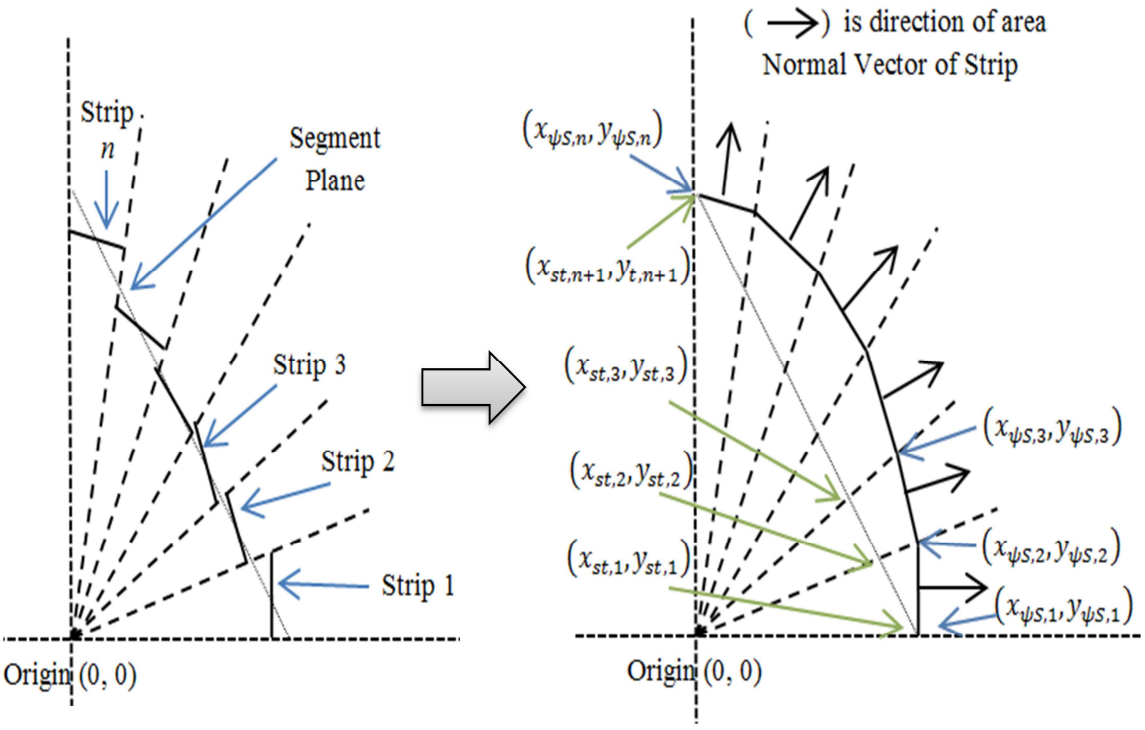

(a) (b)

Figure 5.9: Adjust strip position according to the strip area normal vector direction

Then, the following coordinate of each strip can be calculated by following the equation:

Let the normal direction of strip *n*, $m_{Nor,n}$ be

$$m_{Nor,n} = \frac{\bar{y}_{St,n}}{\bar{x}_{St,n}} \tag{5.39}$$

It is known that multiplication of normal direction slope of plane, m_{Nor} with tangent direction slope of plane, m_{Tang} is equal to -1, $m_{Nor} \cdot m_{Tang} = -1$. Hence, the tangent direction of slope for strip *n* can be calculated by the equation (5.40).

$$m_{Tang,n} = \frac{-1}{m_{Nor,n}} = -\frac{\bar{x}_{St,n}}{\bar{y}_{St,n}} \tag{5.40}$$

Since the original coordinate of strip $n\,(x_{st,n}, y_{st,n})$ is known, the boundary of each strip can be calculated by the equation (5.41).

$$m_{st,n} = \frac{y_{st,n}}{x_{st,n}} \tag{5.41}$$

As mentioned, the new coordinate of strip $n\,(x_{\psi S,n}, y_{\psi S,n})$ is located at the intersection point between the strip surface and the strip boundary. By using the $m_{Tang,n}$ and $m_{st,n}$, two equations of lines can be formed as follow.

$$y_{stB,n} = m_{st,n} x_{stB,n} \tag{5.42}$$

$$y_{stP,n} = m_{Tang,n-1} x_{stP,n} + C_{stP,n} \tag{5.43}$$

Where lines represented by equation (5.42) and equation (5.43) intersect then $y_{stB,n} = y_{stP,n} = x_{\psi S,n}$and $x_{stB,n} = x_{stP,n} = y_{\psi S,n}$. The new coordinate of strip $n\,(x_{\psi S,n}, y_{\psi S,n})$ can be obtained by equation (5.45) and equation (5.46). Also, to ensure each strip is connected between each other, $C_{stP,n}$ can be calculated using the previous known new strip *n – 1* coordinate, $(x_{\psi S,n-1}, y_{\psi S,n-1})$.

$$C_{stP,n} = y_{\psi S,n-1} - m_{Tang,n-1} \cdot x_{\psi S,n-1} \tag{5.44}$$

$$x_{\psi S,n} = \frac{C_{stP,n}}{m_{st,n} - m_{Tang,n-1}} \quad , n = 2\ to\ \mathrm{N}+1 \tag{5.45}$$

$$y_{\psi S,n} = m_{st,n} \cdot x_{\psi,n} \quad , if\ n = 2\ to\ \mathrm{N}+1 \tag{5.46}$$

Whereas in equation (5.45) and equation (5.46), the variable N are total number of divided strip.

The generated radiating wave will take the shape of the hull that generates it. Also, the generated radiating wave propagates outward following the normal direction of wave front. At the same time, the length of wave crest is increased following the tangent direction of wave crest as shown in Figure 5.5. Therefore, if the shape of wave crest for the generated radiating wave is known, then the direction of the radiating wave progressing outward can be easily predicted using the direction of the first wave crest generated by the motion of floating structure.

To obtain the first wave crest of the wave generated by the floating structure, this research assumes the first wave crest would have similar shape of the hull because the wave is generated by the motion of structures through the energy dissipated from the wetted surface of the structure. Since the strip coordinates $(x_{\psi S,n}, y_{\psi S,n})$ represents the curve of the structure hull in two-dimensional plan view can be calculated, the curve fitting technique is applied here to represent the curve of the hull using the coordinates $(x_{\psi S,n}, y_{\psi S,n})$. The fitted curve is assumed same as the curve of the first wave crest of the radiating wave generated by structure motion.

When we introduce quadratic splines method is applied to fit the coordinates$(x_{\psi S,n}, y_{\psi S,n})$. The basic idea about quadratic Splines method is presented in Chapter 4.5. In this part, the solution to solve the quadratic splines was modified so that a more direct method to get the variables on the curve can be obtained. The curve of the hull formed to generate the wave is represented by a series of quadratic equations passing through all the coordinates $(x_{\psi S,n}, y_{\psi S,n})$ as shown in Figure 5.10. The coordinates $(x_{\psi S,n}, y_{\psi S,n})$ is known and calculated by equation (5.53) and equation (5.46). The variable a_n, b_n, c_n can be defined using the quadratic spline technique.

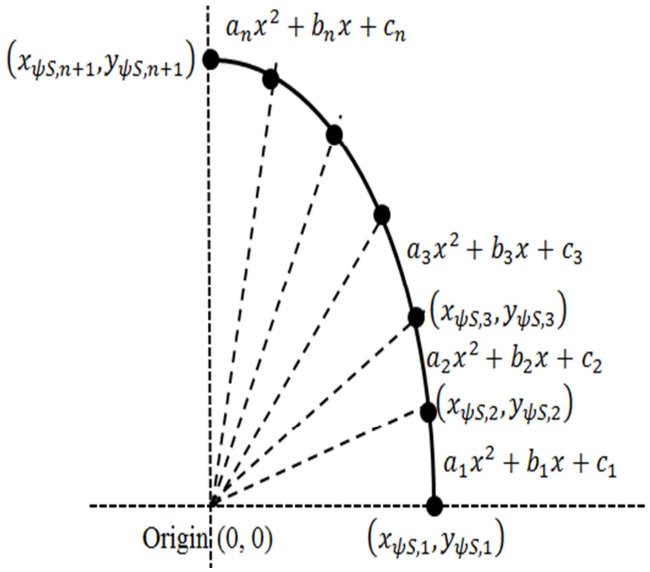

Figure 5.10: The quadratic equation to represent the curve of the hull surface

According to quadratic spline technique as presented in Chapter 4.5, the second derivative at the first point is assumed equal to zero. Also, the first curve $f(x) = a_1 x^2 + b_1 x + c_1$ is linked to the coordinate $(x_{\psi S,1}, y_{\psi S,1})$ and coordinate $(x_{\psi S,2}, y_{\psi S,2})$. Therefore, first curve as shown in Figure 5.10 can be obtained by the equation (5.47) to the equation (5.49).

$$a_1 = 0 \tag{5.47}$$

$$c_1 = y_{\psi S,1} \tag{5.48}$$

$$b_1 = \frac{y_{\psi S,2} - c_1}{x_{\psi S,2}} \tag{5.49}$$

After that, the equation of $f(x) = a_n x^2 + b_n x + c_n$, $n > 1$ can be evaluated by using the conditions of quadratic spline presented by in Chapter 4.5 where the coordinates $(x_{\psi S,n}, y_{\psi S,n})$, n = 2, 3, 4, …. The first derivatives of the curves intersect at the coordinate must be equal. This means that,

$$2a_{n-1} x_{\psi S,n} + b_{n-1} = 2a_n x_{\psi S,n} + b_n = K_n \tag{5.50}$$

Where K_n is the first derivatives of the curves at coordinate $(x_{\psi S,n}, y_{\psi S,n})$.

The variables a_{n-1} and b_{n-1} must be known before the following variables a_n and b_n can be evaluated. Therefore, the variable K_n can be calculated using the value of $a_{n-1}$and b_{n-1}.

$$K_n = 2a_{n-1}x_{\psi S,n} + b_{n-1} \tag{5.51}$$

Besides, two more equations can be obtained by inserting the coordinates $(x_{\psi S,n}, y_{\psi S,n})$and $(x_{\psi S,n+1}, y_{\psi S,n+1})$ into the equation $f(x) = a_n x^2 + b_n x + c_n$.

$$y_{\psi S,n} = a_n {x_{\psi S,n}}^2 + b_n x_{\psi S,n} + c_n \tag{5.52}$$

$$y_{\psi S,n+1} = a_n {x_{\psi S,n+1}}^2 + b_n x_{\psi S,n+1} + c_{n+1} \tag{5.53}$$

By solving the equation (5.51) to equation (5.53), the variables of a_n, b_n, c_n for $n > 1$ can be evaluated by using the equation (5.54) to the equation (5.56)

$$a_n = \frac{y_{\psi S,n+1} - y_{\psi S,n} + K_n \cdot x_{\psi S,n} - K_n \cdot x_{\psi S,n+1}}{{x_{\psi S,n+1}}^2 - 2 \cdot x_{\psi S,n} \cdot x_{\psi S,n+1} + {x_{\psi S,n}}^2} \tag{5.54}$$

$$b_n = K_n - 2 \cdot a_n \cdot x_{\psi S,n} \tag{5.55}$$

$$c_n = y_{\psi S,n} + a_n \cdot {x_{\psi S,n}}^2 - K_n \cdot x_{\psi S,n} \tag{5.56}$$

The equations (5.51), (5.54), (5.55) and (5.56) are repeated until all value of variables a_n, b_n, c_n for each curve is obtained.

As mentioned, the first wave crest would take the shape of the surface of the floating structure. Therefore, the quadratic curve defined in equation (5.54) to equation (5.56) can be represented by the curve of the first wave crest of radiating wave generated by the structure motion. To obtain the total length of wave crest, S_{cST}, the length of wave crest represented by each quadratic curve, $S_{cS,n}$ is summed up. The length of wave crest represented by each

quadratic curve, $S_{cS,n}$ can be evaluated by integrating the first derivative of the quadratic curve.

$$S_{cS,n} = \int_{x_{\psi S,n}}^{x_{\psi S,n+1}} \sqrt{1 + \left(\frac{dy}{dx}\right)^2}\, dx \tag{5.57}$$

Where,

$$\frac{dy}{dx} = 2a_n x + b_n \tag{5.58}$$

The final solution of equation (5.57) is shown in equation (5.59). The procedure to solve the equation (5.57) is presented in Appendix A.

$$S_{cS,n} = \frac{1}{2a_n}\left[\frac{(2a_n + b_n)\sqrt{1 + (2a_n + b_n)^2}}{2} + \frac{\ln\left|\sqrt{1 + (2a_n + b_n)^2} + (2a_n + b_n)\right|}{2}\right]\Bigg|_{x_{\psi S,n}}^{x_{\psi S,n+1}} \tag{5.59}$$

And then, total length of wave crest, S_{cST} can be obtained by the equation (5.60)

$$S_{cST} = \sum_{n=1}^{N} S_{cS,n} \tag{5.60}$$

Where N is the total number of quadratic curves applied to represent the wave crest.

5.2.2. Propagation of Radiating Wave Generated by Floating Structure Motion

The radiating wave created by the structure motion would progress outward following the normal direction of the wave crest which is represented by the quadratic curves. In the Figure 5.11, lets we assume one point P is located at the coordinate (x_P, y_P) somewhere outside the structure which generate the radiating wave. To predict the direction of the radiating wave and the distance travelled by the radiating wave before it arrived at P, the source coordinate(x_S, y_S) which is located at the first wave front must be known. The coordinate $S\ (x_S, y_S)$ is the source location which the radiating wave generated at the location would pass through P. The variable m_{Nor} is the normal direction of the wave crest represented by the parabolic curve and m_{Dir} is the direction of P from S.

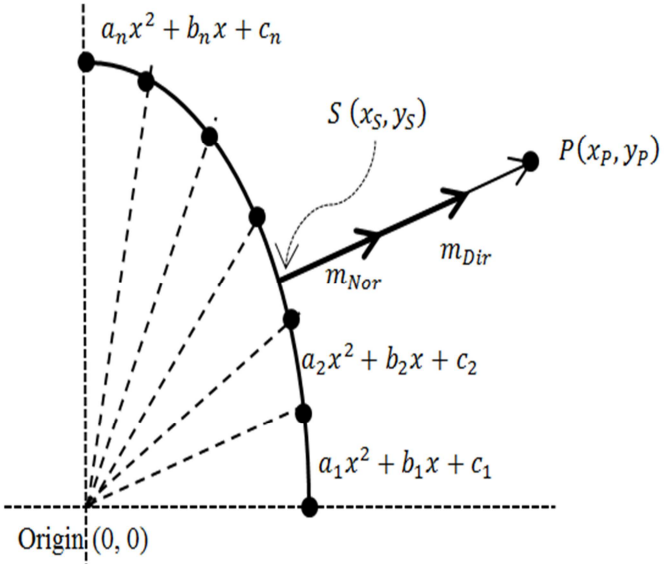

Figure 5.11: The direction of wave propagation from the source location.

As shown in the Figure 5.11, it is obtained that the wave angle of source to coordinate P must be the same as the normal direction of the wave generated at the source so that the generated wave can arrive at coordinate P. This assumption is made based on the Huygens principle. The Huygens Principle is presented in Chapter 4.6. From the Figure 4.4 and Figure 4.5, it is observed that the progressive wave arrived at any location should be in normal direction to the wavelet which is generated by the secondary wave source. Based on this

assumption, the location of source which generates the wave arrive at point *P* can be evaluated.

Assuming that,

$$m_{Nor} = m_{Dir} \tag{5.61}$$

Where,

$$m_{Nor} = \frac{-1}{f'(x)} = \frac{-1}{2a_n {x_S}^2 + b_n} \tag{5.62}$$

$$m_{Dir} = \frac{y_P - y_S}{x_P - x_S} \tag{5.63}$$

$$y_S = f(x_S) = a_n {x_S}^2 + b_n x_S + c_n \tag{5.64}$$

Insert the equation (5.62) to equation (5.64) into equation (5.61), then

$$\frac{1}{2a_n {x_S}^2 + b_n} = \frac{y_P - (a_n {x_S}^2 + b_n x_S + c_n)}{x_P - x_S} \tag{5.65}$$

In equation (5.65), the variables a_n, b_n, c_n, x_P, y_P are known. The only unknown in the equation (5.65) is variable x_S. Rearrange the equation (5.65) by moving all the terms to the left hand side and leave the right hand side to zero to get equation (5.66).

$$(-2{a_n}^2){x_S}^3 + (-3a_n b_n){x_S}^2 + \left(2a_n y_P - 2a_n c_n - {b_n}^2 + 1\right)x_S + (b_n y_P - b_n c_n - x_P) = 0 \tag{5.66}$$

In this research, bisection method is applied to obtain the value of x_S. The bisection method to find the root of the equation is presented at Chapter 4.8. To applied the bisection method, the upper boundary of the equation is equal to $x_{\psi S,n+1}$ and the lower boundary of the equation is equal to $x_{\psi S,n}$. The variable *n* used in the equation (5.62) to equation (5.66) is the number of parabolic equation.

Once the value of x_S is obtained, the value of y_S can be calculated by using equation (5.70). After that, the direction of the radiating wave arrives at the location *P*, θ_{rad} and the distance of location *P* from the source *S*, l_{rad} can be calculated by the equation (5.67) and the equation (5.68).

$$\theta_{rad} = \tan\frac{-1}{2a_n {x_S}^2 + b_n} - \pi \tag{5.67}$$

$$l_{rad} = (x_P - x_S)\cos\theta_{rad} + (y_P - y_S)\sin\theta_{rad} \tag{5.68}$$

To predict the length of wave crest arriving at the location *P*, the curve of the wave-front at location *P* need to be defined. Before the curve of the wave crest can be defined, the coordinates of the wave-front representing the curve must be obtained first. The coordinate of wave-front curve arrives at location *P*, $(x_{\psi P,n}, y_{\psi P,n})$ can be evaluated if the coordinate of source is known.

Let the coordinate of the wave crest at the source be $(x_{\psi S,n}, y_{\psi S,n})$ and this source coordinates are evaluated by equation (5.45) and equation (5.46). Then, the coordinate to represent the curve of wave-front at location *P* can be calculated by the equation (5.69) to the equation (5.71).

$$\begin{aligned} \theta_{\psi S,n} &= \frac{\pi}{2} && if\ n = 1 \\ \theta_{\psi S,n} &= \tan^{-1}\frac{-1}{2a_{n-1}{x_{\psi S,n}}^2 + b_n} && if\ n = 2\ to\ \mathrm{N}+1 \end{aligned} \tag{5.69}$$

$$x_{\psi P,n} = x_{\psi S,n} + l_{rad} * \cos\theta_{\psi S,n} \tag{5.70}$$

$$y_{\psi P,n} = y_{\psi S,n} + l_{rad} * \sin\theta_{\psi S,n} \tag{5.71}$$

Where in the equation (5.69) to equation (5.71), n is the number of coordinate, N is the total available quadratic equation to represent the curve of the wave-front at location *P*.

After the coordinates representing the wave-front pass through the location *P* are known, then the parabolic curve representing the wave-front at the location *P* can be defined by using equation (5.47) to equation (5.56). Then the length of the wave crest represented by each parabolic curve at location *P*, $S_{cP,n}$ can be calculated with similar method applied to calculate the length of the first wave crest generated by structure motion. The equation to calculate the length of wave crest at location *P* is shown in equation (5.72).

$$S_{cP,n} = \frac{1}{2a_n}\left[\frac{(2a_n + b_n)\sqrt{1 + (2a_n + b_n)^2}}{2} + \frac{\ln\left|\sqrt{1 + (2a_n + b_n)^2} + (2a_n + b_n)\right|}{2}\right]\Bigg|_{x_{\psi P,n}}^{x_{\psi P,n+1}} \tag{5.72}$$

Then, total length of wave crest, S_{cPT} can be obtained by the equation (5.73).

$$S_{cPT} = \sum_{n=1}^{N} S_{cP,n} \tag{5.73}$$

If another floating structure arranged nearby is divided into total number of panel, *M*, the equation (5.66) to equation (5.73) should be repeated for *M* times to obtain the information about the distance of the radiating wave progressed from the structure generating the wave to each panel of nearby structure, direction of radiating wave progressed from the structure generating the wave to each panel of nearby structure and the length of wave crest when the radiating wave progressed from the structure generating the wave to each panel of nearby structure.

5.2.3. Amplitude of Radiating Wave Generated by Floating Structure Motion

In the next step, wave amplitude at location *P* can be evaluated if the length of wave chest and the wave attack direction are known. In Chapter 4.3, it is known that the wave energy over a crest length is in the function of wave amplitude, wave length, fluid density and gravity. Since the fluid density and the gravity acceleration are always constant, the wave energy equation as shown in equation (4.106) can be rewritten in the equation (5.74).

$$E_W = C_{Ew} \cdot \zeta_a^2 \cdot \lambda \cdot S_{cPT} \tag{5.74}$$

By rewriting the equation (5.74), the wave amplitude at any location can be evaluated by the following equation (5.75).

$$\zeta_a = \sqrt{\frac{E_W}{C_{Ew} \cdot \lambda \cdot S_{cPT}}} \tag{5.75}$$

Whereas in equation (5.74) and equation (5.75), E_W is the total wave energy over a wave crest, C_{Ew} is a constant and $C_{Ew} = {}^1/_2\,\rho g$, ζ_a is wave amplitude at the location where wave crest occurs, λ is the wavelength, S_{cPT} is the length of the wave crest.

The equation (5.75) is valid if the wave energy carried by each single portion of wave crest is similar. This research assumes that the radiating wave could be generated by each direction of structure motion. Total radiating wave is the summation of the wave generated by each direction of motion by superposition theory. To evaluate the radiating wave generated by the structure in each direction of motion, the motion direction and wave propagation direction should be considered. There are six conditions applied here to evaluate wave energy at each segment of wave crest length.

In surge motion and sway motion, the wave generated follows the direction of structure motion. According to equation (4.125), the total radiating wave energy contributed by the surge motion or sway motion is shared by the length of wave crest in the tangent direction to the motion. Therefore, the wave amplitude at any location can be evaluated by reversing the equation (4.125). Besides, the equation (4.125) assumes that the wave amplitude generated is uniform along the wave crest, while in this part, it is assumed that the wave energy is uniform along the wave crest in tangent direction to the structure motion. Therefore, the wave amplitude generated by the surge motion and sway motion can be calculated by the equation (5.76) and the equation (5.77).

$$\zeta_{a,i} = \sqrt{\frac{E_{W,i} \cdot \cos\vartheta}{C_{Ew} \cdot \lambda \cdot 2(BD + l_{rad})}} \qquad \text{if } i = 1 \qquad (5.76)$$

$$\zeta_{a,i} = \sqrt{\frac{E_{W,i} \cdot \sin\vartheta}{C_{Ew} \cdot \lambda \cdot (FA + AA + 2l_{rad})}} \qquad \text{if } i = 2 \qquad (5.77)$$

In heave motion, the dissipated energy by heave motion is assumed to deliver to the entire wave crest in average. Therefore, the wave amplitude at any location can be evaluated by dividing the total dissipated energy by heave motion with the length of wave crest.

$$\zeta_{a,i} = \sqrt{\frac{E_{W,i}}{C_{Ew} \cdot \lambda \cdot S_{cPT}}} \qquad if\ i = 3 \qquad (5.78)$$

Whereas from equation (5.76) to equation (5.78), S_{cPT} is the length of wave crest generated by the structure motion at location *P*, BD is the half breadth length of the structure, *FA* is the forward perpendicular point of structure, *AA* is aft-ward perpendicular point of structure, l_{rad} is the distance of location *P* from the source *S*, $E_{W,i}$, is the wave energy dissipated by linear motion in *i* direction, *i* = 1 to 3.

The radiating wave amplitude generated by rotational motions are assumed to generate from moments acting in two directions where the roll motion is due to the moments in Y direction and Z direction, pitch motion is due to moments in X direction and Z direction and yaw motion is due to moments in X direction and Y direction. The moments induced by the rotational motions in each direction can be calculated by the equation (5.79) to equation (5.84).

Moments induced by roll motion,

$$M_{Y,4} = \sum_{n=1}^{N} n_{2,n} \cdot z_n \qquad (5.79)$$

$$M_{Z,4} = \sum_{n=1}^{N} n_{3,n} \cdot y_n \tag{5.80}$$

Moments induced by pitch motion,

$$M_{X,5} = \sum_{n=1}^{N} n_{1,n} \cdot z_n \tag{5.81}$$

$$M_{Z,5} = \sum_{n=1}^{N} n_{3,n} \cdot x_n \tag{5.82}$$

Moments induced by yaw motion,

$$M_{X,6} = \sum_{n=1}^{N} n_{1,n} \cdot y_n \tag{5.83}$$

$$M_{Y,6} = \sum_{n=1}^{N} n_{2,n} \cdot x_n \tag{5.84}$$

Whereas from equation (5.79) to equation (5.84), $n_{1,n}$, $n_{2,n}$ and $n_{3,n}$ are the area normal vector of panel *n* in X direction, Y direction and Z direction respectively, x_n is the *x* coordinate of panel *n*, y_n is the *y* coordinate of panel *n*, z_n is the *z* coordinate of panel *n*, $M_{Y,4}$ is the roll moment due to the Y direction motion, $M_{Z,4}$ is the roll moment due to the Z direction motion, $M_{X,5}$ is the pitch moment due to the X direction motion, $M_{Z,5}$ is the pitch moment due to the Z direction motion, $M_{X,6}$ is the yaw moment due to the X direction motion, $M_{Y,6}$ is the yaw moment due to the Y direction motion.

The ratio of roll moment due to the force in Y direction and Z direction can be calculated by equation (5.85) and equation (5.86).

$$Rt_{Y,4} = \frac{M_{Y,4}}{M_{Y,4} + M_{Z,4}} \tag{5.85}$$

$$Rt_{Z,4} = \frac{M_{Z,4}}{M_{Y,4} + M_{Z,4}} \tag{5.86}$$

Where $Rt_{Y,4}$ is the ratio of roll moment in Y direction, $Rt_{Z,4}$ is the ratio of roll moment in Z direction.

The ratio of pitch moment due to the force in X direction and Z direction can be calculated by equation (5.87) and equation (5.88).

$$Rt_{X,5} = \frac{M_{X,5}}{M_{X,5} + M_{Z,5}} \tag{5.87}$$

$$Rt_{Z,5} = \frac{M_{Z,5}}{M_{X,5} + M_{Z,5}} \tag{5.88}$$

Where $Rt_{X,5}$ is the ratio of pitch moment in X direction, $Rt_{Z,5}$ is the ratio of pitch moment in Z direction.

The ratio of yaw moment due to the force in X direction and Y direction can be calculated by equation (5.89) and equation (5.90).

$$Rt_{X,6} = \frac{M_{X,6}}{M_{X,6} + M_{Y,6}} \tag{5.89}$$

$$Rt_{Z,6} = \frac{M_{Y,6}}{M_{X,6} + M_{Y,6}} \tag{5.90}$$

Where $Rt_{X,6}$ is the ratio of yaw moment in X direction, $Rt_{Y,6}$ is the ratio of yaw moment in Y direction.

The wave amplitude at any location due to the roll moment in Y direction can be evaluated by equation (5.91).

$$\zeta_{aY,4} = \sqrt{\frac{E_{W,4} \cdot \sin\vartheta \cdot Rt_{Y,4}}{C_{Ew} \cdot \lambda \cdot (FA + AA + 2l_{rad})}} \tag{5.91}$$

The wave amplitude at any location due to the roll moment in Z direction can be evaluated by equation (5.92).

$$\zeta_{aZ,4} = \sqrt{\frac{1}{C_{Ew} \cdot \lambda}} \cdot \sqrt{f_4 \cdot \left(\frac{S_{cST}}{S_{cPT}}\right) \cdot \left(\frac{y_P}{BD + l_{rad}}\right)} \tag{5.92}$$

Also, the wave amplitude at any location due to the pitch moment in X direction can be evaluated by equation (5.93).

$$\zeta_{aX,5} = \sqrt{\frac{E_{W,5} \cdot \cos\vartheta \cdot Rt_{X,5}}{C_{Ew} \cdot \lambda \cdot 2(BD + l_{rad})}} \tag{5.93}$$

The wave amplitude at any location due to the pitch moment in Z direction can be evaluated by equation (5.94).

$$\zeta_{aZ,5} = \begin{cases} \sqrt{\frac{1}{C_{Ew} \cdot \lambda}} \cdot \sqrt{f_5 \cdot \left(\frac{S_{cST}}{S_{cPT}}\right) \cdot \left(\frac{x_P}{FA + l_{rad}}\right)} & if\ x_P \geq 0 \\ \sqrt{\frac{1}{C_{Ew} \cdot \lambda}} \cdot \sqrt{f_5 \cdot \left(\frac{S_{cST}}{S_{cPT}}\right) \cdot \left(\frac{x_P}{AA + l_{rad}}\right)} & if\ x_P < 0 \end{cases} \tag{5.94}$$

Also, the wave amplitude at any location due to the yaw moment in X direction can be evaluated by equation (5.95).

$$\zeta_{aX,6} = \begin{matrix} \sqrt{\frac{1}{C_{Ew}\cdot\lambda}}\cdot\sqrt{f_6\cdot\left(\frac{S_{cST}}{S_{cPT}}\right)\cdot\left(\frac{x_P}{FA+l_{rad}}\right)} & if\ x_P \geq 0 \\ \sqrt{\frac{1}{C_{Ew}\cdot\lambda}}\cdot\sqrt{f_6\cdot\left(\frac{S_{cST}}{S_{cPT}}\right)\cdot\left(\frac{x_P}{AA+l_{rad}}\right)} & if\ x_P < 0 \end{matrix} \quad (5.95)$$

The wave amplitude at any location due to the yaw moment in Y direction can be evaluated by equation (5.96).

$$\zeta_{aY,6} = \sqrt{\frac{1}{C_{Ew}\cdot\lambda}}\cdot\sqrt{f_7\cdot\left(\frac{S_{cST}}{S_{cPT}}\right)\cdot\left(\frac{y_P}{BD+l_{rad}}\right)} \quad (5.96)$$

Where S_{cST} is the length of first wave crest generated by the structure motion, S_{cPT} is the length of wave crest generated by the structure motion at location P, y_P is the y coordinate at location P, BD is the half breadth length of the structure, FA is the forward perpendicular point of structure, AA is aft-ward perpendicular point of structure, $l_{rad}$the distance of location P from the source S, f_i is the average distribution force caused by the moment which induces the rotational motion (i = 3 to 7).

Average distribution force, f_i that causes the moment in respective direction to generate the wave can be evaluated by estimating the change of wave energy over a single unit crest length in the ratio of moment arm.

Let the wave energy due to the roll moment in Z direction, pitch moment in Z direction, yaw moment in X direction and yaw moment in Y direction be calculated by equation (5.97) to equation (5.100).

$$\partial E_{WZ,4} = f_4\frac{r}{R}\theta_4 \quad (5.97)$$

$$\partial E_{WZ,5} = f_5\frac{r}{R}\theta_5 \quad (5.98)$$

$$\partial E_{WX,6} = f_6\frac{r}{R}\theta_6 \quad (5.99)$$

$$\partial E_{WY,6} = f_7 \frac{r}{R} \theta_6 \tag{5.100}$$

The total wave energy over a total length of wave crest due to one unit radian of rotational motion (assume $\theta_j = 1, j = 4$ to 6) can be calculated by summing up the wave energy in a single unit of length of wave crest.

$$E_{WZ,4} = \sum \partial E_{WZ,4} \cdot \partial S_{cS} = \int f_4 \frac{r}{R} \cdot 1 \cdot dS_{cS} \tag{5.101}$$

$$E_{WZ,5} = \sum \partial E_{WZ,5} \cdot \partial S_{cS} = \int f_5 \frac{r}{R} \cdot 1 \cdot dS_{cS} \tag{5.102}$$

$$E_{WX,6} = \sum \partial E_{WX,6} \cdot \partial S_{cS} = \int f_6 \frac{r}{R} \cdot 1 \cdot dS_{cS} \tag{5.103}$$

$$E_{WY,6} = \sum \partial E_{WY,6} \cdot \partial S_{cS} = \int f_7 \frac{r}{R} \cdot 1 \cdot dS_{cS} \tag{5.104}$$

In general form, let f_i be constant, then the change of wave energy in each unit of wave crest is due to the moment arm $\frac{r}{R}$ then the f_i can be calculated by equation (5.105) to equation (5.108).

$$f_4 = \frac{E_{WZ,4}}{\int \frac{r}{R} \cdot 1 \cdot dS_{cS}} \tag{5.105}$$

$$f_5 = \frac{E_{WZ,5}}{\int \frac{r}{R} \cdot 1 \cdot dS_{cS}} \tag{5.106}$$

$$f_6 = \frac{E_{WX,6}}{\int \frac{r}{R} \cdot 1 \cdot dS_{cS}} \tag{5.107}$$

$$f_7 = \frac{E_{WY,6}}{\int \frac{r}{R} \cdot 1 \cdot dS_{cS}} \tag{5.108}$$

To solve the equation (5.105) to equation (5.108) by numerical method, the wave crest length is divided into several units of small strips, and then sum up the value of each small strip of wave crest length multiplied with the distance of the strip from structure centre position in respective direction of the moment.

$$f_4 = \frac{E_{W,4} \cdot Rt_{Z,4}}{\sum \left[\frac{r_j}{R} \cdot S_{cS,j}\right]} \tag{5.109}$$

Where r or r_j is the distance of the wave crest from the center of structure in Y direction, R is the half breadth length of structure.

$$f_5 = \frac{E_{W,5} \cdot Rt_{Z,5}}{\sum \left[\frac{r_j}{R} \cdot S_{cS,j}\right]} \tag{5.110}$$

Where r or r_j is the distance of the wave crest from the center of structure in X direction, R is the forward perpendicular point of structure if r_j is positive and it is aft-ward perpendicular point if r_j is negative.

$$f_6 = \frac{E_{W,6} \cdot Rt_{X,6}}{\sum \left[\frac{r_j}{R} \cdot S_{cS,j}\right]} \tag{5.111}$$

Where r or r_j is the distance of the wave crest from the center of structure in Y direction, R is the half breadth length of structure.

$$f_7 = \frac{E_{W,6} \cdot Rt_{Y,6}}{\sum \left[\frac{r_j}{R} \cdot S_{cS,j}\right]} \tag{5.112}$$

Where r or r_j is the distance of the wave crest from the center of structure in Y direction, R is the forward perpendicular point of structure if r_j is positive and it is aft-ward perpendicular point if r_j is negative.

Also, from equation (5.109) to equation (5.112), $E_{W,i}$, is the wave energy dissipated by rotation motion in i direction, i = 4 to 6, S_{cS} or $S_{cS,j}$ is the length of wave crest in each strip.

Finally, the radiating wave amplitude due to the rotational motion can be calculated by summing up the wave amplitude due to the dissipated energy in both directions.

$$\zeta_{a,4} = \zeta_{aY,4} + \zeta_{aZ,4} \tag{5.113}$$

$$\zeta_{a,5} = \zeta_{aX,5} + \zeta_{aZ,5} \tag{5.114}$$

$$\zeta_{a,6} = \zeta_{aX,6} + \zeta_{aY,6} \tag{5.115}$$

5.2.4 Potential of Radiating Wave Generated by the Motion of Nearby Structure

Hydrodynamic interaction occurs when more than one floating structure is placed close to each other in one location. To study the effect of radiating wave generated by nearby structure on the motion of the focus structure, the generated radiating wave from nearby structure is considered as an incoming wave progressing to the focus structure. Let the focus structure be structure *P*, the nearby structure generates the radiating wave where it propagates to structure *P* labelled as structure *Q*, then the pattern of radiating wave generated by structure *Q* can be evaluated by using equation(5.16) to equation (5.60) and then the direction, wave propagation distance and the amplitude of the radiating wave arriving at structure *P* can be evaluated using equation (5.61) to equation (5.115).

In Chapter 4.1, the constant panel method is applied to solve the diffraction potential problem. The constant panel method divides the structure into a number of panels and then the diffracted wave potential on the structure wetted surface can be evaluated by diffraction potential theory. In this chapter, it is mentioned that the radiating wave propagated from nearby structure *Q* to the focus structure *P* is treated as extra incident wave acting on the

structure *P*. To study the diffracted effect of the radiating wave generated by nearby structure *Q*, the direction, wave propagation distance and the amplitude of the radiating wave arriving at each panel of focus structure *P* must be evaluated before the diffraction potential theory can be applied.

In Chapter 4.1, the incident wave is initially at the centre position of the structure hence the leading phase, α do not need to be considered as shown in equation (4.9). However, the initial radiating wave generated by nearby structure *Q* is assumed at the centre position of structure Q. Therefore, the leading phase which shows the time required for the radiating wave generated by the structure *Q* arriving on structure *P* must be included in evaluating the effect of the generated radiating wave on the motions of structure *P*. The arrival of potential wave can be written in the equation (5.116).

$$\phi_{R,(P,Q)}(x,y,z) = e^{-Kz+iK(x\cos\beta+y\sin\beta)+i\alpha} \tag{5.116}$$

After expanding the equation above,

$$\phi_{R,(P,Q)}(x,y,z) = e^{-Kz}\cdot e^{iK(x\cos\beta+y\sin\beta)}\cdot e^{i\alpha} \tag{5.117}$$

By applying Euler's law,

$$\begin{aligned}\phi_{R,(P,Q)}(x,y,z) &= e^{-Kz}\cdot[\cos(Kx\cos\beta+Ky\sin\beta)+i\sin(Kx\cos\beta+Ky\sin\beta)]\\ &\cdot[\cos\alpha+i\sin\alpha]\end{aligned} \tag{5.118}$$

Expanding the equation (5.118) using the trigonometry law, it is obtained that the wave potential equation, $\phi_{R,(P,Q)}(x,y,z)$ is formed by four terms in its equation as shown in equation (5.119). The equation of incoming radiating wave (5.119) is similar to the solution of incident wave potential equation (4.30) which is not considered as the leading phase of wave.

$$\begin{aligned}\phi_{R,(P,Q)}(x,y,z) &= e^{-Kz} \\ &\cdot [\cos(Kx\cos\beta)\cdot\cos(Ky\sin\beta)\cdot\cos\alpha \\ &-\sin(Kx\cos\beta)\cdot\sin(Ky\sin\beta)\cdot\cos\alpha \\ &+\sin(Kx\cos\beta)\cdot\cos(Ky\sin\beta)\cdot\sin\alpha+\cos(Kx\cos\beta) \\ &\cdot\sin(Ky\sin\beta)\cdot\sin\alpha \\ &+i\{\cos(Kx\cos\beta)\cdot\cos(Ky\sin\beta)\cdot\sin\alpha \\ &-\sin(Kx\cos\beta)\cdot\sin(Ky\sin\beta)\cdot\sin\alpha \\ &+\sin(Kx\cos\beta)\cdot\cos(Ky\sin\beta)\cdot\cos\alpha+\cos(Kx\cos\beta) \\ &\cdot\sin(Ky\sin\beta)\cdot\cos\alpha\}] \end{aligned} \quad (5.119)$$

By applying similar symmetric and anti-symmetric conditions to obtain equation (4.31), the incoming radiating wave contributing to the force acting on X, Y, Z and N direction can be predicted using the following equation.

$$\begin{aligned}\phi_{R,(P,Q;j)}(x,y,z) &= \zeta_{a,j} \\ &\cdot\{\phi^{Z}_{R,(P,Q)}+i\,\phi^{Z}_{R,(P,Q)}+\phi^{N}_{R,(P,Q)}+i\,\phi^{N}_{R,(P,Q)}+\phi^{X}_{R,(P,Q)}+i\phi^{X}_{R,(P,Q)} \\ &+\phi^{Y}_{R,(P,Q)}+i\phi^{Y}_{R,(P,Q)}\} \end{aligned} \quad (5.120)$$

Where,

$$\left.\begin{aligned}\phi^{X}_{R,(P,Q;j)} &= e^{-Kz}\sin(Kx\cos\beta)\cdot\cos(Ky\sin\beta)\cdot\sin\alpha + \\ &\quad i\,e^{-Kz}\sin(Kx\cos\beta)\cdot\cos(Ky\sin\beta)\cdot\cos\alpha \\ \phi^{Y}_{R,(P,Q;j)} &= e^{-Kz}\cos(Kx\cos\beta)\cdot\sin(Ky\sin\beta)\cdot\sin\alpha + \\ &\quad i\,e^{-Kz}\cos(Kx\cos\beta)\cdot\sin(Ky\sin\beta)\cdot\cos\alpha \\ \phi^{Z}_{R,(P,Q;j)} &= e^{-Kz}\cos(Kx\cos\beta)\cdot\cos(Ky\sin\beta)\cdot\cos\alpha + \\ &\quad i\,e^{-Kz}\cos(Kx\cos\beta)\cdot\cos(Ky\sin\beta)\cdot\sin\alpha \\ \phi^{N}_{R,(P,Q;j)} &= -e^{-Kz}\sin(Kx\cos\beta)\cdot\sin(Ky\sin\beta)\cdot\cos\alpha - \\ &\quad i\,e^{-Kz}\sin(Kx\cos\beta)\cdot\sin(Ky\sin\beta)\cdot\sin\alpha\end{aligned}\right\} \quad (5.121)$$

Where in equation (5.116) to equation (5.121), $\phi_{R,(P,Q)}$ is the wave potential due to radiating wave generated by structure Q acting on the structure P, (x,y,z) are the coordinates

of the panel on the wetted surface of structure *P*, K is wave number , α is the leading phase of wave potential $\phi_{R,(P,Q)}$ at the wetted surface of structure *P*. The α needs to consider the distance required for the radiating wave generated by structure *Q* and its propagation to the wetted surface of structure *P*.

To estimate the diffracted effect of radiating wave generated by structure *Q* when it arrives on structure *P*, the radiating wave potential on each panel can be solved with similar method as incident wave arrives at each panel of structure surface. In equation (4.32), the unknown source strength is arranged on the left hand side of the equation, while the unknown diffracted wave potential and radiating wave potential of structure *P* are arranged on the right-hand side. To obtain the diffraction force of structure *Q's* radiating wave arriving at structure *P*, the equation (4.32) can be modified so that it can obtain the diffraction force due to incident wave, $\phi_I(x,y,z)$, radiating wave force of structure *P* and diffraction force due to radiating wave of structure *Q*, $\phi_{R,(P,Q)}(x,y,z)$ in single step once the unknown at left hand side of equation (4.32) is solved.

$$\begin{pmatrix} A_{1,1} & \cdots & A_{1,N} \\ \vdots & \ddots & \vdots \\ A_{N,1} & \cdots & A_{N,N} \end{pmatrix} \cdot \begin{pmatrix} \phi_{j,1} \\ \vdots \\ \phi_{j,N} \end{pmatrix} = \begin{pmatrix} B_{j,1} \\ \vdots \\ B_{j,N} \end{pmatrix} \tag{5.122}$$

Where *j*=1 to 6 in radiating case and *j*=*D* in diffraction case, and,

$$A_{n,n} = 2\pi \tag{5.123}$$

$$A_{n,m} = \left[-D_{mn} + \left\{ \frac{\partial}{\partial n_Q} G_W(m;n) \right\} \Delta S_n \right] \tag{5.124}$$

$$B_{j,m} = \sum_{n=1}^{N} n_j(n)[-S_{mn} + \{G_W(m;n)\}\Delta S_n] \text{ in radiating case} \tag{5.125}$$

$$B_{j,m} = 4\pi\phi_I(m) \text{ in diffraction case} \tag{5.126}$$

$$B_{j,m} = 4\pi\phi_{R,(P,Q;j)}(m) \text{in interaction case} \tag{5.127}$$

Where subscript *n* is the coordinate of source panel which is located at structure *P*, subscript *m* is the coordinate of respected panel *m* which is located at structure *P*.

The equation (5.122) to equation (5.126) is similar with equation (4.32) to equation (4.36) where the explanation of the matrix and equation (5.122) to equation (5.126) can be found at Chapter 4.1.2. In equation (5.127), the subscript *j* is representing the direction of motion of structure *Q*. Once the matrix equation (5.122) is solved, the radiating wave potential from structure *Q* acting on each panel of structure *P* is obtained as $\phi^{S}_{R,(P,Q;j)}(m)$. Then, the interaction wave force acting on structure *P* due to the wave generated at structure *Q* can be evaluated by equation (5.129).

$$P_d = -\rho \frac{\partial \phi^{S}_{R,(P,Q;j)}(m)}{\partial t} \tag{5.128}$$

Therefore the wave excitation forces and moments in all six directions of motion can be obtained by the equation below (Journee and Massie, 2001).

$$\begin{aligned} F_{(P,i;Q,j)} &= -\iint_{S_B} P_d n_i dS_B \\ &= -\rho w^2 \iint_{S_B} \left(\phi^{S}_{R,(P,Q;j)}\right) n_j dS_B \end{aligned} \tag{5.129}$$

Where in equation (5.128) and equation (5.129), $F_{(P,i;Q,j)}$ is the wave force acting on the structure *P* in direction *i* due to the radiating wave generated by structure *Q* in the motion direction *j*, $\phi^{S}_{R,(P,Q;j)}$ is the solved radiating wave potential generated by the motion of floating structure *Q* in direction *j* and diffracted when it arrives on structure *P*, n_i is the normal vector of the wetted surface area of structure *P*, S_B is the wetted surface area of structure *P* ,w is the wave speed, ρ is fluid density

5.2.5. Interaction Wave Force due to Motion Dissipated Energy

The wave force acting on the structure *P* due to the motion of structure *Q* is evaluated in equation (5.129). However, the energy dissipated by structure *Q* to generate the radiating wave propagating to structure *P* can only be known after the equation (4.32) is solved. To enable the radiating wave due to motion of structure *Q* acting on structure *P* to be solved together with the diffraction effect of incident wave potential, it is easier to assume the energy dissipated by structure *Q* to generate radiating wave is one unit before the motion of structure *Q* is known. In this way, the radiating wave force acting on the structure *P* due to the motion of structure *Q* based on every single unit of energy dissipated by structure *Q* can be evaluated together with the effect of incident wave to the structure *P* using equation (5.122).

After the equation (5.122) is solved for both structure *P* and *Q*, then the radiating wave force acting on structure *P* can be evaluated directly. The dissipated energy due to the motion of structure *Q* is evaluated using equation (4.114). By assuming the total dissipated energy from the motion of structure *Q* is used for generating the radiating wave, the amplitude of the radiating wave can be evaluated using equation (4.106). After that, the relationship between the wave amplitude and wave force can be obtained by using equation (4.77). Hence, the relationship between structure dissipated energy due to damped motion, wave amplitude and wave force can be summarized as follow.

$$E_d = E_W = \frac{1}{2} B\, w^2 {z_a}^2 \tag{5.130}$$

$$\zeta_a \propto \sqrt{E_W} \tag{5.131}$$

$$Ft_{(P,i;Q,j)} \propto \zeta_a \tag{5.132}$$

By combining the equation (5.130) to equation (5.132), it can obtain that the mathematical model gives the relationship between dissipated energy due to the motion of structure *Q* in direction *j* with the radiating wave force acting on structure *P* to induce the motion in direction *i*.

$$F_{(P,i;Q,j)}^{S,n} = C \cdot \sqrt{\frac{1}{2} B_j w^2 {z_{a,j}}^2} \cdot i\alpha \tag{5.133}$$

Whereas from equation (5.130) to equation (5.133), E_d is the dissipated wave energy due to the motion of floating structure, E_W is the radiating wave energy along a wave crest, B_j is the structure damping coefficient in direction *j*, w is wave speed, $z_{a,j}$ is the motion amplitude of floating structure in direction *j*, ζ_a is the radiating wave amplitude generated by the motion of floating structure, $F_{(P,i;Q,j)}^{S,n}$ is the wave force acting on structure *P* to induce the motion in direction *i* due to the motion of structure *Q* in direction *j* moving with motion amplitude z_a in stage n , C is a constant and it is equal to magnitude of $F_{(P,i;Q,j)}$ where it represents the amplitude of wave force acting on structure *P* to induce the motion in direction *i* due to the motion of structure *Q* in direction *j* in every single unit of energy dissipated by the structure Q through its motion, α is the leading phase between the radiating wave force in respective to the phase of incident wave potential.

It is known that the variable $F_{(P,i;Q,j)}^{S,n} = F_{amp}(\cos\alpha_1 + \sin\alpha_1)$ then the variable *C* and α can be calculated using equation (5.134) and equation (5.135).

$$C = \left|F_{amp}\right| \tag{5.134}$$

$$\alpha = \alpha_1 - \alpha_2 - \alpha_3 \tag{5.135}$$

Where α_1 is the phase between the radiating wave force acting on focus structure and the radiating wave generated by the nearby the structure. It is equal to the phase of $F_{(P,i;Q,j)}^{S,n}$, $\alpha_2$is the phase between incident wave arriving on the structure *P* compare to the nearby structure *Q*.

Let we assume the centre coordinate of structure *P* is (x_P, y_P, z_P) and the centre coordinate of structure *Q* is (x_Q, y_Q, z_Q), then the phase α_2 can be calculated by equation (5.136).

$$\alpha_2 = K\left(x_Q - x_P\right)\cos\beta + K\left(y_Q - y_P\right)\sin\beta \tag{5.136}$$

In the equation (5.135), the variable α_3 is the phase between the incident wave arriving on the structure Q and the radiating wave generated by structure Q. If the motion of structure Q is $\boldsymbol{z}_{a,j} = z_{a,j}(\cos\theta + \sin\theta)$, then the phase α_3 should be double of the θ. This is because the time required for the motion of structure to generate the radiating wave is the same as the time required for the incident wave to push the structure Q to move. Therefore, the phase α_3 can be calculated by equation (5.137).

$$\alpha_3 = 2 \cdot \theta \tag{5.137}$$

Where; the phase of the radiating wave that must be considered is shown in Figure 5.12.

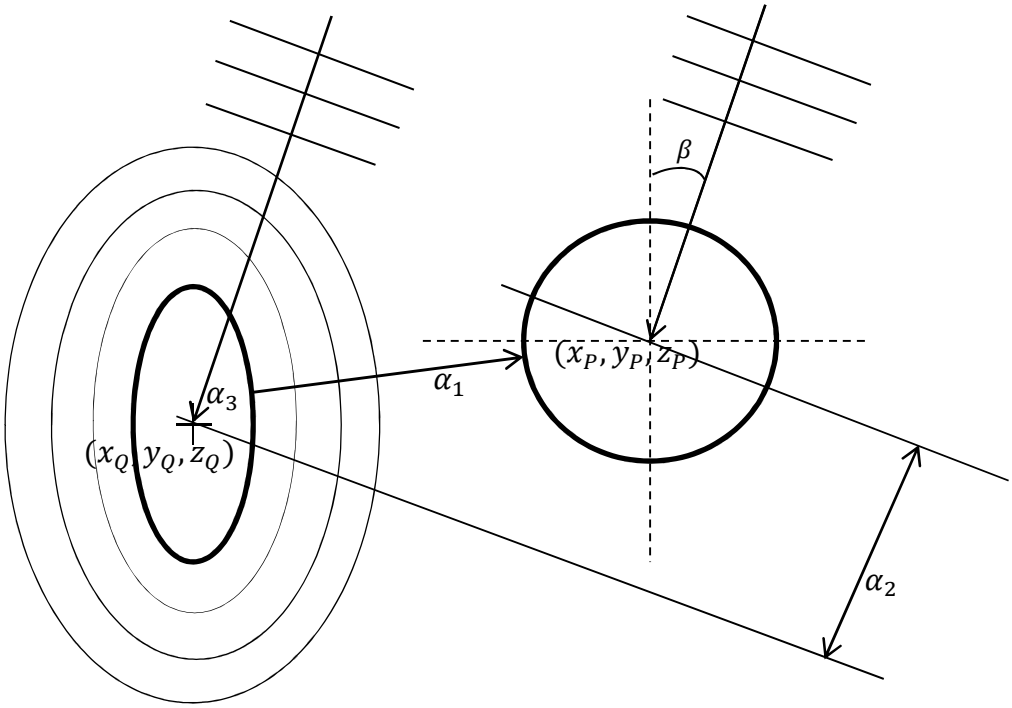

Figure 5.12: Leading phase between radiating wave in respective to incident wave.

In two structures case, the interaction of both structures P and Q can be shown in Figure 5.13.

I → P → Q → P → Q → P …

I → Q → P → Q → P → Q …

Stage 0 Stage 1 Stage 2 Stage 3 Stage 4

(→) is wave propagation direction

I is incident wave

P and *Q* is lable of floating structures

Figure 5.13: Radiating wave interaction between structure *P* and structure *Q*

In the Figure 5.13, I is the wave force due to the incident wave, *P* is the radiating wave due to motion of structure *P* and *Q* is the radiating wave due to motion of structure *Q*. In stage 0, the motions of structure *P* and structure *Q* are induced by incident wave. In stage 1, the motion of structure *P* is induced by the radiating wave force due to the motion of floating structure *Q* in stage 0 while the motion of structure *Q* is induced by the radiating wave force due to the motion of floating structure *P* in stage 0. In this method, it is assumed that the motion of structure in the following stage is due to the radiating wave generated by the motion of nearby floating structure in the previous stage.

As mentioned, the wave force inducing the motion of floating structure in stage 0 only needs to consider the effect of incident wave and it is evaluated by using diffraction potential theory as presented in Chapter 4.1. From stage 1 until stage *n*, the radiating wave force acting on the structure *P* due to the structure *Q*, $F_{i;n}^{P}$ is the summation of radiating wave due to the force generated by each direction of motion of structure *Q*.

$$F_{i;n}^{P} = \sum_{j=1}^{6} F_{(P,i;Q,j)}^{S,n-1} \qquad (5.138a)$$

$$F_{i;n}^{Q} = \sum_{j=1}^{6} F_{(Q,i;P,j)}^{S,n-1} \qquad (5.138b)$$

After the radiating wave force acting on the structure *P* or *Q* needed to induce the motion in direction *i* is known, then the motion of each floating structure in direction *i* can be evaluated using the motion equation (4.82) to equation (4.90). After that, the wave force acting on the floating structure due to the motion of nearby floating structure for stage *n*+1 can be evaluated using the equation (5.133). This process is iterative until the wave force due

to the motion of floating structure in the previous stage is small enough and assumed to be ignored.

After that, the total wave force needed to induce the motion of floating structure can be evaluated by summing up the wave force used to generate the motion of floating structure in every stage by using equation (5.139).

$$F_{i;Tot}^{P} = \sum_{n=0}^{\infty} F_{i;n}^{P} \qquad (5.139a)$$

$$F_{i;Tot}^{Q} = \sum_{n=0}^{\infty} F_{i;n}^{Q} \qquad (5.139b)$$

Where subscript *i* is the direction of motion, superscript *P* or *Q* represents the wave force acting on structure *P* or structure *Q*, $F_{i;Tot}^{P}$ is the total wave force due to incident wave force and total every stage radiating wave force acting on the floating structure *P* inducing the motion in direction *i*, $F_{i;Tot}^{Q}$ is the total wave force due to incident wave force and total every stage radiating wave force acting on the floating structure *Q* inducing the motion in direction *i*, $F_{i;n}^{P}$ is the total wave force due to stage *n* radiating wave force acting on the floating structure *P* inducing the motion in direction *i*, $F_{i;n}^{Q}$ is the total wave force due to stage *n* radiating wave force acting on the floating structure *Q* inducing the motion in direction *i*, subscript *n* is the number of stage and *n*=0 is the wave force due to incident wave.

Then apply the motion equation (4.82) to equation (4.90) to obtain the motion of floating structure in each direction due to the interaction effect. To include the interaction effect, the wave force from the motion equation (4.82) to equation (4.90) is replaced with the wave force due to the incident wave and interaction wave as shown in equation (5.140).

$$A_{ij}^{P}\ddot{X}_{i}^{P} + B_{ij}^{P}\dot{X}_{i}^{P} + K_{i}^{P}X_{i}^{P} = F_{i;Tot}^{P} \qquad (5.140a)$$

$$A_{ij}^{Q}\ddot{X}_{i}^{Q} + B_{ij}^{Q}\dot{X}_{i}^{Q} + K_{i}^{Q}X_{i}^{Q} = F_{i;Tot}^{Q} \qquad (5.140b)$$

Where subscript *i* and *j* are the directions of motion, superscript *P* or *Q* represents the wave force acting on structure *P* or structure *Q*, $F^{P}_{i;Tot}$ is the total wave force due to incident wave force and total every stage radiating wave force acting on the floating structure *P* inducing the motion in direction *i*, $F^{Q}_{i;Tot}$ is the total wave force due to incident wave force and total every stage radiating wave force acting on the floating structure *Q* inducing the motion in direction *i*, $A^{P}_{ij}$is the added mass of the floating structure *P* for direction *i* due to motion in *j* direction,$A^{Q}_{ij}$is the added mass of the floating structure *Q* for direction *i* due to motion in *j* direction, $B^{P}_{ij}$is the damping coefficient of the floating structure *P* for direction *i* due to motion in *j* direction, $B^{Q}_{ij}$is the damping coefficient of the floating structure *Q* for direction *i* due to motion in *j* direction, $K^{P}_{i}$is the restoring force of the floating structure *P* for direction *i*, $K^{Q}_{i}$is the restoring force of the floating structure *Q* for direction *i*, $\ddot{X}^{P}_{i}, \dot{X}^{P}_{i}$ and X^{P}_{i} are the acceleration, velocity and displacement of the motion of structure *P* in direction *i*, $\ddot{X}^{Q}_{i}, \dot{X}^{Q}_{i}$ and X^{Q}_{i} are the acceleration, velocity and displacement of the motion of structure *Q* in direction *i*.

5.3. Summary

In this chapter, the solution to improve the diffraction potential theory by using the drag equation is explained. The consideration taken to combine both the theories to form the proposed method is discussed in this chapter. After that, this chapter also presents the development of the proposed method to estimate the interaction effect when two structures are arranged near to each other. The concepts used to develop the method and the mathematical models developed from the concepts are also explained in this chapter. The calculation procedures by using the proposed method explained in this chapter is discussed in the Chapter Six.

Chapter 6

6.0. Numerical Solution of Hydrodynamic of Floating Structures

6.1. Prediction of the RAO of Single Structure

The diffraction potential theory is an effective solution to predict the RAO of floating structure. The diffraction potential theory is suitable to predict the motion of large structure because the significant wave diffraction effect is portrayed on large structure. The accuracy of diffraction potential theory has been tested by many previous researchers. However, it is observed that the diffraction potential theory would over predict the RAO in damping dominant region. Therefore, this research tries to integrate the diffraction potential theory with the drag equation to improve the diffraction potential theory in predicting the RAO of floating structure especially in damping dominant region.

The flow chart of proposed method showing the procedure to estimate the RAO of floating structure using diffraction potential theory is shown in Figure 6.1. The Figure 6.1 also shows the modification of the diffraction potential theory with the drag equation. In the figure, the black color shape is the original diffraction potential theory solution steps applied to predict the motion of floating structure. On the other hand, the red color shape shows the modification on the solution of original diffraction potential method with drag equation.

In Figure 6.1, the flow chart shows the procedure to predict the RAO of floating structure. The execution starts with the input of the wave data to the simulation program developed by using the proposed method. After that, the offset data and the hydrostatic data of the floating structure are also required by the proposed simulation program. The proposed simulation program will loop for each wavelength input by the user to predict the floating structure's RAO in the selected wavelength.

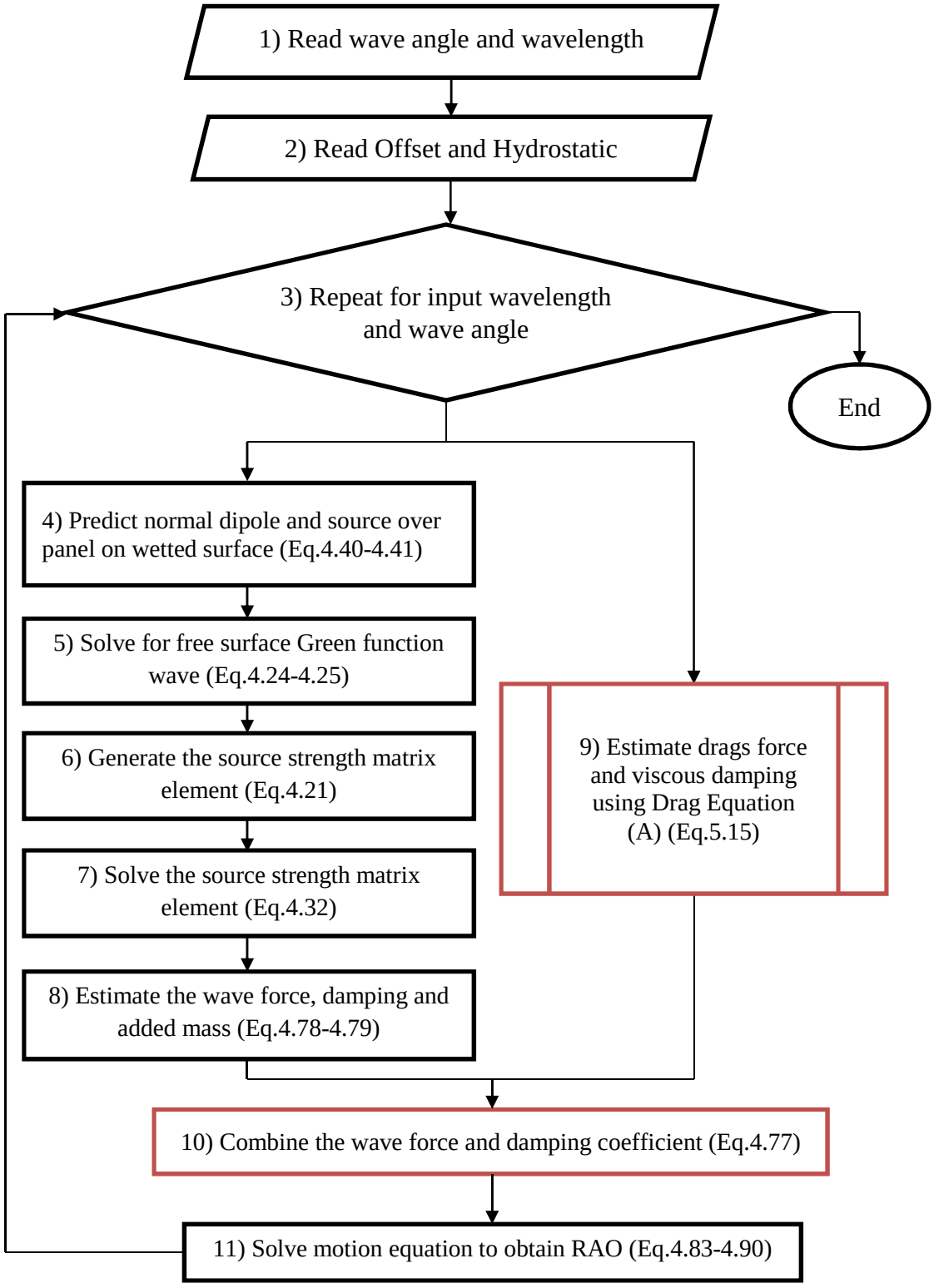

Figure 6.1: The proposed method using diffraction potential theory with drag equation

The potential of wave over the structure wetted surface is solved using Green function numerically as shown in equation (4.21). The equation (4.21) consists of two terms that are required to estimate which are the dipole, D_{mn}, source, S_{mn} and the Green surface wave, $G_W(P_m, Q_n)$. In step number 4), the proposed simulation program will start with predicting the dipole and source of panel *m* due to the panel *n* using equation (4.40) and equation (4.41). By using both the equations the source strength between panel *m* with panel *n* on wetted surface is calculated. If the wetted surface is represented by N number of panel, then the process is required to be repeated N × N times because $m = 1, 2, 3 \ldots$ N and $n = 1, 2, 3 \ldots$ N.

In the next step, step number 5) is conducted to predict the real part of the wave term using the Green function. In this step, the term $G_W(P_m, Q_n)$ and $\frac{\partial}{\partial n_Q} G_W(P_m, Q_n)$ is predicted using equation (4.24) and equation (4.25). Where equation (4.24) is used to predict the real part of the wave term using three dimensions of Green function and the equation (4.25) is the derivative to the wave term predicted by equation (4.24). Equations to predict the real part of the wave term using three dimension Green function are shown from equation (4.47) to equation (4.75).

After that, total number of N equations can be obtained to represent the wave potential on N number of panels constructed on the wetted surface of the structure using the equation (4.21). In step number 6), the matrix equation (4.32) is constructed by collecting all the variables to represent the potential on each panel generate by equation (4.21). After that, the matrix equation (4.32) is solved by using Gauss's elimination method using pivoting technique in step number 7).

After solving the matrix equation (4.32), the value of radiation wave potential and the diffraction wave potential on each panel is calculated directly from the right-hand side of the matrix equation (4.32). In the next step, the added mass and damping coefficient is calculated using equation (4.78) and equation (4.79). The wave force acting on the structure is calculated using equation (4.77).

In step number 9), the drag equation is introduced to predict the drag force and viscous damping acting on the floating structure. The method is presented in Chapter 5.1 and the detail flow chart for the subroutine is shown in Figure 6.3. The damping based on the drag equation is predicted using the first term of equation (5.15) and the drag force is predicted using the second term of equation (5.15). The drag equation only applies in predicting the heave motion since the heave motion of structure is always over predicted by diffraction

potential theory in damping dominate region. While other direction of motion is directly predicted using the wave force, damping and added mass are calculated by diffraction potential theory.

In step number 10), the RAO of structure is calculated. The RAOs of surge, pitch, sway, roll and yaw motion is predicted using equation (4.83), equation (4.84), equation (4.87), equation (4.88) and equation (4.90) respectively. As mentioned, the drag equation is only applied to improve the heave RAO predicted by diffraction potential theory. The combination of the damping and wave force predicted by diffraction potential theory and drag equation is shown in equation (5.5). Therefore, in equation (4.89), the B_{33} is the total radiation damping from diffraction theory and viscous damping from drag equation. Also the term E_3 is the total wave force predicted by diffraction potential theory and drag equation. Finally, the heave RAO is predicted by using equation (4.89).

6.2. Prediction of RAO due to Interaction Effect

In this study, the interaction between two floating structures is assumed to happen when one structure generates the radiating wave and propagate to a nearby structure to increase the wave force added on the nearby structure. Therefore, if the wave force due to the wave generated by the motion of nearby structure is known, then total wave force acting on the floating structure can be estimated by summing up the wave force due to the incident wave and interaction radiating wave propagated from the nearby structure to the influence structure by using superposition technique. The programming flow chart to show the procedure applied to predict the RAO of floating structure in interaction phenomena is shown in Figure 6.2.

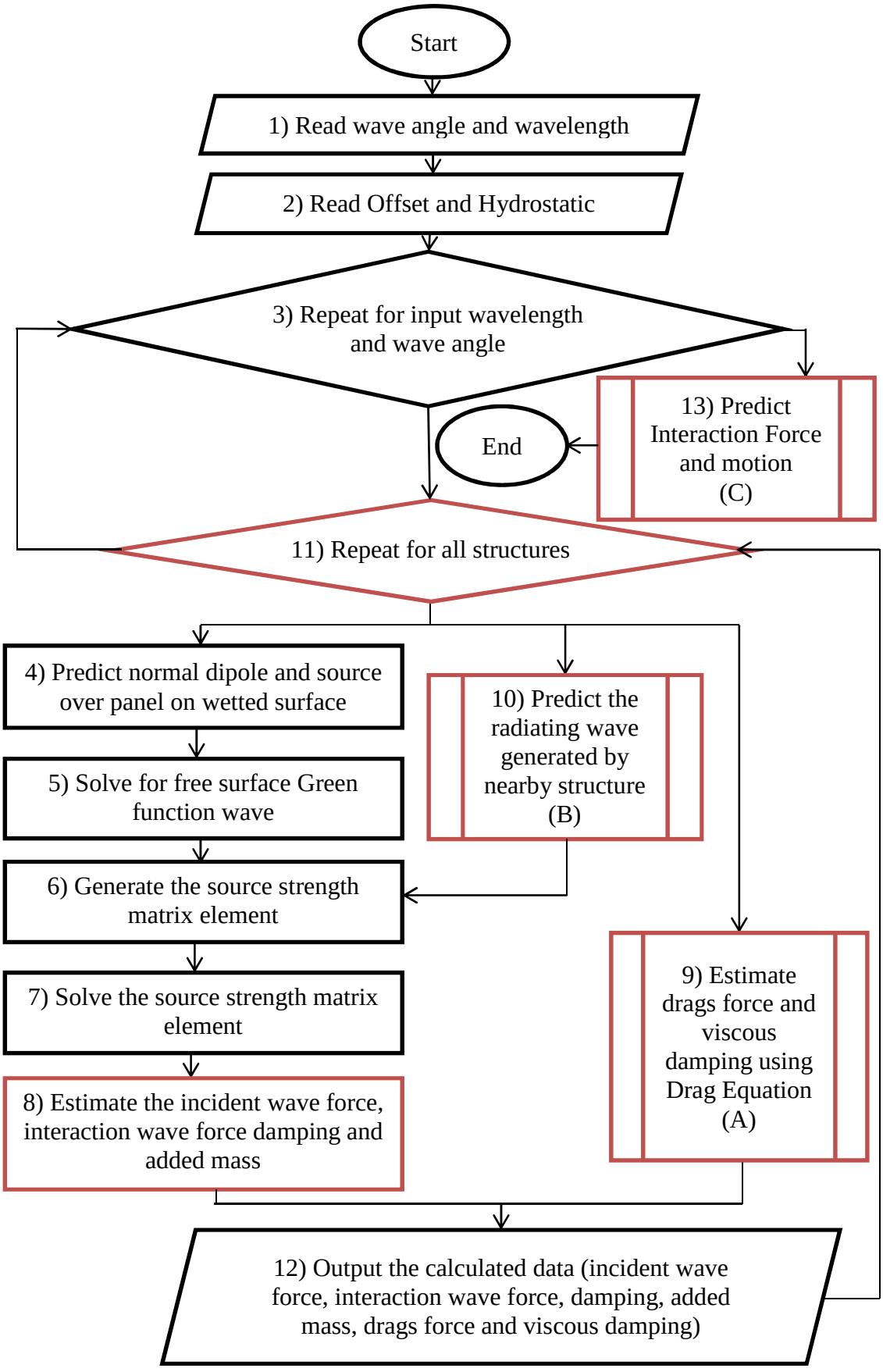
Start
1) Read wave angle and wavelength
2) Read Offset and Hydrostatic
3) Repeat for input wavelength and wave angle
End
13) Predict Interaction Force and motion (C)
11) Repeat for all structures
4) Predict normal dipole and source over panel on wetted surface
5) Solve for free surface Green function wave
6) Generate the source strength matrix element
7) Solve the source strength matrix element
8) Estimate the incident wave force, interaction wave force damping and added mass
10) Predict the radiating wave generated by nearby structure (B)
9) Estimate drags force and viscous damping using Drag Equation (A)
12) Output the calculated data (incident wave force, interaction wave force, damping, added mass, drags force and viscous damping)

Figure 6.2: The proposed method to predict RAO of floating structure on interaction case

In the Figure 6.2, the black color shape is the original diffraction potential theory calculation solutions applied to predict the motion of floating structure. It is similar to the procedure applied to predict the RAO of floating structure in single structure cases. On the other hand, the red color shape shows the modification on the original diffraction potential solution so it is able to predict the RAO of floating structure due to interaction with another structure. In the Figure 5.2, the mathematical model from task number 1) until task number 9) are similar to the mathematical model used to predict the RAO of single structure by diffraction potential theory, presented in Chapter 6.1.

There are a few tasks added into the original code to enable the single structure diffraction potential theory solution to estimate the interaction effect between two floating structures. The tasks added are from task 10) until task 13). In task number 10), a subroutine used to estimate the radiating wave generated by the nearby floating structure propagating to the influence structure is included in the calculation. The mathematical model used in task number 10) is presented in Chapter 5.2, equation (5.16) until equation (5.115). From the equations, the arrival of the radiation wave generated by nearby structure on each panel of influence structure is estimated in propose to form the matrix equation (5.122) using equation (5.127). At this moment, the dissipated energy from the nearby structure will still remain unknown. So the amplitude of wave generated by the motion of nearby structure is in function of unit of energy dissipated by the motion of structure in this stage. The flow chart of proposed method to estimate the propagated radiation wave generated by nearby structure is shown in Figure 6.4. In the matrix equation (5.122), the left hand side variables are identified by using Green function which is similar to the mathematical model used to predict the left hand side variables of matrix equation (4.32). At the right hand side of the matrix equation (5.122), they are calculated by using equation (5.125), equation (5.126) and equation (5.127) where the equation of (5.125) to equation (5.127) are targeted to find the radiating wave potential of the influence structure, diffracted wave potential of the influence structure and the interaction wave potential of the influence structure.

In task number 8), the wave force due to the radiating wave generated by nearby structure is calculated by using equation (5.129) after the matrix equation (5.122) is solved. After that, the same process is required to repeat for another structure as shown in task

number 11). In task number 12), all calculated wave forces, damping and added mass in every selected wavelength are recorded and saved into a file which will be used for future task.

Task number 13) shown in Figure 6.2 is conducted after the damping of both structures, added mass of both structures, wave force act on both structures due to the incident wave and interaction effect are calculated. In the task number 13), the motion of floating structure due to the incident wave and wave generated by nearby structure are calculated by using the motion equation as shown in equation (4.83), equation (4.84), equation (4.87), equation (4.88), equation (4.89) and equation (4.90). The dissipated energy due to the motion of floating structure is calculated using equation (5.130). And then, amount of wave force acting on the influence structure due to the motion of nearby structure can be calculated using equation (5.133). By summing up the wave force due to the incident wave and the wave force due to the radiating wave generated by nearby structure in superposition technique, the total wave force due to the interaction is obtained. The detail of the task number 13) is presented in Figure 6.5.

6.3. Estimation of Viscous Damping and Drag Force

The viscous damping and the drag force acting on the floating structure are calculated using the drag equation. The proposed method based on the drag equation was developed in this research so the execution can involve the viscous effect. The flow chart of proposed method for executing the viscous damping and drag force is shown in Figure 6.3.

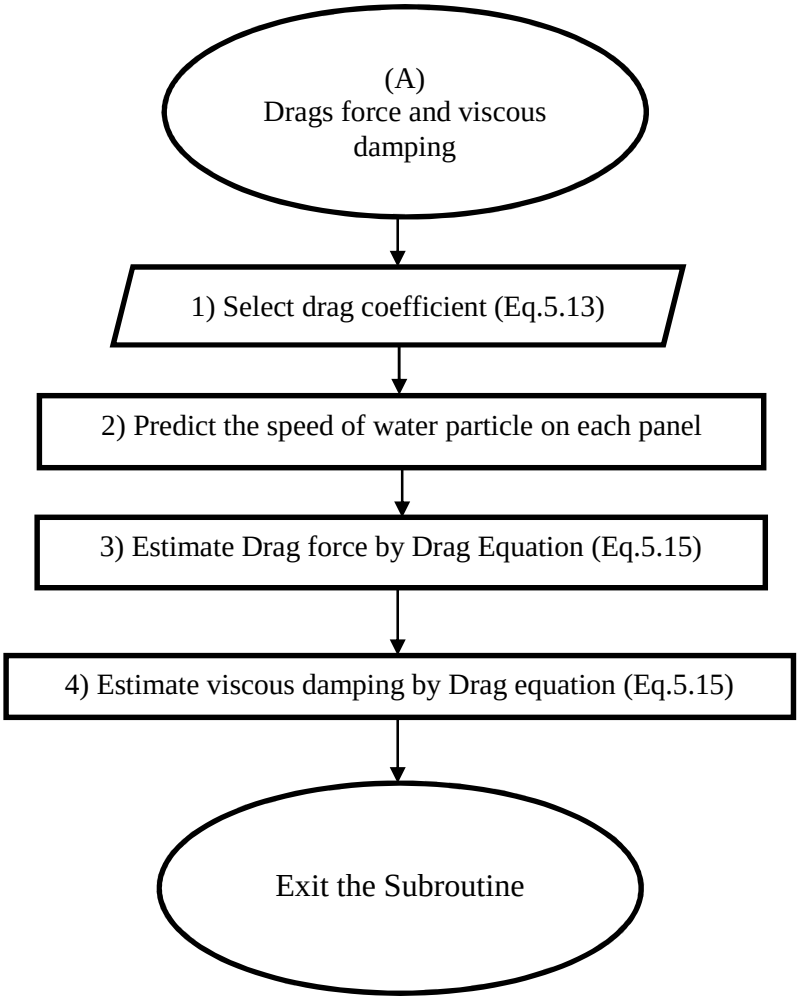

Figure 6.3: Prediction of damping and drag force using drag equation

The procedure to estimate the viscous damping and drag force is shown in Figure 6.3. In this research, improvement of heave RAO predicted by diffraction potential theory is only conducted on the round shape FLNG. In task number 1), the drag coefficient for the round shape FLNG is selected from Table 5.1. The ratio of diameter to draught for the round shape FLNG is calculated using the structure data provided to the simulation program.

In task number 2), the Z-direction of water particle speed on each panel is calculated using the equation (5.13). Since the area of panel and area normal vector of the panel are known, then the drag force acting on the structure is calculated using the first term of equation (5.15) directly. And then, in task number 4), the viscous damping predicted by using the drag equation is calculated using the second term of equation (5.15). In the equation (5.15), the

total drag force and damping acting on the round shape FLNG is calculated by summing up the drag force and damping acting on each panel at the wetted surface.

6.4. Prediction of the Propagation of Radiating Wave Generated by Structure Motion

To predict the wave force due to the wave generated by the motion of nearby structure, the propagation direction of the radiation wave generated by motion is required to be predicted first. The procedure to predict the radiation wave generated by the nearby structure propagating to the influence structure is shown in Figure 6.4.

In this study, interaction involves two floating structures which are round shape FLNG and tanker ship. In task number 1), the global coordination of both structures was selected to be used in this calculation. In task number 2), the first wave crest generated by the motion of floating structure is predicted and represented by quadratic equation (5.52). The variables a_n, b_n, c_n which determine the curve of the quadratic equation (5.52) are calculated using the equation (5.54) to equation (5.56).

After that, the information about the wave generated by the nearby structure arriving on each panel of the influence structure can start to be predicted as shown in task number 3). In this task, the dissipated energy due to the motion of nearby floating structure in each direction is assumed as one unit. The wave amplitude of the wave generated by motion of nearby structure in each direction of motion arriving on the influence structure is calculated using the equation (5.76) to equation (5.78) and equation (5.113) to equation (5.115). The direction of the radiating wave generated by motion of nearby structure arriving on the influence structure is calculated using equation (5.67) and the distance of the wave propagated from the hull generates wave to the influence structure is calculated using the equation (5.68).

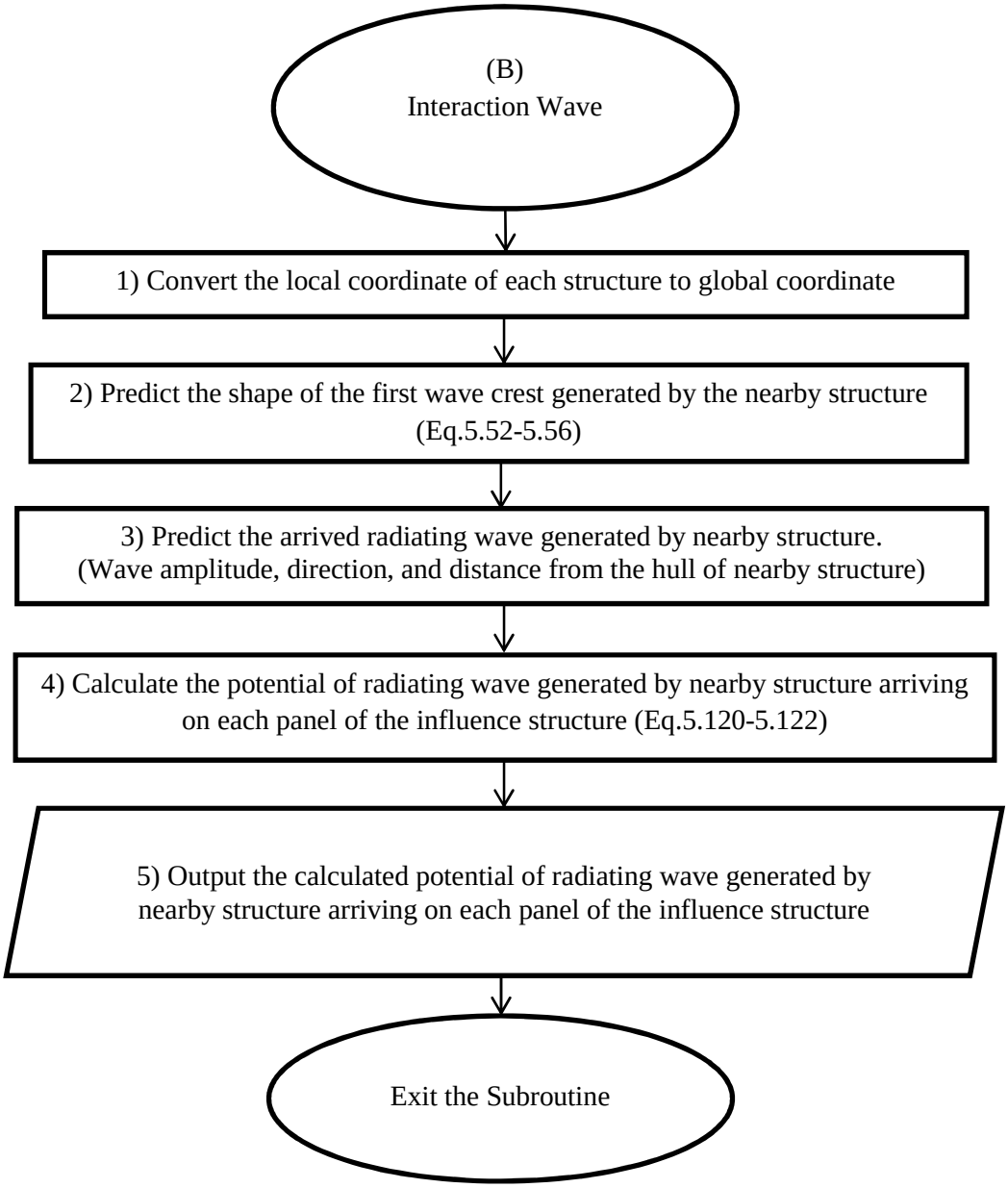

Figure 6.4: The flow chart of proposed method to predict the propagation wave generated by structure motion

In task number 4), the potential of the wave generated by motion of nearby structure arriving on the influence structure is calculated using the equation (5.120) and equation (5.121). Since floating structure is allowed to move in six directions, a total of six interaction wave potentials are obtained in this task. Then, the predicted interaction wave potentials are inserted into the right hand side of matrix equation (5.122) so the interaction wave forces acting on the influence structure are calculated.

The task number 5) is proposed to output the potential of radiating wave generated by motion of nearby structure arriving on the influence structure. This data is later used to calculate the drag force and viscous damping due to the interaction wave.

6.5. Prediction of the Interaction Wave Force

After the added mass, damping coefficient and wave force due to the incident wave for both structures are calculated, the wave force due to the interaction between two floating structures can be predicted. The flow chart to predict the interaction wave force is shown in Figure 6.5.

Added mass, damping, wave force due to incident wave, wave force due to the wave generated by motion of nearby structure in the unit of energy dissipated is solved by using the proposed method developed based on diffraction potential theory. The viscous damping and drag force due to the incident wave are solved using the drag equation. In task number 1) in this subroutine, data required to form the motion equation is transferred from the solution of diffraction potential theory to this subroutine.

In task number 3), the RAO due the incident wave is calculated using the motion equation. The RAO of surge, pitch, sway, roll, heave and yaw are calculated using equation (4.83), equation (4.84), equation (4.87), equation (4.88), equation (4.89) and equation (4.90) respectively. After the RAO of the floating structures are estimated, the energy dissipated by the floating structures to generate the radiating wave is estimated using the equation (5.130). In task number 5), the interaction wave force acting on the influence floating structure due to the interaction wave generated by the nearby structure in each direction of motion is calculated using equation (5.133). The total wave force to cause the motion of influence structure in each direction is calculated using equation (5.138).

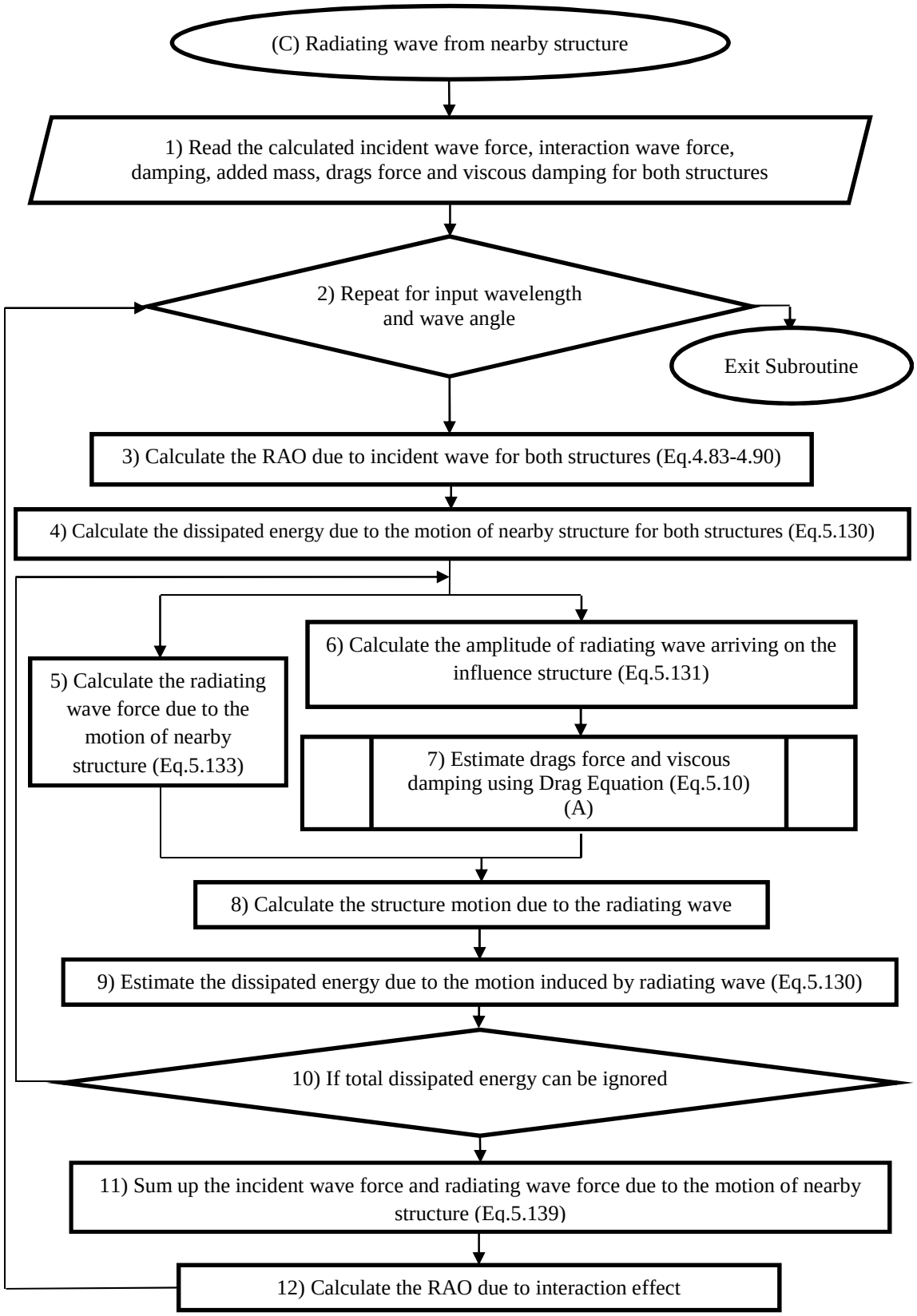

Figure 6.5: Programing flow chart to predict the propagation wave generated by structure motion

In task number 6), the radiating wave amplitude generated by the motion of nearby structure arriving on the influence structure is predicted by using the equation (5.131). The equation (5.131) gives the relationship between the wave amplitude and the dissipated energy of the structure motion. The amplitude of the radiating wave generated by the motion of nearby structure due to one unit of the energy dissipated by the structure motion is calculated in Chapter 6.4. The interaction wave amplitude arriving on the influence structure is calculate by multiplying the amplitude of radiating wave due to one unit of energy dissipated by the structure (Explain in Chapter 6.4) with the square root of the dissipated energy due to the structure motion (Equation 5.130).

Task number 7) is conducted after the amplitude of interaction wave arriving on each panel is estimated. By knowing the amplitude of the interaction wave, speed of water particle motion in Z-direction can be calculated using equation (5.10) and then the viscous damping and the drag force acting on the structure is predicted using the drag equation. The output from task number 7) is the viscous damping and drag force due to the interaction wave.

In task number 8), the damping and wave force executed by the diffraction potential theory and drag equation are summed up. Then, the structure motion due to the interaction wave force is calculated using the motion equations. Up to this step, the motion of the floating structure predicted is due to the interaction wave force in first stage.

After that, task number 9) is conducted using the equation (5.130) to calculate the dissipated energy due the structure motion induced by first stage of interaction wave. If the dissipated energy due to the structure motion induced by this stage of interaction wave cannot be negligible, then task number 5) to task number 9) are repeated to predict the interaction wave force in the next step. The wave force used in the repeated calculation is the interaction wave force of previous stage. The calculation process is repeated until the dissipated energy in the stage of interaction is negligible.

In task number 11), the wave force due to the incident wave and the wave force due to the interaction wave in each stage is summed up together by superposition principle. The equation used to calculate the total wave force is shown in equation (5.139). In task number 12), the motion equation for each direction of motion is used to calculate the RAO of the floating structure due to the interaction with nearby structure. To calculate the RAO due to interaction, the total wave force estimated in task number 11) is used in the calculation of task

number 12). After that the same process is repeated for the other wavelength (task number 2) until the RAO for all the selected wavelengths are calculated.

6.6. Numerical Setup for the proposed method

The proposed method was developed to predict the RAO of floating structure. The procedures to execute the RAO of single floating structure system are shown in Figure 6.1. The original programming code for diffraction potential theory is modified to predict the RAO in interaction condition as shown in Figure 6.2. In this research, the programming code is written in programming language visual-basic 2010. The interface of the self-developed programming code is shown in Appendix B. In this book, two floating structures are selected to be simulated by the proposed method. The selected models are round shape FLNG and the KVLCC2 model's shuttle tanker. The model particular for both models are listed in Table 3.1 and Table 3.2.

In this research, the numerical simulation data for single structure system and two floating structures interaction system were generated by using the self-developed proposed method based on the diffraction potential theory and diffraction potential theory with improvement on heave motion prediction by drag equation. The numerical method applies constant panel method to compute the wave force acting on the floating structure. The constant panel method divides the structure wetted surface into a number of panels so that each panel is representing a small amount of area on the wetted surface of the structure. The wave potential on each panel is solved using the Green function which is presented in Chapter Four. After that, the total wave force acting on the floating structure is calculated by summing up the wave force acting on each panel constructed on the wetted surface of floating structure.

In this research, the self-developed programming code for proposed method used 3370 panels for round shape FLNG and 3672 panels for KVLCC2 shuttle tanker to compute RAO of floating structure either in single structure system or in interaction system. The numbers of panels for both the structures were decided from the grid independent study. Based on the grid independent study, it is found that the peak motion response value of the structures would not have much change if the number of panels for both structures used in the research is increased. The self-developed programming code for proposed method only constructs the panel on the wetted surface because only the wetted surface is affected by the wave effect.

The mesh of both floating structures used in the execution is shown in Figure 6.6 and Figure 6.7.

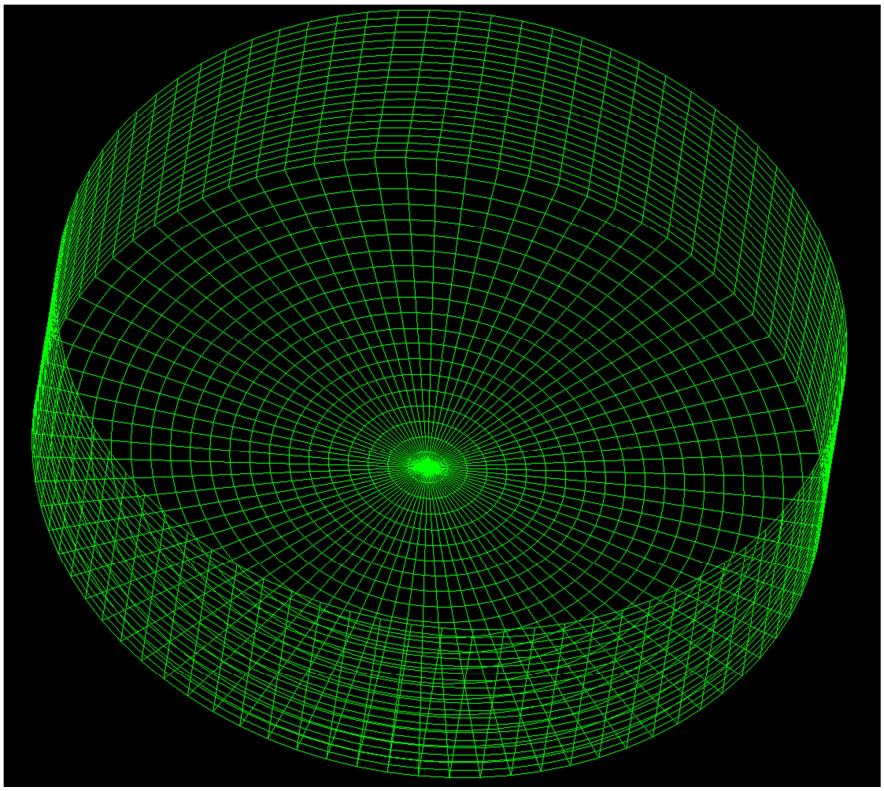

Figure 6.6: Mesh of round shape FLNG applied in the prediction of the RAO by using self-developed programming code

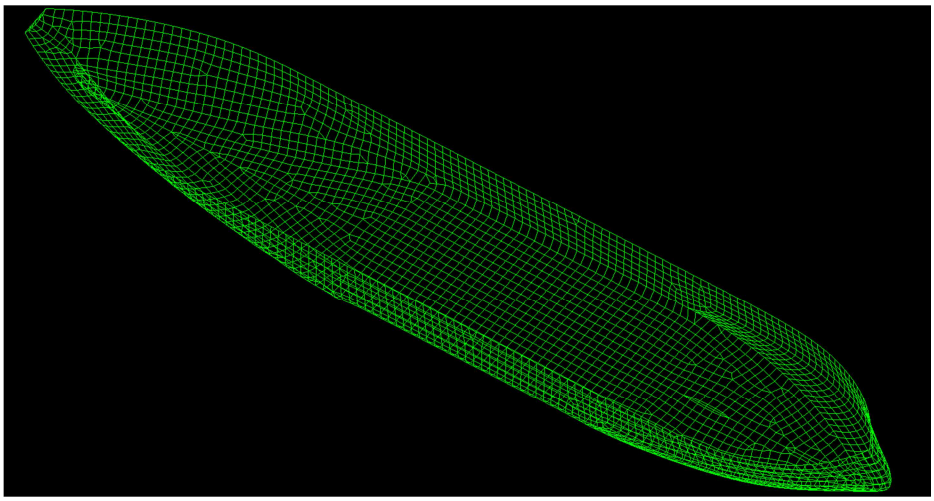

Figure 6.7: Mesh of KVLCC2 tanker ship applied in the prediction of the RAO by using self-developed programming code

As presented in Chapter One, the research also proposed to study the effect of existing of nearby floating structure on the motion of round shape FLNG. To simulate the RAO of round shape FLNG in interaction cases, same amount of mesh for the condition when FLNG is alone and when FLNG is interacting with KVLCC2 is used in the computation. The arrangement of structures and the mesh in computing the RAO in interaction cases is shown in Figure 6.8.

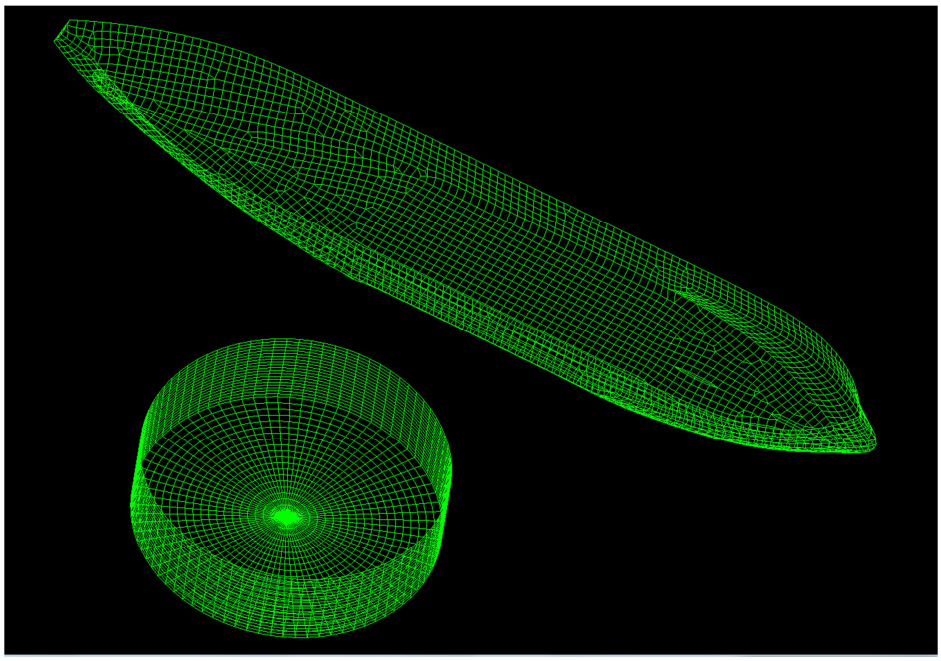

Figure 6.8: Mesh of round shape FLNG and KVLCC2 tanker ship applied in the prediction of the RAO by using self-developed programming code.

The diffraction potential theory calculates the RAO of floating structure in regular wave condition. The wave amplitude used in the simulation is settled to 1 unit for any condition. The execution is repeated to obtain the RAO data of the structure in selected range of wavelength. According to Det Norske Veritas (DNV) recommended practice published in year 2011, the computations are normally performed for at least 30 frequencies for a motion analysis conducted in the frequency domain. Besides, the guideline is also recommended to increase the number of computation if the motion's natural frequency is lies within the wave spectral frequency range. To detect the peak response of the RAO, the wavelength spacing used for computations was selected through iterative process. Where the selected wavelength spacing use for the computations should able to detect magnitude of peak motion response similar with the magnitude of peak motion response detect by the computations using finer

wavelength spacing. In this research, total 153 wavelengths were selected to be executed by the proposed method so the RAO tendencies can be plotted. The selected list of wavelengths is shown in Table 6.1.

Table 6.1: Selected wavelength used to simulate by self-developed programing code

List 1: Selected Wavelength (λ)								
Model Scale	Full Scale	λ/D_{FLNG}	Model Scale	Full Scale	λ/D_{FLNG}	Model Scale	Full Scale	λ/D_{FLNG}
(m)	(m)	(m/m)	(m)	(m)	(m/m)	(m)	(m)	(m/m)
0.5	55	0.491	1.7	187	1.670	*3.060	336.62	3.006
0.6	66	0.589	1.8	198	1.768	3.1	341	3.045
0.7	77	0.688	*1.889	207.81	1.856	3.2	352	3.143
*0.765	84.15	0.751	1.9	209	1.866	3.3	363	3.242
0.8	88	0.786	2	220	1.965	3.4	374	3.340
0.9	99	0.884	2.1	231	2.063	3.5	385	3.438
*0.999	109.91	0.981	2.2	242	2.161	*3.513	386.42	3.451
1	110	0.982	*2.248	247.31	2.208	3.6	396	3.536
1.1	121	1.081	2.3	253	2.259	3.7	407	3.635
1.2	132	1.179	2.4	264	2.358	3.8	418	3.733
*1.264	139.12	1.242	2.5	275	2.456	3.9	429	3.831
1.3	143	1.277	2.6	286	2.554	*3.997	439.67	3.926
1.4	154	1.375	2.7	297	2.652	4	440	3.929
1.5	165	1.473	2.8	308	2.750	4.1	451	4.028
*1.561	171.74	1.533	2.9	319	2.849	4.2	462	4.126
1.6	176	1.572	3	330	2.947	4.3	473	4.224
List 2: Selected Wavelength (λ)								
Model Scale	Full Scale	λ/D_{FLNG}	Model Scale	Full Scale	λ/D_{FLNG}	Model Scale	Full Scale	λ/D_{FLNG}
(m)	(m)	(m/m)	(m)	(m)	(m/m)	(m)	(m)	(m/m)
4.4	484	4.322	*7.557	831.23	7.423	10.8	1188	10.609
4.5	495	4.420	7.6	836	7.466	10.9	1199	10.707
*4.5122	496.34	4.432	7.7	847	7.564	11	1210	10.806
4.6	506	4.519	7.8	858	7.662	11.1	1221	10.904
4.7	517	4.617	7.9	869	7.760	11.2	1232	11.002
4.8	528	4.715	8	880	7.859	11.3	1243	11.100
4.9	539	4.813	8.1	891	7.957	11.4	1254	11.198
5	550	4.912	8.2	902	8.055	11.5	1265	11.297
*5.057	556.45	4.968	8.3	913	8.153	11.6	1276	11.395
5.1	561	5.010	8.4	924	8.251	11.7	1287	11.493
5.2	572	5.108	*8.444	928.85	8.295	11.8	1298	11.591
5.3	583	5.206	8.5	935	8.350	11.9	1309	11.690
5.4	594	5.305	8.6	946	8.448	12	1320	11.788

5.5	605	5.403	8.7	957	8.546	12.1	1331	11.886
5.6	616	5.501	8.8	968	8.644	12.2	1342	11.984
5.7	627	5.599	8.9	979	8.743	12.3	1353	12.083
5.8	638	5.697	9	990	8.841	12.4	1364	12.181
5.9	649	5.796	9.1	1001	8.939	12.5	1375	12.279
6	660	5.894	9.2	1012	9.037	12.6	1386	12.377
6.1	671	5.992	9.3	1023	9.136	12.7	1397	12.475
6.2	682	6.090	9.4	1034	9.234	12.8	1408	12.574
*6.245	686.97	6.135	9.5	1045	9.332	12.9	1419	12.672
6.3	693	6.189	9.6	1056	9.430	13	1430	12.770
6.4	704	6.287	9.7	1067	9.528	13.2	1452	12.967
6.5	715	6.385	*9.758	1073.40	9.585	13.4	1474	13.163
6.6	726	6.483	9.8	1078	9.627	13.6	1496	13.360
6.7	737	6.582	9.9	1089	9.725	13.8	1518	13.556
6.8	748	6.680	10	1100	9.823	14	1540	13.752
6.9	759	6.778	10.1	1111	9.921	14.2	1562	13.949
7	770	6.876	10.2	1122	10.020	14.4	1584	14.145
7.1	781	6.974	10.3	1133	10.118	14.6	1606	14.342
7.2	792	7.073	10.4	1144	10.216	14.8	1628	14.538
7.3	803	7.171	10.5	1155	10.314	15	1650	14.735
7.4	814	7.269	10.6	1166	10.413	15.2	1672	14.931
7.5	825	7.367	10.7	1177	10.511	15.4	1694	15.128

λ/D_{FLNG} is ratio of wavelength to the diameter of round shape FLNG

* is the selected wavelength for conduct the motion experiment test

** wave amplitude used in the simulation is 1 meter.

6.7. Numerical Setup for ANSYS AQWA

This study also generates the comparative data using commercial software ANSYS AQWA to compare the RAO of round shape FLNG calculated by different numerical software. In this research, only the hydrodynamic diffraction numerical model of ANSYS-AQWA is used to calculate the RAO of round shape FLNG. In general, the hydrodynamic diffraction of ANSYS AQWA predicts the RAO of the floating structure based on diffraction potential theory. The basic mathematical model used by the ANSYS AQWA is similar to the mathematical model used to develop the proposed method. ANSYS AQWA also applies panel method to compute the wave force acting on the floating structure and use the computed wave force to predict the RAO of floating structure.

To simulate the RAO of round shape FLNG when it alone and when it interacting with KVLCC2 shuttle tanker, the particular of the round shape FLNG and KVLCC2 model as

shows in the Table 3.1 and Table 3.2 were used. In this research, the round shape FLNG model was designed using AutoCAD software then the image file of the structure is exported in .iges file type before it is imported to ANSYS AQWA. The mesh used in the computation by ANSYS AQWA was generated by the ANSYS Design Modeler. The number of panels used in the computation by ANSYS AQWA for round shape FLNG is 3680 on whole structure surface and 1948 panel on wetted surface. The amount of panel used for KVLCC2 ship is 2461 on whole structure surface and 2131 panels on wetted surface. The number of mesh used to simulate the hydrodynamic characteristic of the structures using ANSYS AQWA was check by grid independent study. From the study, it is found that increase the number of mesh compare to the number of mesh used in this research would not causes the significant change to the peak motion response value of floating structure. Besides that, same simulation setting in the ANSYS AQWA for the condition when FLNG is alone and when FLNG is interacting with KVLCC2 was used in the computation simulate the RAO of round shape FLNG in interaction cases. The sample of mesh constructed by ANSYS software is shown in Appendix C.

In addition, the range of wavelengths simulate by ANSYS AQWA is from 39 meter to 2498 meter in full scale where it is 0.36 meter to 22.71 meter after converted to model scale. The total number of wavelengths selected from the range is 40. The same condition is applied to simulate for the condition when the round shape FLNG is alone and the round shape FLNG is interacting with the KVLCC2 tanker ship.

6.8. Summary

This chapter presents the programming flow chart to simulate the RAO of floating structure. The equations applied in each task of numerical computation are stated in this chapter to explain the execution step of the proposed method. After that, the input data required to insert into the numerical software before the simulation can be performed is presented. The developed proposed method presented in this chapter is required to be validated by using experiment test. The setup of the experiment test is presented in Chapter Seven. The comparison of RAO predicted by the developed proposed method and experiment test is presented in Chapter Eight.

Chapter 7

7.0. Experiment on Hydrodynamic Interaction of FPSO-Shuttle Tanker

This chapter is proposed to present the motion experiment conducted in this research, generating a comparative result in order to validate the proposed method. The experiments were conducted for the cases where round shape FLNG is alone in the wave tank and round shape FLNG is interacting with KVLCC2 tanker ship. In interaction study, the models of both floating structures were arranged in two selected distances. Photos for the experiment test are presented in Appendix D. Besides, this chapter also present the procedures to analyse the experimental result so that the RAO of floating structures can be obtained from the experimental test.

7.1. Models Selection and Design

In this research, the full size models were scaled to models size with the scale ratio of 1 to 110. To conduct the cases study in this research, two floating structures were selected. One of the objective in this research is to study the hydrodynamic behaviour of new generation round shape FLNG. The round shape FLNG is selected in this research because the available published literature about the hydrodynamic behaviour for this FLNG is limited. The round shape floating structure was introduced by Saven Marine ASA and the first unit of the round shape floating structure designed by the company to commence operations is name as Sevan 300 in year 2007. Currently, the Sevan 300 is operated by Petrobras S.A. on the Piranema field where the water depth of the location is 1100 meters (Saven Marine, 2016a). To design the round shape FLNG in this research, the model particular was referred to the largest round shape floating structure which success developed by Sevan Marine ASA, which named as

Sevan 1000 (Saven Marine, 2016b). The Sevan 1000 model has been modified in this research so the round shape FLNG in this research has a larger displacement compare to Saven 1000 in full scale. The model particular for the round shape FLNG used in the research is presented in Table.7.1.

Table.7.1: Model particular for round shape FLNG

Symbol	Model	Full scale
Diameter (m)	1.018	**111.98**
Depth (m)	0.4401	**48.41**
Draught (m)	0.2901	**31.91**
Free board (m)	0.150	**16.5**
Displacement (m^3)	0.2361	**314249**
Water plane Area (m^2)	0.814	**9849**
KG (m)	0.225	**24.8**
GM (m)	0.069	**7.6**
K_{xx} (m)	0.268	**29.48**
K_{yy} (m)	0.268	**29.48**
K_{zz} (m)	0.360	**39.60**
CB		**0.785**
CW		**0.785**

Besides, the shuttle tanker was selected in this research to generate the interaction effect to the round shape FLNG. The shuttle tanker selected in this research is KVLCC2 ship model. The KVLCC2 ship model was selected in this research because the model has the displacement closer to the round shape FLNG. The information of the KVLCC2 model used in this research was referred to SIMMAN 2014 workshop and National Maritime Research Institute, Japan (NMRI). The SIMMAN 2014 and NMRI were provided all the required information about the KVLCC2 tanker ship such as the model particular, offset data and operation condition and the model IGES file which required to run the simulation in ANSYS AQWA software (SIMMAN, 2014; NMRI, 2016). The model particular for the KVLCC2 model used in the research is presented in Table.7.2.

Table.7.2: Model particular for KVLCC2

Symbol	Model	Full scale
Length between perpendicular (m)	2.9091	320
Water line length (m)	2.9591	325.5
Breadth (m)	0.5273	58
Depth (m)	0.2727	30
Draught (m)	0.1891	20.8
Displacement (m^3)	0.2349	312677
Water Plane Area (m^2)	1.3843	16750
CB	0.8098	
CW	0.9	
LCB (m), fwd+	0.1012	11.136
LCG (m), fwd+	0.1012	11.136
KG (m)	0.138	15.18
GM_T (m)	0.0272	2.992
GM_L (m)	3.34	367.4
K_{xx} (m)	0.0696	7.656
K_{yy} (m)	0.24	26.4
K_{zz} (m)	0.24	26.4

7.2. Considered Variables

There were few variables considered in this research to study the effect on the motions response of round shape FLNG. In this study, the dependent variables are the six direction motions response of round shape FLNG. The symbol use to represent the motions is as follows:

Motion of round shape FLNG, X_j

Where i = 1, 2… 6 to represent surge, sway, heave, roll, pitch and yaw motion of round shape FLNG

The factors influence the RAO of round shape FLNG studied in this research, which included arrive of incident wave and the arrangement of floating structures in interaction cases. When the round shape FLNG is alone, the RAO of the round shape FLNG is only

influenced by wave propagation direction and wavelength. In this research, only the effect of wavelength to the RAO of FLNG was studied. Therefore, the motion of FLNG in head sea condition was simulated with different wavelength in this research.

In the interaction cases, the effect of arrangement to the RAO of FLNG was studied in this research. There are many factors of interaction, which could influence the RAO of the FLNG as highlighted in the literature review. In this study, only the effect of separation distance was considered here to test the accuracy of the proposed method. The arrangement of the structure tested to simulate is shown in Figure 3.2.

Figure 7.1 shows the selected arrangement simulated by using the proposed method. In the interaction cases study, two factors were considered in this research. The considered factors are the incident wavelength and the gap distance between round shape FLNG with second structure. In each selected gap distance between FLNG with second structure, the simulation was conducted with a number of selected wavelengths in the desired range of wavelength to predict the tendencies of the RAO.

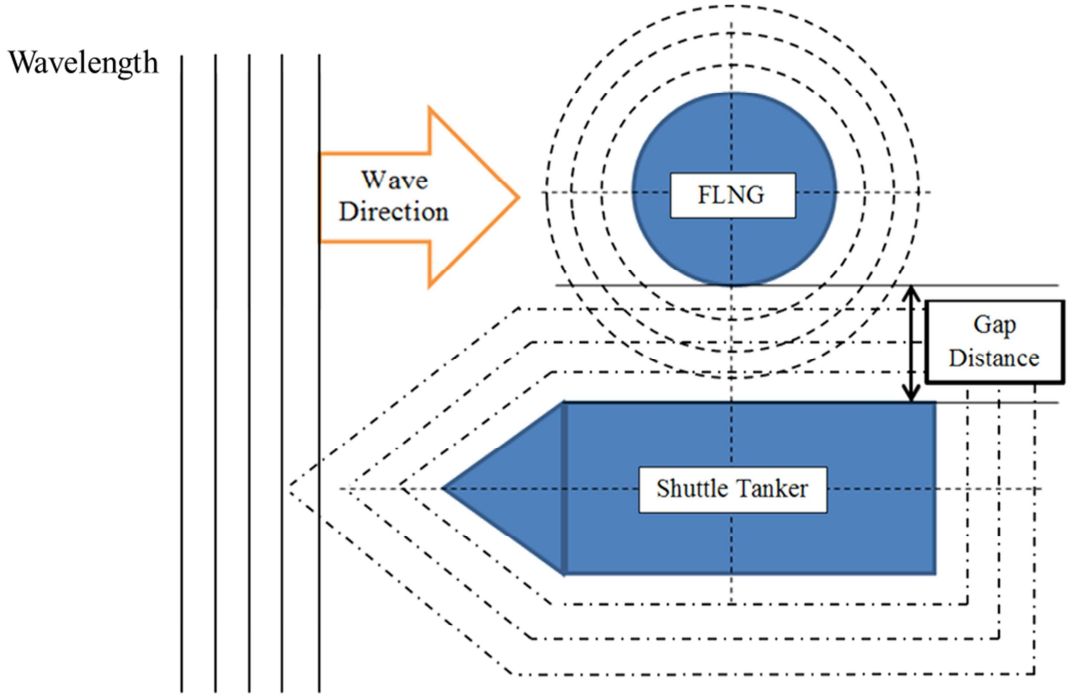

Figure 7.1: Arrangement of structures in interaction cases study

7.3. Data Collection

There are three main groups of FLNG RAO data collected to validate the proposed method in this research and study effect of interaction to the RAO of round shape FLNG. First group of data is the RAO of FLNG predicted by the proposed method. The proposed method was used to predict the RAO of FLNG when it is alone and when it interacts with second floating structure. The second group of data is the RAO of FLNG estimated by using commercial software, ANSYS AQWA. The ANSYS AQWA was used to simulate the RAO of FLNG in the similar cases with the RAO predicted by the proposed method. The RAO data from the ANSYS AQWA were used to conduct a comparative study between the RAOs of round shape FLNG estimated by proposed method with commercial software. The third group of data required in this research is the motion experiment data. The experiment was conducted in the regular wave condition. The RAO of the floating structure in each regular wave test was estimated by proper process with the time domain motion data.

To obtain the tendencies of the RAOs, the regular wave simulation was repeated to different wavelengths within the selected range of wavelength required to study. After that, the RAO of the FLNG in each wavelength was obtained from each simulation result. The RAO tendencies were shown by plotting the RAO of FLNG in each wavelength against the wavelength, which induces the motion. This process was used to collect the RAO data simulated by the proposed method, ANSYS-AQWA software and the regular wave motion experiment. The simulation data collected from this research to validate the proposed method and study the RAOs of Round Shape FLNG in the selected cases are shown as follow in Table 7.3:

Table 7.3: Ranges of the independent variables

Variable		Range
Gap Distance(m):	**Gap Distance 1**	0.5 to Diameter of FLNG
	Gap Distance 2	0.3 to Diameter of FLNG
FLNG and KVLCC2 arrangement angle		Parallel Head sea
Ratio of wavelength to FLNG length		0.5 up to 10

- The model used in the study was constructed in the scale 1:110

7.4. Experiment Setup for Wave Induce Motion Test

In the study, the experiment was conducted in wave dynamic tank owned by National Research Institute of Fisheries Engineering (NRIFE), Japan. The length, width and depth of the wave dynamic tank are 60m, 25m and 3.2m respectively. In this dynamic tank, the gravity wave is generated by 80-segment plunger type wave maker and each plunger is driven by individual 1.8kw AC servo. The plungers are arranged along the width of the dynamic wave tank at the end of the tank. The plungers have the capability to generate regular wave in the range of wave period from 0.3 seconds to 4.0 seconds with the maximum wave height of 0.4 meter within the wave period mentioned. The dynamic wave tank used for the experiment task is completed with passive type wave absorber. The wave absorber was constructed by three-slope solid structure coated with roughening bars with the length of 12.4m each. The slope of the solid structure at waterline is inclined at 7.0 degrees. The Figure 7.1 shows the facility of the dynamic wave tank used to conduct the motion experiments test in this research.

Figure 7.1: The wave dynamic tank used to conduct motion experiment in this research

7.4.1. Round Shape FLNG Model Installation

In the study, the Round Shape FLNG model was designed and constructed. The model was tested in wave dynamic experiment tank to obtain the wave induce motion response of the structure. The round shape FLNG model was constructed based on full scale model where its diameter at designed draught is 112m. In the experiment, the round shape FLNG model was scaled down with the ratio of 1:110.

To increase the displacement of the constructed round shape FLNG model, steel blocks were arranged inside the model carefully so that the centre of gravity was adjusted to the designed condition before the experiment. The mass of the steel blocks were measured by using weighting scale shows in Figure 7.2 before it is arranged inside the FLNG model. The required draught of the FLNG model during model test was marked on the surface of the FLNG model as shown in Figure 7.3. To ensure the final weight of model was settled to designed condition, the draught of the model was checked after the steel blocks arranged in the model.

Figure 7.2: Measure the mass of steel blocks before arranged the steel block into round Shape FLNG model

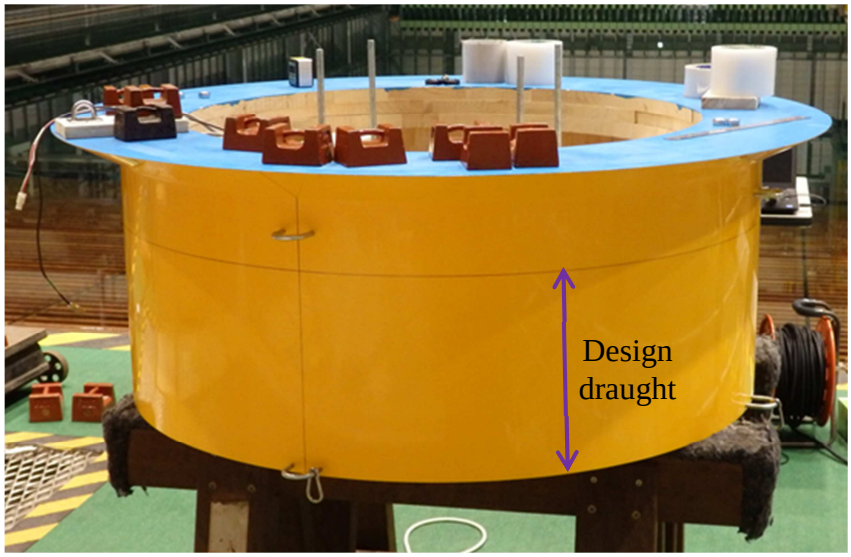

Figure 7.3: Marking of design draught of the round shape FLNG model.

After that, inclining test was conducted to check the final centre of gravity of the round shape FLNG. The steel blocks as shown in the Figure 7.4 was adjusted and then the inclining test is repeated until the desired condition was obtained. In the inclining test, bevel box was used to measure the angle of inclination of the round shape FLNG when the position of steel block was shifted. From the inclining test, the equation 7.1 is used to calculate the distance between centre of moment to the centre of gravity of the model.

$$GM_T = \frac{w_B \, d_S}{W_S \, tan\theta_{In}} \tag{7.1}$$

Where, w_B weight of steel block which shifted, d_S is the distance the steal block shifted from original position in transvers direction, W_S is the total weight of the model and θ_{In} is the angle the model inclines after the steel block shifted.

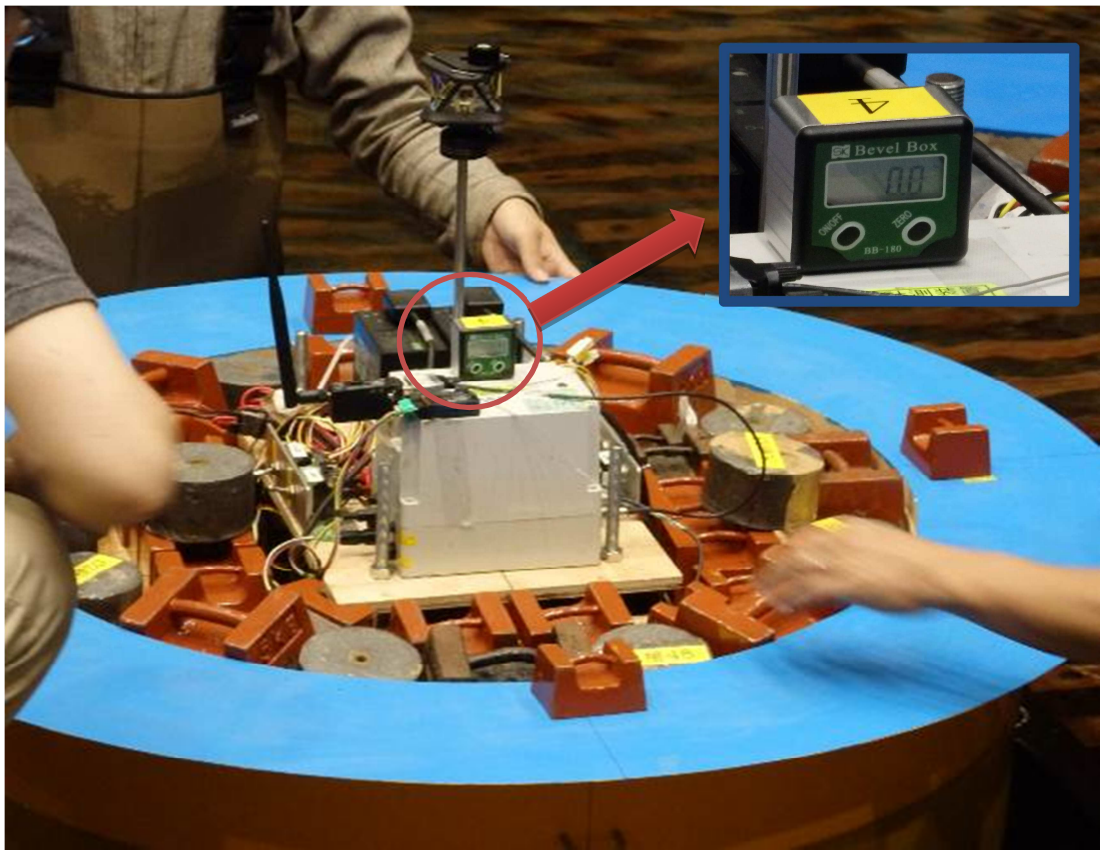

Figure 7.4: Inclining test to identify the position of the centre of gravity for round shape FLNG.

Besides, decay test was also carried out to identify the particular for the round shape FLNG model. In roll decay test, the rolling angle was measured by using gyroscope. The result of roll decay test is shows in Figure 7.5. Natural period of the roll motion was also obtained from the decay test. From the decay test, the roll natural period obtained is 2.47 seconds in model scale. The radius of gyration for roll direction also calculated based on the decay test result to ensure the round shape FLNG model has been modelling properly. Since the round shape FLNG is four sided symmetry model, then the radius of gyration for pitch direction is assumed similar with the radius of gyration for roll direction in this research. The procedure to calculate the natural frequency and radius of gyration of the FLNG model from decay test is presented in Appendix E. The particular of the models is summarized and presented in Table 3.1.

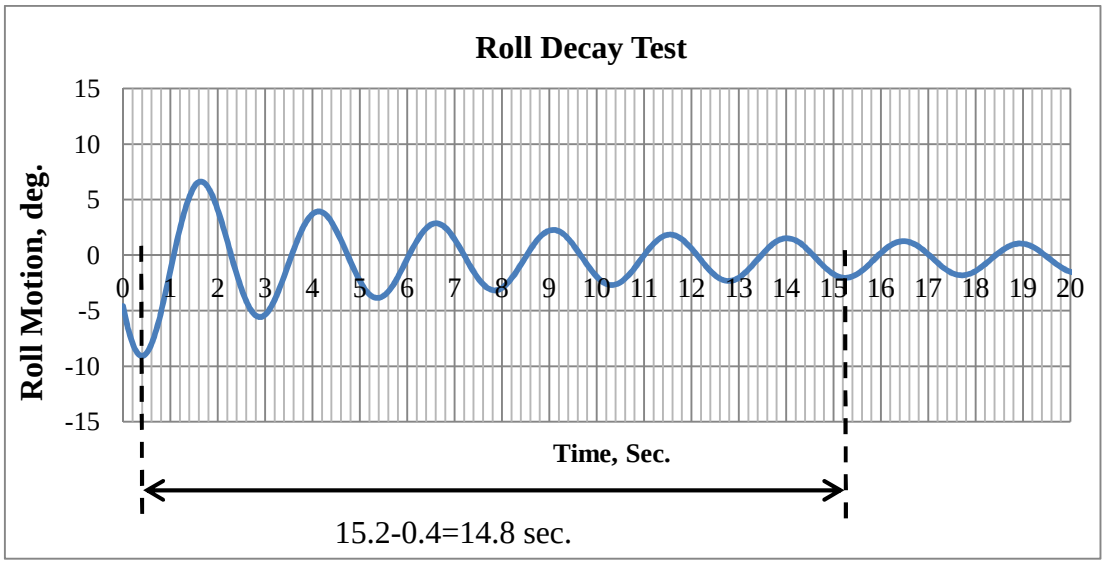

Figure 7.5: Round shape FLNG's Roll decay result

After that, the round shape FLNG model was brought to the middle of wave dynamic tank and fixed in the middle of the tank by four model scale mooring lines which were connected between the fairleads located at the bottom of FLNG model with the anchors that sank into the bottom of tank. Each anchor used in the experiment weighed 20kg in the air. The position of the anchors and the arrangement of the mooring lines inside the tank were the same for the case when the round shape FLNG was alone and when the round shape FLNG was interacting with KVLCC2 tanker model. The mooring arrangement is showed in Figure 7.6 and the view of FLNG model inside wave dynamic tank after it was installed with mooring lines is shown in Figure 7.7.

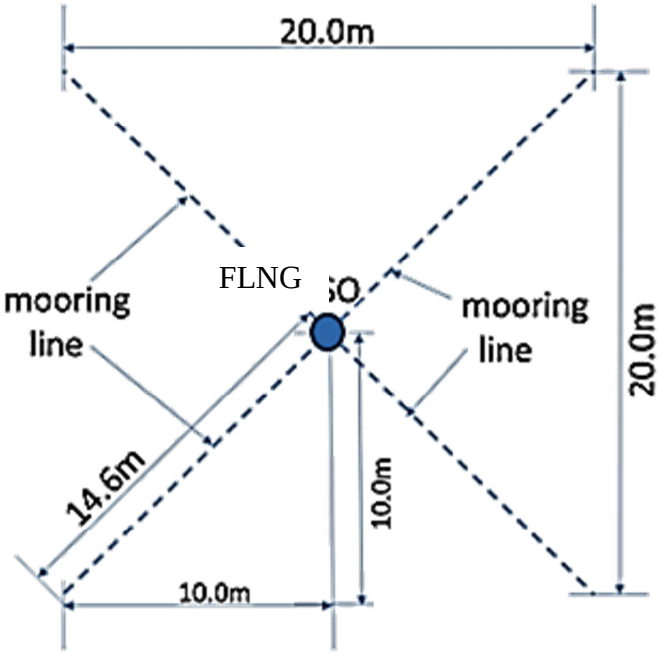

Figure 7.6: Arrangement of mooring lines and anchor in wave basin

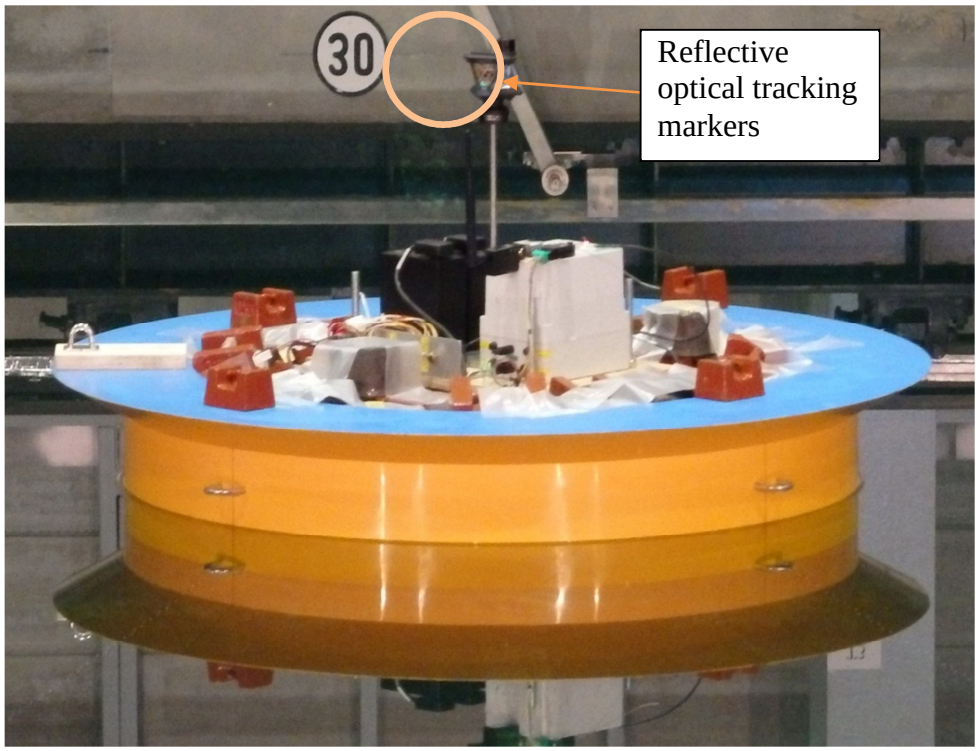

Figure 7.7: Round shape FLNG model fixed with mooring lines in wave basin in static condition

The soft mooring lines were selected to fix the model at the dynamic wave tank to avoid large movement of the round shape FLNG model due to the drift force from wave

particle motion. The mooring line selected to fix the structure was assumed to have negligible effect on the wave frequency motion.

The mooring lines were designed by using the catenary theory. The mooring line profile used in this experiment is shown in Figure 7.8 and the segment particular is shown in Table 7.1. The size of these mooring lines was pre-determined before the model experiment and the suitability of the mooring lines were analysed using numerical software to simulate the mooring performance in both static and dynamic condition.

The restoring force which is able to be generated by the mooring lines to avoid the round shape FLNG model from experiencing large amount of slow drift motion is shown in Figure 7.9. Besides, the surge and sway natural frequency for round shape FLNG model attached in this mooring are 32 seconds.

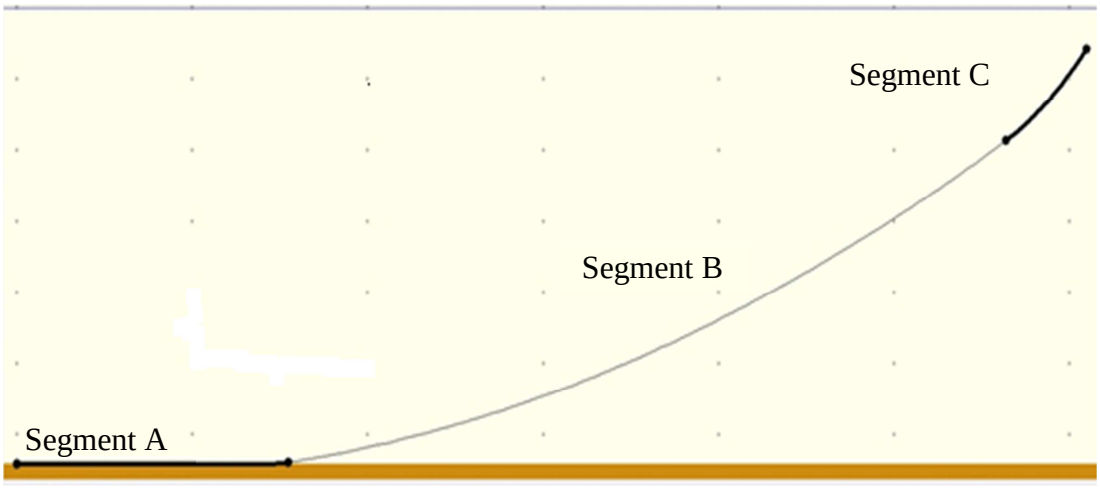

Figure 7.8: Mooring line profile

Table 7.1: Mooring line segment information

Particular	Segment A	Segment B	Segment C
	Model	Model	Model
Nominal Diameter (mm)	3.0	3.0	3.0
Type	Chain	Wire Rope	Chain
Segment Length (m)	4.0	9.4	1.4
Air Weight (kg/m)	0.16	0.0369	0.16
Water weight in water (kg/m)	0.1425	0.03119	0.1425
Model scale water density:			

1000kg/m^3			
Breaking Load (KN)	10.79	5.40	10.79
Modulus Elasticity (GPa)	114.59	61.00	114.59

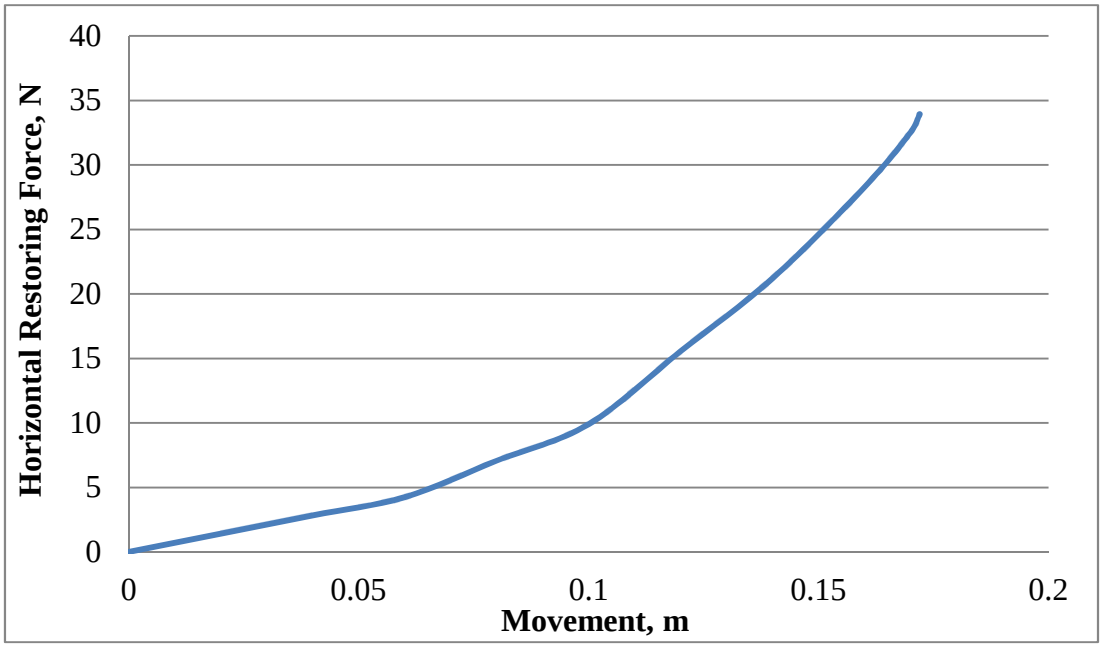

Figure 7.9: FLNG restoring force due to mooring effect

7.4.2. Natural Period of the Round Shape FLNG

The natural period of the round shape FLNG is able to calculate using the equation 7.2 if the restoring force and the mass term in each direction of motion are known. The restoring force can be contributed from the mooring system and the structure hydrostatic term. On the other hand, the natural period of the floating structure also can be obtained through the decay experiment. Natural period of each direction of motion of this round shape FLNG is shows in Table 7.2.

$$T_{n,i} = 2\pi \sqrt{\frac{\sum M_i}{c_i}} \qquad (7.2)$$

Where, in equation (7.2), the i = 1 to 6 which represent the motion of 6 DoF, $\sum M_i$ is the mass term which also take consider the added mass term and c_i is the restoring force in the direction *i*.

Table 7.2: The natural period of the round shape FLNG for each direction of motion

Natural Period	**Period, T_n (Seconds)**		**Wavelength, λ (meter)**		**λ/D_{FLNG}, (meter/meter)**
Direction of Motion	Model	Full Scale	Model	Full Scale	
Surge	32.0	335.62	1598.78	175866.0	1570.20
Sway	32.0	335.62	1598.78	175866.0	1570.20
Heave	1.49	15.63	3.47	381.3	3.404
Roll	2.47	25.91	9.53	1047.8	9.355
Pitch	2.47	25.91	9.53	1047.8	9.355
Yaw	7.46	78.24	86.89	9557.8	85.34

In Table 7.2, the natural period of surge, sway, heave and yaw motion were calculated using the equation 7.2, while the natural period of roll and pitch motion were calculated from the decay test. According to Boulluec (2014), the natural period of surge, sway and yaw motion are related to the mooring system used. To calculate the natural period of surge, sway and yaw motions using the equation 7.2, the restoring force due to the mooring system acting on the round shape FLNG is required to estimate first.

On the other hand, the heave natural period of the round shape FLNG is depended on the hydrostatic term. In this study, the heave restoring force was directly calculated from the hydrostatic term. Besides that, the roll and pitch natural period is also able to calculate directly from the hydrostatic term of the round shape FLNG. However, since the decay test for these direction are available, then the natural period of the pitch and roll motion show in Table 7.2 were estimated from the decay test data. As information, the sample calculations to predict the natural period of surge, heave and pitch motions are presented in Appendix E.

7.4.3. KVLCC2 Model Installation

To study the effect of second structure to the motion of round shape FLNG model, KVLCC2 model was selected to induce the interaction effect that influenced the RAO of the round shape FLNG model. In this research, several positions of the KVLCC2 model with respect to

the round shape FLNG model were selected in the experiment test to obtain the influence of interaction to the RAO of round shape FLNG model. The Figure 7.10 shows the position of the KVLCC2 tanker model after the model was installed in the tank. To reduce the time required to shift the position of the KVLCC2 tanker model in the wave tank, the KVLCC2 tanker model was attached to the carriage using two soft springs. Both springs connected the carriage with the KVLCC2 model in horizontal plane to avoid the influence of sprints onto the vertical motion of the KVLCC2 model.

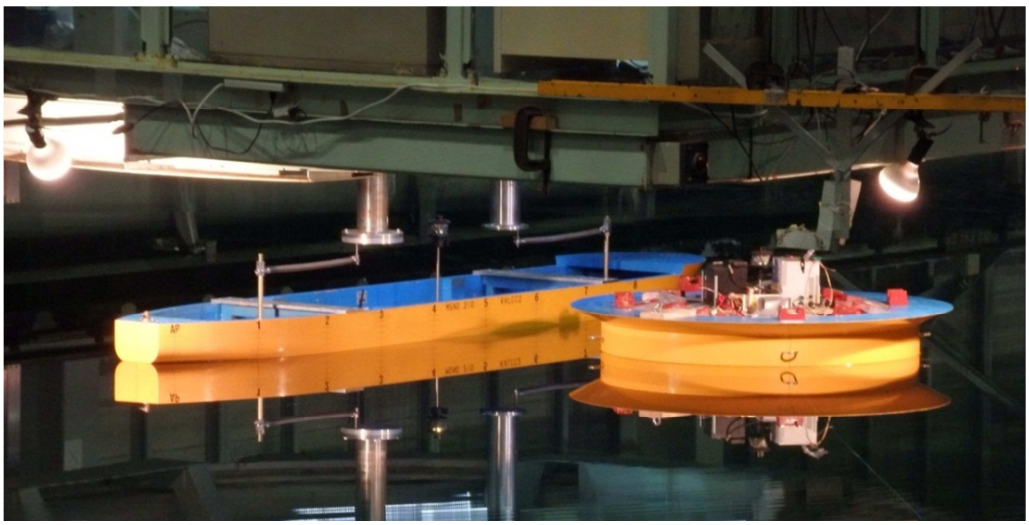

Figure 7.10: The position of Round Shape FLNG and KVLCC2 tanker in interaction motion experiment.

The positions of the connected rods installed in the KVLCC2 model are shown in the Figure 7.11. The information of the springs is listed in Table 7.4.

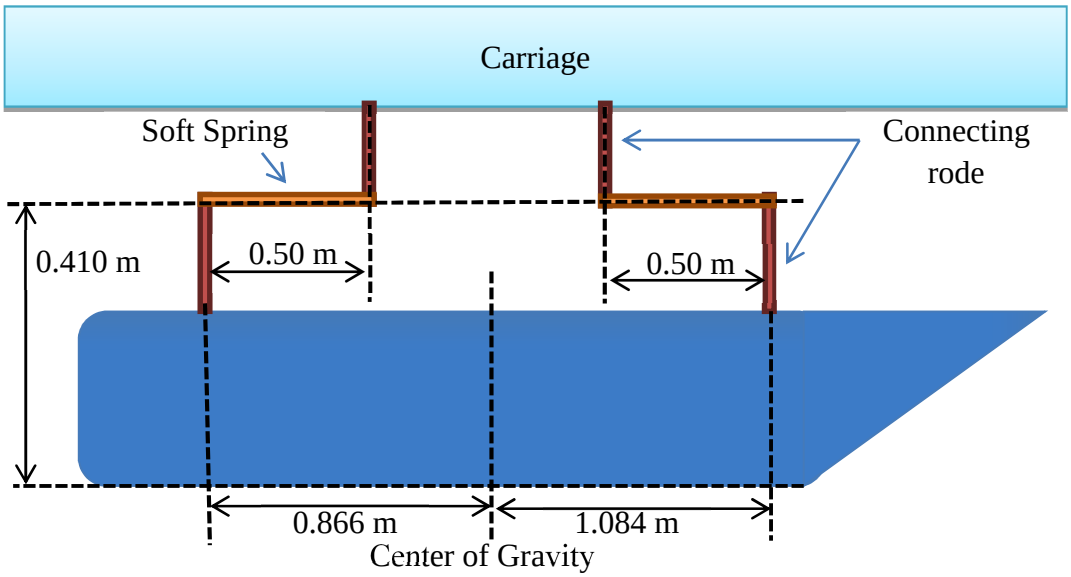

Figure 7.11: The location of connection point and fix point to join the soft spring

Table 7.4: Particular of Soft Spring used to attach the KVLCC2 Model

Particular	Model Scale	Full Scale
Fix Point Forward (m)	1.967	216.41
Fix Point Aft-ward (m)	-2.005	-220.60
Connection Point Forward (m)	1.468	161.51
Connection Point Aft-ward (m)	-1.505	-165.60
Length Between Fix Point and Connection Point (m)	0.5	55
Spring Stiffness (KN/m)	0.2066	2500
Pretension of spring (KN)	0.02066	27500
Spring Upstretched Length (m)	0.4	44

7.4.4. Measurement Instrument of Model Test

The same measurement devices were used to measure the motion of models in single round shape FLNG experiment test and the test of interaction between round shape FLNG with KVLCC2 model. The round shape FLNG model and KVLCC2 model experienced the motion in six degrees of freedom (DoF) during the experiment. The linear DoF motions of the round shape FLNG models on model size were measured by theodolite camera system as shown in Figure 7.12a. The theodolite camera is able to capture the position of the reflective optical tracking markers which is shown in Figure 7.12b automatically. The reflective optical tracking marker was placed on top of round shape FLNG model. Since the theodolite camera is only able to measure the distance between model from the camera and the angle between

optical marker respective to the camera, then mathematical model is required to calculate the position of model in wave basin tank based on the data measured from theodolite camera. During the experiment, the position of the FLNG model was calculated by the data measurement software provided by the laboratory. The interface of the software to calculate the position of model and the mathematical model apply by the software to calculate the model position is presented in Appendix F. Besides, the sample of the data measured by the theodolite camera is also presented in Appendix F.

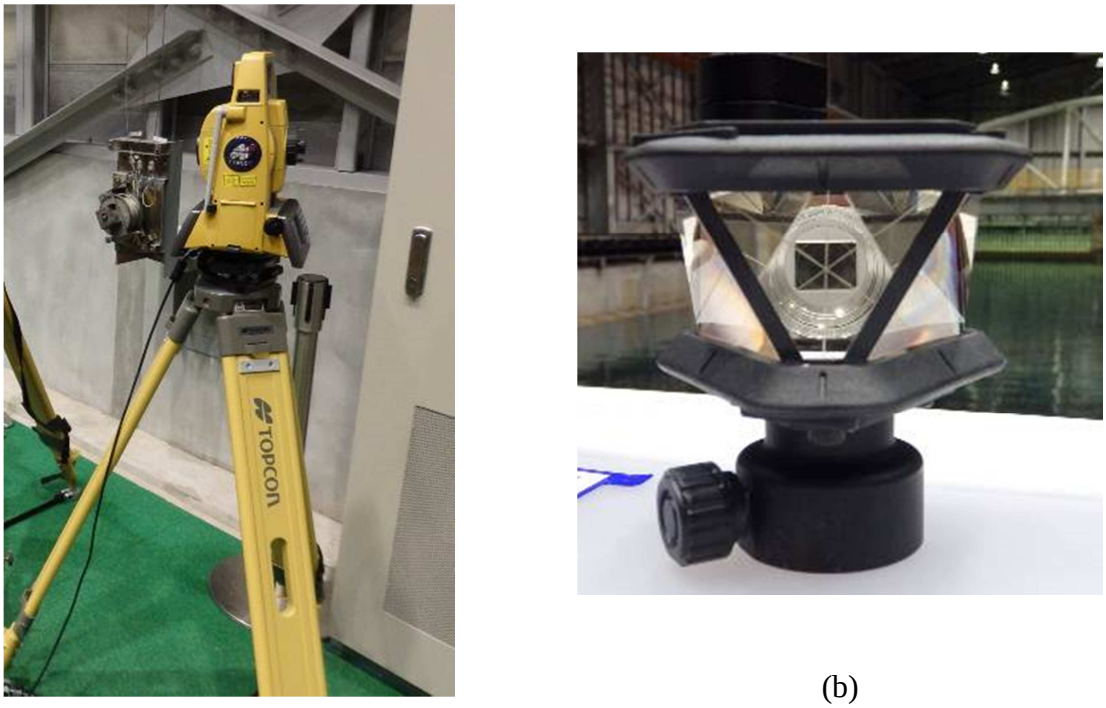

(a) (b)

Figure 7.12: Theodolite camera system to capture linear motion of FLNG model

The Rotational DoF motions of the FLNG models were measured by gyroscope shown in Figure 7.13. The gyroscope was installed at the centre of buoyancy of the FLNG during the experiment test. The rotational motion of the model is able to measure by the gyroscope directly. During the experiment, computer software was provided from the laboratory and used to receive the signal from the gyroscope. The interface of the software is presented in Appendix F.

Figure 7.13: Gyroscope to capture model rotational motion of FLNG model

A servo-type wave height measurement device as shown in Figure 7.14 was attached to the carriage which was located at the position between models and wave generator to record the wave height generated by the wave generator in the single round shape FLNG model test.

Figure 7.14: Servo-type wave height measurement device used to measure generated wave height

All the measurement devices were linked to separate computer to maximize the consistency of the measuring speed. To synchronize the device and ensure all devices start and stop measure the data without delay, the wireless remote controller as shown in Figure 7.15 was used to give instructions to start and stop all measurement devices. During the

experiment test, the theodolite camera and gyroscope measured the motion data of the round shape FLNG with the rate of 20 data per second. The servo-type wave height measurement device measured the wave height with the rate of 100 data per second.

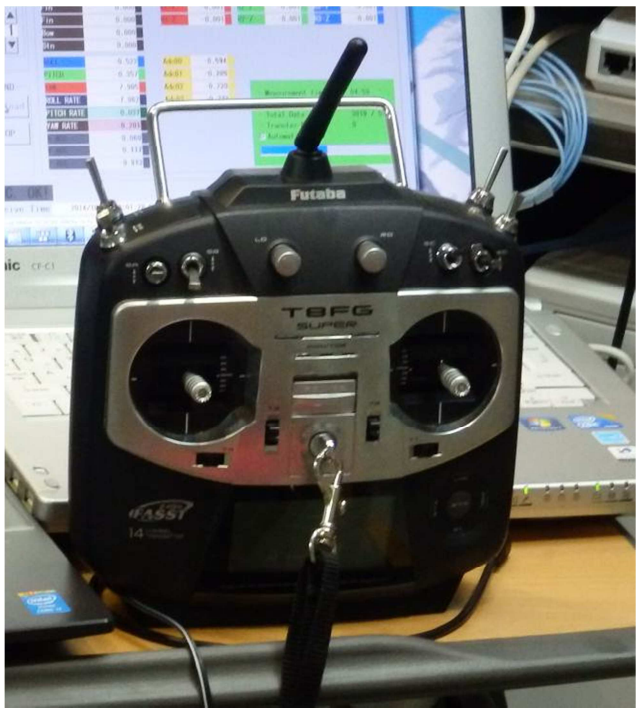

Figure 7.15: Wireless remote controller used to synchronize the start function and stop function of all measurement devices in the experiment

The location of the measurement devices during the experiments is shown in Figure 7.16 to Figure 7.18. The reflective optical tracking markers and gyroscope were installed in the round shape FLNG. The theodolite camera was installed beside the wave dynamic tank to capture the motion of the round shape FLNG model. The servo-type wave height measurement device was attached to the carriage and the position of the carriage was shifted to the middle position between wave generator and the model in single structure wave motion experiment. In interaction motion experiments, the carriage was arranged in parallel direction with the models.

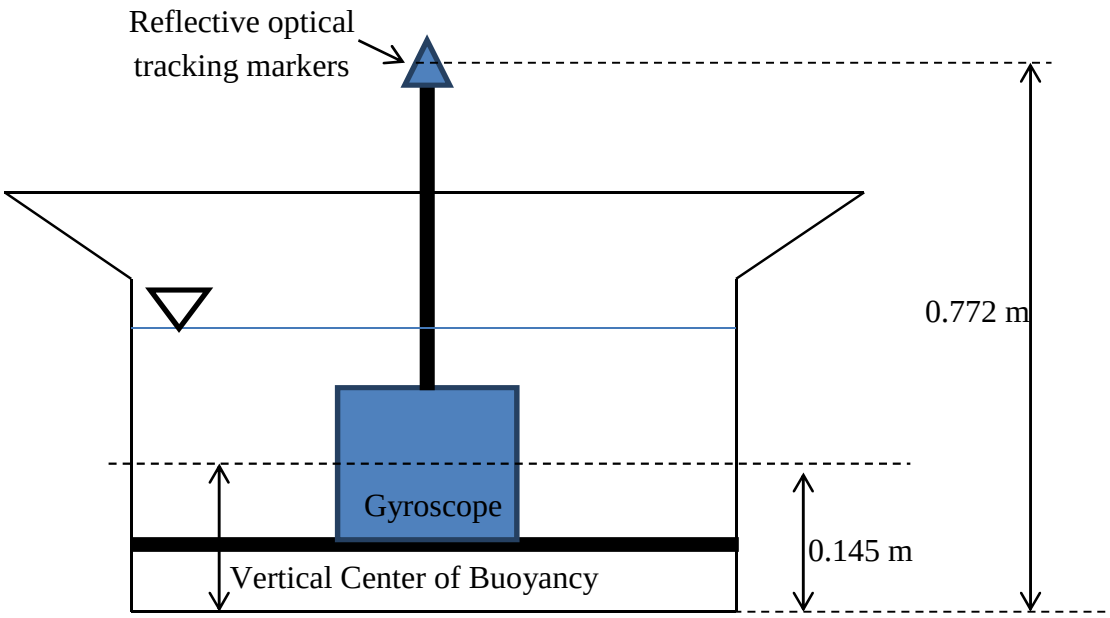

Figure 7.16: The position of the gyroscope and reflective optical tracking markers

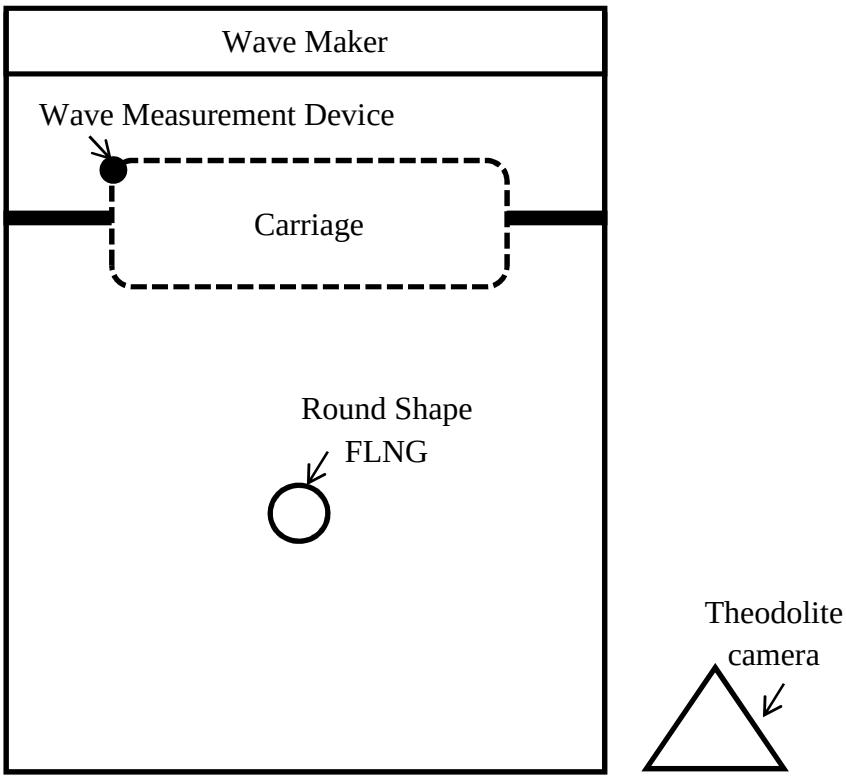

Figure 7.17: Location of model and measurement device in single structure motion experiment

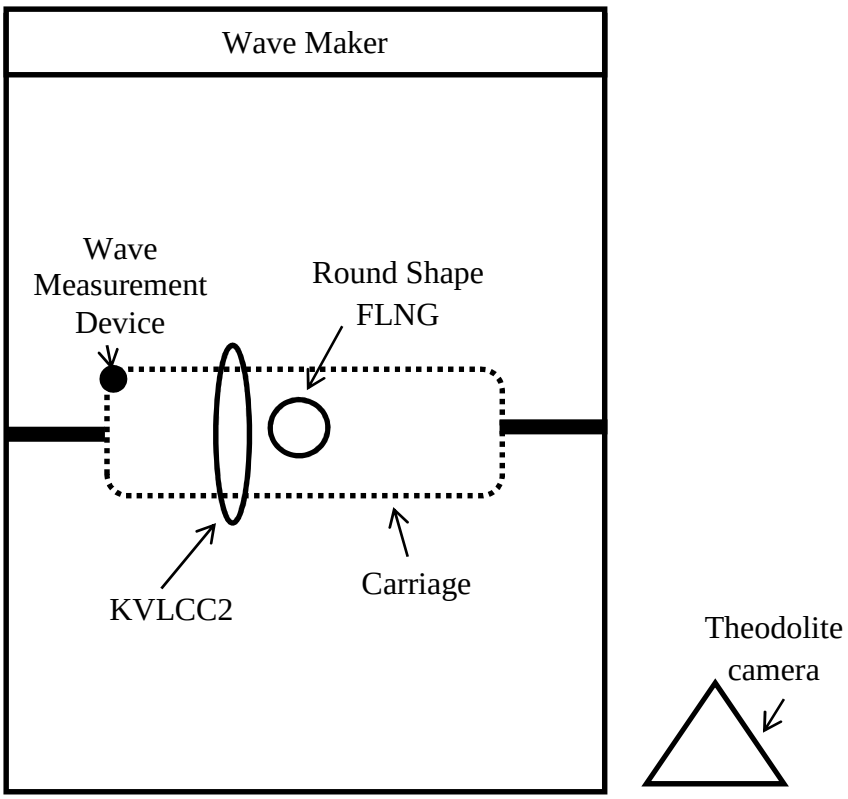

Figure 7.18: Location of model and measurement device in interaction motion experiment

7.4.5. Experiment Test Condition

The experiment tests were conducted in regular wave condition. In these experiments, the wavelengths were properly selected so that it can obtain the tendency of all motion responses in response to different wavelengths. The experiments for single structure motion test and interaction motion test were conducted in head sea condition. In initial planning, the regular wave motion experiments were conducted with a total of 12 wavelengths for each case. In order to predict the motion behaviour of round shape FLNG with higher accuracy through experiment method, two more run of regular wave experiment was made to the single round shape FLNG case and three more run of regular wave experiment was made to the interaction motion experiments with the gap distance of 0.51 meter. The list of selected wave condition is presented in Table 7.5.

Table 7.5: Selected wavelength for motion experiments

No	Wave Period (s)	Wave Height (m)	Wavelength (m)	Wave Slope	λ/D_{FLNG}

	Model Scale	Full Scale	Model Scale	Full Scale	Model Scale	Full Scale		
1	0.7	7.34	0.04	4.4	0.765	84.155	1/19.1	0.751
2	0.8	8.39	0.04	4.4	0.999	109.916	1/25.0	0.981
3	0.9	9.44	0.04	4.4	1.265	139.113	1/31.6	1.243
4	1.0	10.49	0.04	4.4	1.561	171.744	1/39.0	1.533
5	1.1	11.54	0.04	4.4	1.889	207.810	1/47.2	1.856
6	1.2	12.59	0.04	4.4	2.248	247.312	1/56.2	2.208
7	1.4	14.68	0.04	4.4	3.060	336.618	1/76.5	3.006
8	1.6	16.78	0.04	4.4	3.997	439.665	1/99.9	3.926
9	1.8	18.88	0.04	4.4	5.059	556.451	1/126.4	4.970
10	2.0	20.98	0.04	4.4	6.245	686.976	1/156.1	6.135
11**	2.2	23.07	0.04	4.4	7.557	831.241	1/188.9	7.423
12	2.5	26.22	0.04	4.4	9.758	1073.401	1/243.9	9.585
13*	1.5	15.73	0.04	4.4	3.512	386.424	1/87.8	3.449
14*	1.7	17.83	0.04	4.4	4.512	496.340	1/112.8	4.431
15**	2.1	22.02	0.04	4.4	6.885	757.391	1/172.1	6.763
16**	2.3	24.12	0.04	4.4	8.259	908.526	1/206.5	8.113

Remark:

* The wave condition only applied for case single round shape FLNG and case FLNG interaction motion experiments in the gap distance between models equal to 0.51 meters.

** The wave condition only applied for case FLNG interaction motion experiments in the gap distance between models equal to 0.51 meters.

*** Run number 11 was not applied for case FLNG interaction motion experiments in the gap distance between models equal to 0.51 meters.

- The models were arranged in head sea condition in all experiments.
- λ/D_{FLNG} is ratio of wavelength to the diameter of round shape FLNG

7.5. Experimental Data Analysis

The data measured from the experiments was required to be processed carefully so that the response amplitude operator, RAO of floating structures can be obtained. It has two major processes required to conduct to the data measured from the devices so that the RAO of structures' motion can be obtained. The first process is transferring the linear motion data

from the measuring point which was located at the reflective optical tracking markers to the centre of gravity because the RAO of structures' motion is describing the motion of floating structure at its centre of gravity.

Secondly, the time domain data measured from the devices required to transfer into frequency domain to obtain different motion amplitude of the floating structure. This procedure also recommended by ITTC (2002) in order to obtain the average amplitude and period of waves and responses. Besides, The motion of floating structure in wave induce motion can be separated into two types which are the wave frequency motion where this motion is depended on the wave frequency and the slow drift motion where the motion is depended on the wave drift force and mooring system. The RAO floating structure's motion describe the response of floating structures due to the wave frequency motion. Therefore, process the motion data in frequency domain by proper Fourier series transformation method is able to provide the experiment result with higher accuracy.

7.5.1. Transferring the Linear Motion Data to the Centre of Gravity of the Structure

The height of the reflective optical tracking markers is 0.547m above the vertical centre of gravity of the round shape FLNG model. This means that the position of the FLNG in wave tank measured by the theodolite camera is not located at the centre of gravity of the model. To obtain the exact position of the model referring to the centre of gravity of the model, the linear motion data must be transferred to the centre of gravity of the model. To transfer the data, respective roll, pitch and yaw motion of the model occurred at the same time must be considered in the calculation. The relationship between the positions of the reflective optical tracking markers and the position of centre of gravity of the model by considering the roll, pitch and yaw motions are shown in Figure 7.19.

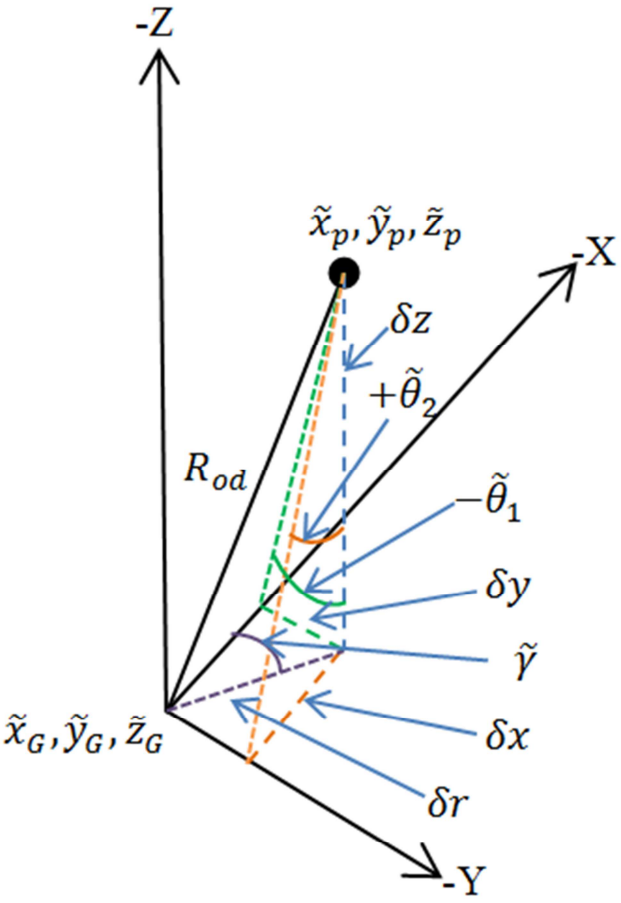

Figure 7.19: The relationship between the positions of reflective optical tracking markers and position of centre of gravity of model

From the Figure 7.19, $\tilde{x}_p, \tilde{y}_p, \tilde{z}_p$ represent the X, Y and Z position of the reflective optical tracking markers while $\tilde{x}_G, \tilde{y}_G, \tilde{z}_G$ are the X, Y and Z position of the center of gravity of model. The relationship between both the position is in the function of length of rod, R_{od} , roll angle ($\tilde{\theta}_1$), pitch angle ($\tilde{\theta}_2$), yaw angle ($\tilde{\theta}_3$) and model initial heading angle ($\tilde{\gamma}$). Therefore, the position information at the centre of gravity of the model can be calculated as follow.

$$\tilde{x}_g = \tilde{x}_p - \delta x \tag{7.3}$$

$$\tilde{y}_g = \tilde{y}_p - \delta y \tag{7.4}$$

$$\tilde{z}_g = \tilde{z}_p - R_{od} + \delta z \tag{7.5}$$

Where, $\delta x, \delta y$ and δz can be calculated by using the following equations.

$$\delta z = \left[\frac{{R_{od}}^2}{Tan^2(\tilde{\theta}_1) + Tan^2(\tilde{\theta}_2) + 1}\right]^{1/2} \tag{7.6}$$

$$\delta r = \left[{R_{od}}^2 - \delta z^2\right]^{1/2} \tag{7.7}$$

$$\alpha = Tan^{-1}\left(\frac{Tan\,\tilde{\theta}_1}{Tan\,\tilde{\theta}_2}\right) \tag{7.8}$$

$$\delta x = \delta r\, Cos(\tilde{\theta}_3 + \alpha + \tilde{\gamma}) \tag{7.9}$$

$$\delta y = \delta r\, Sin(\tilde{\theta}_3 + \alpha + \tilde{\gamma}) \tag{7.10}$$

After the position of model, referring to its centre of gravity, is obtained for the entire time series, the information can be used to calculate all 6 degree of motions of model. In this experiment setup, the rotational motions of the FLNG models were measured by gyroscope installed in the centre of gravity of the model, hence, the measured roll, pitch and yaw motion by the gyroscope were used directly as the model rotational motions data. However, extra treatment is needed for the linear motions which were measured by theodolite camera because the time domain position data obtained from the theodolite camera is the model position in the wave tank without considering its initial direction. By considering the model initial position and initial heading direction, the position data returned from theodolite camera can be used to obtain the model surge, sway and heave motion. In Figure 7.20, the plan drawing shows the difference of global coordinate where these data are measured by theodolite camera with the local coordinate system which is required to calculate the linear motion of the FLNG due to the wave.

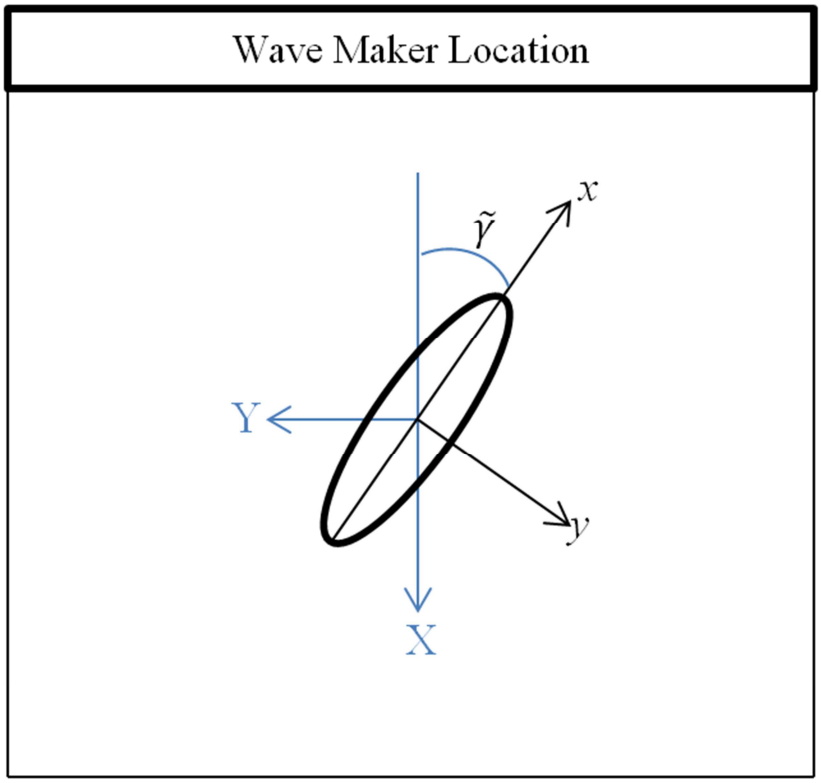

Figure 7.20: Plan view of coordinate system

In Figure 7.20, X and Y represent the global directions used in the experiment setup while *x* and *y* are the local directions where the zero position of local coordinate system is located in the model centre of gravity before the wave arrives. The model initial heading angle ($\tilde{\gamma}$) is measured from wave propagation direction and positive clockwise direction. Let the zero global coordinates be located at the model centre of gravity at calm sea condition, the 6 DoF motions of the model are calculated by following equations.

$$L = (X^2 + Y^2)^{1/2} \tag{7.11}$$

$$\beta = Tan^{-1}\frac{Y}{X} \tag{7.12}$$

And the six degree freedoms of motion for the round shape FLNG are calculated from equation (7.13) to equation (7.18).

$$\text{Surge}, X_1 = L\ Cos(\beta - \gamma + 180) \quad (7.13)$$

$$\text{Sway}, X_2 = L\ Sin(\beta - \gamma + 180) \quad (7.14)$$

$$\text{Heave}, X_3 = Z_g \quad (7.15)$$

$$\text{Roll}, X_4 = \theta_1 \quad (7.16)$$

$$\text{Pitch}, X_5 = \theta_2 \quad (7.17)$$

$$\text{Yaw}, X_6 = \theta_3 \quad (7.18)$$

7.5.2. Fast Fourier Transformation Series

The experiment data collected in time series provides the information of wave frequency motion for all 6 degree of motion and slow drift motion at horizontal plane motion. To split the different motion data, the analysis were conducted in frequency domain where the amplitude of the different types of motion are extracted from the motion amplitude occurring at the respective frequency.

According to sampling theorem, discretely frequency (*Fs*) of signal data must be at least twice the highest continuous motion signal frequency (*F*). The continuous motion signal frequency should be discrete using the rate of the sampling frequency, 1/*Fs*. Let the discrete sample of the continuous motion signal have the magnitude of *x(k)*, k=1,2,3,…,*n* and period between the sample is 1/*Fs* than a function of a continuous signal, *f(t)* can be reconstructed back from the discrete sample by the equation below.

$$f(t) = \sum_{k=1}^{k=n} x(k)\ sinc(t \times fs - k) \quad (7.19)$$

Where,

$$sinc(x) = \frac{\sin(\pi\, x)}{\pi\, x} \tag{7.20}$$

To convert the data in time domain to the frequency domain, Fast Fourier Transform method is applied. The relationship between function in the time domain, f(t) and frequency domain F(f) can be related by the equation below.

$$F(f) = \int_{-\infty}^{\infty} f(t) e^{-j2\pi f(t)} dt \tag{7.21}$$

Also, for the variable *j*, it represents the square root of (-1) in the natural exponential function.

$$e^{j\theta} = \cos(\theta) + j\sin(\theta) \tag{7.22}$$

Therefore, the discrete data can be written in complex number form as follows:

$$x_i = x(i)_{real} + j\, x(i)_{imaginary} \tag{7.23}$$

And,

$$x(i)_{real} = \sum_{k=0}^{k=n} X(k) \times \cos\left(\frac{2\pi k i}{n}\right) \tag{7.24}$$

$$x(i)_{imaginert} = \sum_{k=0}^{k=n} X(k) \times \sin\left(\frac{2\pi k i}{n}\right) \tag{7.25}$$

And, $i = 2^b$ is the number of data require by Fast Fourier Transform method where *b* can be any integer number larger than or equal to 1.

Finally, the magnitude, phase and frequency of the signal can be calculated by following equations.

$$X(i)_{magnitude} = \|X(i)\| = \frac{2 \times \sqrt{x(i)_{real}{}^2 + x(i)_{imaginert}{}^2}}{n} \quad (7.26)$$

$$X(i)_{phase} = tan^{-1}\left[\frac{x(i)_{imaginert}}{x(i)_{real}}\right] \quad (7.27)$$

$$X(i)_{frequency} = i \times \frac{Fs}{n} \quad (7.28)$$

7.5.3. Execution of Response Amplitude

To calculate the response amplitude operator, the amplitude of the generated wave and the amplitude of motion in each direction must be known. The experiments conducted in this research recorded the wave data and motion data in all six directions. The amplitude of wave and motions were obtained after the experimental data processed using the mathematical models explained in Chapter 7.2.1 and Chapter 7.2.2.

The wave amplitude and the wave frequency generated by the wave maker were actually obtained from the frequency domain data. In regular wave experiment, only one peak would be obtained if the collected wave data plot in frequency domain. By identifying the peak value and corresponding frequency of the peak value from the wave data plotted in frequency domain, the wave amplitude and the wave frequency were obtained.

The wave frequency motion of the floating structure was identified after the wave frequency was known when the collected wave data was processed. The amplitude of the structure wave frequency motion was identified from the collected motion data plotted in frequency domain. The amplitude of the wave frequency motion was obtained by finding the amplitude of motion occurred in the frequency similar to the wave frequency from the motion data plotted in frequency domain.

After that, the response amplitude operator, RAO was calculated by dividing the amplitude of motion with the amplitude of wave with the same frequency. The equation to

find the RAO for linear motion and rotational motion is shown in equation (7.29) and equation (7.30) respectively.

$$RAO_F = \frac{X_i(F)}{\varsigma(F)} \tag{7.29}$$

$$RAO_F = \frac{X_i(F)}{K \cdot \varsigma(F)} \tag{7.30}$$

Where $X_i(F)$ is the amplitude of the motion in direction i occur at the frequency F,$\varsigma(F)$is the amplitude of the wave in frequency F and K is the wave number.

7.5.4. Experiment Data Analysis Program

To fasten up the data analysis process and reduce the mistake in data analysis process, numerical programming code was developed in this research to process the collected data. The interface of the developed programming code is shown in Figure 7.21. The programming code applies the equation (7.3) until equation (7.18) to transfer the time series motions data of the floating structures model to the centre of gravity of the model. After that, the programming code transforms the time series motion data to the frequency domain form using the equation (7.19) to equation (7.28). To calculate the RAO of the floating structure, the programming code applies the solution explained in chapter 7.2.3 and the equation (7.29) to equation (7.30). The calculated results are then output to excel file for further study.

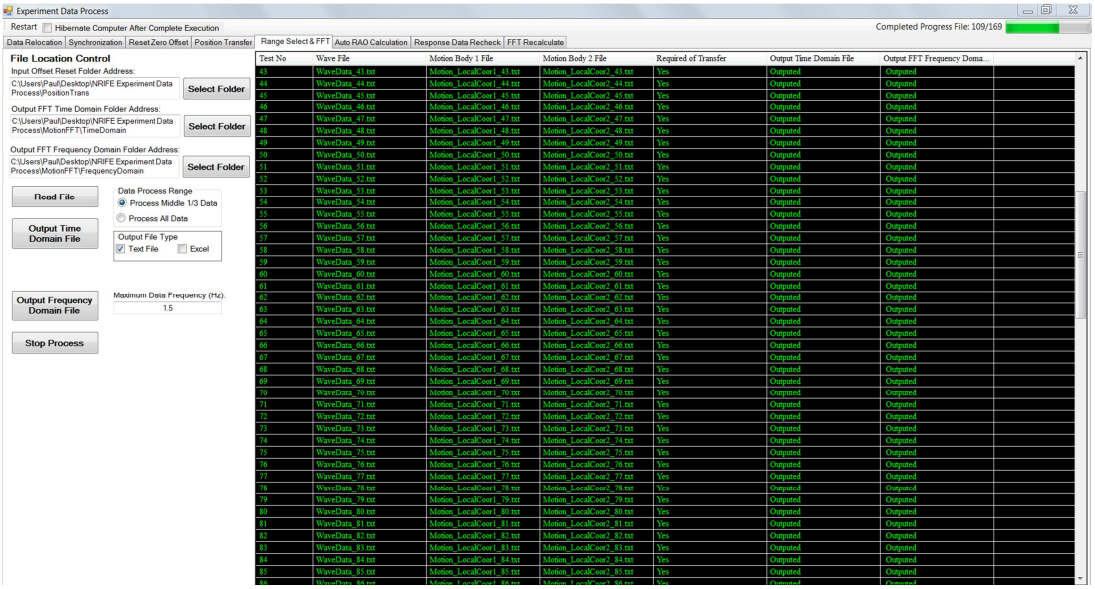

Figure 7.21: Interface of the self-developed experiment data processing programming code

7.6. Sample of Wave Frequency Motion of Round Shape FLNG estimate from Motion Experiment

The data from motion experiment were collected in time domain series. In this research, the round shape FLNG was fixed in the middle of wave tank using model scale mooring lines. Since the mooring lines were used to attach the FLNG model, the FLNG model experienced the wave frequency motion and low frequency motion during the experimental test. According to Dercksen and Wichers (1992), they commented that the low frequency motion is induced by wind, current and wave drift force, but the wave frequency motion is induced by first order wave force. In this research, the main objective is to study the motion of round shape FLNG induced by the first order wave force. Therefore, the wave frequency motion data are required as extras from the experiment test.

As example, the time series motion data for the round shape FLNG motion experiment in the wavelength equals to 2.27 metres are shown in Figure 7.22 to Figure 7.24. The sample experiment results shown in these figures are the data collected from the experiment conducted in the condition FLNG alone in the wave tank. Since the FLNG is in head sea condition, then the motion of the FLNG induced is only in the direction of surge, pitch and heave. Besides, the time series wave data, which induce the motion of FLNG is shown in the Figure 7.25.

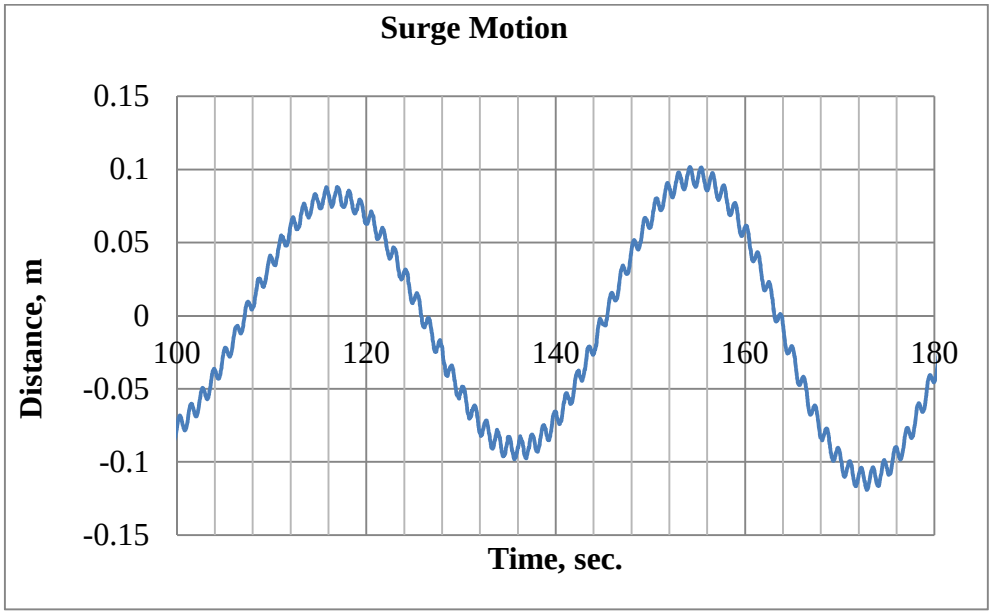

Figure 7.22: Surge motion of FLNG measure from head sea single structure motion experiment test with wavelength 2.27 meters

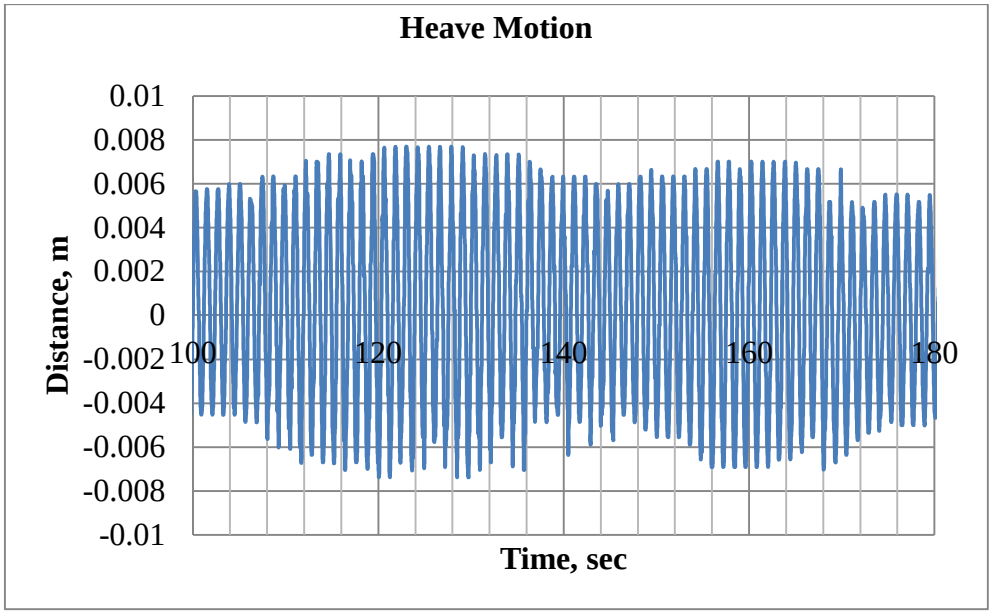

Figure 7.23: Heave motion of FLNG measure from head sea single structure motion experiment test with wavelength 2.27 meters

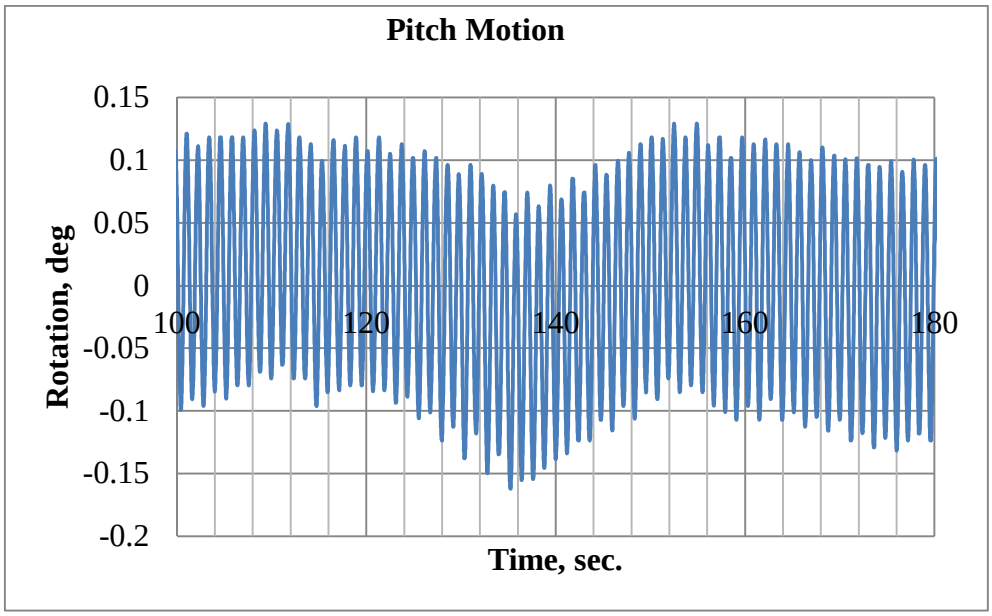

Figure 7.24: Pitch motion of FLNG measure from head sea single structure motion experiment test with wavelength 2.27 meters

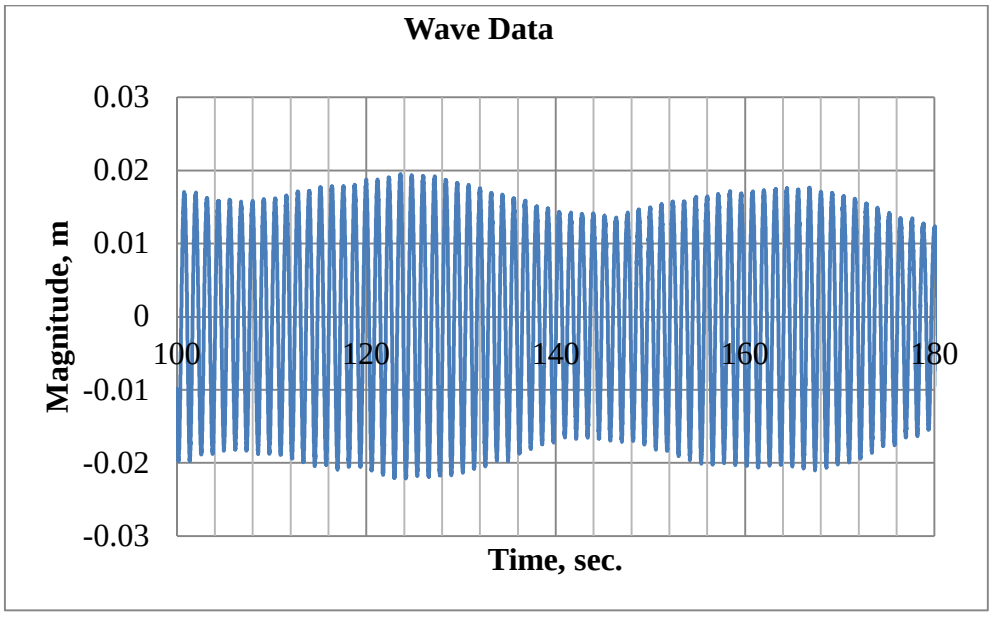

Figure 7.25: Wave data from head sea single structure motion experiment test with wavelength 2.27 meters

From Figure 7.22 to Figure 7.24, the low frequency motion only exists in surge direction in this selected experiment data. This is because the low frequency motion only happens in the horizontal plane. As shown in Figure 7.22, it is observed that the round shape

FLNG model experiences the wave frequency motion, where the frequency of this motion in this selected experiment data is 0.83 Hz. At the same time, the round shape FLNG also experiences a low frequency motion in the frequency of 0.0309 Hz. In the experiment test, the low frequency surge motion was induced from a slow vary drift force due to the effect from water particle motion.

To split the wave frequency motion and low frequency motion from the time domain motion data, the time domain data were converted to the frequency domain. In frequency domain, the magnitude of the motion, which existed in each motion frequency is shown in the corresponding frequency. In this research, the Fourier series transformation method as presented in Chapter 7.2.2 was applied to transform the motion data from time domain to frequency domain. The frequency domain data for surge, heave and pitch RAO of round shape FLNG in the selected sample are shown in Figure 7.26 to Figure 7.28. The wave data are also transformed to frequency domain, which is shown in Figure 7.29.

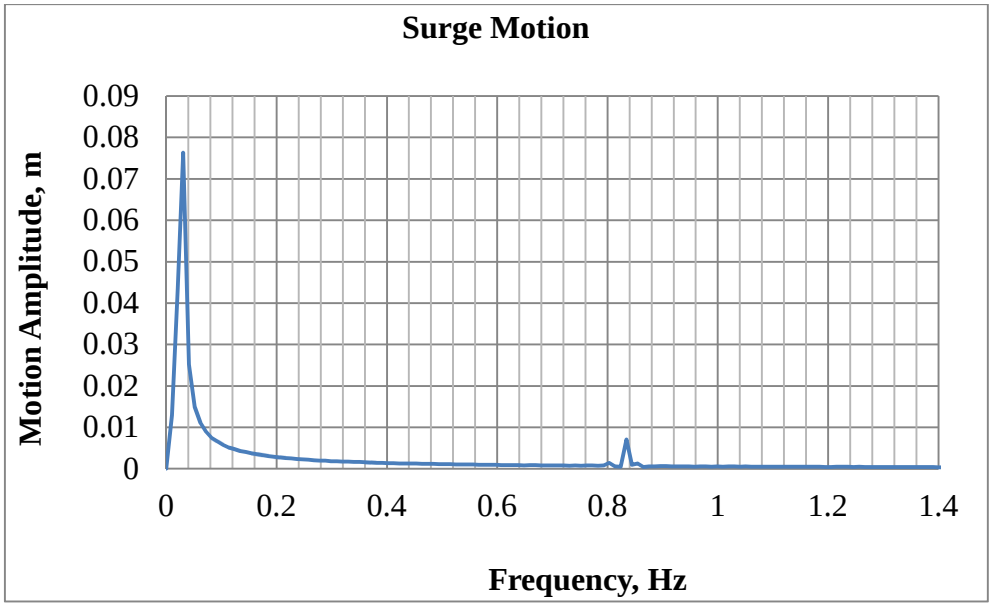

Figure 7.26: Frequency domain surge RAO of round shape FLNG in wavelength 2.27 meters

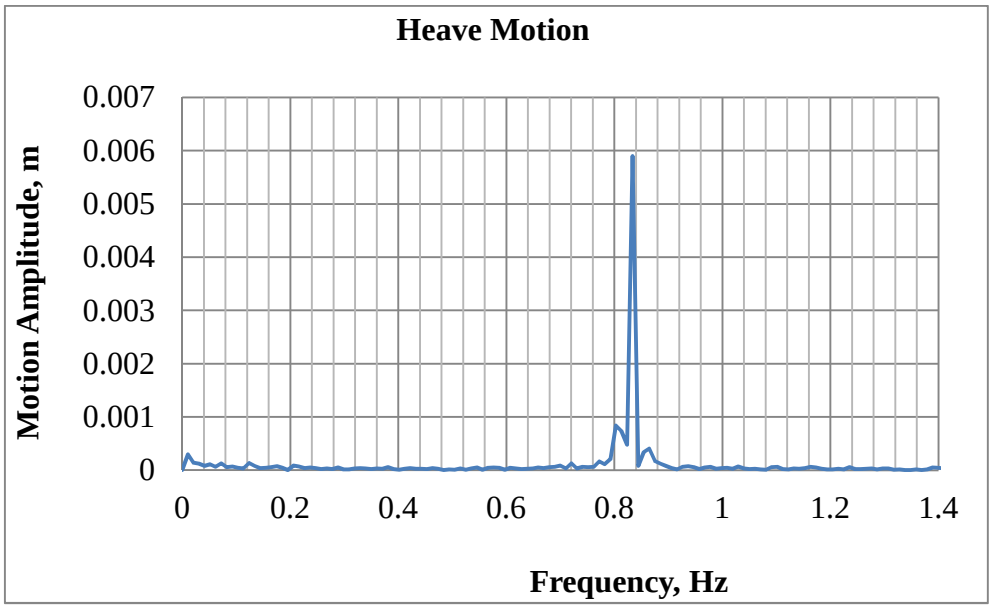

Figure 7.27: Frequency domain heave RAO of round shape FLNG in wavelength 2.27 meters

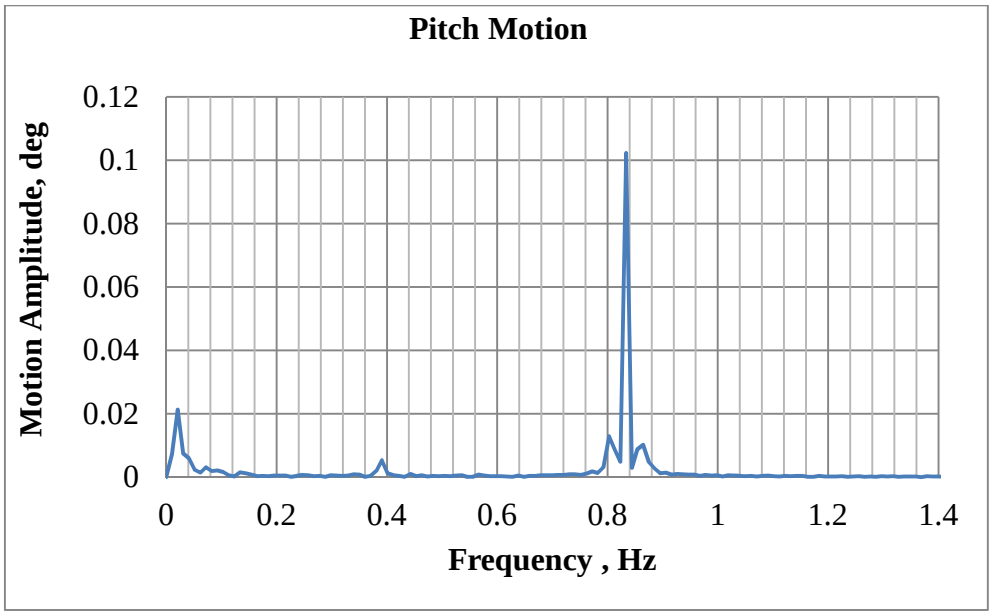

Figure 7.28: Frequency domain pitch RAO of round shape FLNG in wavelength 2.27 meters

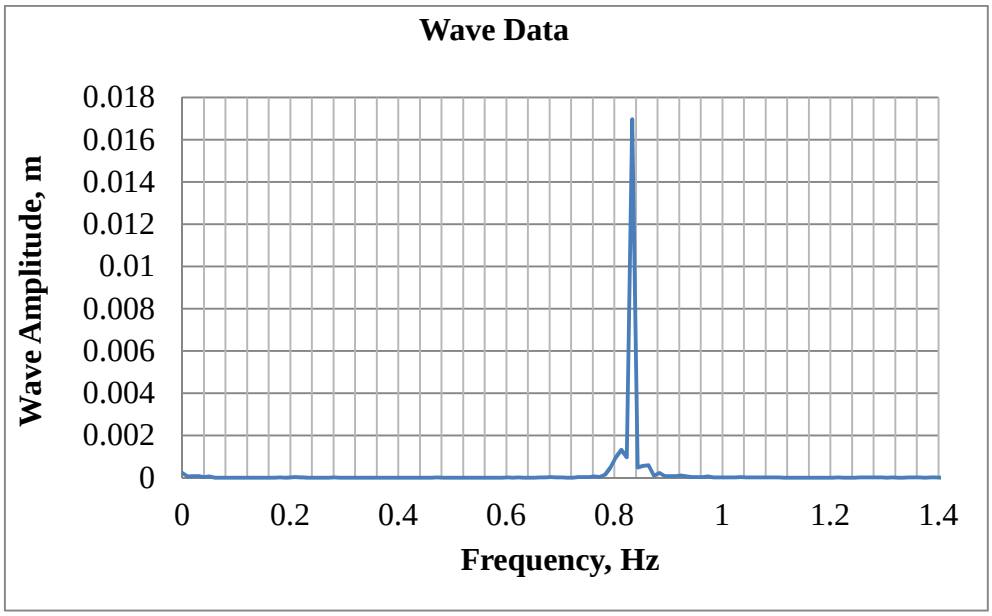

Figure 7.29: Frequency domain wave data in wavelength 2.27 meters

From Figure 7.29, it is observed that the actual generated wave has a frequency of 0.833 Hz, where the generated wave frequency is close to the desired wave frequency. In Figure 7.26 to Figure 7.28, it is observed that the magnitude of the surge and heave motion of round shape FLNG in the frequency, which is the same as the wave frequency is ranged at 0.0071 metres and 0.0059 metres respectively, while the pitch motion at the frequency is at 0.1023 degrees.

As mentioned in the previous part, the round shape FLNG experiences two types of motion in horizontal plane. The wave frequency motion in surge direction has the oscillation frequency, which is the same as the wave frequency. According to Dercksen and Wichers (1992), the low frequency motion in surge direction is depended on the natural frequency of mooring system. Typically, the frequency of the low frequency motion is much lower compared to the frequency of wave frequency motion. In the experiment test, the round shape FLNG experiences a low frequency motion with the frequency of 0.0309 Hz in model scale.

In this research, the wave frequency motion of round shape FLNG is studied. The proposed method calculated the wave frequency motion of round shape FLNG without considering the effect of mooring system. This is because the effect of mooring in the wave frequency motion is negligible for large structure, such as FLNG. The suggestion to ignore the effect of mooring in estimating the wave frequency motion is also supported by Soares et al. (2005), where he obtained the panel method without including the mooring force in

estimating the RAO amplitude of large size floating structure used in his studies, which was able to provide a good accurate prediction compared to the experiment results. In his experimental test, he also included the mooring system to simulate the mooring effect in horizontal plane motion. Hence, the same methodology was applied here to validate the proposed method.

7.7. Summary

This chapter discusses the experiment setup to collect the comparative data to validate the proposed mathematical models. After that, this chapter also explains the method used to process the experimental data until the response amplitude operator of the floating structure in each direction is able to estimate from the collected experimental data. The experimental results obtained were used to validate the proposed method and the results are shown in Chapter Eight.

Chapter 8

8.0. Simulation on Hydrodynamic Interaction of FPSO-Shuttle Tanker

This chapter discusses the estimated RAO of the round shape FLNG structure. The RAO of the round shape FLNG was predicted by the proposed method discussed in Chapter Six. Besides, experiment study was conducted to evaluate the RAO of round shape FLNG. From the motion experiment test, comparative data used to validate the proposed method was obtained. In addition, numerical comparative study was conducted in this research. The RAO of the round shape FLNG was also estimated using the ANSYS AQWA software. The RAOs of round shape FLNG predicted by the mentioned methods are shown in this chapter.

Besides, this chapter consists of two main parts, which are RAO of round shape FLNG when it is free from interact with other floating structures and the RAO of the round shape FLNG when it is interacting with another floating structure. In the second part of this chapter, the RAO of round shape FLNG when interacting with the KVLCC2 tanker arranged in two different gap distance is presented. The motions response of the round shape FLNG when interacting with second structure was also estimated using the proposed method in this research, ANSYS AQWA and experiment method. The influence of the second floating structure to the RAO of round shape FLNG due to the difference gap distance is also discussed in this chapter.

8.1. Response Amplitude Operator of Single Round Shape FLNG

The RAO of round shape FLNG was predicted by using the proposed method and compared with the result predicted by ANSYS AQWA and motion experiment test. The proposed method predicted the RAO of round shape FLNG based on the diffraction potential theory. In

heave motion, the heave RAO was predicted by using *Jaswar and Siow drag damping correction method* (see section 5.1) where in this method the damping and exciting force calculated by diffraction potential theory are improved by using the drag equation in order to estimate the viscous effect. The proposed method was able to estimate the damping, added mass and wave force of the round shape FLNG and then, solve the motion equation to obtain the RAO of the round shape FLNG.

8.1.1. Added Mass and Damping Coefficient of the Round Shape FLNG

The added mass and damping coefficient of the round shape FLNG was predicted by the proposed method in this research. Since the round shape FLNG is the symmetry in X-direction and Y-direction, then the discussion is only focused in surge, pitch, heave and yaw condition. The added mass and damping in sway direction in any wavelength is similar with the added mass and damping in surge direction. The added mass and damping in roll direction are similar with the added mass and damping in pitch direction in this four sides symmetry structure.

Let the added mass predicted by proposed method in surge, pitch, heave and yaw directions are labelled as A_{11}, A_{55}, A_{33} and A_{66} respectively. The predicted added mass in each direction of motion response is shown from Figure 8.1 to Figure 8.4.

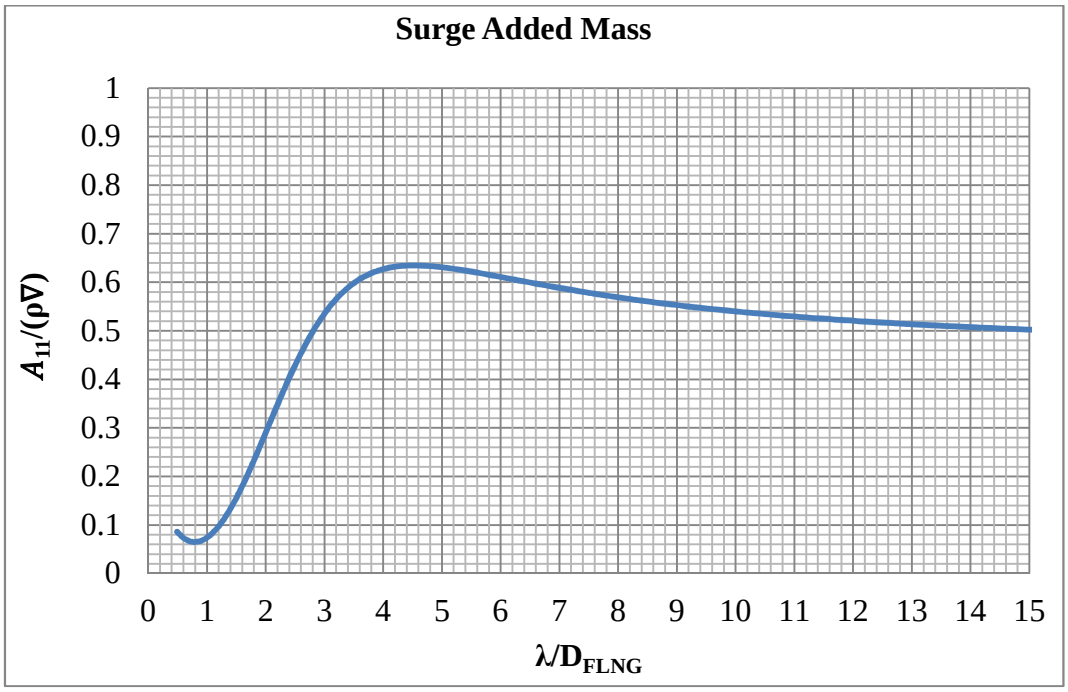

Figure 8.1: Surge added mass of round shape FLNG predicted by the proposed method

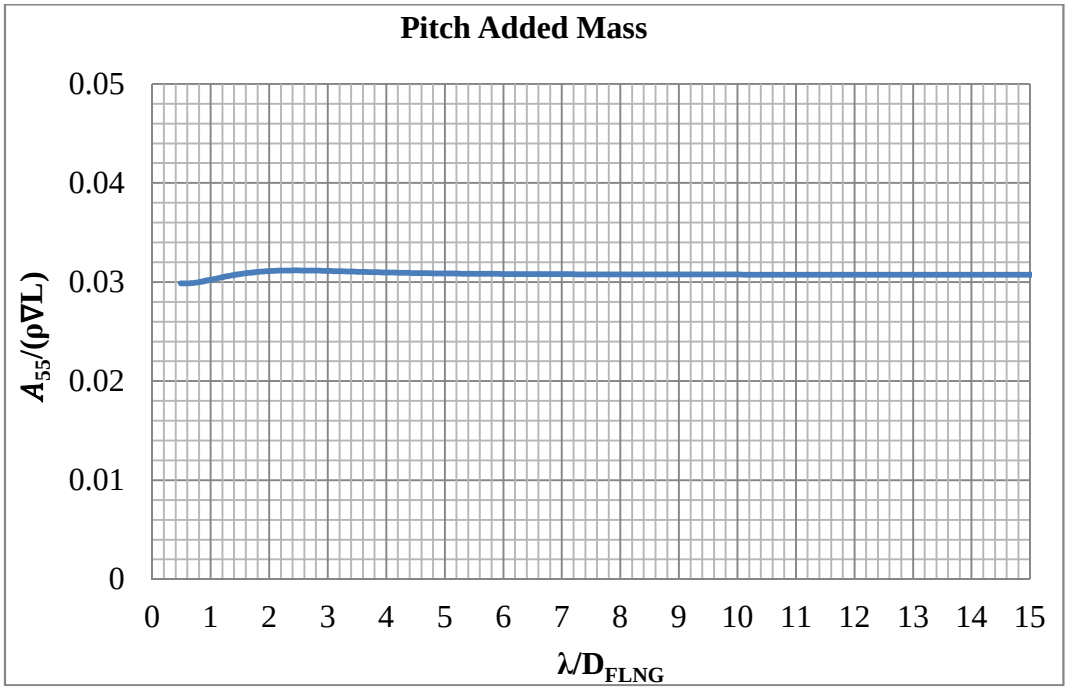

Figure 8.2: Pitch added mass of round shape FLNG predicted by the proposed method

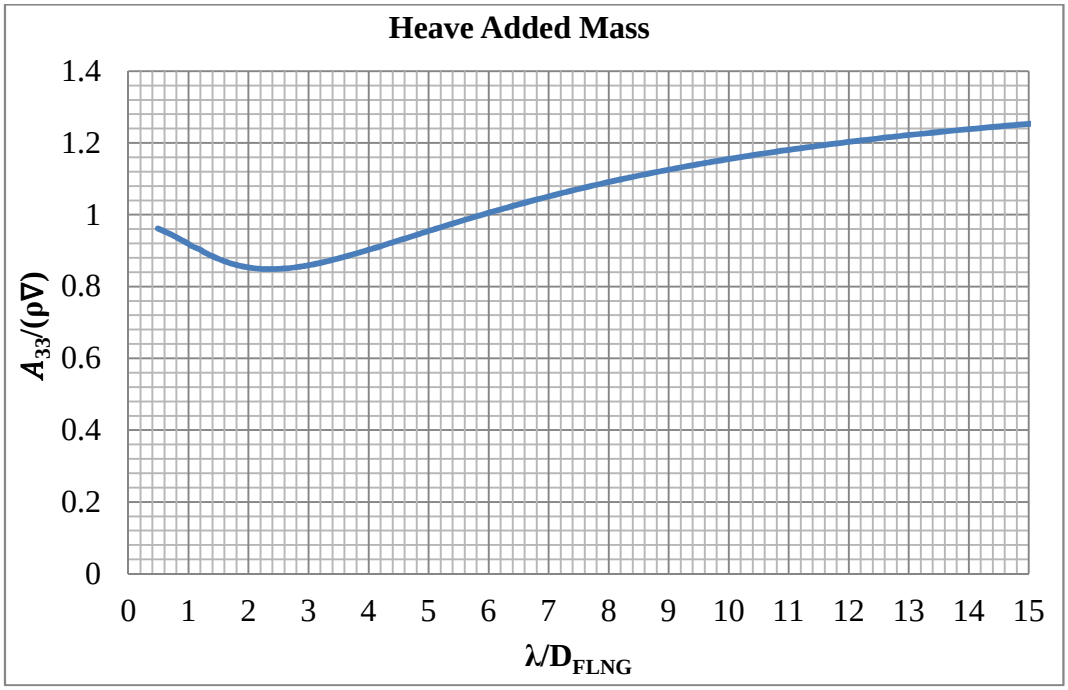

Figure 8.3: Heave added mass of round shape FLNG predicted by the proposed method

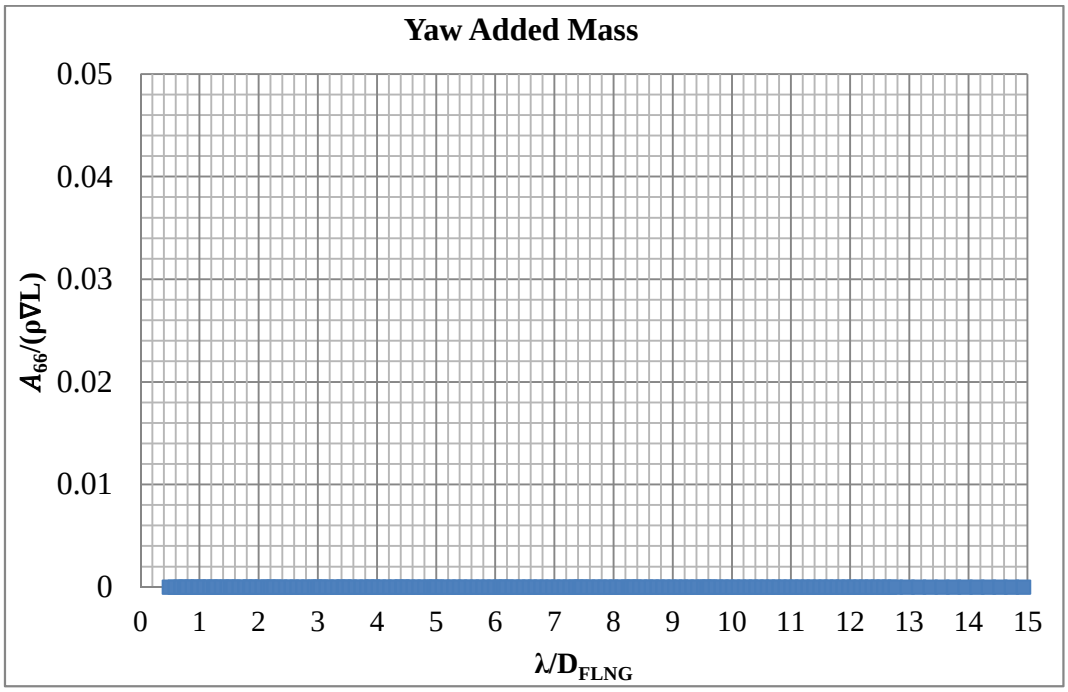

Figure 8.4: Yaw added mass of round shape FLNG predicted by the proposed method

In Figure 8.1 to Figure 8.4, the added mass in each direction of motion predicted by the proposed method was plotted against the ratio of wavelength to the structure length, λ/D_{FLNG}. The surge added mass and heave added mass show in Figure 8.1 and Figure 8.3 were non-dimensional with the mass of the structure, $\rho\nabla$ while the pitch added mass and yaw added mass shown in Figure 8.2 and Figure 8.4 were non-dimensional with the mass of the structure multiplied by structure length, $\rho\nabla L$.

From the Figure 8.1, the estimated surge added mass of the round shape FLNG increased from the ratio of λ/D_{FLNG} 0.5 to 4.0 gradually. If the ratio λ/D_{FLNG} is larger than 4.0, the surge added mass starts to decrease slowly by increasing the ratio of λ/D_{FLNG}. This means that the surge added mass of round shape FLNG is small if the wavelength is short. The added mass of pitch motion is shown in Figure 8.2. The estimated non-dimensional added mass of pitch motion was around 0.03 in the selected range of wavelength. The added mass of pitch motion had not much of changes if the wavelength increased up to λ/D_{FLNG}, which equals to 15 as shown in Figure 8.2.

The predicted heave added mass of the round shape FLNG was varied from the range of 0.8 to 1.2 in the selected range of wavelength. This means that the added mass of the round shape FLNG in heave motion is almost equal to the weight of the structure. Higher heave added mass would help to shift the resonance frequency of heave motion to a longer

wavelength region. The yaw motion added mass predict by the proposed method is shown in Figure 8.4. From Figure 8.4, it shows that the yaw added mass is almost zero in any condition. The added mass for yaw motion is relatively low because the round shape FLNG is a cylinder type structure and less fluid particle would accelerate with the yaw motion of the structure.

In compared to other study, it is found that the tendencies of surge added mass and heave added mass calculated by the proposed method is similar with the result from Perwitasari (2010). Where she has been conducted a research to study the mooring system of round shapes FPSO. However, the peak added mass for the surge and heave direction calculated by the proposed method is slightly higher. The different magnitude of the added mass coefficient obtained from both study is because the size of round shape floating structure used is different where the size of the FLNG in this research is slightly larger compare to the size of floating structure used in previous study. Besides that, the tendency of pitch added mass coefficient of round shape FLNG predicted by the proposed method is also almost similar with the pitch added mass tendency predicted by Jiang et al. (2012). In their study, they used higher order boundary element method (HOBEM) to calculate the hydrodynamic coefficient of the cylinder type floating structure.

On the yaw direction, the added mass for yaw motion calculated is always zero in any wavelength because the shape of the hull of the structure. As shown in the equation (4.78), the equation to calculate the added mass is in the function of surface normal vector. The round shape FLNG is the cylinder type structure, so the yaw normal vector is zero for this type of structure. From this finding, it can be expected that the round shape FLNG have very limited capability to accelerate the fluid particle in yaw direction. Therefore, the predicted yaw added mass of this FLNG by proposed method is always zero.

On the other hand, the damping coefficient predicted by the proposed method on surge, pitch, heave and yaw directions are represented by symbols B_{11}, B_{55}, B_{33} and B_{66} respectively in this thesis. The damping coefficients are estimated by the proposed method developed based on diffraction potential theory. The predicted damping coefficient in each direction of motion response is shown from Figure 8.5 to Figure 8.8.

In Figure 8.5 to Figure 8.8, the damping coefficient of round shape FLNG in each direction of motion predicted by the proposed method was plotted against the ratio of wavelength to the structure length, λ/D_{FLNG}. The surge damping coefficient and heave

damping coefficient shown in Figure 8.5 and Figure 8.17 were non-dimensional with the mass of the structure and angular wave speed, ρ∇w while the pitch added mass and yaw added mass shown in Figure 8.6 and Figure 8.8 were non-dimensional with the mass of the structure, angular wave speed and structure length, ρ∇wL.

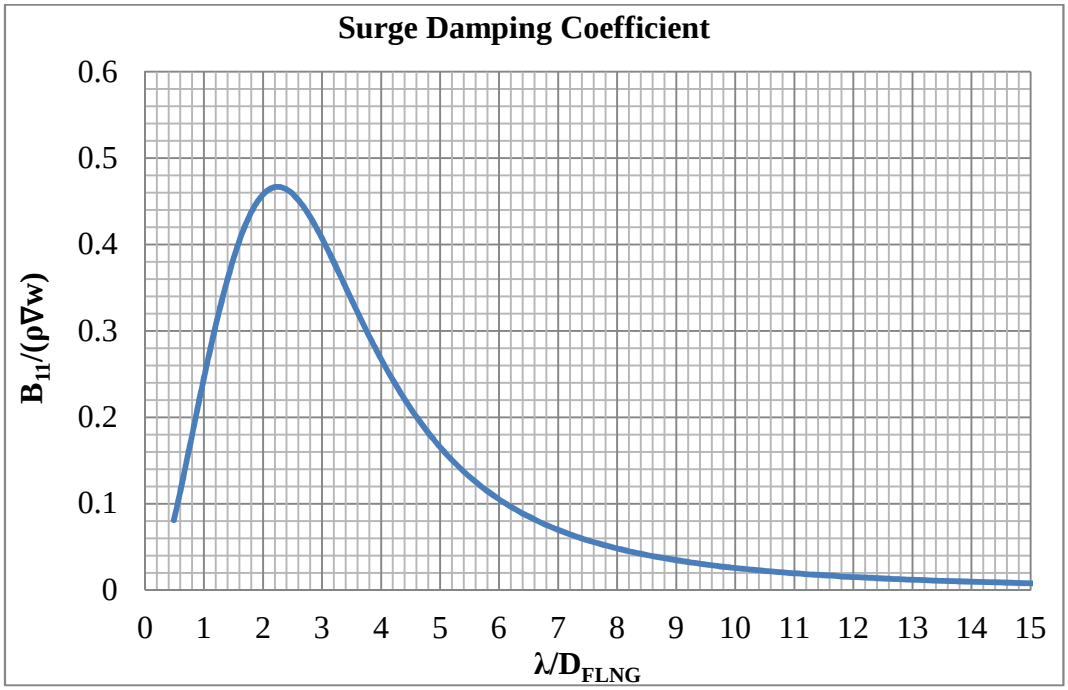

Figure 8.5: Surge damping coefficient of round shape FLNG predicted by the proposed method

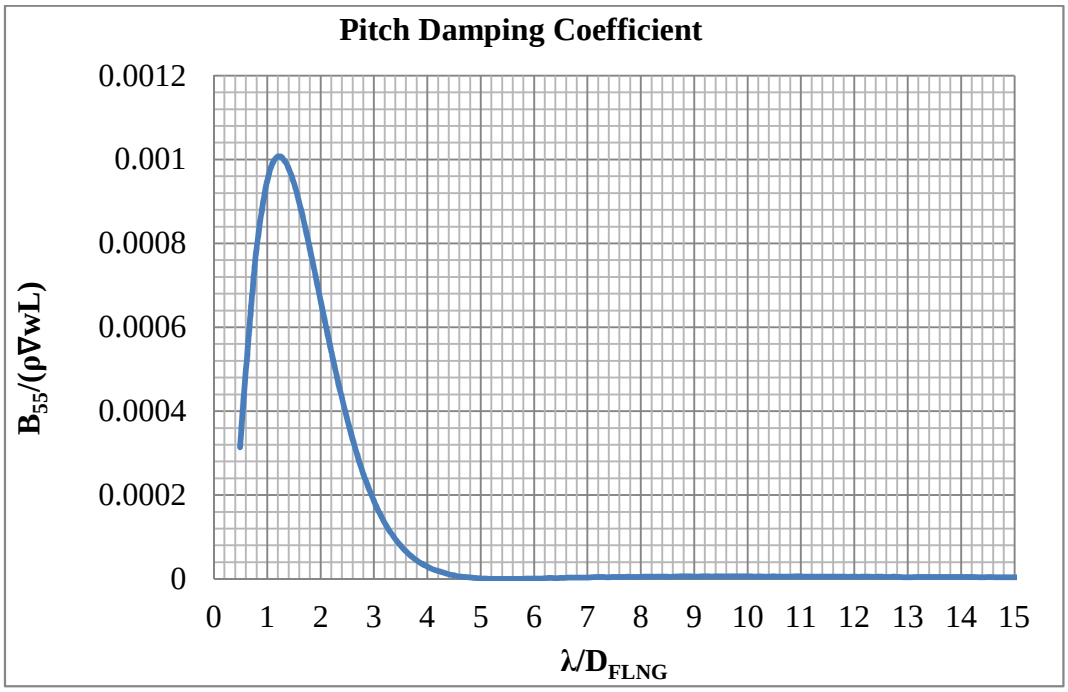

Figure 8.6: Pitch damping coefficient of round shape FLNG predicted by the proposed method

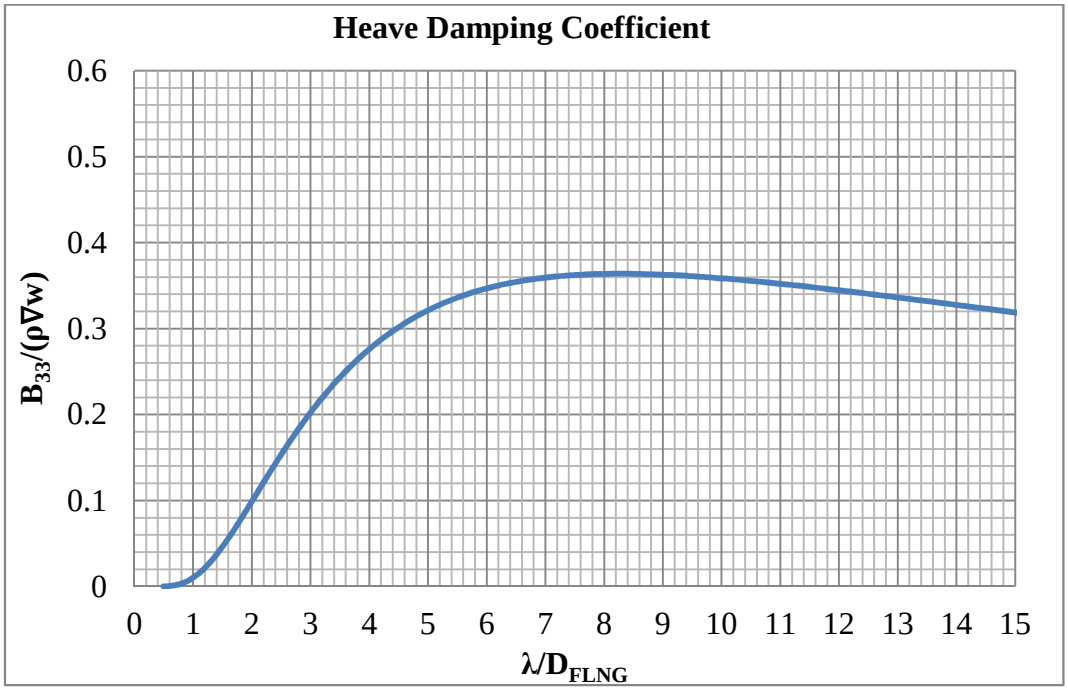

Figure 8.7: Heave damping coefficient of round shape FLNG predicted by the proposed method

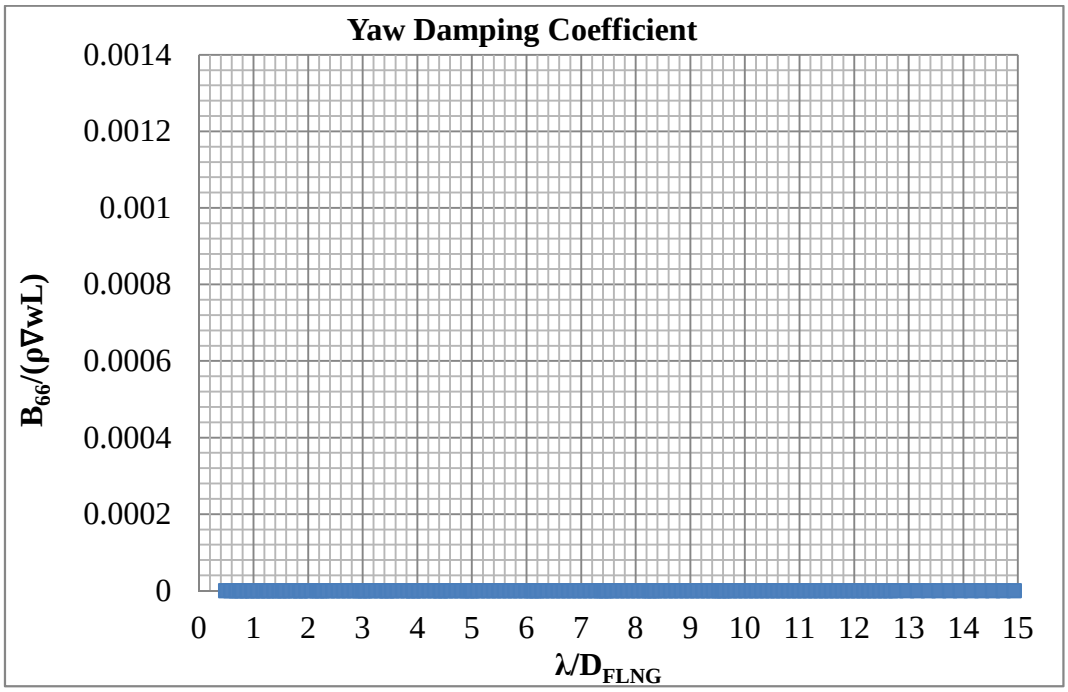

Figure 8.8: Yaw damping coefficient of round shape FLNG predict by the proposed method

From Figure 8.5, the estimated surge damping coefficient of the round shape FLNG is maximum at the ratio of λ/D_{FLNG} equal to 2.2 and the maximum surge damping is equal to 2. After that, increased of the ratio of λ/D_{FLNG} caused the surge damping coefficient decreased. This means that the surge motion would follow the wave when the wavelength is sufficiently long. The damping coefficient of pitch motion is shown in Figure 8.6. The estimated damping coefficient of pitch motion achieved maximum value of 0.01 when the ratio of λ/D_{FLNG} is around 1. The pitch damping coefficient of this structure is almost zero when the ratio λ/D_{FLNG} is larger than 5. From the estimated pitch damping coefficient, the pitch motion of this structure is larger in the long wavelength region compared to the short wavelength region.

The predicted heave damping coefficient of the round shape FLNG was increasing gradually when the ratio of λ/D_{FLNG} increased. The heave damping coefficient is almost constant after the ratio λ/D_{FLNG} is larger than 6. The yaw damping coefficient predicted by the proposed method is shown in Figure 8.8. Similar with the yaw added mass, the yaw damping coefficient was almost zero in any wavelength predicted by the proposed method. The proposed method was developed based on potential theory. Therefore, only radiation damping coefficient was predicted by the proposed method for yaw motion. Since the round

shape FLNG is a cylinder type structure, then the capability of the structure to dissipate the energy in yaw motion is very limited due to the amount of water particle, which can be accelerated by yaw motion of the structure is very small.

By comparing the tendencies of surge damping, pitch damping and heave damping predicted by proposed method in this research with the previous literature, it was found that the tendencies of surge damping and heave damping for the FLNG predicted by this research is almost similar with the results presented by Perwitasari (2010). In her study, she used WADEM software to calculate the hydrodynamic coefficient of the round shape floating structure. Besides, the pitch damping tendency estimated in this research is also similar with the pitch damping tendency predicted by Jiang et al. (2012) by using HOBEM method.

As predicted by the proposed method, both the surge damping coefficient and pitch damping coefficient is small in long wavelength region. These tendencies observed because the floating structure typically would move follow the wave motion when the wavelength is long. When the motion of the FLNG is move follow the wave motion, then the amount of motion energy able to dissipate to fluid and generate the radiating wave become lesser. From this point of view, the radiation damping coefficient for both the surge and pitch direction predicted by the proposed method is smaller in long wavelength region is quite agree with the normal phenomena.

From the mathematical point of view, the damping coefficient for each direction is in the function of area normal vector as shown in equation (4.79). When the wavelength is long, the potential of wave acting on the every unit of wetted are of FLNG is almost similar due to lower wave diffraction effect. Therefore, the cancellation of damping force is happened for surge and pitch direction. This is because the area normal vectors of the wetted area for these two directions in forward part of FLNG and aft-ward part of FLNG are in opposite sign. This cancellation of damping force are not happen to the heave direction since the area normal vector of this FLNG structure for vertical direction are all in the similar direction and pointing downward. In addition, the proposed method predicted the damping using potential theory where the potential theory is the linear theory and neglects the viscous effect. Since the viscous effect is neglected, then the damping predicted by the proposed method is only the radiating damping. Therefore, the damping for the yaw motion predicted by the proposed method is always zero because of the area normal vector of this FLNG for yaw direction is zero and the viscous effect was neglected from the calculation of damping coefficient.

8.1.2. Wave force act on the Round Shape FLNG

In this research, the wave force act on the wetted surface of round shape FLNG was estimated by the proposed method, which was developed based on diffraction potential theory. In this chapter, the wave force act on the structure in head sea condition is discussed. In head sea condition, the wave force act on the floating structure is only able to induce surge, pitch and heave motion. Hence, only the surge force, pitch moment and heave force are discussed here.

The wave force act on surge, pitch and heave direction be labelled as symbols E_1, E_5 and E_3 in this thesis. The estimated wave force acts on the round shape FLNG by diffraction potential theory are shown in Figure 8.9 to Figure 8.11.

The wave forces act on the round shape FLNG in head sea condition were plotted against the ratio of wavelength to structure length, λ/D_{FLNG} are shown in Figure 8.9 to Figure 8.11. The amplitude of wave force act on surge direction and heave direction as shown in Figure 8.9 and Figure 8.11 were non-dimensional with the fluid density, ρ, gravity acceleration, g, wave amplitude, ζ_a and the water plane area, A_W. The pitch moment shown in the Figure 8.10 was non-dimensional with the fluid density, ρ, gravity acceleration, g, wave amplitude, ζ_a, water plane area, A_W and the length of the structure.

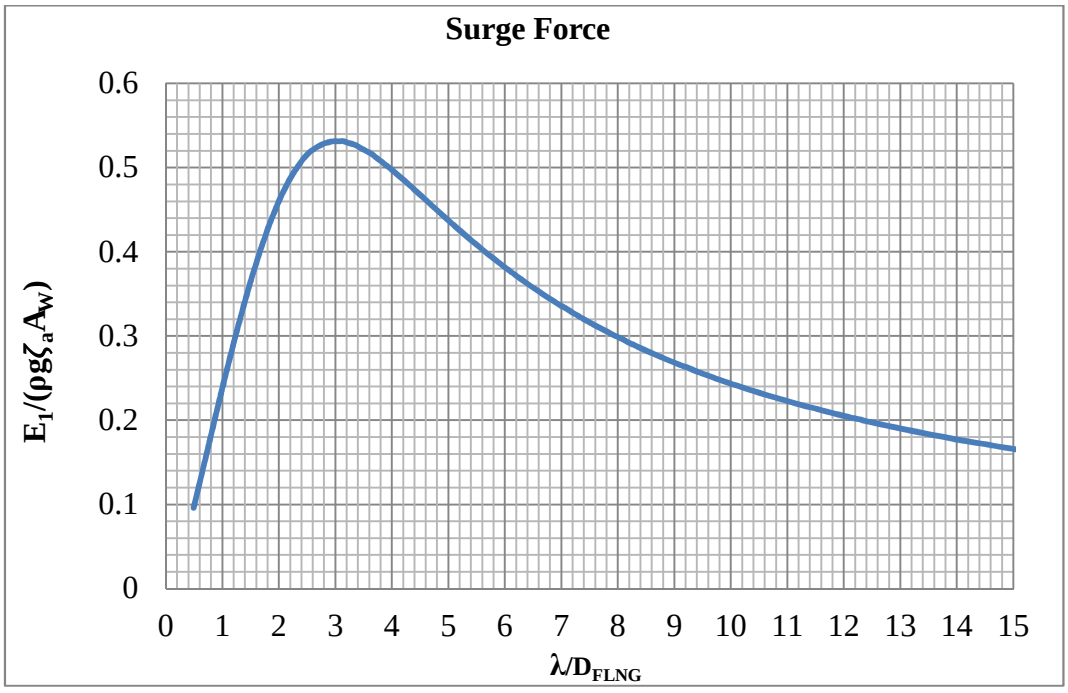

Figure 8.9: Surge wave force act on round shape FLNG predicted by the proposed method

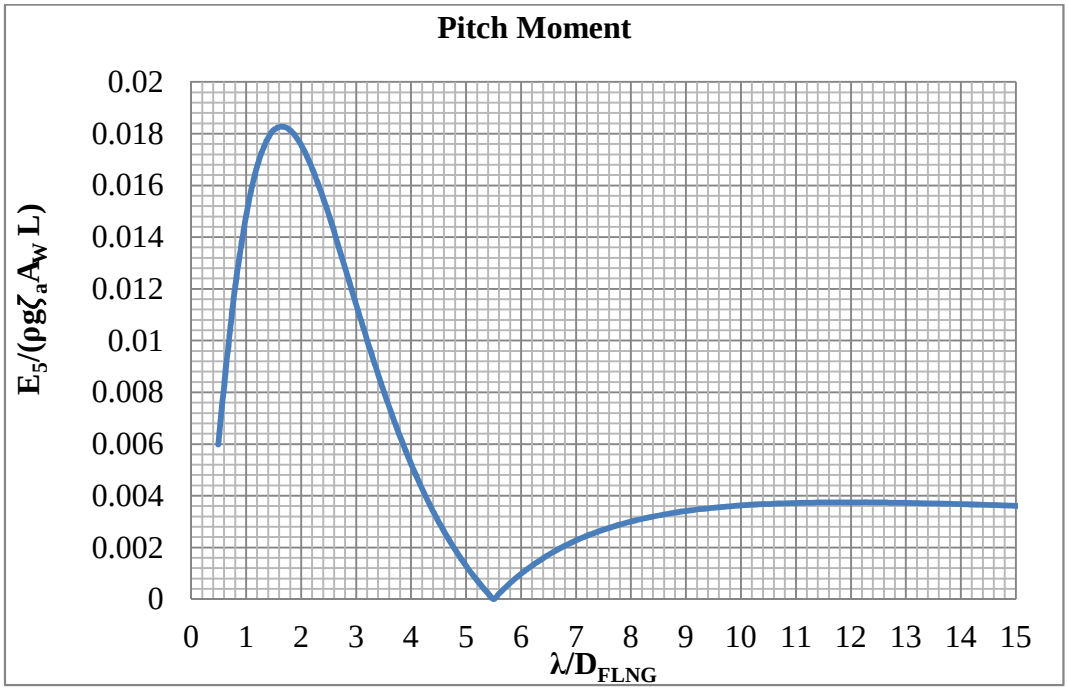

Figure 8.10: Pitch wave moment act on round shape FLNG predicted by the proposed method

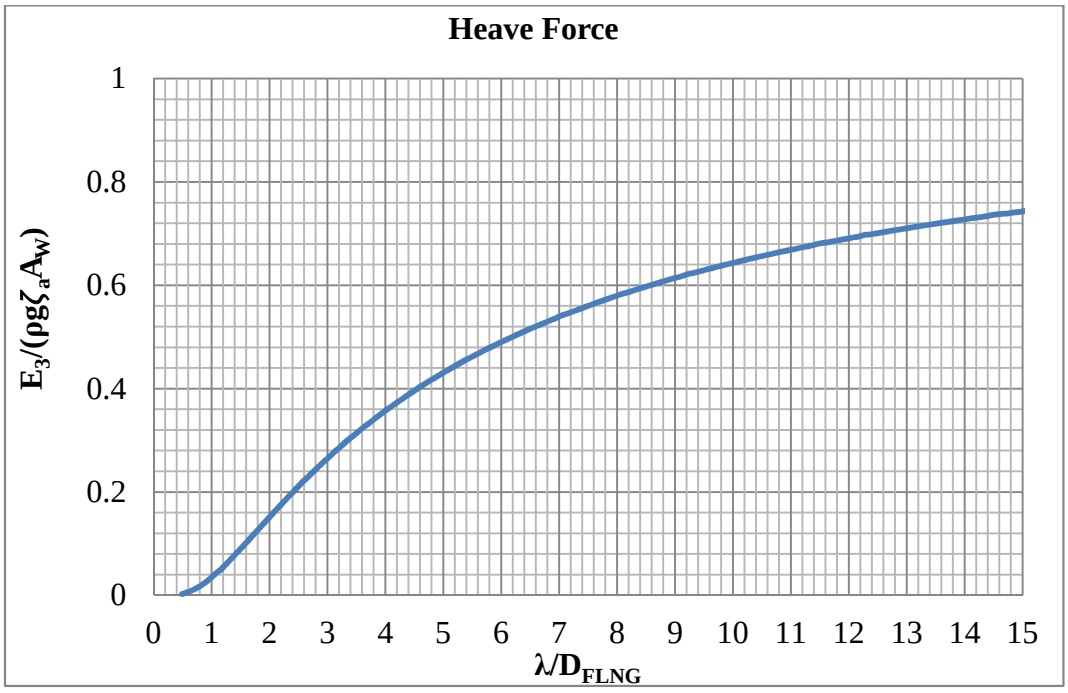

Figure 8.11: Heave wave force act on round shape FLNG predicted by the proposed method

In Figure 8.9, the wave force act on the surge direction achieved maximum amplitude at the ratio λ/D_{FLNG}, which is equal to 3. After that, the wave force act on the surge direction decreased gradually when the wavelength increased. The pitch moment of the round shape FLNG induced by the wave in head sea condition is shown in Figure 8.10. The predicted pitch moment achieved maximum at the ratio λ/D_{FLNG} is equal to 1.5. The pitch moment was almost zero when the ratio λ/D_{FLNG} is equal to 5.5. After that, the pitch moment of round shape FLNG increased slowly with the increased of wavelength.

The heave force, which induces the heave motion to the round shape FLNG is shown in Figure 8.11. The heave force shown in the Figure 8.11, which is predicted by the proposed method was developed based on diffraction potential theory. The heave force predicted increased when the wavelength increased and trended to become constant at long wavelength. Round shape FLNG would experience a larger heave force in long wavelength region predicted by the proposed method.

From the literature, it is obtained that the tendencies of the surge and heave exciting forces predicted by the proposed method are similar with the results obtained by Perwitasari (2010). The surge exciting force for this FLNG is trend to reduce by increase of wavelength is because the surge motion of FLNG is followed wave motion in long wavelength. When the wavelength become longer, the time for FLNG to accelerate and decelerate become longer. Therefore the wave load on the FLNG to cause the structure move follows the wave become lesser.

On the other hand, the heave wave exciting force is shown increased and trend to become constant at long wavelength. The heave exciting force predicted by the proposed method was increased if the wavelength was increased. This is because increase the wavelength is able to increase amount of wave load on the heave direction. As presented by equation (4.77), the equation shows that the wave exciting force is in the function of floating structure's area normal vector and the wave potential. The entire wetted surface of this FLNG model has the area normal vector all pointing downward. Therefore, the change of heave exciting force direction is depending on the velocity of wave motion. When the wavelength is increased, the amount of heave wave force acting in same direction across the FLNG is increasing. This causes the amount of heave exciting wave force increases when the wavelength becomes longer. However, when the wavelength is increased to very long wavelength condition, the change of heave wave force direction across the FLNG wetted

surface area is no happened. So, the heave wave exciting force start to become constant by increase of wavelength as presented in the Figure 8.11.

By compared to the result obtained by Jiang et al. (2012), it was found that the tendency of pitch exciting force is slightly different between the prediction of proposed method and Jiang et al. (2012). The different between the pitch exciting force tendency between both the researches is the proposed method detect the cancellation of pitch moment happened at the λ/D_{FLNG} equal to 5.5. From the equation to calculate the wave exciting as presented in equation (4.77), the wave exciting force acting on each wetted surface of FLNG is in function of the surface area normal vector. The area normal vector in pitch direction is in opposite sign for forward part of structure's wetted surface and aft-ward part of structure's wetted surface. When the wavelength at λ/D_{FLNG} is equal to 5.5, it was found that the total pitch moment acting on the forward part of FLNG and aft-ward part of FLNG was same. Therefore, the cancellation of the pitch moment was happened and the total pitch moment becomes zero at this wave condition. Besides, it was found that the pitch moment was trend to become constant at long wavelength because the FLNG is move follow the wave. The constant pitch moment at long wavelength is predicted able to encounter by the pitch restoring force to avoid large pitch motion at long wavelength region.

8.1.3. Influence of Drag Equation in the Heave Damping and Heave Force

The proposed method applied diffraction potential theory to predict the added mass, damping and wave forces or wave moment act on the round shape FLNG to induce the motions to the round shape FLNG. The diffraction potential theory only predicted the radiation damping of the floating structure without considering the viscous effect. Neglect of viscous effect in the calculation causes over-prediction on RAO by the proposed method in some conditions. In the selected round shape FLNG model, the proposed method over-predicted the heave RAO of the Round shape FLNG in the damping dominant region. The damping dominant region of the round shape FLNG is located at the wavelength around 381 metres or wave period of 15.6 seconds in full scale. From the study, it is possible of ocean wave occurring at the wave period around the 15.6 seconds so the accuracy on the prediction of heave RAO at the damping dominant region is important to ensure the safety of the selected round shape FLNG operated at open sea.

To improve the heave motion predicted by the proposed method, the heave RAO predict by the propose method is calculated using the diffraction potential theory with drag equation. The diffraction potential theory is responsible to predict the heave added mass, heave radiation damping and heave diffraction force. The drag equation used in the calculation is responsible to calculate the viscous damping and the drag force act on the floating structure. The proposed method introduced to improve the accuracy on predicts the heave motion is explained in Chapter 5.1.

The heave damping predicted by the proposed method which developed using diffraction potential theory with drag equation is shown in Figure 8.12. The Figure 8.12 shown the non-dimensional heave damping calculated by diffraction potential theory, drag equation and summation of both the heave damping by both the method. From the comparison, it is obtained that the heave damping calculated by both the methods have almost similar tendency at the selected range of wavelength. The heave damping predicted by both methods was increased gradually when wavelength was increased.

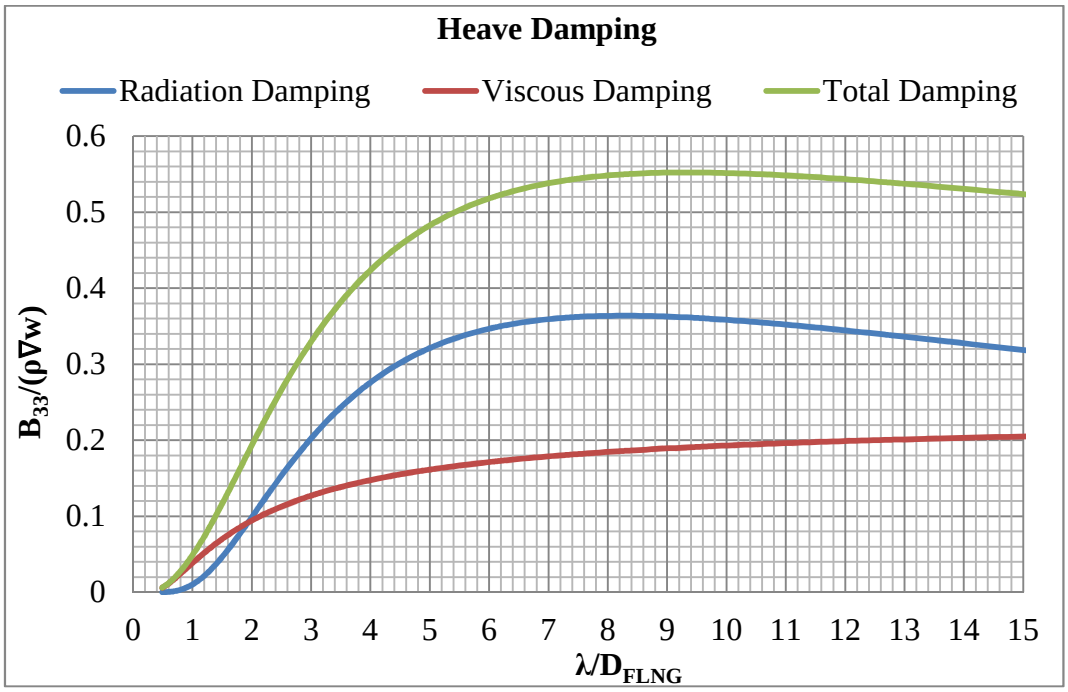

Figure 8.12: Comparison of heave damping coefficient of round shape FLNG predict by propose method

From Figure 8.12, the viscous damping calculated by the drag equation was slightly larger compared to the radiation damping estimated by diffraction potential theory at the ratio λ/D_{FLNG}, which is below than 2. If the ratio λ/D_{FLNG} is larger than 2, the radiation damping is larger compared to the viscous damping. Besides, the tendency of the radiation heave damping and viscous heave damping is almost stable when the ratio λ/D_{FLNG} is larger than 5.

According to Kvittem et al. (2012), the wave diffracted effect is more dominant to the large size structure compare to the viscous effect because the wave is mostly diffracted from the structure when the undisturbed incident wave interacting with the large size floating structure. The estimated viscous damping coefficient by the drag equation is lower compared to the radiation damping estimated by the diffraction potential theory as presented in the Figure 8.12 is because of the wave diffraction effect is more dominated in this round shape FLNG. However, according to Loken (1981), he stated that the damping coefficient typically under-estimate by the diffraction potential theory since the viscous effect is ignored. From this Figure 8.12, it is showed that the ignored viscous damping by the diffraction potential theory is almost one third of the total damping coefficient for this selected FLNG structure. Hence, it is cannot avoided of over predict of structure motion response by the diffraction potential theory especially in damping dominant region.

To obtain the total damping for heave motion of round shape FLNG, the magnitude of damping coefficient predicted by drag equation and diffraction potential theory were sum up together in this research. As shown in Figure 8.12, the total damping which sum-up the damping predicted by the two mentioned methods increased the damping coefficient for the heave motion of round shape FLNG. The tendency of the radiation damping and viscous damping for this selected structure is almost similar within the selected range of wavelength. Besides, the tendency of total damping is similar with the tendency of the damping coefficient calculated by both the method but the magnitude of the total damping coefficient is larger than the damping coefficient only predict by diffraction potential theory.

As mentioned, the heave motion of the FLNG dominated by damping term is located at a wavelength around 385 metres, where the ratio λ/D_{FLNG} equals to 3.44. By referring to Figure 8.12, the damping coefficient obtained by summing up the damping calculated from both the methods is around 0.376 as compared to the radiation damping coefficient, which was predicted by diffraction potential theory is 0.239. At this calculated magnitude, it is summarised that the addition viscous damping by using drag equation able to increase the

damping coefficient and reduce the amount of over-prediction of the heave RAO estimated at the damping dominant region.

Besides, involving the drag equation in the calculation introduces the drag force in the motion equation. The total heave force calculated by the proposed method is the summation of diffraction force calculated by diffraction potential theory and the drag force calculated by drag equation. As shown in Figure 8.13, the heave force calculated by the diffraction potential theory increased gradually when the ratio λ/D_{FLNG} increased.

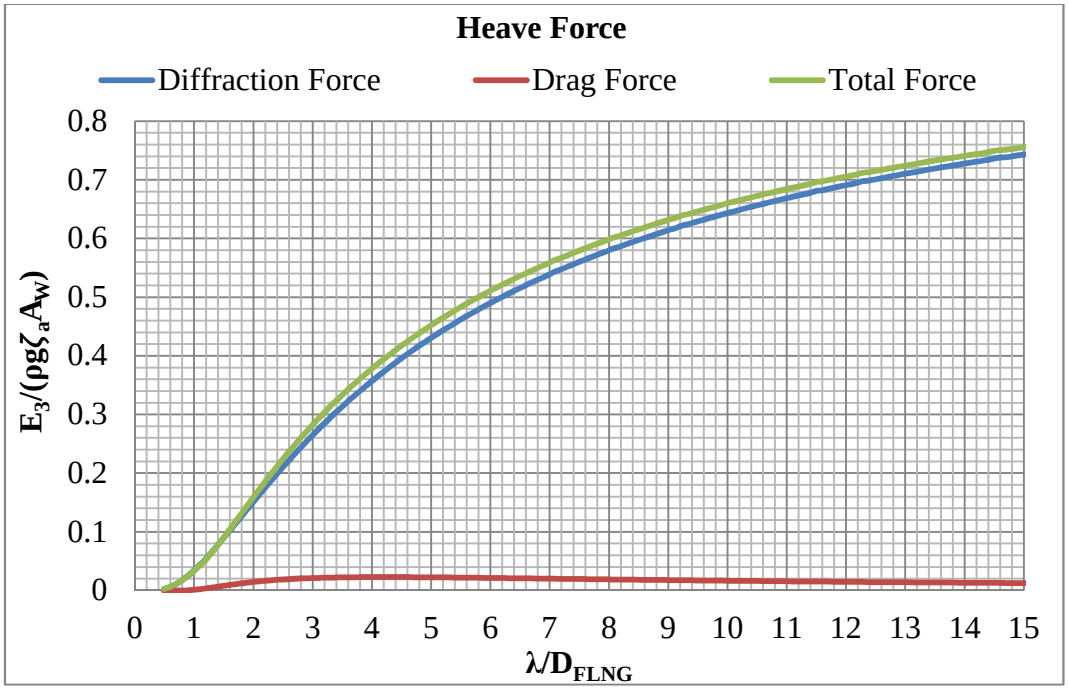

Figure 8.13: Comparison of heave force of round shape FLNG predicted by the proposed method

The drag force calculated by drag equation is shown in Figure 8.13. The figure shows that the tendencies of heave force predicted by both methods are different between each other. The heave force calculated by the drag equation is almost zero at the ratio λ/D_{FLNG} below one. At the longer wavelength region, the wave drag force in heave direction is almost unchanged when the wavelength increased. The magnitude of the heave force calculated by the drag equation is much lower compare to the diffraction force calculated by diffraction potential theory. This is because the diffracted effect is much higher compare to drag effect for the round shape FLNG structure. This opinion is also similar with the finding obtained by Kvittem et al. (2012) in their study. The higher diffraction force acting on the FLNG because

the large size round shape FLNG is able to diffract most of the incident wave. The large size structure is considered as an obstacle for the propagation of wave so the wave would be diffracted around the structure especially the wavelength is shorter than the length of the structure. When the wavelength is longer than the length of structure, the fluid particle is able to drag around the floating structure. But, the size of the structure is still play a main role to determine the phenomena of fluid particle pass through the structure. Since the displacement and the length of the round shape FLNG is very large, then the amount of fluid particle drag over the wetted surface of the structures is still much smaller compare to amount of fluid particle diffracted from the FLNG.

To combine the heave force contributed by both the methods, the superposition theory was applied. In this study, the heave force calculated by the diffraction potential theory and the drag force calculated the linearly drag term from the drag equation were total up to calculate the heave RAO. Both the heave forces contributed by both the methods were total up by vector summation theory.

By referring to Figure 8.13, it is obtained that the tendency of total heave force which total up by involved the diffraction force and drag force is mostly follow the tendency of heave force calculated by diffraction potential theory. This tendency is obtained because the diffraction force of the round shape FLNG is much higher compare to the drag force. The existing of the drag force from the drag equation in the calculation only give limited influence to the total heave force estimate by proposed method. Compared to the influence of drag effect to the total heave damping, it is obtained that involved the drag effect in calculate the heave RAO would able to reduce the estimate heave RAO calculated by proposed method especially in the damping dominant region.

8.1.4. Estimated Response Amplitude Operator of Round Shape FLNG

The results applied to study the round shape FLNG's RAO were collected from the numerical simulation and experiment method. The numerical results were generated using ANSYS AQWA software and proposed method based on Diffraction Potential Theory and Diffraction potential theory with drag equation. The experiment results used to study the RAO of the new FLNG were conducted in regular wave condition.

In the motion experiment, the wavelengths were properly selected so it can obtain the tendencies of all direction of FLNG motion responses in the function of difference

wavelength. In this part, the response amplitude of round shape FLNG model in head sea condition is discussed. As shown in Figure 8.14 to Figure 8.16, the tendency of surge, pitch and heave RAO obtained by both the numerical and experimental method is agreed between each other.

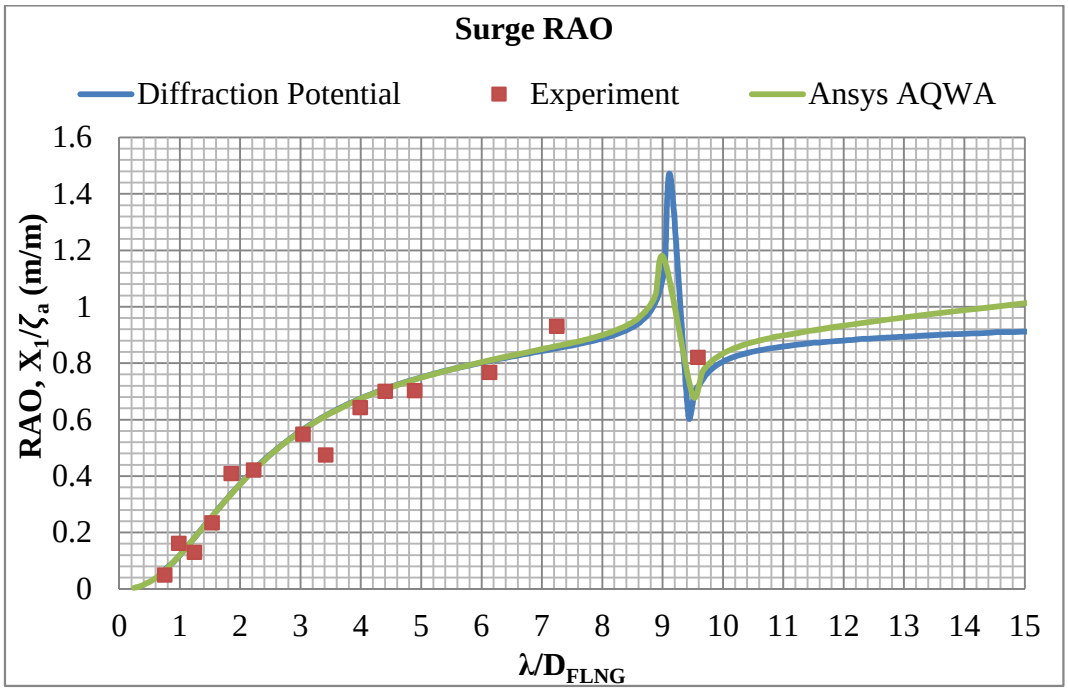

Figure 8.14: Surge RAO predicts by proposed method (diffraction potential theory), experiment and ANSYS AQWA

The comparative study was conducted to compare the RAO of round shape FLNG predicted by the proposed method to ANSYS AQWA. The comparison between the surge RAOs of the round shape FLNG predicted by both methods is shown in Figure 8.14. As shown in Figure 8.14, the surge RAO predicted by the proposed method and ANSYS AQWA is almost similar when the wavelength λ/D_{FLNG} below 10. Both the proposed method and ANSYS AQWA have predicted same tendency and almost similar magnitudes of surge RAO because both methods were developed using similar concept that is diffraction potential theory. However, when the wavelength λ/D_{FLNG} larger than 10, it was obtained that the surge RAO of proposed method was trend to become stable by increased of wavelength while the surge RAO predicted by Ansys AQWA was trend to increase by increased of wavelength. This observation obtained because the proposed method only consider the motion of FLNG due to the first order wave force while ANSYS AQWA take consideration of wave frequency

motion and the slow varying motion. According to Herbich et al. (1999), the slow varying motion of the FLNG typically becomes more dominant compared to the wave frequency motion when the wavelength becomes very long. Due to the consideration taken by the Ansys AQWA, the surge motion response predicted by Ansys AQWA do not become constant with the increase of wavelength.

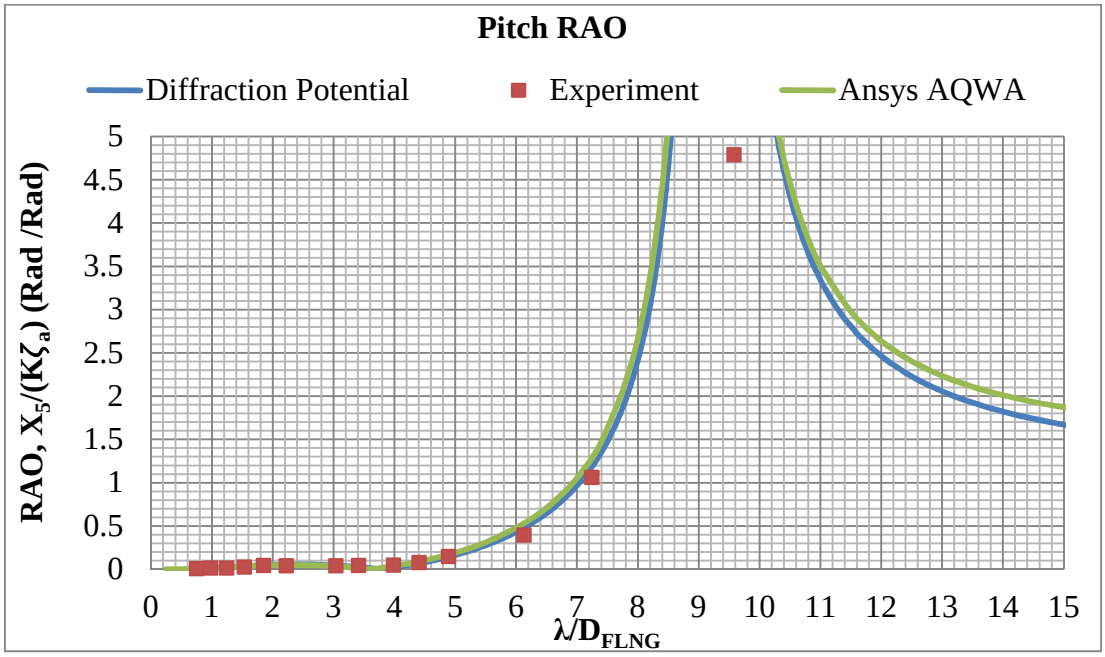

Figure 8.15: Pitch RAO predicts by proposed method (diffraction potential theory), experiment and ANSYS AQWA

Comparison between the pitch RAOs predicted using proposed method with ANSYS AQWA commercial code is shown in Figure 8.15. The tendency of the pitch RAO predicted by both methods was similar between each other. By comparing with the experimental result, both the proposed method and ANSYS AQWA commercial code was able to generate the same tendency of pitch RAO compared to experimental result. Besides, the proposed method and the ANSYS AQWA were successes to predict the peak RAO of the pitch motion. The peak pitch RAO of this FLNG predicted by the proposed method and ANSYS AQWA is happened at its pitch natural frequency where the corresponding wavelength for the pitch natural frequency is at λ/D_{FLNG} equal to 9.53. From the Figure 8.15, the pitch motion response predicted was very small at short wavelength region and start to increase exponential at λ/D_{FLNG} equal to 4. This is because the pitch damping coefficient is high at the short wavelength region and almost zero at the long wavelength region. The large pitch damping

for this FLNG at short wavelength condition is able to reduce the pitch RAO of this round shape FLNG. This observation shows that the FLNG is very stable at short wavelength region.

The numerical method predicted that the surge motion tendency experience has a large difference of RAO between the ratio λ/D_{FLNG} 8.5 to 10. However, due to lack of experimental data in this region, the actual condition is difficult to predict. From the Table 7.2, the natural period for surge motion of this round shape FLNG is happened at the λ/D_{FLNG} equal to 1570 where it is far away from the wavelength the surge motion tendency fluctuates detected by both the proposed method and ANSYS AQWA. In this research, the large fluctuates of the surge motion tendency is caused by the coupling effect between surge and pitch motion. This is because the experiment and numerical result also showed that the designed FLNG model experienced large pitch motion at long wavelength region. The large pitch motion response at the wavelength λ/D_{FLNG} around 9.5 is because the resonance effect. From the decay test result, it was obtained that the natural frequency of the pitch motion is happened at the wavelength λ/D_{FLNG} equal to 9.53. As shown in Figure 8.6, the pitch damping coefficient for the round shape FLNG is very low and almost zero in the wavelength where resonance happened. The low pitch damping coefficient of pitch motion when resonance happened causes the predict pitch motion response become significant high. In addition, by comparing the pitch and surge response tendency calculation by the proposed method and ANSYS AQWA, it is showed that the large change of surge tendency between the ratio λ/D_{FLNG} 8.5 to 10 is due to the coupling motion with pitch response. The resonance of pitch motion, which caused the pitch motion to increase significantly which is also influenced the surge RAO of this designed model.

Comparing between the predicted heave tendency using proposed method and ANSYS AQWA, it was observed that the proposed method developed was based on diffraction potential theory without any extra viscous effect, which predicted similar tendency and magnitude of heave RAO of round shape FLNG compared to ANSYS AQWA. In comparison to the experimental result, it was noted that the proposed method without involved viscous effect and ANSYS AQWA commercial code over predicted the heave RAO of round shape FLNG in damping dominant region. To reduce the amount of over-prediction on heave RAO in damping dominant region, the proposed method was developed to involve the viscous effect in predicting the heave RAO. The proposed method developed, which was

based on diffraction potential theory and drag equation is shown in the blue colour line in Figure 8.16. By this proposed method, the predicted magnitude of heave RAO of round shape FLNG is much lower in the damping dominant region. The maximum heave RAO shifted from 2.4 to 1.7 after the viscous effect was considered in the calculation.

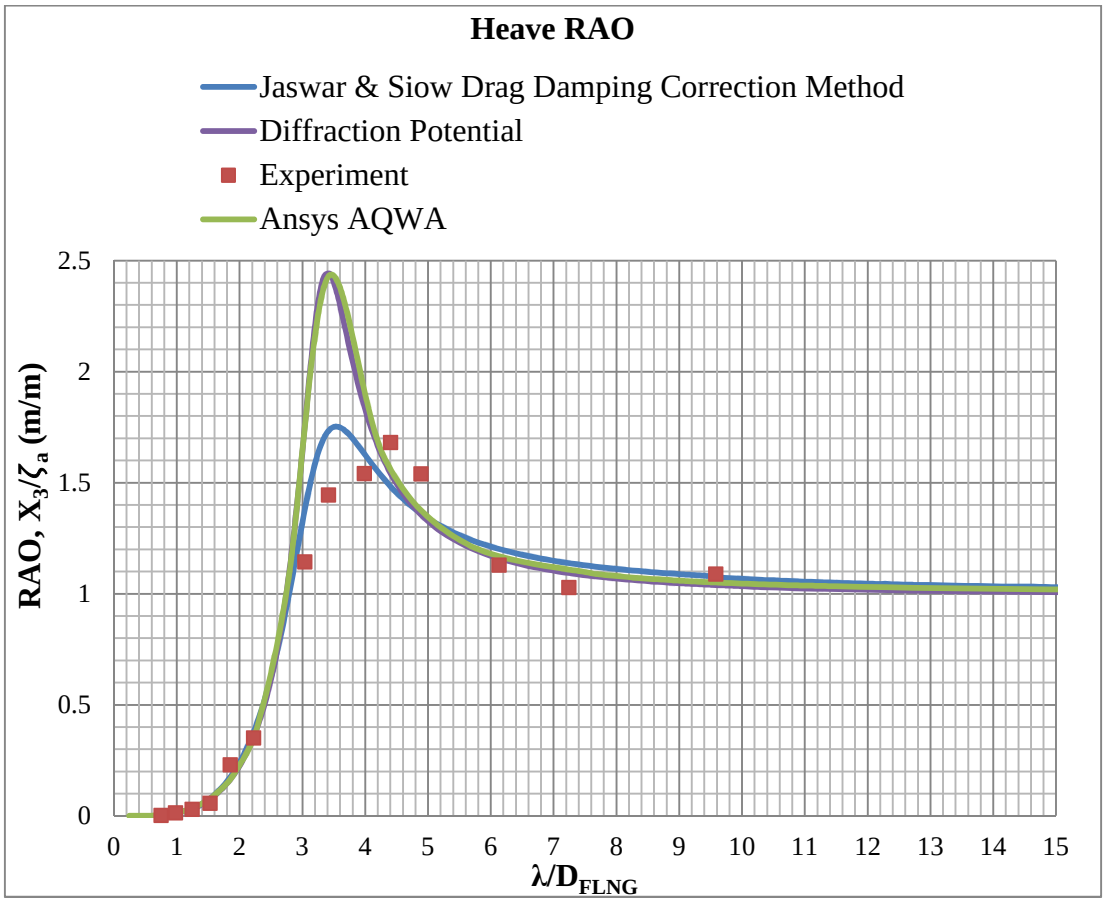

Figure 8.16: Heave RAO predicts by the proposed method (diffraction potential theory and Jaswar & Siow drag damping correction method), experiment and ANSYS AQWA

Moreover, the result from proposed method showed a good agreement with experiment result in predicting the heave response tendency. Due to the involvement of the extra viscous damping estimated by the drag equation in the calculation, the heave response of the round shape FLNG model predicted by the proposed method at the damping dominant region did not show a significance over prediction error. From Figure 8.16, the maximum heave response predicted by the proposed method is 1.74, while the maximum heave response predicted by experiment method is 1.68. Comparing the heave response tendency predicted by both the methods, Figure 8.16 also showed the heave response tendency estimated by the

proposed method (blue line), which was fixed quite well to the heave response data collected from experiment (red dot). This showed that the proposed method, which combined the drag equation with diffraction potential theories can be an alternative method, which was applied to predict the heave response of this round shape FLNG even in damping dominant region and obtain reasonably accurate results.

However, compared experiment result to numerical result, it was observed that the peak heave RAO was shifted to longer wavelength region in experiment result. From the Table 7.2, the corresponding wavelength for heave natural frequency is located at λ/D_{FLNG} equal to 3.40. The peak heave RAO for this FLNG predicted by the proposed method was happened at the wavelength closer to the heave natural frequency compared to experiment result. One of the reasons causes the peak heave RAO predicted by experiment result to shift to longer wavelength region is because of the mooring line. Although, Heurtier (2010) stated that there are limited mooring effect on the heave motion of large floating structure. But, the existing of mooring system can causes the stiffness and mass of the floating system increase. According to the Cheema et al. (2014), the small change on the stiffness and mass of the floating system could cause the shift of the motion natural frequency. Hence, the peak heave RAO predicted by experiment test is shifted slightly into longer wavelength region.

Besides, reason for the numerical method used in this research could not detect the shift of peak heave RAO compared to the experiment result is because of the under-estimated of the heave added mass. Chung (1994) has been conducted a study to compare the added mass coefficient predict by the three-dimension diffraction potential theory and the added mass coefficient predict by the experiment test. According to Chung (1994), his research found that the added mass coefficient predict by the diffraction potential theory typically 10% to 20% lower than the experiment value. From the mathematical point of view, the natural period for heave motion is in direct function to the mass term. Lower predicting of the heave added mass coefficient by the diffraction potential theory used in the research could be a reason for the numerical method predict the peak heave RAO happened at the shorter wavelength region compare to experiment value. Therefore, the numerical method used in the computation of this research predicted the heave natural period is located at the shorter wavelength region compared experiment method.

In general, it is observed that the proposed method is able to predict the six DoF wave motion responses of the round shape FLNG in good accuracy if it is compared to experiment

result. Since this designed FLNG model has four symmetry sides (bow and stern symmetry, port-side and starboard side symmetry), then the study conducted in the head sea condition is enough to present the RAO characteristics of this model.

8.2. RAO of Round Shape FLNG When Interacting with another Structure

The RAO of round shape FLNG interacting with another structure was predicted by using proposed method and compared with the result predicted by ANSYS AQWA and motion experiment test. In this research, the KVLCC2 model was chosen to interact with the round shape FLNG model. In this case, the KVLCC2 was arranged in the parallel arrangement with the round shape FLNG. The measurements of gap distance between the both floating structures selected to simulate and conduct experiment test are 0.5 to the breadth of FLNG and 0.3 to the breadth of FLNG. The measurements of gap distance between both structures in full scales are 56.1 metres and 34.1 metres, as well as the model scales are 0.51 metres and 0.31 metres.

8.2.1. Wave Exciting Force act on the Round Shape FLNG

In this research, the proposed method predicts the RAO of round shape FLNG based on the wave force acting on the round shape FLNG. The interaction wave force act on the round shape FLNG was predicted based on the radiating wave generated by the nearby structure. The method used to predict the propagation of radiating wave and character of the radiating wave generated by the nearby structure, which arrived at the round shape FLNG was developed based on the method presented in Figure 6.2 and Figure 6.4. The sample of the radiating wave generated by the round shape FLNG in heave motion and direction of the wave propagate is shown in Figure 8.17.

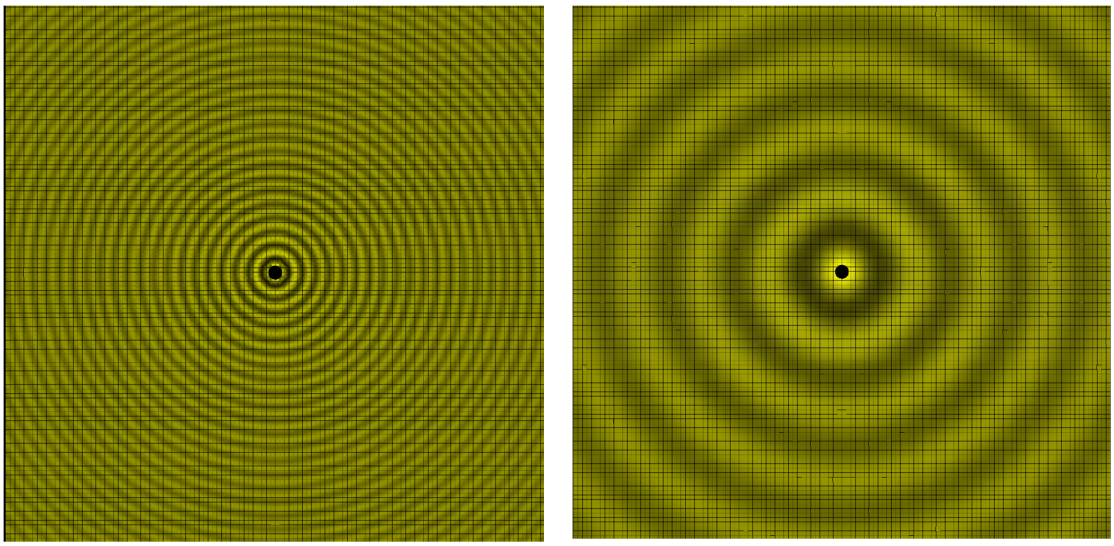

(a) (b)

Figure 8.17: Predicted propagation of radiation wave generated by round shape FLNG. (a) wavelength equal to length of FLNG, (b) wavelength equal to 5 times of length of FLNG

After the potential of the interaction wave generated by the motion of nearby structure is estimated, the interaction wave force contributed to induce the motion of round shape FLNG is predicted using the method present by Figure 6.2 and Figure 6.5. The wave forces or wave moments to induce the motion in each direction is shown from Figure 8.18 to Figure 8.23.

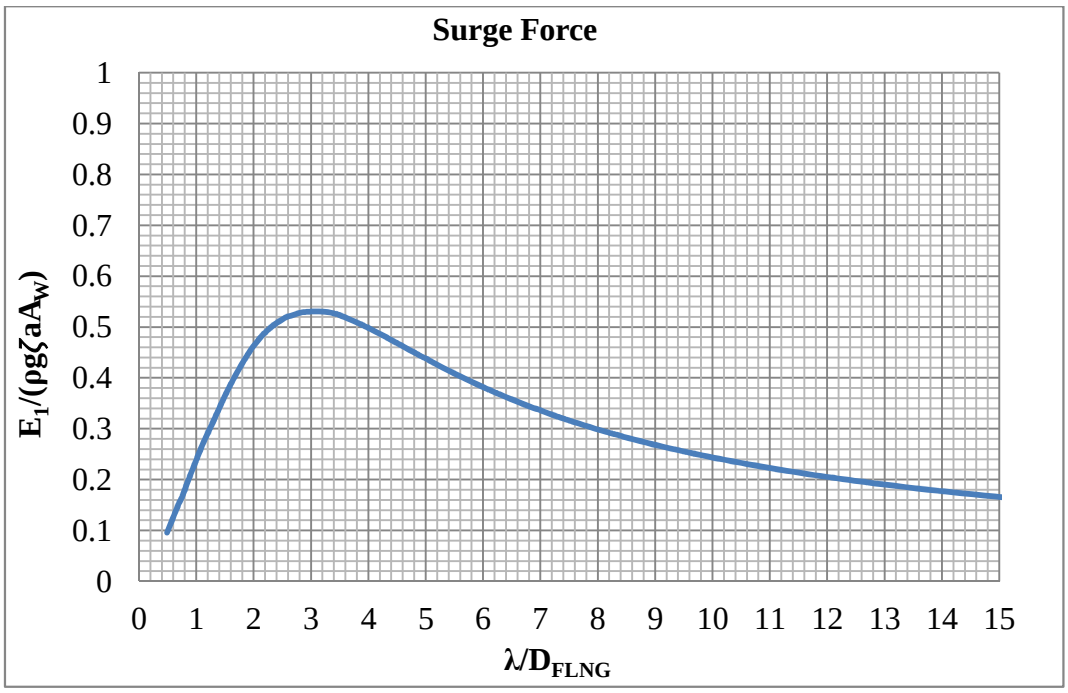

(a)

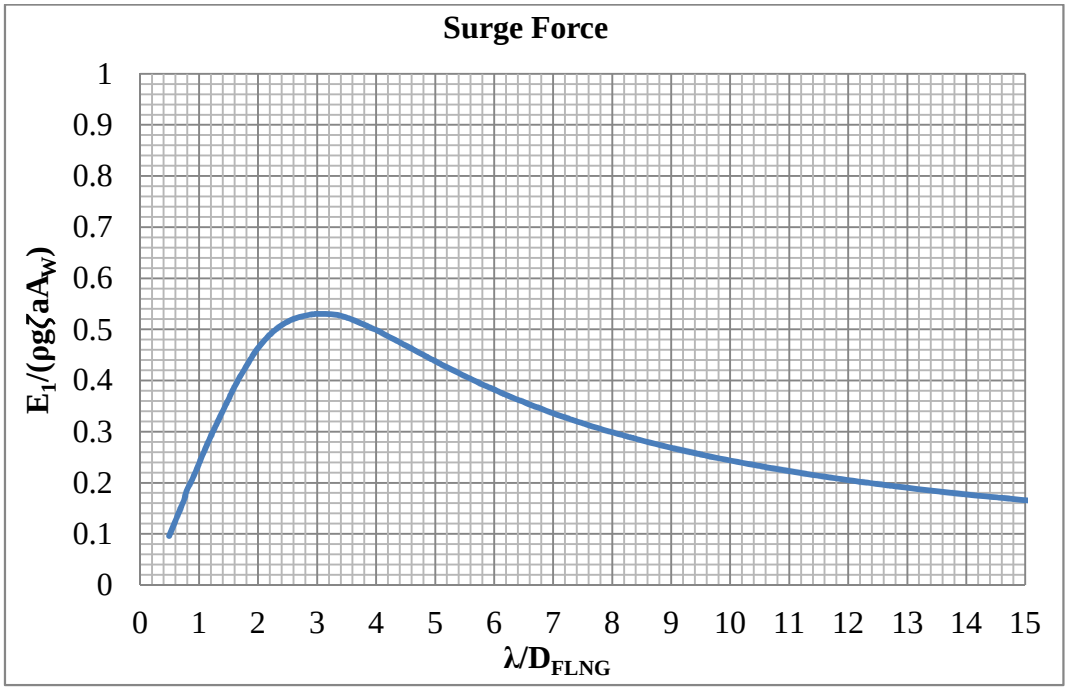

(b)

Figure 8.18: Total surge direction wave force act on the round shape FLNG. (a) Interaction in gap distance 0.3 to the breadth of FLNG (b) Interaction in gap distance 0.5 to the breadth of FLNG

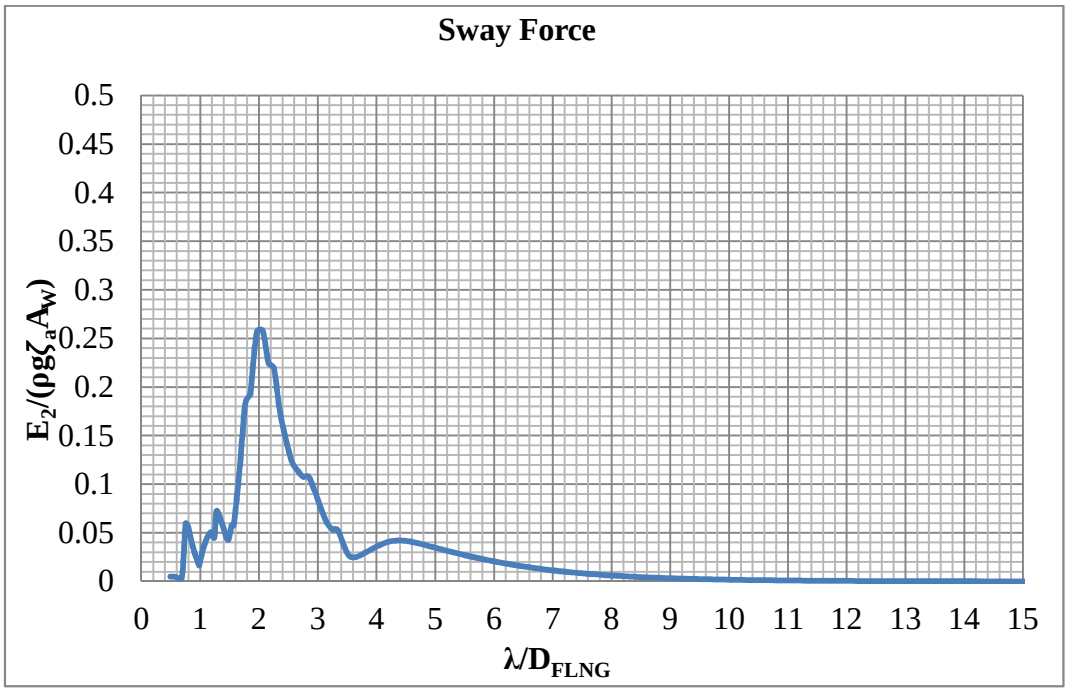

(a)

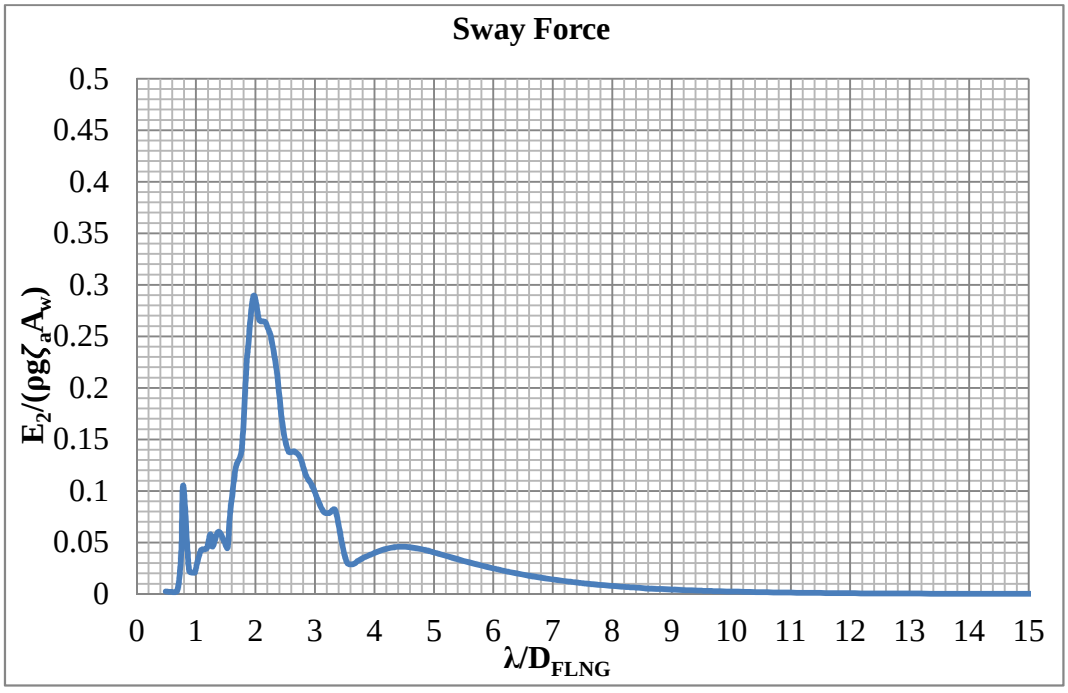

(b)

Figure 8.19: Total sway direction wave force act on the round shape FLNG. (a) Interaction in gap distance 0.3 to the breadth of FLNG; (b) Interaction in gap distance 0.5 to the breadth of FLNG

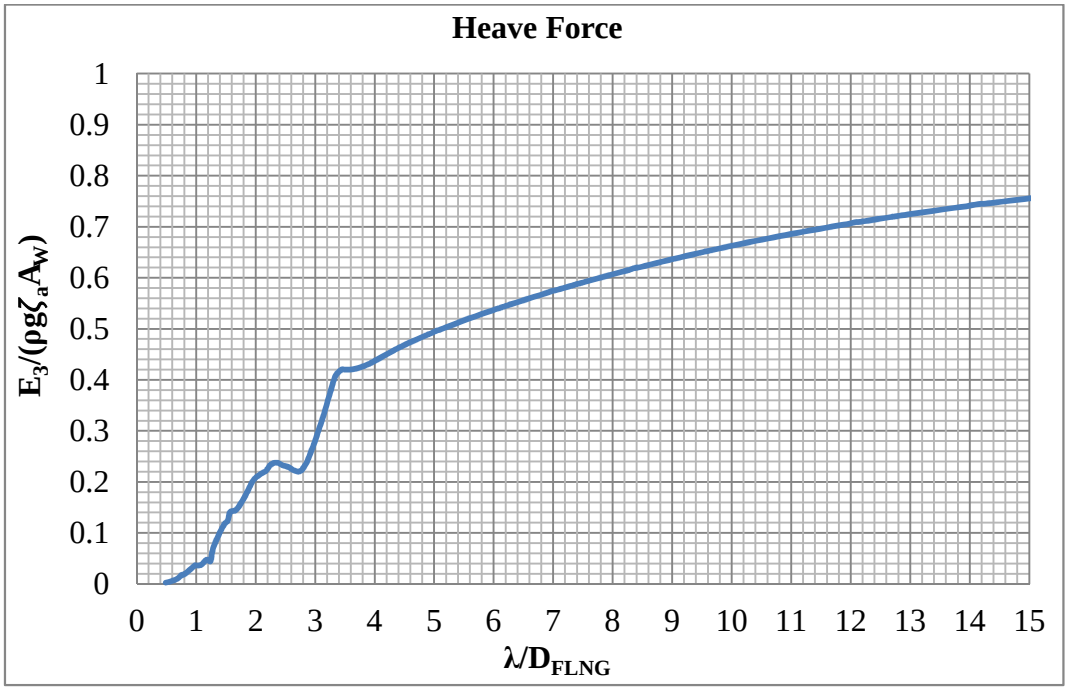

(a)

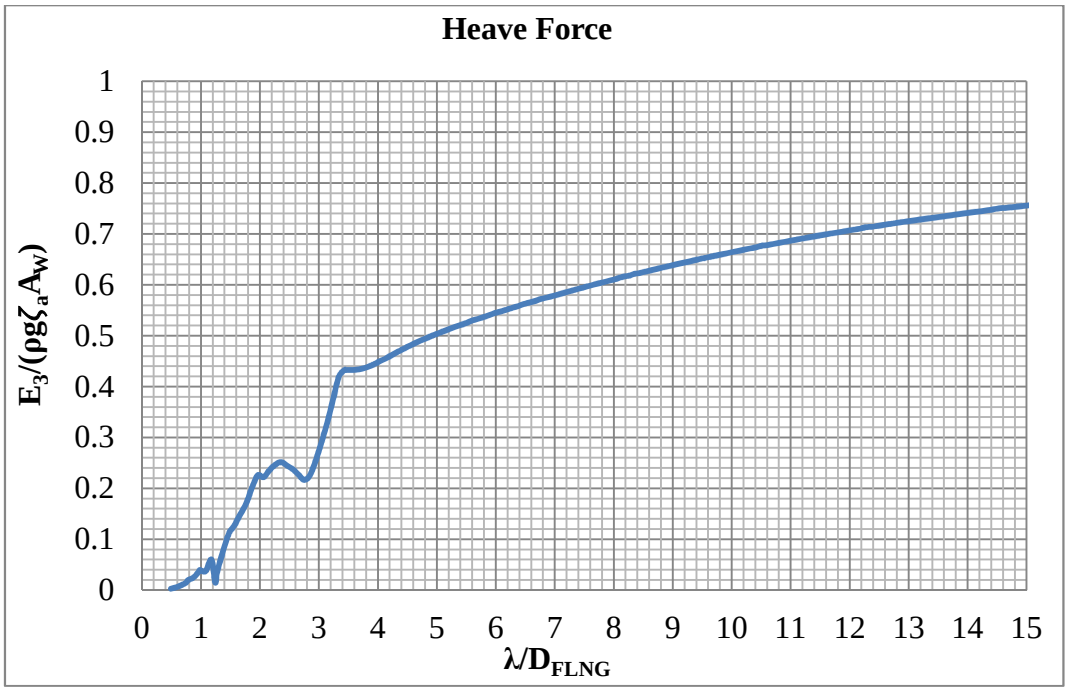

(b)

Figure 8.20: Total heave direction wave force act on the round shape FLNG. (a) Interaction in gap distance 0.3 to the breadth of FLNG; (b) Interaction in gap distance 0.5 to the breadth of FLNG

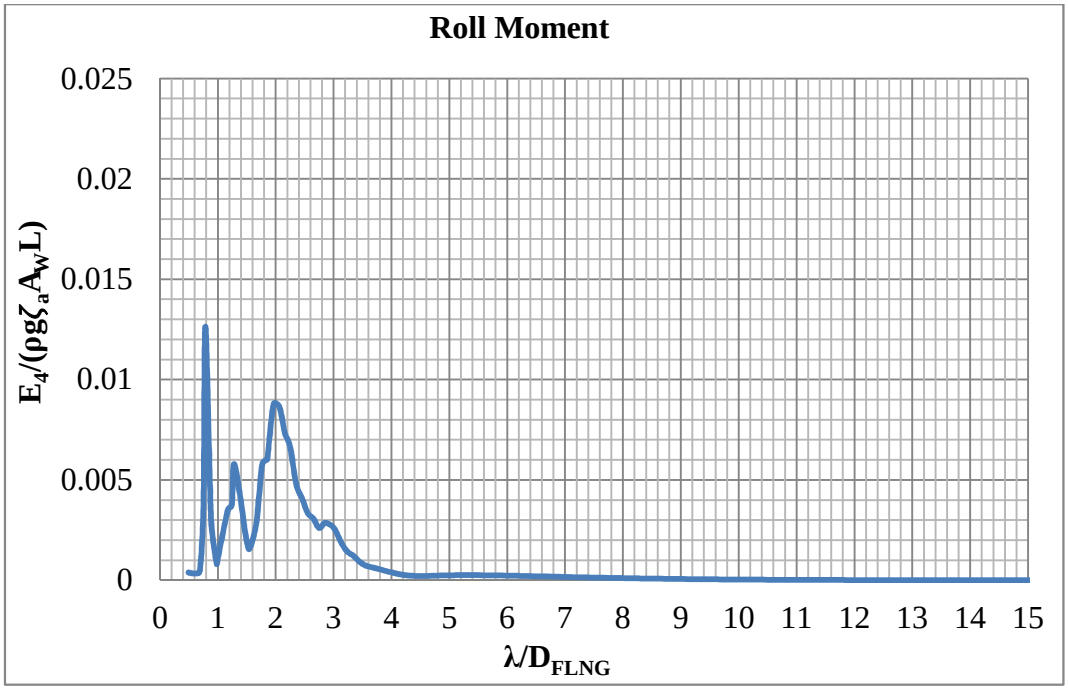
Roll Moment
0.025
0.02
0.015
0.01
0.005
0
E4/(ρgζaAwL)
0 1 2 3 4 5 6 7 8 9 10 11 12 13 14 15
λ/DFLNG

(a)

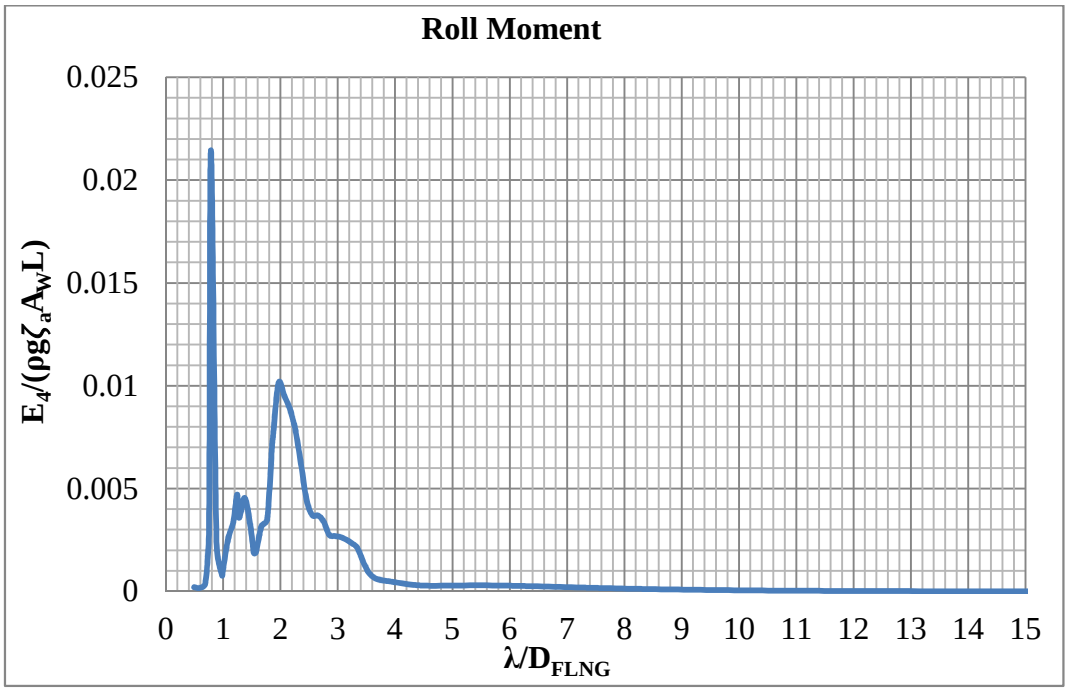
Roll Moment
0.025
0.02
0.015
0.01
0.005
0
E4/(ρgζaAwL)
0 1 2 3 4 5 6 7 8 9 10 11 12 13 14 15
λ/DFLNG

(b)

Figure 8.21: Total roll direction wave moment act on the round shape FLNG. (a) Interaction in gap distance 0.3 to the breadth of FLNG; (b) Interaction in gap distance 0.5 to the breadth of FLNG

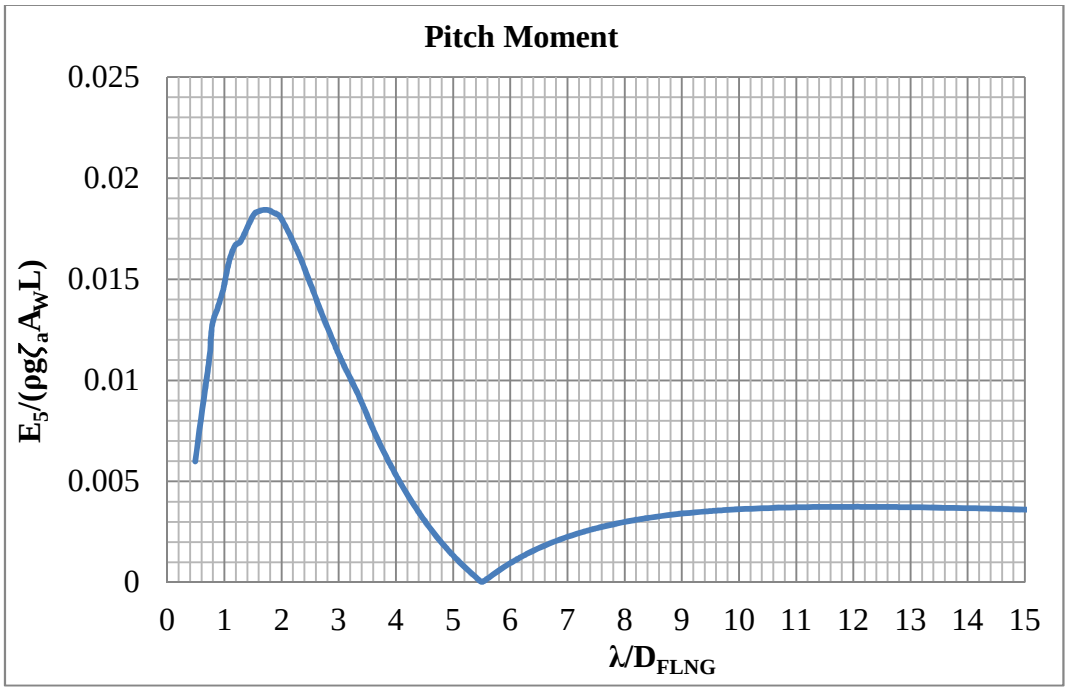

(a)

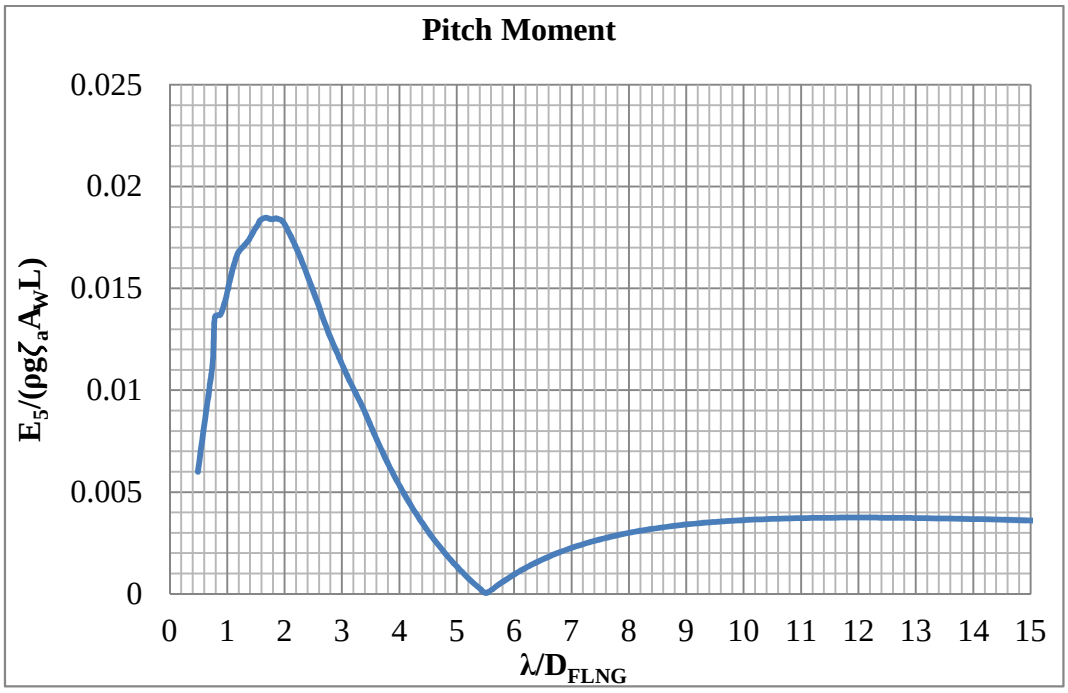

(b)

Figure 8.22: Total pitch direction wave moment act on the round shape FLNG. (a) Interaction in gap distance 0.3 to the breadth of FLNG; (b) Interaction in gap distance 0.5 to the breadth of FLNG

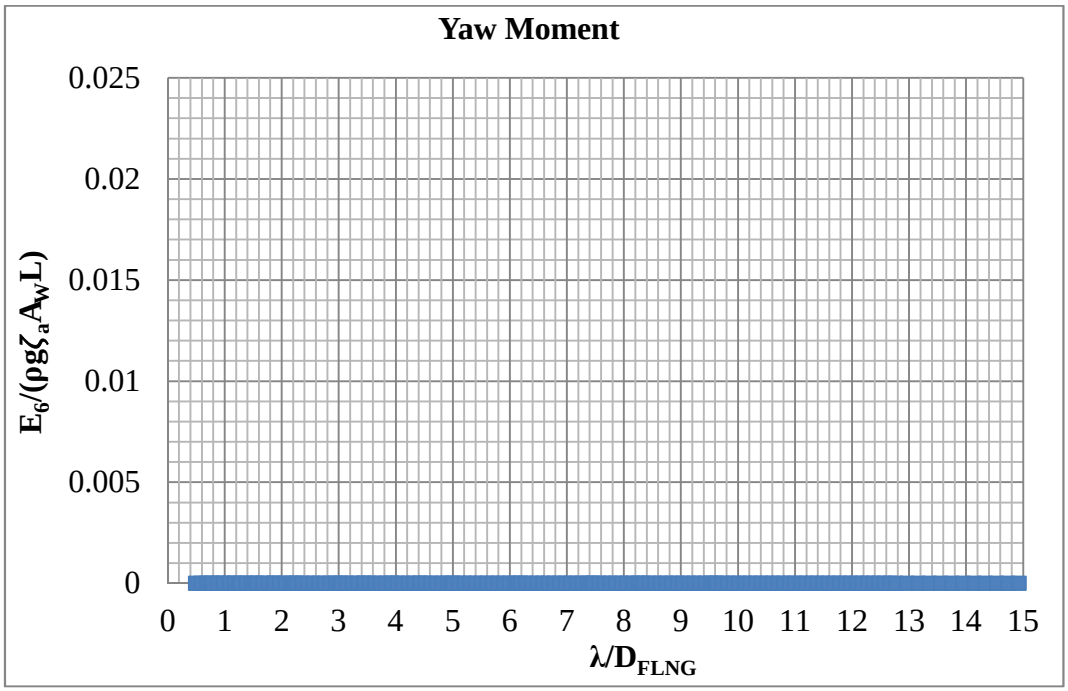

(a)

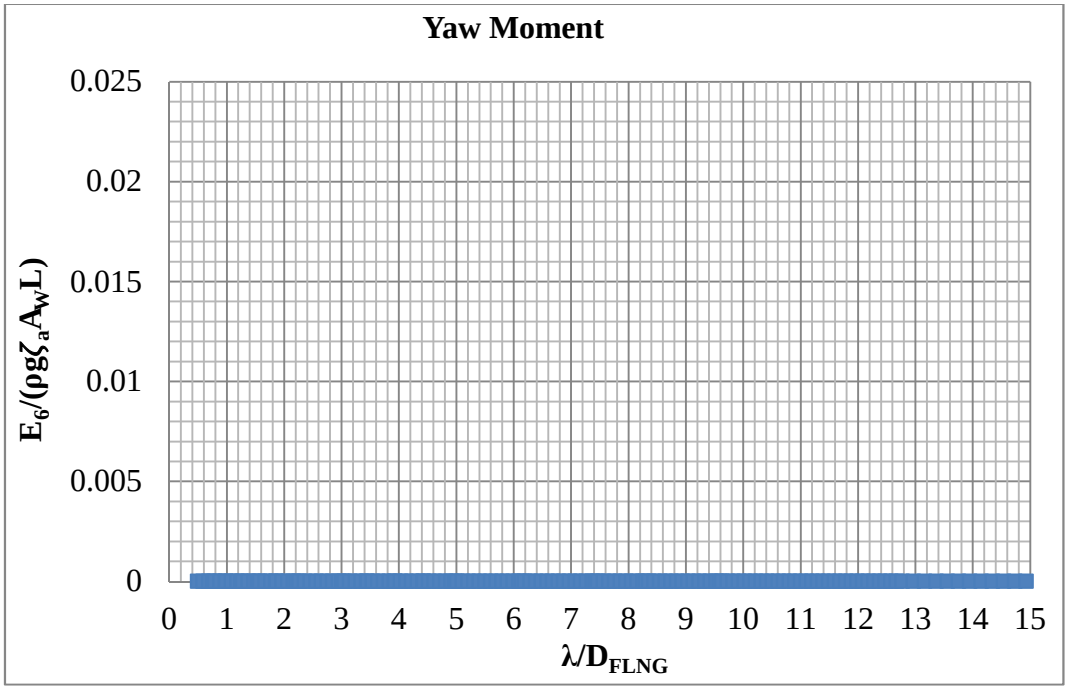

(b)

Figure 8.23: Total yaw direction wave moment act on the round shape FLNG. (a) Interaction in gap distance 0.3 to the breadth of FLNG; (b) Interaction in gap distance 0.5 to the breadth of FLNG

The wave force act on the round shape FLNG to induce the motion in each direction for the condition when it is interacting with KVLCC2 arranged with the gap distance 0.5 to the breadth of FLNG and 0.3 to the breadth of FLNG is shown in Figure 8.18 to Figure 8.21. The interaction tests were conducted in both floating structures arranged in parallel head sea arrangement. The simulated wave force for surge, sway, heave, roll, and pitch, yaw direction was plotted against the ratio of wavelength to the diameter of round shape FLNG, λ/D_{FLNG} in Figure 8.18 to Figure 8.21. The wave forces acting on surge, sway and heave direction shown in the figures were non-dimensioned with density of fluid, gravity acceleration, wave amplitude, and water plane area of round shape FLNG. However, the wave induced moment in roll, pitch and yaw direction was non-dimensioned with density of fluid, gravity acceleration, wave amplitude, water plane area of round shape FLNG, and length of round shape FLNG.

In the Figure 8.18, the wave force act on the surge direction achieved maximum amplitude at the ratio λ/D_{FLNG}, which is equal to 3 for both the interaction cases. After that, the wave force act on the surge direction decreased gradually when the wavelength increased. In comparison with the surge forces induced by wave in both the selected interaction conditions, the surge force in both the interaction cases is almost similar within the selected range of wavelength. The pitch moment of the round shape FLNG induced by wave for both the selected interaction cases is shown in Figure 8.22. The predicted pitch moment achieved maximum at the ratio λ/D_{FLNG}, which is equal to 1.5 and the pitch moment was almost zero when the ratio λ/D_{FLNG} equal to 5.5 at both the selected interaction cases. In compared to the wave moment induce the pitch moment in the both cases, it was obtained that the influence of structures gap distance to the pitch moment for the round shape is limited.

The wave forces acting on sway direction is shown in Figure 8.19. From Figure 8.19, it was observed that the strong interaction wave forces act on round shape FLNG in the region, where the ratio of λ/D_{FLNG} is below 4.5. If the wavelength is longer than the ratio of λ/D_{FLNG}, which is equal to 4.5, the wave force act on sway direction start to decrease to zero

by increasing the wavelength. The tendency of wave force act on sway direction for both the selected interaction cases is similar within the range of the selected wavelength. However, the interaction wave force was observed stronger at the interaction case, where the KVLCC2 arranged in the gap distance 0.5 to the breadth of FLNG. The similar observation was obtained for the wave induces roll moment as shown in Figure 8.21. The roll moments due to the effect of interaction in both selected cases are stronger in short wavelength region compared to the roll moment due to interaction effect in long wavelength region. The roll moment was also mostly larger in the case, where the KVLCC2 is arranged in the gap distance 0.5 to the breadth of FLNG within the selected range of wavelength for the simulation.

The heave force induces the heave motion to the round shape FLNG in both the interaction cases as shown in Figure 8.20. The heave force is predicted to increase when the wavelength increases in both the interaction cases. Round shape FLNG is predicted to experience a larger heave force in long wavelength region by the proposed method. On the other hand, the heave force estimated for both the interaction cases is almost similar between each other as shown in Figure 8.20. The influence of changes of the interaction gap distance to the wave force act on heave direction is not very distinct for the selected round shape FLNG structure.

The wave moment act on the round shape FLNG in yaw direction for both the selected interaction cases is shown in Figure 8.23. From Figure 8.23, the yaw moment due to the interaction effect is negligible in any wavelength. This observation also explains the reason of yaw motion of this round shape FLNG as shown in Figure 8.29, which is very small and can be neglected in any wavelength.

From the discussed wave force tendencies for each direction of motion, it was observed that the interaction between floating structures only influenced the wave force for sway, heave and roll direction for this parallel head sea arrangement. This is because the interaction wave generate by the motion of floating structure in parallel head sea arrangement only propagate in sway direction. Therefore, the interaction wave potential does not contribute any wave force to the surge direction and pitch direction. In these interacting cases, the surge exciting force and pitch exciting moment shown in the Figure 8.19 and Figure 8.22 existed in the calculation is due to the effect from the incident wave. By compared the magnitudes and tendencies of the surge force and pitch moment in interacting cases (Figure

8.19 and Figure 8.22) to the surge force and pitch moment when the FLNG is alone (Figure 8.9 and Figure 8.10), this obtained that the surge force and pitch moment are similar between the condition where the FLNG is alone and when the FLNG is interacting with shuttle tanker. This is because the wave propagation direction is the important parameter to determine the direction of the wave force induces by the interaction wave. Since no any interaction wave is propagated across the round shape FLNG in surge direction, then surge force and pitch moment remain unchanged when it is interacting with the LNG shuttle tanker in parallel head sea condition.

From the Figure 8.23, the yaw moment shown it is remain zero and does not influenced due to the interaction effect. The yaw moment does not increased in the interaction cases are because of the shape of the round shape FLNG. The cylindrical structure is typically have very limited yaw motion because the propagation of wave from any direction does not induce the yaw moment. The reason for the zero yaw moment in any wavelength predicted by the proposed method in the interaction cases is because of the area normal vector in yaw direction. From the equation (4.77), it is shown that the wave exciting force is in the function of wave potential, wetted surface area and the area normal vector. Since the area normal vector in yaw direction for this round shape FLNG is always zero, so the zero yaw moment calculated by the proposed method is agreed with the expectation when refer to the mathematical equation to calculate the yaw moment.

The interaction between round shape FLNG and the LNG shuttle tanker in parallel head sea condition causes the change of the wave exciting force in sway, heave and roll direction. Only the wave forces in these three directions were influenced in interaction cases because the interaction wave is propagated across the round shape FLNG in sway direction. As shown in the Figure 8.19 and Figure 8.21, both the sway force and roll moment were only excited in the interaction cases. When the round shape FLNG is alone in head sea condition, the sway force and roll moment do not exist because no incident wave propagated in sway direction in head sea condition. The sway force and roll moment in the selected interaction cases all are contributed from the interaction wave generated by the motion of nearby floating structure. Compare to previous research, Zhu et al. (2006) and Kagemoto and Yue (1987) also obtained this similar finding. Both the previous researches also detected exist of the sway force and roll moment when the floating structure interacting with nearby structure in parallel head sea arrangement.

On the other hand, the calculated heave force by proposed method also influenced by interaction effect. The heave force in short wavelength region become fluctuates as shown in Figure 8.20 in interaction cases. The heave motion of the round shape FLNG is able to influence by the interaction effect if another floating structure arranged nearby it regardless of any arrangement. This is because the propagation of wave in any direction toward the FLNG would cause the change of wave potential in heave direction. From the Figure 8.20, the heave exciting force is the summation of the wave force due to incident wave and the wave force due to the interaction effect.

In addition, from the calculated sway force, heave force and roll moment, the tendencies of the exciting forces show that the effect of interaction between floating structure is stronger in short wavelength region. This finding is also similar with the research outcome from Kashiwagi et al. (2005). The effect of interaction is stronger in short wavelength region is because of the wave radiating and diffracting phenomena. The diffraction and radiation effect of the floating structure is more dominant in the short wavelength region. Higher amount of the wave can be diffracted and radiated from the nearby LNG shuttle tanker which arranged near to the round shape LNG in shorter wavelength region. This cause the FLNG receive higher amount of wave exciting force due to the interaction effect in short wavelength condition. According to Faltinsen (1990), the wave diffraction and radiation is the dominant parameter must be considered when analyse the motion of floating structure in the ratio of wavelength to structure length below 5. In long wavelength region, the floating structure has enough time to response to the incident wave and the motion of the floating structure is typically following the wave. Therefore, the amount of radiating wave able to generate by the motion of floating structure become very limited. This causes the interaction effect in long wavelength region is smaller compare to short wavelength region.

One of the main targets of this research is to study the wave frequency motion response of the round shape FLNG. The motion experiment was conducted to obtain the six DoF RAO of the round shape FLNG. Therefore, the proposed method is only validated by comparing the RAO of the FLNG which estimated by proposed method to the RAO of the similar model which estimated by experiment test in this research. However, the wave exciting is also an important parameter must be study to predict the RAO of the FLNG. According to Ohkusu (1998), validate the hydrodynamics numerical method by using experiment test can be achieved by compare the RAO of floating structure estimated by

numerical method to result obtained from experiment method. The experiment tests are indeed practically useful to study the applicable of the proposed numerical method. However, some should understand that the good agreement of the predicted structure RAO by numerical method in compare to the RAO estimated by experiment test does not directly shows the theoretical approach is correctly estimated the wave exciting force. This is because the total wave exciting force is an integrated effect of hydrodynamic pressure on the wetted surface of the floating structure. Besides, the RAO from the experiment is the combination result of the effect of all hydrodynamic parameter such as added mass, damping, restoring force and wave exciting force. The motion experiment was selected in this research to validate the proposed method because the objective of the research is to develop the numerical method which is able to estimate the RAO of the FLNG. The wave exciting force shown in this sub-chapter is proposed to present the idea on the effect of interaction to the tendency of wave exciting force. The wave exciting force is a main parameter to ensure the motion characteristic of the FLNG is modelling correctly. If the wave exciting force is the main target of the research, the analytical experiment such as measurement of fluid pressure distribution and flow visualization will be necessary to conducted to check the fluid particle motion and this would be a another study could be extended from the current study.

8.2.2. Estimated RAO of Round Shape FLNG When Interacting with another Structure

The RAO of round shape FLNG when interacting with LNG shuttle tanker (KVLCC2) was estimated using proposed method, experimental test and ANSYS AQWA. The proposed method developed from diffraction potential theory with drag equation was further developed to enable it for estimation of the influence of second structure to the RAO of round shape FLNG. The solution of proposed method applied to simulate the RAO of Round Shape FLNG in interacting with second structure was shown in Figure 6.2.

Due to the influence from interaction, the round shape FLNG experienced the motion in all six directions of motion although in head sea condition. The motion responses of round shape FLNG when interacting with LNG shuttle tanker are shown in Figure 8.24 to Figure 8.29. In Figure 8.24 to Figure 8.29, each shows the RAO of round shape FLNG in each direction of motion when the KVLCC2 model is arranged in the distance of 0.5 to the breadth of FLNG and 0.3 to the breadth of FLNG. The RAO of the round shape FLNG predicted by

proposed method, experiment test and ANSYS AQWA was plotted in the same figure to illustrate the difference of the RAO tendency obtained from each different method.

From the Figure 8.24 to Figure 8.29, the research obtained that the interaction between round shape FLNG with the LNG shuttle tanker in parallel head sea arrangement did not causes the interaction effect to the round shape FLNG in the surge, pitch and yaw direction. The interaction effect on the motion of FLNG in this arrangement is observed in the direction of sway, heave and roll. This observation is similar with the research which has been conducted by Zhu et al. (2006) and Kagemoto and Yue (1987). The reason to obtain this result is because the generated wave due to interaction effect between FLNG with LNG shuttle tanker is only propagated in the sway direction. Therefore, the extra wave force due to the interaction effect does not contribute to the surge, pitch and yaw exciting force. This reason also explained in the sub-chapter 8.2.1 where the sub-chapter present the calculated wave exciting force for each direction of motion in both the interaction cases.

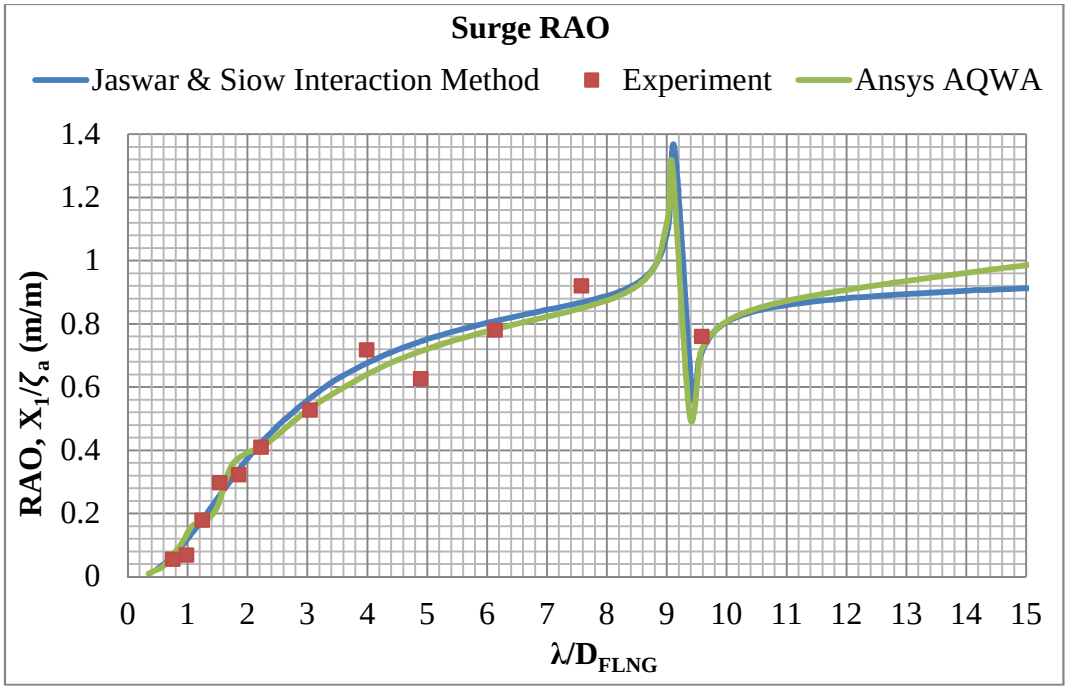

(a)

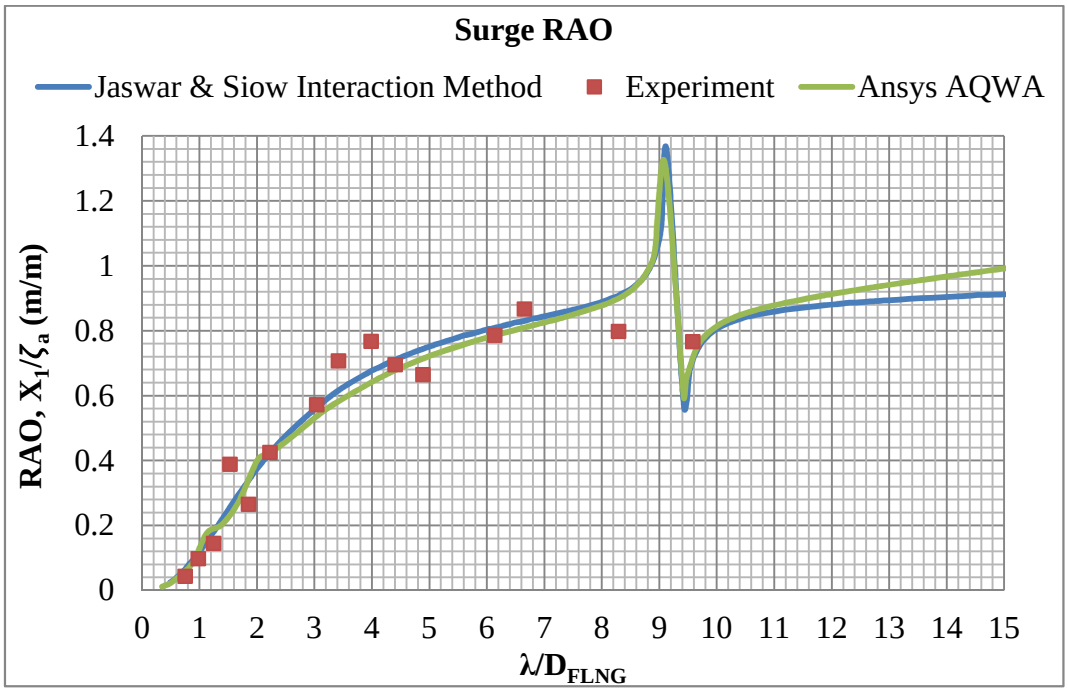

(b)

Figure 8.24: Surge RAO of round shape FLNG in interaction cases. (a) Interaction in gap distance 0.3 to the breadth of FLNG (b) Interaction in gap distance 0.5 to the breadth of FLNG

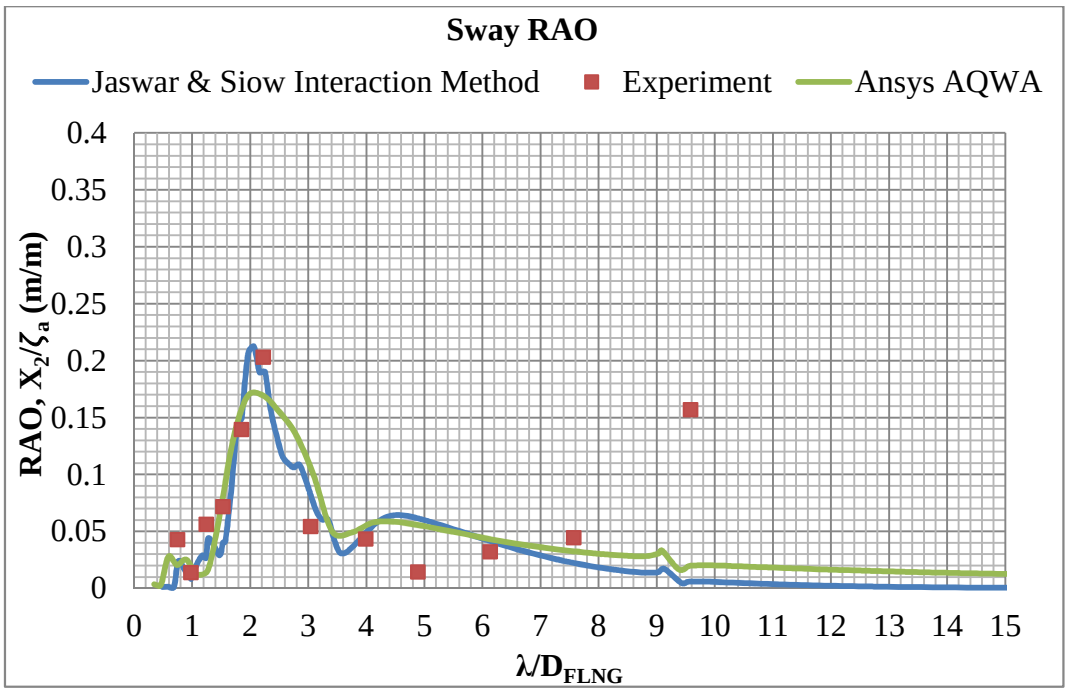

(a)

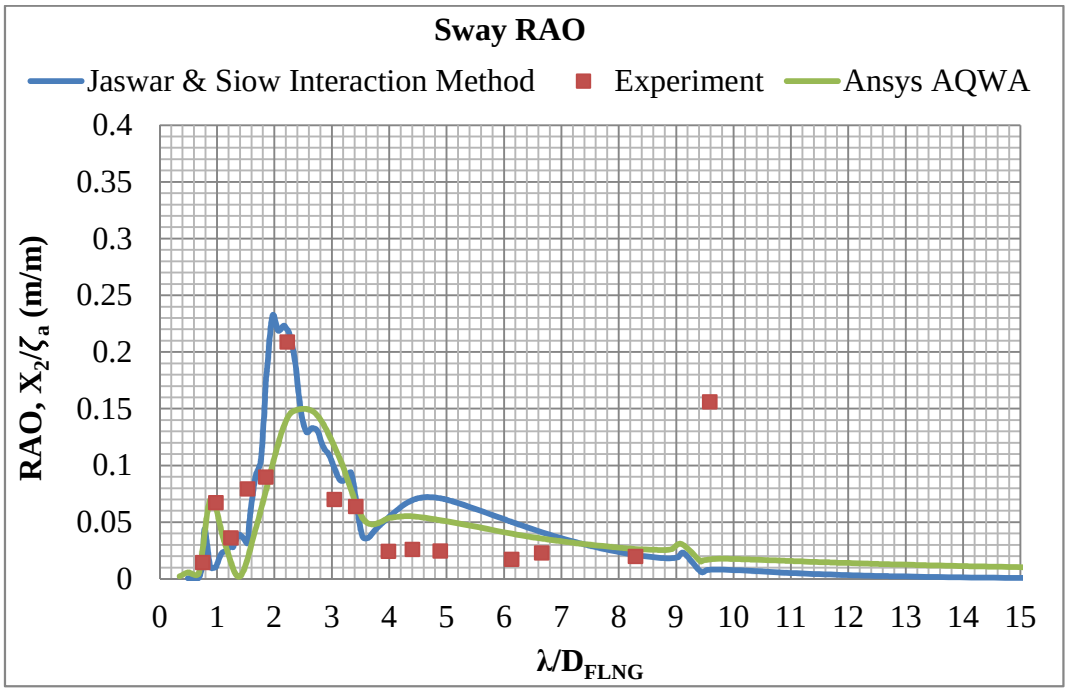

(b)

Figure 8.25: Sway RAO of round shape FLNG in interaction cases. (a) Interaction in gap distance 0.3 to the breadth of FLNG; (b) Interaction in gap distance 0.5 to the breadth of FLNG

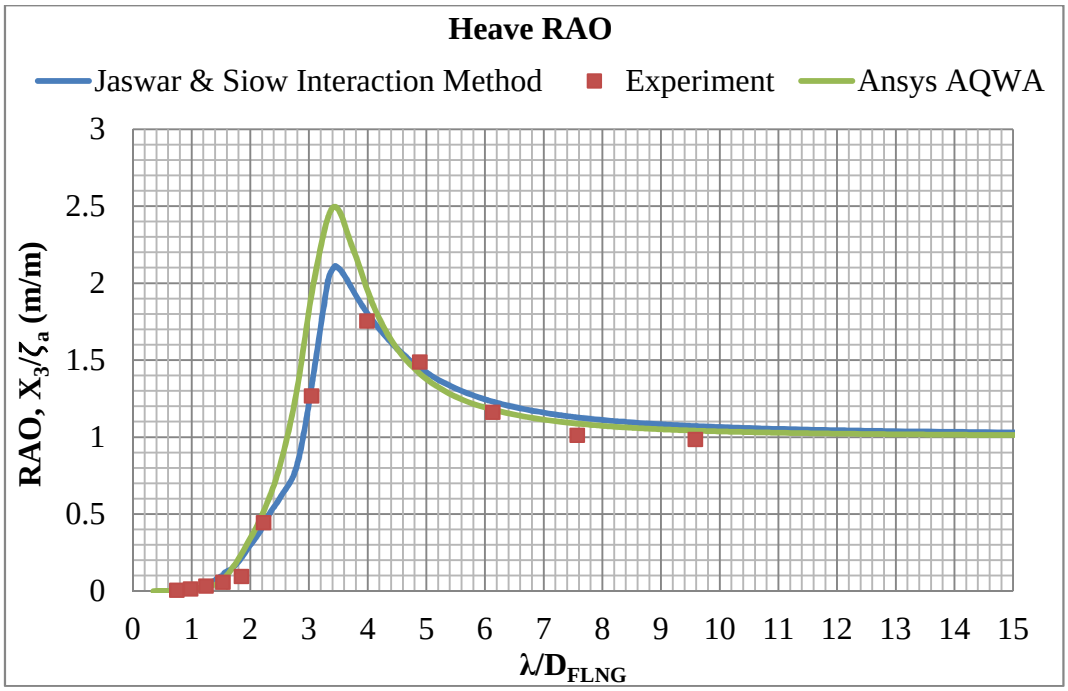

(a)

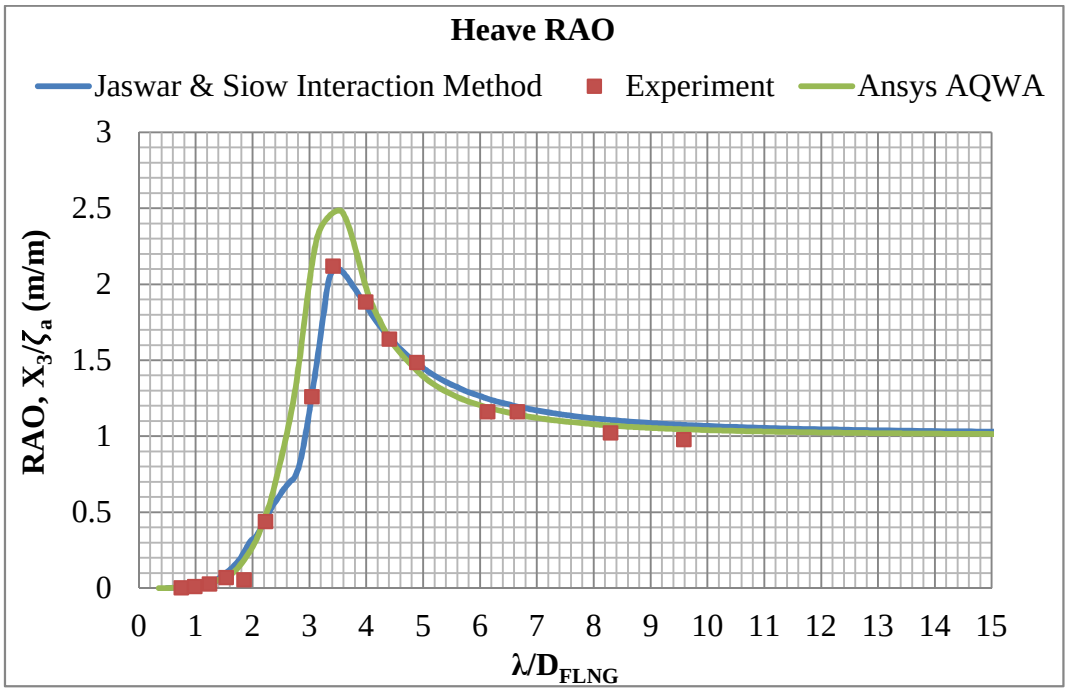

(b)

Figure 8.26: Heave RAO of round shape FLNG in interaction cases. (a) Interaction in gap distance 0.3 to the breadth of FLNG; (b) Interaction in gap distance 0.5 to the breadth of FLNG

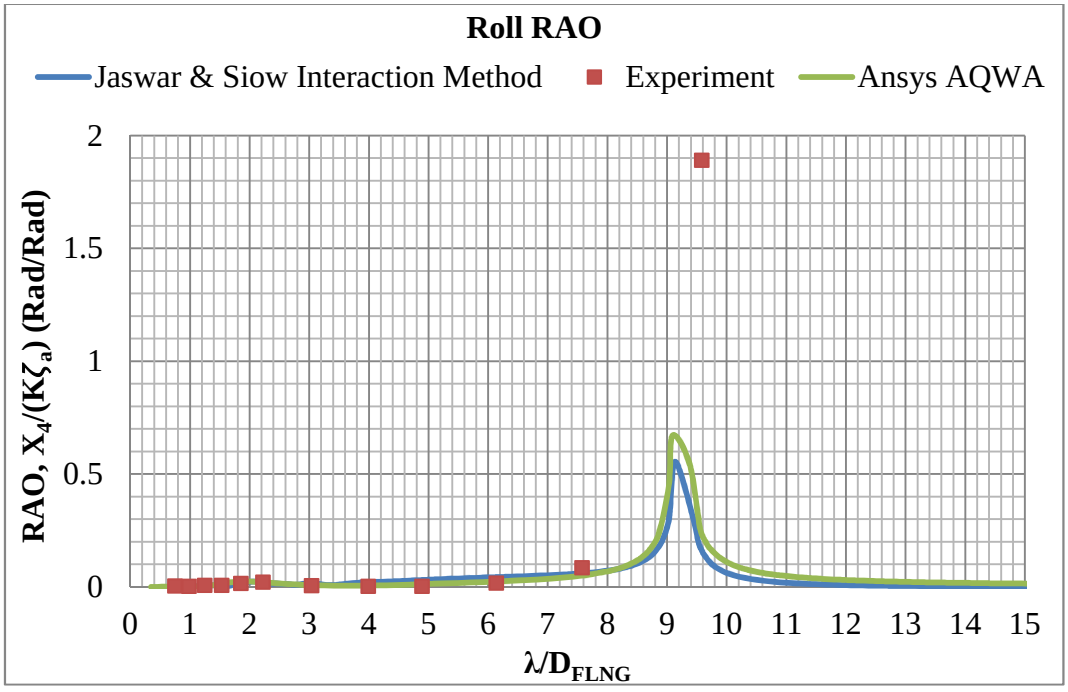

(a)

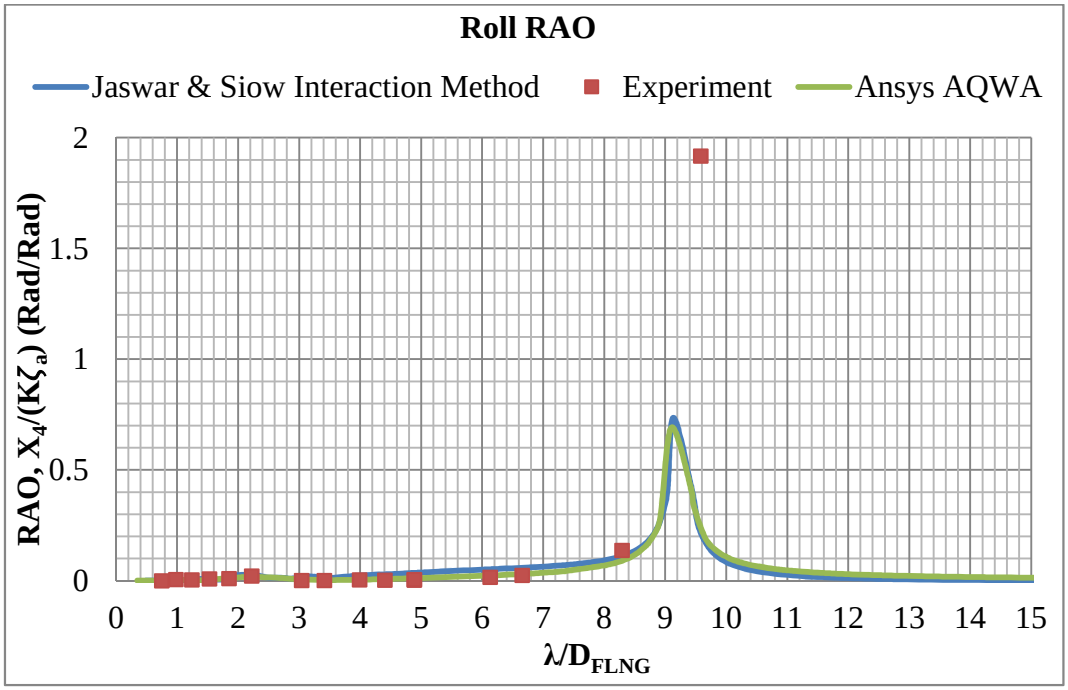

(b)

Figure 8.27: Roll RAO of round shape FLNG in interaction cases. (a) Interaction in gap distance 0.3 to the breadth of FLNG; (b) Interaction in gap distance 0.5 to the breadth of FLNG

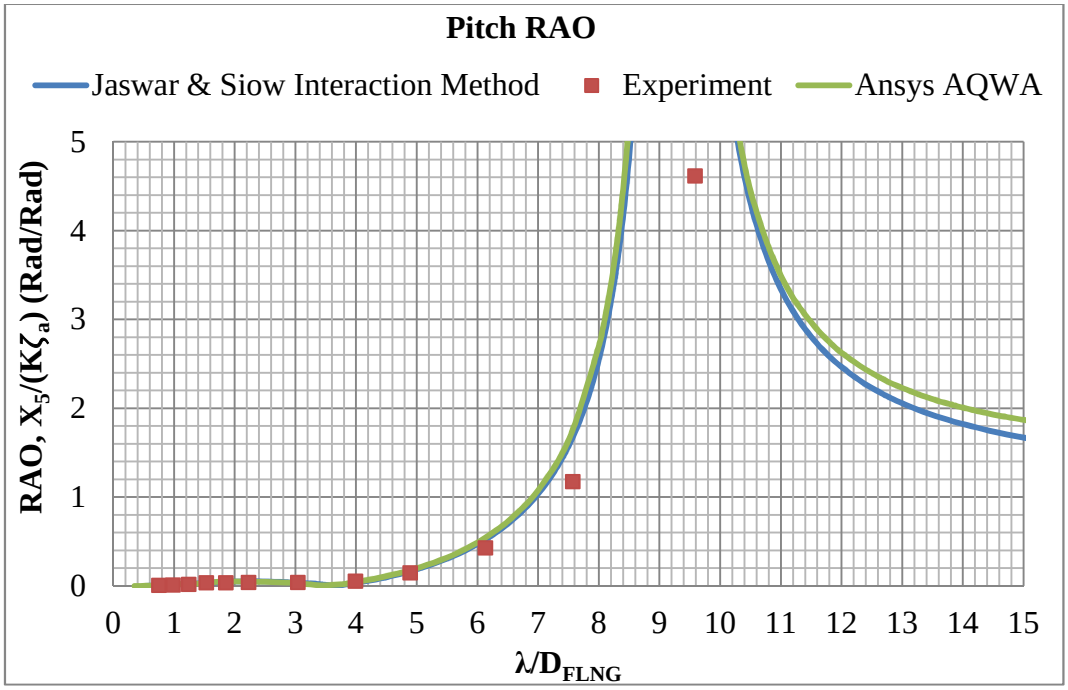

(a)

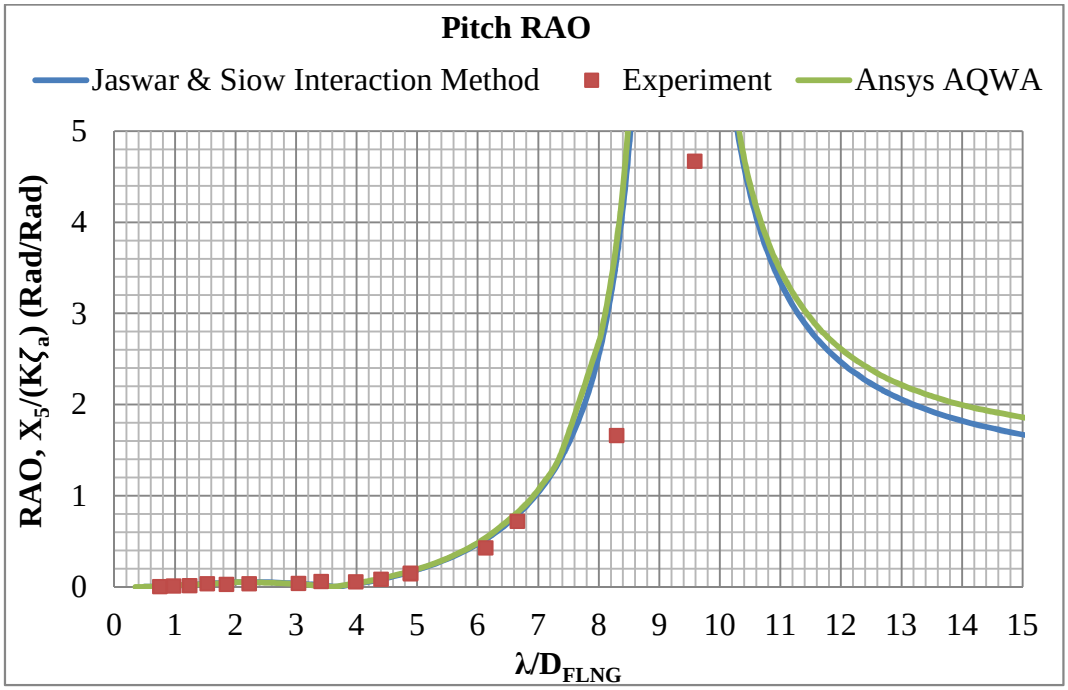

(b)

Figure 8.28: Pitch RAO of round shape FLNG in interaction cases. (a) Interaction in gap distance 0.3 to the breadth of FLNG; (b) Interaction in gap distance 0.5 to the breadth of FLNG

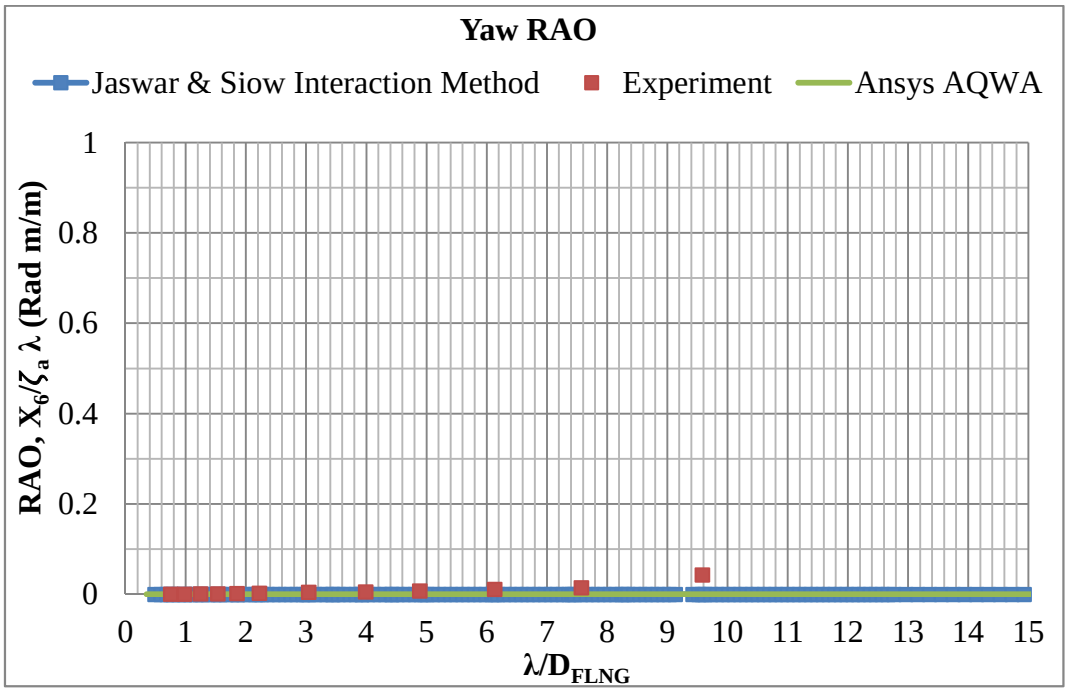

(a)

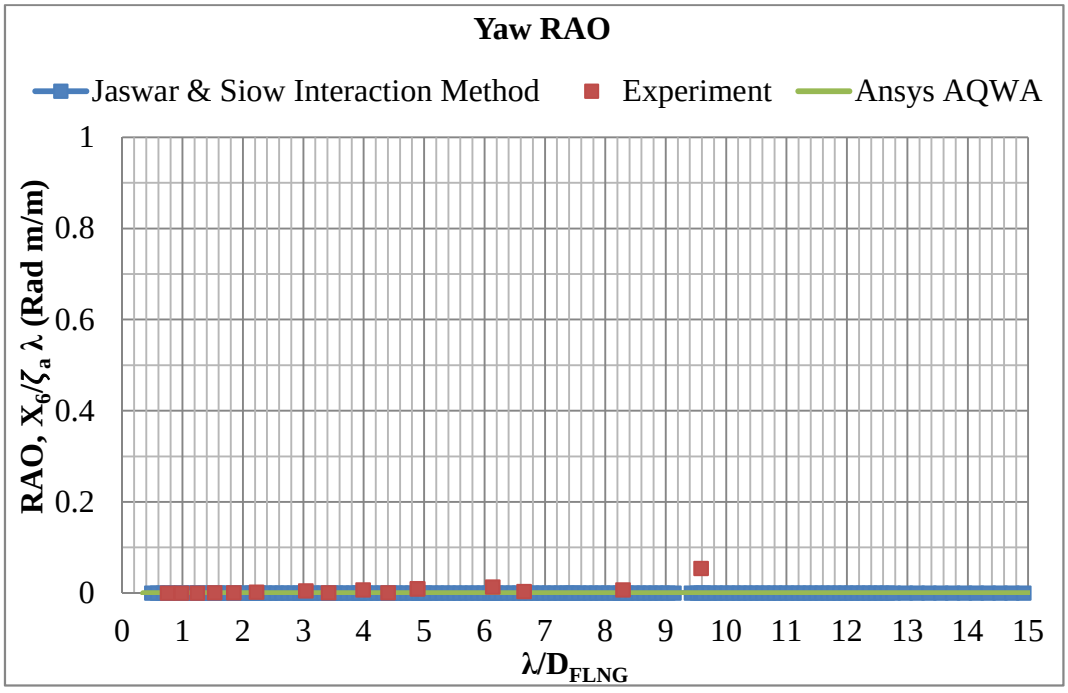

(b)

Figure 8.29: Yaw RAO of round shape FLNG in interaction cases. (a) Interaction in gap distance 0.3 to the breadth of FLNG; (b) Interaction in gap distance 0.5 to the breadth of FLNG

The Figure 8.24 shows the surge RAO of round shape FLNG in the condition interacting with the KVLCC2 tanker ship at gap distance 0.5 to the breadth of FLNG and 0.3 to the breadth of FLNG. From this figure, it shows the proposed method predicted almost similar tendency of the surge RAO of round shape FLNG compared to the experimental result and ANSYS AQWA commercial code in the condition FLNG interacting with second floating structure. Similar surge RAO obtained in the interaction cases compare to no interaction cases because the surge motion of FLNG is only induced by the incident wave. Interaction between floating structures in parallel head sea arrangement do not increase the surge exciting force which induce the surge motion of the FLNG. The surge RAO of the round shape FLNG when KVLCC2 model was arranged in the gap distance 0.5 to the breadth of FLNG and 0.3 to the breadth of FLNG is increasing gradually if the wavelength is increasing. Similar with the Surge RAO of round shape FLNG when it is alone, the surge RAO of the round shape FLNG in interaction phenomena is predicted to experience a large change of surge RAO between the ratio λ/D_{FLNG} 8.5 to 10. The natural frequency for FLNG's surge motion is at the wavelength λ/D_{FLNG} equal to 1570. Therefore, fluctuation of the tendencies of surge RAO is not because of the resonance effect. By comparing the surge and pitch response tendency shown in Figure 8.24 and Figure 8.28, it can relate the large change of surge tendency between the ratio λ/D_{FLNG} 8.5 to 10, which may be due to the coupling motion of pitch response.

Figure 8.28 shows the tendency of pitch RAO of round shape FLNG predicted by proposed method, experimental test and ANSYS AQWA. In comparison, the pitch RAO prediction by proposed method shows an agreement with the experiment result in the selected range of wavelength. Similar as surge motion, the pitch motion is induced by the incident wave. Interaction between FLNG and shuttle tanker did not affect the pitch motion due to the arrangement of the floating structures. The tendency of the pitch RAO predicted by proposed method is quite similar with the ANSYS AQWA result for the wavelength in the ratio of λ/D_{FLNG}, which is below 3.8. If the ratio of λ/D_{FLNG} is larger than 3.8, the proposed method predicts a higher pitch RAO compared to the pitch RAO predicted by ANSYS AQWA in both the interaction cases. From the decay test, it is obtained that the pitch natural frequency is at λ/D_{FLNG} equal to 9.35. From the Figure 8.28, the peak RAO of pitch motion is happened at it natural period due to the resonance effect. The pitch RAO is large at the long wavelength

because the pitch damping coefficient of the round shape FLNG is small at the long wavelength region.

The sway RAO of the round shape FLNG is shown in Figure 8.25. The sway motion of the FLNG is only existed in the interaction cases due to the interaction effect. The wave exciting force contribute to the sway motion is come from the interaction wave. The sway RAOs predicted by proposed method and experimental method are agreed with each other. The tendency of the sway motion predicted by proposed method is slightly different compared to the tendency of sway motion predicted by ANSYS AQWA in the ratio λ/D_{FLNG} from 0.5 to 3.5. However, if the wavelength at the ratio λ/D_{FLNG} is larger than 3.5, the sway motion predicted by ANSYS AQWA and proposed method is almost similar. From the Figure 8.25, the peak sway RAO for the FLNG is found at λ/D_{FLNG} around 2 for both the interaction cases. The peak sway RAO happened in the wavelength is because of strong interaction effect. Due to the interaction effect, the peak sway exciting force is observed at the similar wavelength as the wavelength for peak sway RAO. In comparing with the experiment result, both the proposed method and ANSYS AQWA under predict the sway RAO of the round shape FLNG at the ratio of λ/D_{FLNG}, which is equal to 9.5, where the sway RAO predicted by the experiment test is increased, but the proposed method and ANSYS AQWA cannot predict the similar tendency. The reason for the proposed method and Ansys AQWA do not predict the similar sway RAO compare to experiment result at λ/D_{FLNG} equal to 9.5 because both the numerical method do not consider the mooring effect in the calculation. The higher sway RAO predicted by the experiment test is believed causes by the coupling effect between sway direction to pitch direction. According to Journee and Massie (2001), the symmetry floating structure such as the round shape FLNG and the LNG shuttle tanker have negligible coupling effect between surge-pitch and sway-roll motion because the two set of motion equations is distinguished for this symmetry structure. However, if the floating structure is connected by a mooring line, then it is possible for the coupling effect exist between the surge-pitch and sway-roll motion via the mooring cable.

The roll RAO of round shape FLNG is shown in Figure 8.27. Similar with the sway motion, the roll motion of the round shape FLNG is only existed in interaction cases. This is because there are no incident wave can be generated the roll moment in head sea arrangement. In comparison with the experiment result, the proposed method is able to predict the roll RAO of round shape FLNG at short wavelength region. When the ratio of λ/D_{FLNG} is below 3.5, the

proposed method predicted the roll motion or round shape FLNG quite accurate. However, if the λ/D_{FLNG} is larger than 3.5, the roll motion predicted by the proposed method is larger than the roll RAO predict by experiment test. In roll RAO, the ANSYS AQWA is shown, which is better fixed with experimental result compared to proposed method. The higher roll motion predicted by the proposed method compared to ANSYS AQWA is due to higher roll moment predicted by proposed method in both the interaction cases. The estimated roll natural frequency from decay test is at λ/D_{FLNG} equal to 9.35. From Figure 8.27, the proposed method predicted the roll RAO of round shape FLNG is larger at the long wavelength condition because of the resonance effect and the damping predicted by the proposed method is small at long wavelength condition. Besides, the experiment result is also predicted much higher roll RAO at λ/D_{FLNG} equal to 9.5 compared to the roll RAO estimated by the proposed method and ANSYS AQWA. The reason for this difference between numerical result and experiment result is because of the mooring line used in the experiment. The mooring line causes the coupling effect between surge-pitch motion and the sway-roll motion but the coupling effect via the mooring line is not considered in the numerical calculation due to the limitation of the numerical method.

The heave RAO of round shape FLNG is shown in Figure 8.26. In general, the tendency of heave RAO predicted by proposed method and ANSYS AQWA is quite similar within the selected range of wavelength. The figure also shows that both the numerical methods and the experiment result show that the peak heave RAO is happened at the heave motion natural period. However, the magnitude of heave RAO predicted by proposed method is smaller compared to the heave RAO predicted by ANSYS AQWA at the ratio of λ/D_{FLNG} from 2.5 to 4.5. The smaller heave RAO predicted by using proposed method compared to ANSYS AQWA is due to the involvement of viscous effect calculated by using the drag equation. Compared with the experimental result, it is observed that the heave motion tendency predicted by the proposed method is fixed better to experimental result compared to the tendency of heave motion predicted by ANSYS AQWA. The proposed method is able to reduce the predicted heave RAO because viscous damping is considered in the calculation. In damping dominant region, the RAO of the floating structure is more dependent on the damping coefficient in the motion equation. Better prediction of damping coefficient helps to improve the prediction of RAO in the damping dominant region.

The yaw RAO of round shape FLNG predicted by the proposed method compared to the experimental result and ANSYS AQWA is shown in Figure 8.29. From Figure 8.29, it shows that the yaw motion of the round shape FLNG predicted by the proposed method is very small and insignificant compared to the motion in other directions. The yaw motion for this round shape FLNG is very small because the yaw moment is not induced by the incident wave and interaction effect. The yaw moment is negligible for this FLNG because the FLNG is no able to capture the wave in yaw direction due to the shape of the FLNG. The tendency of yaw RAO predicted by proposed method is similar with the tendency of yaw RAO predicted by the experimental method and ANSYS AQWA. In both the interaction cases selected to study in this research, it shows that the effect of the interaction between FLNG with the KVLCC2 does not induce the yaw motion to the FLNG.

8.3. Comparison RAO of Single Round Shape FLNG without Interaction and RAO of Round Shape FLNG Interacting with another Structure

The RAOs of round shape FLNG when it is alone and interacting with KVLCC2 model were predicted using the proposed method, experimental method and ANSYS AQWA commercial code in this research. To study the effect of interaction between floating structures to the RAO of round shape FLNG, the RAO results estimated by proposed method and experimental tests are further studied here. The estimated RAOs of round shape FLNG when it is alone and interacting with KVLCC2 with the gap distance 0.3 to the breadth of FLNG, as well as when it is interacting with KVLCC2 with the gap distance 0.5 to the breadth of FLNG are shown in Figure 8.30 to Figure 8.35.

From Figure 8.30 to Figure 8.35, the RAO tendencies shown in the figures are plotted against the ratio of wavelength to length of the Round Shape FLNG, λ/D_{FLNG}. The figures are proposed to show the comparison of the RAOs of FLNG in different selected conditions. As mentioned, the conditions selected to study the RAOs of round shape FLNG are when the FLNG is alone and interacting with KVLCC2, where the second structure is arranged in the gap distance 0.5 to the breadth of FLNG and when the FLNG is interacting with KVLCC2, where the second structure is arranged in gap distance 0.3 to the breadth of FLNG. In all the selected conditions, both the floating structures are arranged in parallel arrangement and head sea condition.

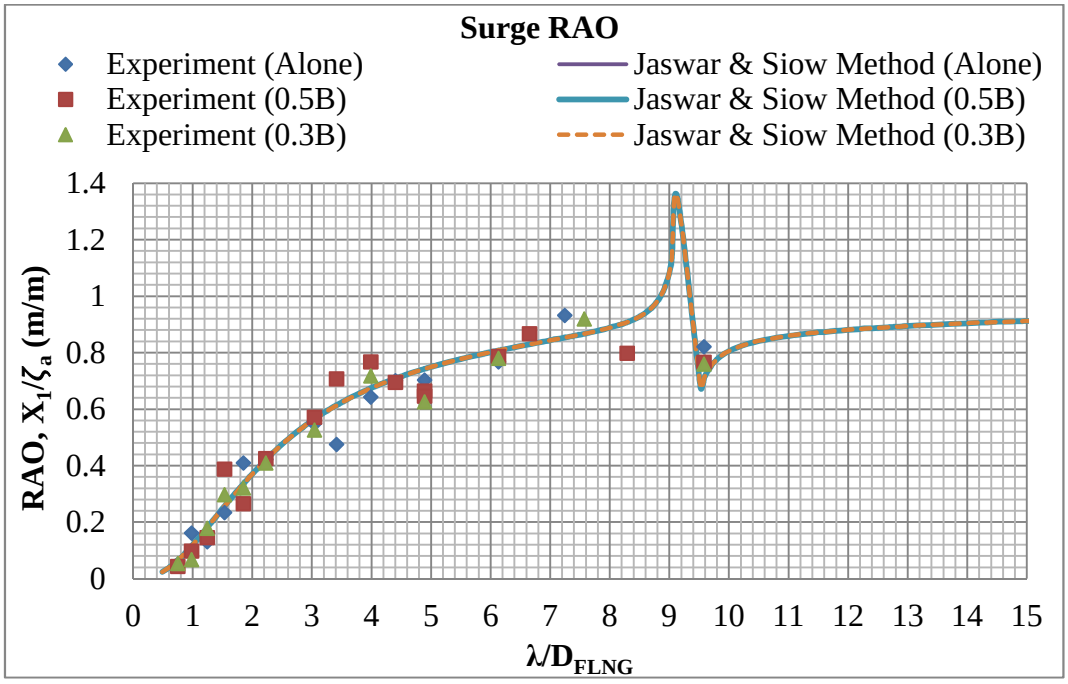

Figure 8.30: Comparison of round shape FLNG surge RAO when it alone with when interacting with another floating structure arranged in gap distance 0.5 to breadth of FLNG and in gap distance 0.3 to breadth of FLNG

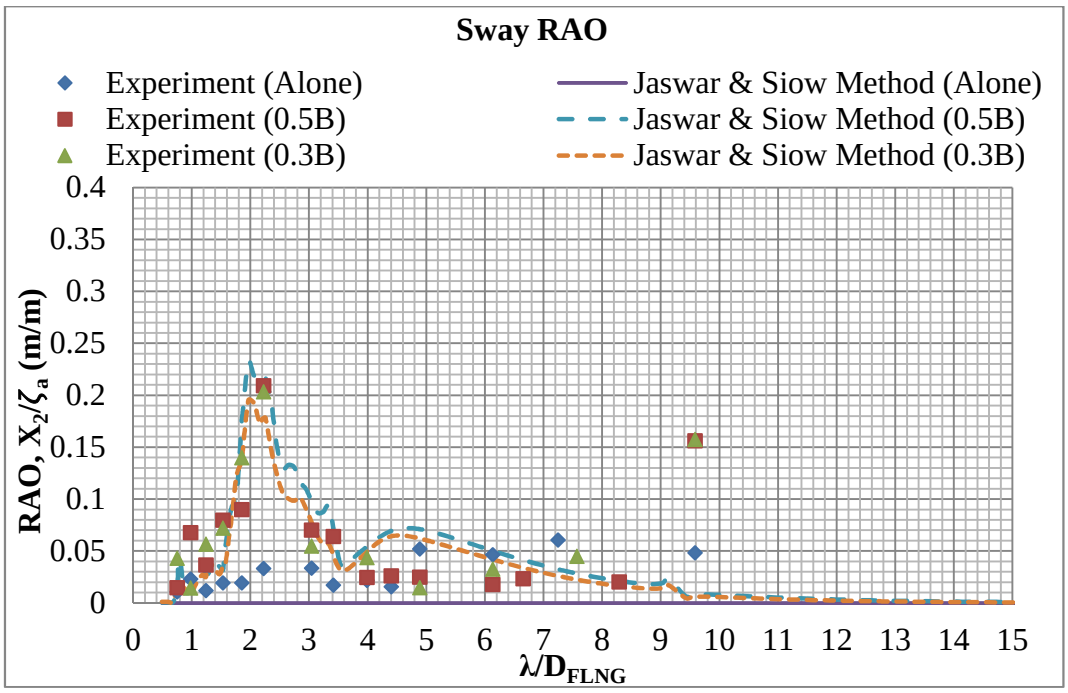

Figure 8.31: Comparison of round shape FLNG sway RAO when it alone with when interacting with another floating structure arranged in gap distance 0.5 to breadth of FLNG and in gap distance 0.3 to breadth of FLNG

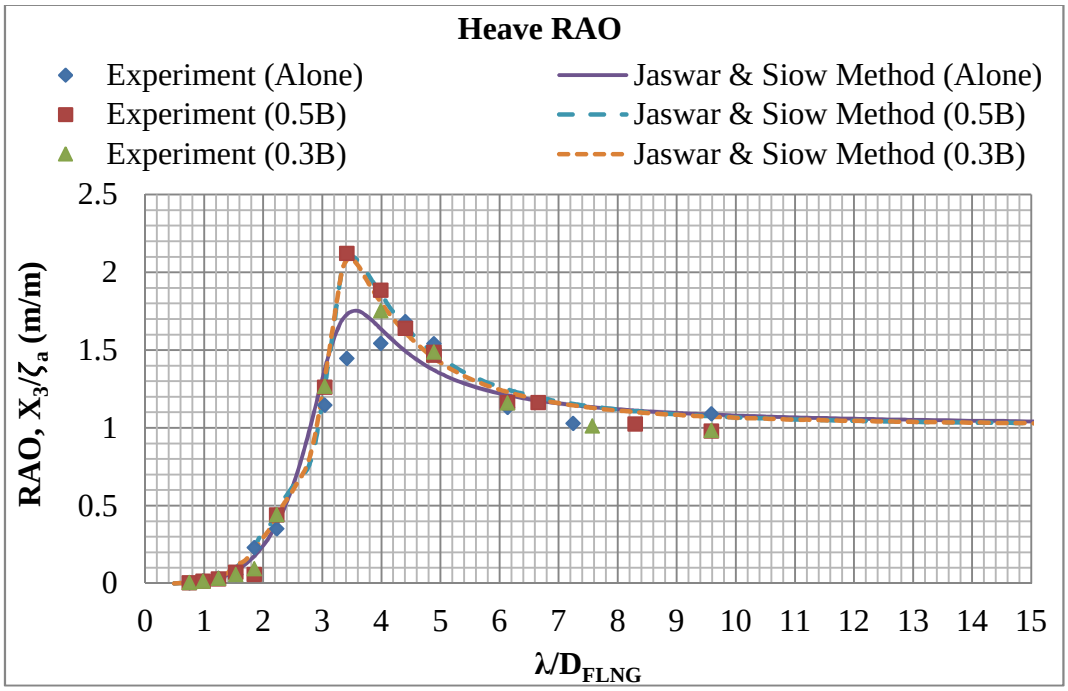

Figure 8.32: Comparison of round shape FLNG heave RAO when it alone with when interacting with another floating structure arranged in gap distance 0.5 to breadth of FLNG and in gap distance 0.3 to breadth of FLNG

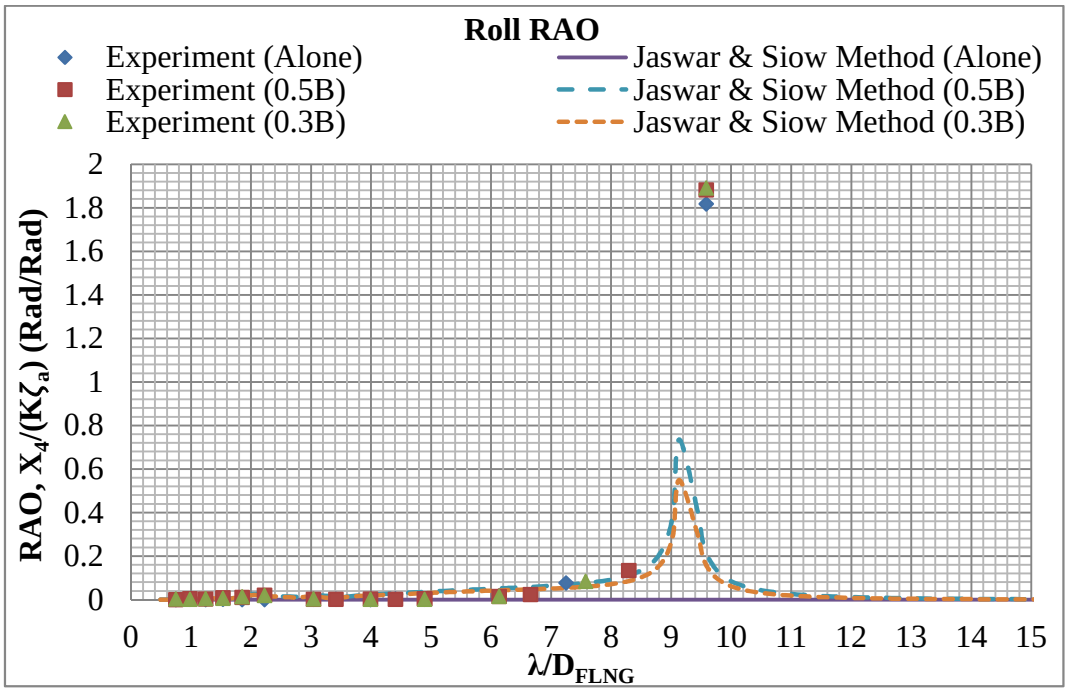

Figure 8.33: Comparison of round shape FLNG roll RAO when it alone with when interacting with another floating structure arranged in gap distance 0.5 to breadth of FLNG and in gap distance 0.3 to breadth of FLNG

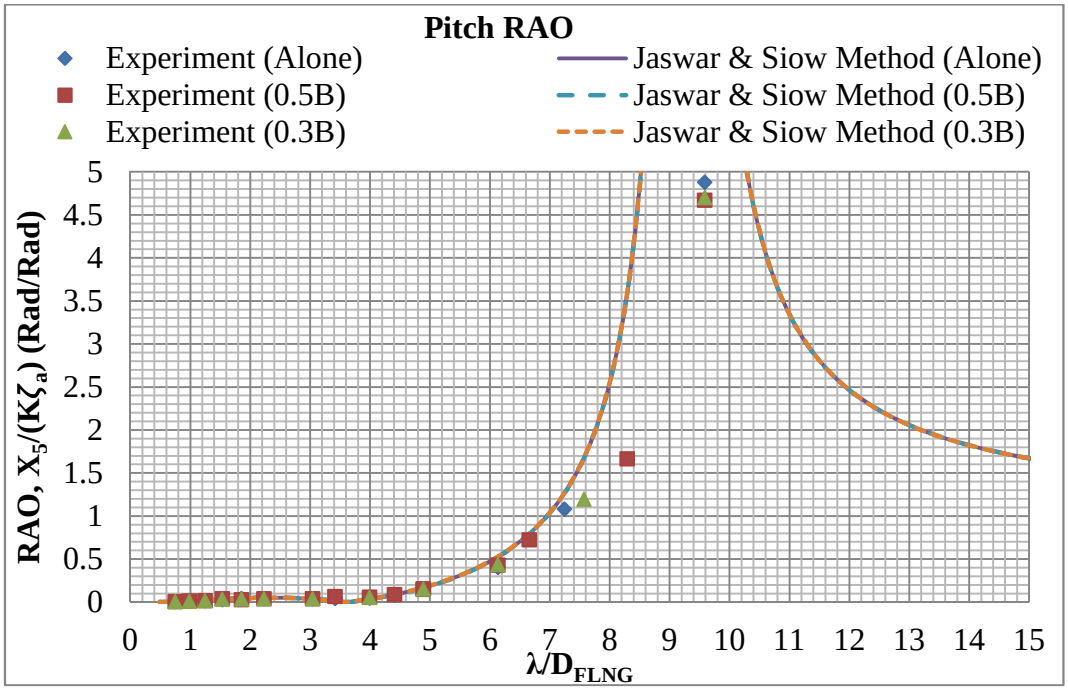

Figure 8.34: Comparison of round shape FLNG pitch RAO when it alone with when interacting with another floating structure arranged in gap distance 0.5 to breadth of FLNG and in gap distance 0.3 to breadth of FLNG

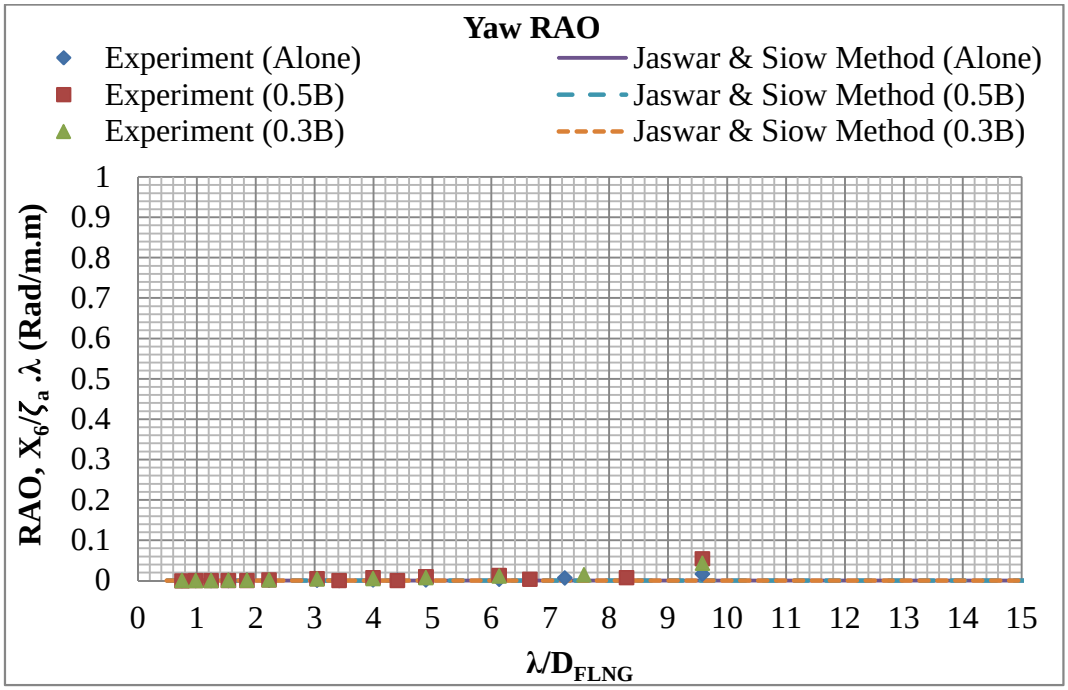

Figure 8.35: Comparison of round shape FLNG yaw RAO when it alone with when interacting with another floating structure arranged in gap distance 0.5 to breadth of FLNG and in gap distance 0.3 to breadth of FLNG

From Figure 8.30 to Figure 8.35, it is observed that the interaction between rounded-shape FLNG with KVLCC2 only gives very limited influence to the surge motion and pitch motion of the FLNG. In this research, the interaction studies are conducted to parallel head sea condition. Therefore, the generated wave due to the motion of nearby structure only propagates in sway direction. Since the interaction wave only propagate in sway direction in the parallel head sea arrangement, then the interaction wave generated by nearby structure does not influence the wave force to the surge and pitch direction. The surge motion and pitch motion for the round shape FLNG are induced by the incident wave. This finding is proved by both the experiment result and numerical result. The obtained results show that the surge RAO and pitch RAO when the FLNG is alone and when the FLNG is interacting with nearby structure in parallel head sea arrangement is similar.

From the Figure 8.30 and Figure 8.34, it can be observed that the surge RAO fluctuated at long wavelength due to the coupling effect with the pitch motion. From the decay test, the recorded pitch natural frequency is location at the wavelength λ/D_{FLNG} equal to 9.53. According to Clauss et al. (1992), most of the survival dominant wave period of a 100

year wave is happened in the range of 14 seconds to 17 seconds. In full scale, the pitch natural period is existed at 25.9 seconds. The predicted pitch natural period for this round shape FLNG is much exceeding the most of the survival dominant wave period of a 100 year wave observed by Clauss et al. (1992). The good dynamic stability of this FLNG is able to achieve by large pitch damping coefficient at shorter wavelength region. From the Figure 8.34, the pitch RAO for this FLNG is almost zero at shorter wavelength and the pitch motion start to increase after wavelength, λ/D_{FLNG} equal to 4.0. The corresponding wave period for the wavelength λ/D_{FLNG} equal to 4.0 is 17 seconds. From this finding, it is shows that the pitch RAO is start to increase after the most of the survival dominant wave period of a 100 year wave observed by Clauss et al. (1992). So, it can be summarized that this round shape FLNG is a very stable FLNG in it operating environment. Besides, this opinion also supported by Lamport and Josefsson (2008) where they found that the advantage of this round shape floating structure is it have better stability compare to ship shape floating structure in most of the survival dominant wave period of a 100 year wave.

On the other hand, the sway RAO and roll RAO of the round shape FLNG are showing strong interaction effect in the interaction cases. Especially in sway direction, the RAO of round shape FLNG achieved maximum response around 0.2 at the ratio λ/D_{FLNG}, which is equal to 2 in both the selected interaction cases. This observation is similar with the finding reported by Zhu et al. (2006) and the finding from research of Kagemoto and Yue (1987), where they also obtained that the interaction of floating structure in parallel head sea condition would lead to strong interaction effect in sway motion.

In comparison, the sway RAO is negligible as predicted by the proposed method and experimental result when the round shape FLNG is alone. This is because the wave force due to the incident wave contributes to inducing the sway motion in head sea condition, which does not exist. However, due to the existence of the KVLCC2 arranged nearby the round shape FLNG structure, the motion of the KVLCC2 will generate the wave by dissipating its motion energy to the fluid. After that, the generated wave by KVLCC2 motion is propagated to influence round shape FLNG, as well as induces the sway motion and roll motion of round shape FLNG. This opinion to explain the existence of sway and roll motion in round shape FLNG in interaction cases is similar with the comment from Hong, S.Y. et al. (2005) to their finding in their research.

Besides, comparison of the sway RAO of round shape FLNG when it is alone to the interaction cases, it is observed that the interaction of KVLCC2 to round shape FLNG is stronger in short wavelength condition compared to the long wavelength condition. This is because the interaction wave force is stronger in the shorter wavelength region. The peak sway RAO in the interaction cases is not happened in the sway natural frequency. The peak sway RAO interaction cases happened at λ/D_{FLNG} around 2 is because the sway exciting force due to the interaction wave maximum at this wavelength. The sway RAO of the round shape FLNG in both interaction cases reduced after the ratio of λ/D_{FLNG} equals to 4 and it was almost of no sway motion of round shape FLNG when the ratio of λ/D_{FLNG} equals to 10. The finding is similar with the outcome obtained from the previous research conducted by Kashiwagi et al. (2005). They studied the hydrodynamic interaction between floating structure using HOBEM method and their research showed that the hydrodynamic interaction forces are more dominant in the motion equation in the shorter wavelength region.

In the roll RAO shown in Figure 8.33, the roll motion of round shape FLNG does not exist when the FLNG is alone. In interaction cases, the roll motion is induced due to the influence of interaction wave generated by the motion of nearby structure. The peak motion response of roll motion of the FLNG is predicted to occur at the ratio λ/D_{FLNG}, which is equal to 9.2. The large roll RAO existed at the long wavelength region in both interaction cases because the roll damping is small at the long wavelength region. Hence, small interaction wave force act on the FLNG is able to induce the large roll motion to the floating structure.

Comparing the sway RAO and the roll RAO predicted by the proposed method and experiment result, it is observed that both the sway RAO and roll RAO is under estimation by the proposed method at the λ/D_{FLNG} around 9.5. The higher sway RAO and roll RAO predicted by the experiment result is due to the coupling effect between sway-roll direction with the surge-pitch direction. As mentioned in the previous part of this chapter, this phenomenon is well explained by Journee and Massie (2001). The coupling effect between surge-pitch and sway-roll direction is negligible for the symmetry floating structure such as the round shape FLNG. However, if the mooring line is used in the experiment, so the coupling effect between the surge-pitch direction and sway-roll direction can be existed via the mooring line. Since the proposed method calculate the wave frequency motion without consider the existing of the mooring line, so the coupling effect due to exist of the mooring

line is no able to estimate by the proposed method. Therefore, the sway RAO and roll RAO estimate by proposed method at the wavelength, λ/D_{FLNG} around 9.5 is under estimated.

The heave RAOs for the round shape FLNG are shown in Figure 8.32. Comparing the heave RAO estimated by the proposed method with the experimental test for the selected cases, it is observed that the influence of interaction between round shape FLNG with KVLCC2, which is stronger in the damping dominant region of the heave motion for this FLNG structure. Strong interaction effect is observed in the damping dominant region of heave motion because the heave motion is very sensitive to the change of heave exciting force when the damping is low. The heave motion is easy to amplify by the wave exciting force when the heave damping coefficient is low. Therefore, the heave RAO for both the interaction cases is much higher compared to the heave RAO for the case, where round shape FLNG is alone at the damping dominant region.

To estimate the heave RAO of the round shape FLNG, the damping coefficient for heave motion is required to be predicted accurately. The potential theory typically under-predicted the damping coefficient since the theory ignored the viscous effect in the calculation. Over-predicting of RAO of the floating structures by diffraction potential theory in resonance region by using the potential theory without considering the viscous effect was reported by Loken (1981) and Lu et al. (2011). In this research, the heave RAO predicted by the proposed method was developed from the diffraction potential theory and drag equation. The proposed method involves the diffraction effect and viscous effect in calculating the heave RAO of round shape FLNG. The predicted maximum heave RAO of round shape FLNG by proposed method is close to the experimental result, where the estimated heave RAO of round shape FLNG in both interaction cases is around 2.1, but the maximum heave RAO of the FLNG when it alone and estimated by proposed method is around 1.75. The increase of heave RAO of round shape FLNG is due to the extra interaction wave force transferred to the round shape FLNG through the interaction wave generated by the motion of LNG shuttle tanker.

Besides, it is observed that the peak RAO for the heave motion estimate by experiment test was shifted to the shorted wavelength in the interaction cases. The heave natural frequency is located at the λ/D_{FLNG} equals to 3.40. From the comparison, the peak heave RAO for the interaction cases is happened closer to the heave natural period compare to the peak heave RAO for the case when the FLNG is alone. There are two possible reason can

cause the peak heave RAO to shift to different wavelength. First, in interaction cases, the interaction effect is much stronger in shorter wavelength region and this finding is well study by Kashiwagi et al. (2005). So the wave exciting force due to interaction effect in the shorter wavelength is much stronger and the interaction effect will reduce by increase of wavelength. Due to the larger heave exciting force obtain in shorter wavelength, then the peak heave RAO is possible to shift to the shorter wavelength in interaction cases.

On the other hand, the effect of the wave amplitude use in motion experiment to estimated RAO of the floating structure has been studied by Liu and Papanikolaou (2012). From their research, they found that the different wave amplitude used in the experiment test can cause the peak heave RAO and peak pitch RAO to shift slightly to other wave period. The reason for this shifting may due to the change of the added mass of the motion in different wave amplitude. They commented that the shifting of the peak heave RAO happened at different wavelength due to the different wave amplitude is difficult to detect by the numerical method they apply in the research. For this study, the wave amplitude is typically higher in the interaction cases compare to the case where the FLNG is alone due to the interaction effect. This is because total wave amplitude in the interaction cases is the summation of the wave amplitude due to the incident wave and the interaction wave generate by the motion of floating structure. Since the total wave amplitude to induce the motion in interaction cases and FLNG alone case is slightly difference, so the little shifting of the peak heave RAO is observed from the experiment test.

The yaw RAO is shown in Figure 8.35. The similar tendency of yaw RAO is predicted by proposed method and experimental test. It is observed that the yaw motion of the round shape FLNG does not exist in the cases, where the FLNG is alone and interacting with another floating structure. This is because the round shape FLNG is a cylindrical structure and the wave propagates from any direction, which is not able to induce the yaw moment to move the round shape FLNG in a yaw direction. This opinion is also explained by the Figure 8.23, where the Figure 8.23 shows that the yaw moment is no existed in any wavelength for both the interaction cases and FLNG alone case.

In general, the existence of the KVLCC2 structure arranged nearby the round shape FLNG would induce the sway motion and roll motion to the FLNG. However, the interaction effect gives more significant influence to the sway motion in shorter wavelength region. The heave RAO of the round shape FLNG at damping dominant region is increased when it

interacts with KVLCC2 tanker. By shifting the KVLCC2 tanker to the gap distance closer to the FLNG, the RAO of the round shape FLNG in all six directions has not changed much. In this study, the measurements of gap distance of both floating structures are 0.5 to the breadth of FLNG and 0.3 to the breadth of FLNG. If the gap distance of round shape FLNG is reduced 40% from the distance of 0.5 to the breadth of FLNG to 0.3 to the breadth of FLNG, both the experiment result and the result from proposed method only show a little bit of change on the RAO on both the interaction cases. This means that the interaction of the round shape FLNG with the KVLCC2 tanker in parallel arrangement is not very strong. The effect of interacting with KVLCC2 tanker only influences the RAO of FLNG in sway and roll motion, as well as the heave motion at damping dominant region.

8.4. Summary

In this chapter, the discussions are focused on the comparing the tendencies of round shape FLNG's RAO predicted by the proposed method with the RAO tendencies estimated by experimental test and ANSYS AQWA. From the comparison in this chapter, it is obtained that the proposed method able to estimate the RAO of round shape FLNG with good accuracy in both single FLNG case and selected interaction cases. The estimated RAO results in this chapter shown that involved the viscous effect in the calculation as suggested in proposed method able to reduce the amount of over-prediction in round shape FLNG's heave RAO. The predicted heave RAO by involved viscous effect is closer to experiment result. Finally, this chapter also discuss the effect of interaction to the RAO of round shape FLNG and the experiment test to validate the proposed method. In next chapter, the conclusion of this research is draw based on this result and discussion highlighted in this chapter.

,

Chapter 9

9.0. Gap Distance of Semi-Submersible – TLP in Tandem Arrangement

9.1. Concept of Gap Distance

The number of offshore exploration activity in deep water area is increasing now day due to reduce of natural source in land or near shore area. In deep water area, floating structures are only alternative to apply for the oil and gas exploration process. However, the motion of floating structure is easily influence by wave and this arise a safety issue especially in multiple floating structure system. During LNG offloading process, the FPSO and ship is required to arrange in small distance to ensure the effectiveness of the offloading process. Hence, the study of the gap distance in multiple floating structures becomes important to ascertain the safety of the structures arrangement and avoid of accident to occur.

Response of structures to environment at open water is an important criterion required to evaluate to ensure the system operates safely. The comparison between single floating structures with multiple structures made by Siow et al (2013) showed that the hydrodynamic interaction effect may cause the floating structures to experience larger motion amplitude in all six types of motion. This phenomenon can cause accidents on floating structures such as crash between structures. Therefore, multi structures operation should give more attention during design and it requires more accurate analysis of hydrodynamic interactions between closely moored structures [Hong, S. Y, 2005].

To avoid collision occur in multiple floating structures system, the proper arrangement of the floating structures is required. One of the factors must evaluate in structures arrangement is the distance between floating structures. The ocean wave is one of the energy sources to generate the motion of floating structures. The gap distance between floating

structures is changed depend on the motion of both floating structures from time to time. This causes the study of the influence of structures motion to reduce of the distance between structures respect to the original distance become significant important to avoid accident occur.

To understand changing distance between floating structures due to the motion induced by wave, Siow et al (2013) studied theoretical concept on the effect of structure motions to the reduce of gap distance between floating structure and conduced an experimental study. In this research, the analysis of influence of wave to the minimum distance between structures is focused. The mentioned minimum gap distance means minimum distance between two floating structures achieved due to surge motions induced by wave. To study this, the semi-submersible and TLP models are selected and arranged in tandem arrangement. The model experimental is conducted from wavelength around 2 meters to 9 meters. The analysis is made to obtain the relationship between minimum gap distance between both the selected structures to the effect of structures' motion response and wave condition.

9.2. Literature Review

Matos et.al commented that the vertical plane motions induced by heave, roll and pitch should be kept adequately low to guarantee the safety of the floating structure, risers and umbilical pipes and other important facilities use in oil production [Matos, 2011]. The operability and safety of floating bodies operation are greatly determined by the relative motions between them. So, the accurate motion prediction of two bodies included all the hydrodynamic interaction is greatly important [Koo, 2005].

Motions of floating structures can be analysed by applying strip theory and potential theory. A number of notable studies were carried out to study hydrodynamic interaction phenomena such as [Ohkusu, 1974] and [Kodan, 1984].

Hess and Smith (1965), Van Oortmerssen (1979) and Loken (1981) studied on non-lifting potential flow calculation about arbitrary 3D objects. They utilized a source density distribution along the structure surface and solved for distribution necessary to lake the normal component of the fluid velocity zero on the boundary. Also, Wu etal (1997) studied the motion of a moored semi-submersible in regular waves numerically and experimentally. In their mathematical formulation, the moored semi-submersible was modeled as an

externally constrained floating body in waves, and derived the linearized equation of motion [Wu, 1997].

Yilmaz and Incecik (1996) analysed the excessive motion of moored semi-submersible. They developed two different time domain techniques due to mooring stiffness, viscous drag forces and damping; the mathematic models are strong nonlinearities in the system. In the first technique, first-order wave forces acting on a structure which considered as a solitary excitation force and evaluated by using the Morison equation. In the second technique, mean drift forces were used to calculate slow varying wave forces and simulate slow varying and steady motions [Yilmaz, 1996]. Söylemez (1995) has developed a technique to predict damaged semi-submersible motion under wind, current and wave. An approaching equation of motion based on Newton's second law was used in the research to develop a nonlinear numerical technique for both intact and damaged condition in time domain.

Besides, the hydrodynamic interaction effect was studied by Kashiwagi (2010). He introduced a hierarchical interaction theory in the framework of linear potential theory used to study hydrodynamic interactions between a large numbers of columns supporting flexible structure. He also furthers the research to investigate wave drift force and moment on two side by side arranged ships by using Higher-Order Boundary Element Method (HOBEM). His research obtained that the hydrodynamic interaction force is more predominant in the motion equation in the shorter wavelength region due to resonant phenomena. Kashiwagi was also concluded that the intensity of the interaction force is dependent upon the ratio of the wavelength to the separation distance between two adjacent cylinders. After that, Kashiwagi was also investigated the applicability of wave interaction theory apply to simulate the small gap length condition. The study obtained that the wave interaction theory able to predict the motion accurately if the separation between the structures is satisfied with the addition theorem of Bessel functions.

Besides, Choi and Hong (2002) were also applied HOBEM to analysis hydrodynamic interactions of multi-body system. Clauss et al. analyzed the sea-keeping behavior of a semi-submersible in rough waves in the North Sea by numerical and experimental method. They used panel method TiMIT (Time-domain investigations, developed at the Massachusetts Institute of Technology, 2002) for wave-structure interactions in time domain. The theory behind TiMIT is strictly linear and thus applicable to moderate sea condition only.

On the other hand, Spyros (2004) was also purposed a design oriented semi-analytical

method to solve the radiation problem and evaluate the hydrodynamic and interaction coefficients. An analytical solution to solve hydrodynamic diffraction problem of arrays of elliptical cylinders were also introduced by Ioannis and Spyros (2011). In the research, he obtained that the variation of hydrodynamic loading on the interaction cases is in relative to the wave heading angle. Besides, the effect of structures numbers affects to hydrodynamic interaction was also covered by Tajali et al (2011). Their research results indicated that by increase the number of pontoons can cause the peak frequency and peak amplitude for all motion increase.

A numerical method also employed by Zhu et.al (2008) to study the effect of gap in multiple box shape structures system. In that study, the potential for incident wave and scattering wave were ignored, the motion of the structures is assumed only affected by radiated wave. The gap distance was ranged from 1% of breadth to 50% of breadth. The simulation showed that the hydrodynamic interaction between floating structures can caused by the surge, sway and heave motion; however, only sway motion shows a strong interaction at certain resonance wave number. And then, Zhu et al (2008) also conducted a research on hydrodynamic resonance phenomena of three dimensional multiple floating structures by applying linear potential theory in time domain. The gap was limited to 1% compared to the breadth. The research found that peak force response on floating bodies at resonance frequency is same between frequency domain technique and time domain technique. This proved that the time domain technique can be an alternative to investigate hydrodynamic interaction phenomena between floating bodies in small gap.

Zhao et.al (2012) was carried out a study of hydrodynamic interaction between FLNG vessel and LNG carrier which arranged in side by side arrangement. They were observed that the hydrodynamic interactions give more influence to the surge, sway and yaw motions. In addition, they also discovered that the interaction between structures able to affect the load on the structures connection systems.

In addition, few experimental tests were carried out to obtain the motion response of structures. A model test related to interaction between semi-submersible and TLP was carried out by Hassan Abyn et al (2014). In continue Hassan Abyn et.al (2014) also tried to simulate the motion of semi-submersible by using HydroSTAR and then analyze the effect of meshing number to the accuracy of execution result and execution time. Besides that, K.U. Tiau et.al (2012) was simulating the motion of mobile floating harbor which have similar hull form as

semi-submersible by using Morison Equation. To investigate the interaction effect to structures motions, C. L. Siow et.al were made a comparison on the motion of semi-submersible when it alone to interaction condition by using experimental result.

To evaluate the effect of the motion to the change of distance between floating structures, the conceptual study was carried out by Siow et.al. This study obtained that the wavelength and the initial distance between floating structures are the main factors influence the minimum distance possible to achieve by the floating structure. The experimental study of minimum gap distance between floating structures also conducted by Siow et al. to propose an empirical equation which can use to define the minimum achievable distance between floating structures when the motion is induced by wave.

From the series of reviews, it obtain that a lot of effort was made by many researchers to study the hydrodynamic interaction phenomena. The literature review also shown that the previous research on this area are preferred to study on the effect of hydrodynamic interaction to wave forces acting of structures, change of hydrodynamic coefficient and structures motion in response to wave. To improve the safety of the multiple floating structures system which arranged in small gap distances, this research is proposed to evaluate the change of the gap distance due to the motion of floating structures which induced by wave.

9.3 Model Experimental

In this study, model experiment was conducted to study the minimum gap length of the floating structures arranged in small gap. The experiment was made at UTM's towing tank. The long, wide and deep for this towing tank are 120m, 4m and 2.5m. In addition, gravity wave can be generated by this tank has the range of wave period from 0.5 to 2.5 sec with maximum wave heights 0.44m. The experiments were conducted for the conditions where the semi-submersible arranged behind the TLP structure. The distance between both structures in model scale is 310 mm in this experiment tests.

9.3.1 Models particulars

In this experiment, the semi-submersible model was constructed based on GVA 4000 type model. Both the semi-submersible and TLP model were scaled down with ratio 1:70. Upon the model completely constructed, inclining test, swing frame test, oscillating test, decay test

and bifilar test were carried out to identify the hydrostatic particular for both the semi-submersible and TLP. Results collected from there tests were summarized as in table 1.

Table 9.1: Principal particular of Models

Character	TLP	Semi	Unit
Length	57.75	66.78	**m**
Width	57.75	58.45	**m**
Draft	21	16.73	**m**
Displacement	23941	14921	**m^3**
Water Plan Area	715	529.6	**m^2**
Number of Columns	4	4	
Pontoon length	31	66.78	**m**
Pontoon depth	7.28	6.3	**m**
Pontoon width	9.73	13.3	**m**
Pontoons centerline separation	-	45.15	**m**
Columns longitudinal spacing (centre)	-	45.58	**m**
Column diameter	-	10.59	**m**
GM_T	7.77	2.87	**m**
GM_L	7.63	4.06	**m**
K_{XX}	26.11	31.64	**m**
K_{YY}	26.46	26.95	**m**
K_{ZZ}	30.8	35	**m**
CG_Z	**-6.37**	**-0.28**	**m**

9.3.2. Motion tests

The floating structures were assumed to experience six degrees of freedom. The six DOF motions of the models were moored on springs and measured by optical tracking system (Qualisys Camera).

Water-proof load cells are attached to the springs at the model fairlead locations to measure applied tension force on the model from the mooring springs directly. The purpose of this setup is to avoid any losses in force. Lightweight ring gauge load cells used here are

sufficiently sensitive to provide a good signal for small mooring line tensions. The measured mooring line tensions are recorded by Dewetron Data Acquisition System (DAQ).

Due to the limitation of this tank, the tendons, risers and moorings are not actually presented in the model tests. Therefore, this model setup was expected had less damping and caused larger motion amplitude at model scale compared to the prototype.

Soft lateral springs were attached to the TLP and Semi-submersible to give horizontal restoring force to prototype TLP tendons and Semi-submersible moorings. One Side of the soft lateral spring was clamped to the mooring posts attached to the carriage and other side of the ends was connected to load cells at model side to measure the spring tension forces at the model. Anchor locations for the springs were proper selected to ensure mooring lines of the model make 45 degree angle with respect to the fairlead attachment points on the model. The spring pretension and spring stiffness applied in the test was same as horizontal stiffness required for the system to match the natural periods of the horizontal motion (surge, sway) for the TLP and Semi-submersible. Due to limitation of water deep, almost horizontal springs set considered for compensation of horizontal forces (Figure 1). Also, the TLP and Semi-submersible are connected between each other by two connectors to control the gap between the floating bodies (Figure 2).

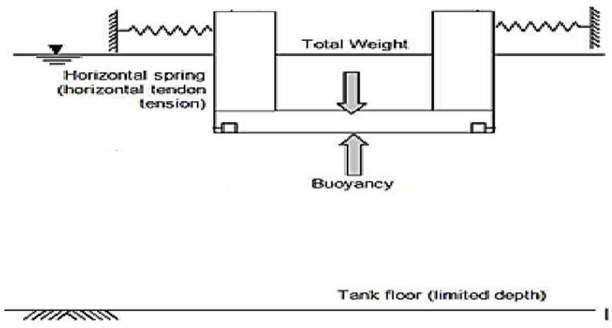

Figure 9.1: Model test set-up in available water depth

Hydrodynamic interaction between floating structures model test for TLP and Semi-submersible was set up as shown in figure 2. In the arrangement, progressive wave firstly attached TLP model before semi-submersible.

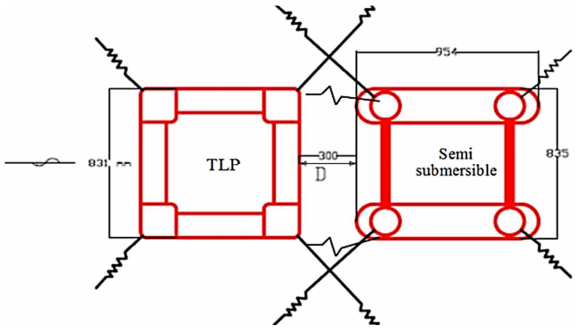

Figure 9.2: Layout TLP and semi-submersible model experimental set up (Dimension is in model scale).

Figure 9.3: TLP and Semi-Submersible set up into towing tank.

The models were attached to tow carriage by springs and regular waves generated by wave-maker at the end of towing tank (figure 3). At the start and end of these tests, the model was carefully held to prevent large offsets due to sudden wave exciting forces which could damage the mooring springs. The measurement starts to take when the wave height starts to become constant. In this model test, wave periods were carefully chosen to cover the models' natural period. The selected wave condition is shown in table 2.

Table 2: Input wave parameter for model test.

Wave Parameter	
No	**Variable**

	T(s)	λ (m)	H(1/20) (cm)	H(1/40) (cm)	H(1/60) (cm)
1	1.25	2.44	12.2		
2	1.46	3.33		8.3	
3	1.65	4.25		10.6	
4	1.85	5.34		13.3	
5	1.97	6.03		15.1	
6	2.15	7.14		17.8	
7	2.50	9.39			15.6

9.4. Theory of Gap Distance between Structures

The gap distance between floating structures is assumed effected by the relative motion between two floating structures. In this study, the gap distance between floating structures which arrange in tandem arrangement is studied. Only surge motion is influence the gap distance between floating structures in this study.

The figure 4 showed that two floating structures arranged in a separate distance, *l*. Hence, the same wave will arrive at the in front structure to induce the motion before it is proceeded to induce the motion at behind structures. Therefore, leading phase between two structures is existed due to the time required by the wave travel from one structure to another structure.

From the theoretical point of view, the leading phase between structures can be calculated if the separate distance between structures and the wavelength, λ is known. The equation to calculate the leading phase between structures as follow:

$$\alpha = \frac{l}{\lambda} \times 2\pi \qquad (9.1)$$

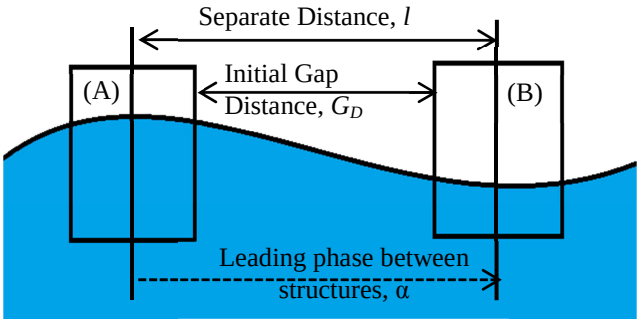

Figure 9.4: Progressive wave and Structure interaction.

The equation (1) shown that the leading phase between structures, α is in the ratio of structures separation distance, l to the wave length, λ.

Due to the arrangement of structure, it is obtained that wave arrived on structure (B) always leading by a phase, α respect to structure (A). Therefore, the motion on the structure (B) will always have a leading phase of α compare to structure (A). In this case, the surge motion of the floating structures can be represented as following equation.

$$X_A(t) = \bar{X}_A \sin(-wt + \beta_A) \qquad (9.2)$$

$$X_B(t) = \bar{X}_B \sin(\alpha - wt + \beta_B) \qquad (9.33)$$

Where $X_A(t)$ and $X_B(t)$ is the surge motion for structure (A) and structure (B), $\bar{X}_A$ and $\bar{X}_B$is the surge amplitude for structure (A) and structure (B), β_A and $\beta_B$is the leading phase between wave to structure motion for structure (A) and structure (B), α is the leading phase between structures, w is the wave speed in rad/seconds and t is the time in seconds.

Next, the change of gap distance between two floating structures can be calculated based on the relative motion of the floating structures. The gap distance between two floating structures, $G(t)$ in tandem arrangement can be calculated by considered the original gap distance, $G_{initial}$, surge motion of both structures. The simplified equation as follows,

$$G(t) = G_{initial} + [X_A(t) - X_B(t)] \qquad (9.4)$$

$$G(t) = G_{initial} + [\bar{X}_A \sin(-wt + \beta_A) - \bar{X}_B \sin(\alpha - wt + \beta_B)] \qquad (9.5)$$

From the equation (4), it is obtained that the individual surge motion of the floating structures will contribute to the change of gap distance between floating structures when the wave progress pass through the floating structures.

Based on the equation (5), it is obtained that the gap distance is changed according to time. The minimum gap distance in the specific wave condition will depend on the response of the structures' motion response, wavelength and original gap distance. The function of the minimum gap distance between two floating structures possible to achieve can be represented in following function.

$$G_{min} \propto f(M_{struc-1}, M_{struc-2}, \lambda, G_{initial}) \quad (9.6)$$

Where G_{min} is the nearest gap distance between two floating structure achieved due to surge motion, $M_{struc-1}$ and $M_{struc-2}$ is the surge motion of structures 1 and structures 2 and $G_{initial}$ is the initial structures distance before the wave arrive.

9.5. Experimental Data Analysis

The experiment in this research is interested to find the possible minimum gap distance between two floating structures when the motion is induced by wave. The Qualisys Camera is used in the experiment to record the time domain position coordinate of the floating structures in wave tank. The changing of distance between two floating structure in time domain was calculated by considering the changing of position in the tank for both the TLP and semi-submersible respective to its original position. The equation to calculate the distance between two floating structures, $G(t)$ in the function of time, t, initial gap length, $G_{initial}$ and the amount of gap, $G(t)$ decrease in time as follow:

$$G(t) = G_{initial} + G(t) \quad (9.7)$$

Where; the amount of gap $G(t)$ decrease in time is calculated as follows:

$$G(t) = M_{struc-1}(t) - M_{struc-2}(t) \quad (9.8)$$

Where; $M_{struc-1}(t)$ is the position of in front structure which is TLP and $M_{struc-2}(t)$ is the position of behind structure which is Semi-Submersible in this experiment. Zero position is located at the structures' individual initial position before advance by incident wave.

To obtain the minimum gap distance possible to achieve by the motion of both structures, the time domain gap distance data, $G(t)$ is converted to frequency domain, $G(F)$ to obtain the amplitude of the minimum gap length. The relationship between the minimum gap distance with the structures' motion and wave condition is defining using the experimental data which converted to frequency domain.

9.6. Model Experiment Result

The regular wave experiment was conducted in head sea condition and the floating structures arranged in tandem arrangement. From the data recorded, the gap distance between floating structures was calculated by equation (8).From the conceptual study, it is obtained that the minimum achieved gap distance between floating structures is in the function$G_{min} \propto f(M_{struc-1}, M_{struc-2}, \lambda, G_{initial})$. Due to the experiment is only conducted in same initial gap distance, hence only the relationship between minimum achieved gap length with structures motion and wavelength is focused and discussed here.

The figure 5 and 6 showed the distribution of amount of gap length reduced verses the structure motion and summation of structures motion. From both the figure, it is obtained that the gap length between floating structures is reduced in the linear relationship to the individual structure motion and the summation of structures motion. From both the figures, it is clearly obtained that the larger structures motion will lead to closer distance between floating structures. This observation shown that the better mooring systems which can reduce the structure horizontal motions and help to reduce the possibility of clashing between floating structures.

From the finding, it can be represented the relationship between amount of gap distance decrease compare to initial gap distance is in the linear function to the structures motion where

$$G_{Reduce} \propto (M_{struc-1} + M_{struc-2}) \qquad (9.9)$$

Since the structures motion in wave condition is often represent by the response amplitude operator, hence the above function can be written in the following format

$$G_{Reduce} \propto \left(RAO_{Surge_{struc}-1} + RAO_{Surge_{struc}-2}\right)\frac{W_H}{2} \qquad (9.10)$$

Also, the equation to link the amount of the gap distance can be reduced due to the structures motion can be written as an equation as follow

$$G_{Reduce} = C \cdot \left(RAO_{Surge_{struc}-1} + RAO_{Surge_{struc}-2}\right)\frac{W_H}{2} \qquad (11)$$

From the equation (11), the amount of gap reduced is assumed linearly to the structures motion. The constant C in the equation (11) is assumed involved the other variables which will affect the amount of gap length reduced due to structures motion. In the study, this constant C is defined from wavelength and structures arrangement.

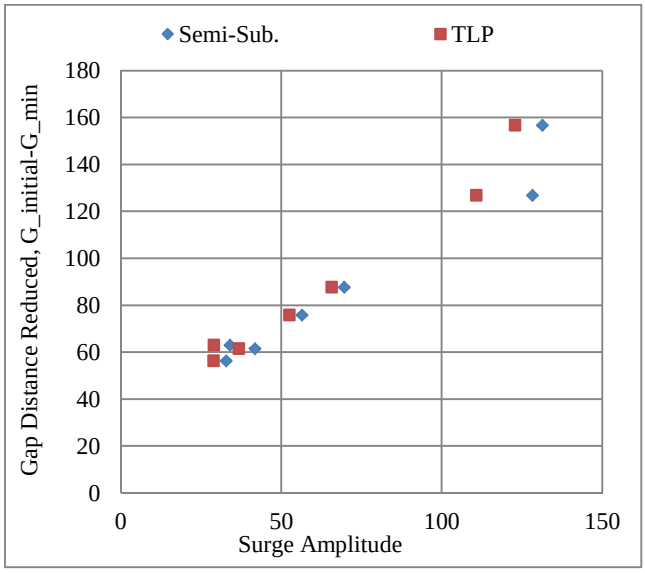

Figure 9.5: Comparison between surge amplitudes of TLP and Semi-submersible to the amount of gap length reduced respect to initial gap length.

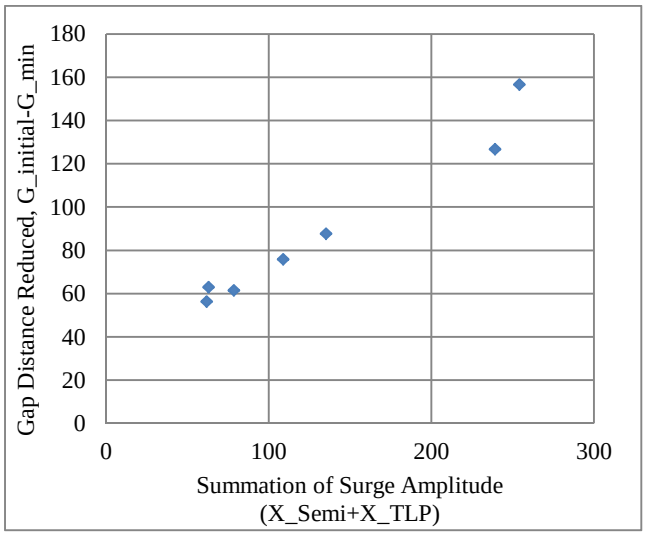

Figure 9.6: Comparison between amounts of gap distance reduced respect to initial gap distance to the summation of surge amplitude of TLP and Semi-submersible.

To study the effect of wavelength to the amount of gap distance can be reduced due to the structures motion, the figure 7 is plotted against wavelength in axis-x. The axis-y at figure 7 is equal to the amount of gap distance reduced divided by the total summation surge amplitude of both the semi-submersible and TLP.

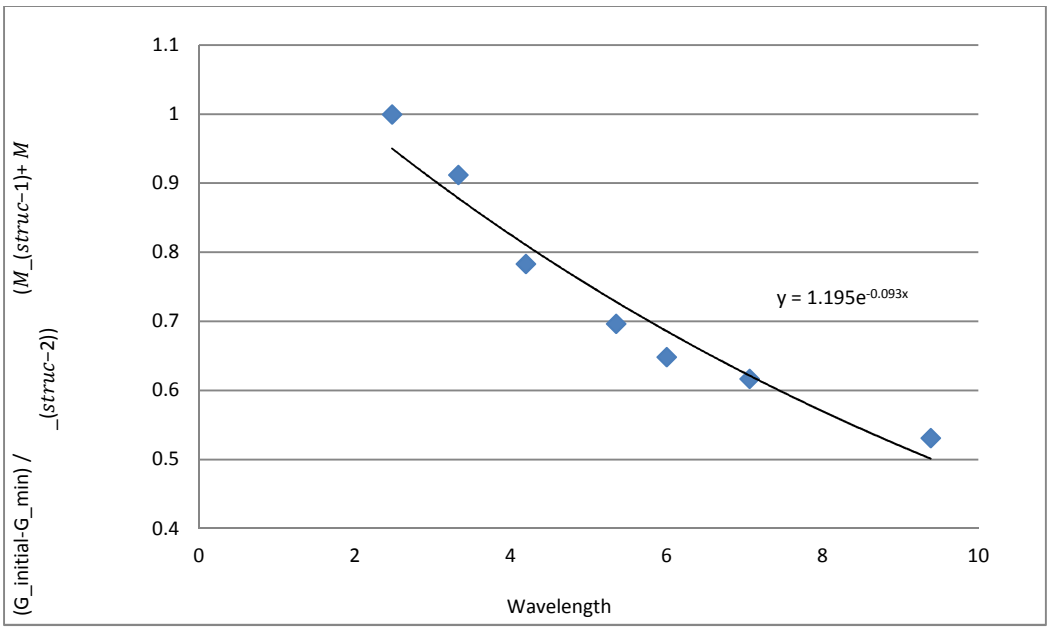

Figure 9.7: The tendency of ratio of amounts of gap distance reduced to wavelength.

From the figure 7, it is observed that the exponential curve is able to fix well with the experiment data. In this study, the equation to link both the axis-y and axis-x in figure 7 is

$$y = C_1 e^{C_2 x} \tag{9.12}$$

Where, y is $(G_{initial} - G_{min})/(M_{struc-1} + M_{struc-2})$, x is wavelength, λ and $C_1$and C_2 is the constant and in this arrangement and selected models the value is 1.195 and -0.093 respectively.

From the figure 7, it is showed that if the wavelength become longer, the amount of gap distance reduced due to the motions is lesser. This mean that the in very long wave condition, the reduction of gap distance between floating structures respectively to the initial gap distance become very less and the effect of gap reduced due to the motion of structure can be ignored.

To obtain the empirical equation which can be apply to predict the minimum gap distance between floating structures in wave induced condition, the equation (12) can be used and rearranged as follow:

$$y = C_1 e^{C_2 x} \tag{9.13}$$

$$\frac{G_{initial} - G_{min}}{M_{struc-1} + M_{struc-2}} = C_1 e^{C_2 \lambda} \tag{9.14}$$

$$G_{min} = G_{initial} - (M_{struc-1} + M_{struc-2}) * C_1 e^{C_2 \lambda} \tag{9.15}$$

Also, from equation (11), we can rewrite the equation to include the structure response amplitude operator as follow

$$G_{min} = G_{initial} - \left(RAO_{Surge_{struc-1}} + RAO_{Surge_{struc-2}}\right)\frac{W_H}{2} * C_1 e^{C_2 \lambda} \tag{9.16}$$

9.7. Discussion and Analysis

From the Figure 8, the empirical equation showed well agreed with experiment's result. The comparison in Table 3 shown the percentage of difference between the result obtained by empirical equation and experiment is relatively small. The trend of change for the minimum gap to wavelength between both methods is similar as shown in the figure 8. The minimum observed gap length in this study is occurring at wavelength around 7.07meters. This is because both the floating structures experienced the largest surge motion in this wavelength.

In the comparison between experimental result and the empirical equation, it is observed that the introduced empirical equation (equation 9.16) can be fixed will with the experimental result directly measured from experiment. Based on the Table 3, the largest different between these two results is around 4.11%. This shown that the introduced empirical equation is fixed with the experimental result for this selected experiment model. However, to ensure the accuracy of the calculated result from the empirical equation, the RAO of the structures must be executed correctly. This is because the empirical equation is very sensitive with the RAO of both the structures.

The weakness in this empirical equation is the effect of the arrangement or initial distance between floating structures is no take into the consideration. This is because the experiment is only conducted for same initial gap distance. It is predicted that if the initial gap distance is changed, the constant, C_1 and C_2 in the equation (16) will change. Therefore, the accuracy of this empirical equation for other models is required to recheck.

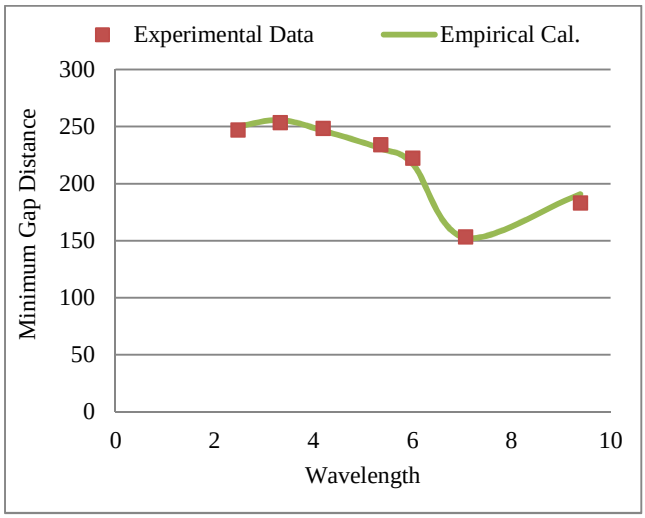

Figure 9.8: Predicted minimum gap distance between floating structures based on experimental data and empirical calculation.

In this study, the relationship between the amount gap distance reduced due to the structures motion and the wavelength is studied. From the experimental result, it can be observed the strong relationship is existed between the reduced gap distance with the structures motions and wavelength. To reduce the possibility of crash between structures, the structures horizontal plane motions should be properly control and analysis. Because the better control of structures motion is the initial step to avoid large change on the distance between floating structures.

Table 9.3: Comparison minimum gap distance predicted by empirical calculation to experimental data.

Wavelength, m	Percentage different between empirical and experimental result, %
2.48	1.27
3.33	0.85
4.20	0.83
5.35	1.41
6.00	2.20
7.07	0.46
9.39	4.11

References

1. Abyn, H., Maimun, A., Jaswar, Rafiqul Islam, M., Magee, A., Bodagi, B., Pauzi, M. (2012).Model Test of Hydrodynamic Interactions of Floating Structures in Regular Waves.Proc. of The 6th Asia-Pacific Workshop on Marine Hydrodynamics (APHydro2012).UTM, Malaysia.
2. Abyn, H., Maimun, A., Jaswar, Rafiqul Islam, M., Magee, A., Bodagi, B., Pauzi, M. (2012). Effect of Mesh Number on Accuracy of Semi-Submersible Motion Prediction.Proc. of the 6th Asia-Pacific Workshop on Marine Hydrodynamics (APHydro2012).UTM, Malaysia (2012).
3. Adibah Fatihah Mohd Yusof, Siow C.L, J.Koto, 2017, Effect of Turret Location on Hydrodynamic Motion of Ship-Shaped FPSO, Journal of Subsea and Offshore -science and engineering-, Vol.10(1), pp.9-20.
4. Adibah, C.L Siow, Jaswar Koto, 2017, Optimization of Turret Location for FPSO, The Fourth Conference, Ocean, Mechanical & Aerospace –scientists & engineers-, Universitas Andalas, Padang, Indonesia.
5. Afrizal, E., Mufti, F. M., Siow, C. L. and Jaswar (2013). Study of Fluid Flow Characteristic around Rounded-Shape FPSO Using RANS Method. The 8th International Conference on Numerical Analysis in Engineering. Pg. 46 – 56.
6. Ali, M. T., Rahaman, M. M., and Anan, T. (2010). A Numerical Study on Hydrodynamic Interaction for a Small 3-D Body Floating Freely Close to a Large 3-D Body in Wave. *Proceedings of The International Conference on Marine Technology*. 11-12 December. Dhaka, Bangladesh, 279-284.
7. ANSYS. (2012). AQWA User Manual.
8. Arslan, T., Pettersen, B., and Andersson, H. I. (2011). Calculation of the Flow around Two Interacting Ships. *The IV International Conference on Computational Methods in Marine Engineering*. 28-30 September 2011. Lisbon, Portugal, 254-265.
9. C.L Sow, Jaswar Koto and Hassan Abyn. (2014). Semi-Submersible Heave Response Study Using Diffraction Potential Theory with Viscous Damping Correction. Journal of Ocean, Mechanical and Aerospace Science and Engineering. Vol.5, 23-29.
10. Cengel, Y. A., and Cimbala, J. M. (2010). *Fluid Mechanics Fundamentals and Application.* (2 ed.). New York, America: McGraw-Hill.

11. Chakrabarti, S. (2000). Hydrodynamic interaction forces on multi-moduled structures. *Ocean Engineering*. 27 (10), 1037-1063.
12. Chakrabarti, S. K. (2001). Response due to moored multiple structure interaction. *Marine Structures*. 14 (1-2), 231-258.
13. Chapra, S. C., and Canale, R. P. (2010). *Numerical Method for Engineers.* (6^{th}-ed.). New York, US: McGraw Hill Higher Education.
14. Chatjigeorgiou, I. K. (2011). Three dimensional wave scattering by arrays of elliptical and circular cylinders. *Ocean Engineering*. 38 (13), 1480-1494.
15. Chatjigeorgiou, I. K., and Mavrakos, S. A. (2010). An analytical approach for the solution of the hydrodynamic diffraction by arrays of elliptical cylinders. *Applied Ocean Research*. 32 (2), 242-251.
16. Choi, Y. R., Hong, S. Y. (2002). An analysis of hydrodynamic interaction of floating multi-body using higher-order boundary element method.Proc. of 12th ISOPE.Kita-Kyushu.
17. Chung, J. S. (1994). Added Mass and Damping on an Oscillating Surface-Piercing Circular Column with a Circular Footing. *International Journal of Offshore and Polar Engineering*. 4 (1), 11-17.
18. Clauss, G. F., Schmittner, C., Stutz, K. (2002). Time-Domain Investigation of a Semi-Submersible in Rogue Waves. Proc. of the 21st International Conference on Offshore Mechanics and Arctic Engineering (OMAE2002).
19. Clauss, G., Lehmann, E. and Östergaard, C. (1992). Offshore Structures: Volume I: Conceptual Design and Hydromechanics. London, United Kingdom: Springer-Verlag.
20. Clauss, G., Stempinski, F., Dudek, M., and Klein, M. (2009). Water depth influence on wave–structure-interaction. *Ocean Engineering*. 36 (17-18), 1396-1403.
21. Cozijn, J. L., and Bunnik, T. H. J. (2004). Coupled Mooring Analysis for a Deep Water Calm Buoy. *23^{rd} International Conference on Offshore Mechanics and Arctic Engineering*. 20-25 June. Vancouver, Canada, 1-11.
22. Dercksen, A., and Winchers, J. E. W. (1992). A Discrete Element Method on a Chain Turret Tanker Exposed to Survival Condition. *6^{th} International Conference on Behaviour of Offshore Structures: BOSS '92*. 7-10 July. London, UK, 1-13.
23. Det Norske Veritas, DNV (2011). DNV-RP-H103. Oslo, Norway: Det Norske Veritas.
24. Drilling Info, Oil and Gas Offshore Rigs: a Primer on Offshore Drilling, http://info.drillinginfo.com/offshore-rigs-primer-offshore-drilling/

25. Faltinsen, O. M. (1999). Sea Loads on Ships and Offshore Structures. Cambridge, United Kingdom: Cambridge University Press.
26. Fang, M. C., and Chen, G. R. (2001). The Relative Motion and Wave Elevation between Two Floating Structures in Waves. *Proceedings of the Eleventh International Offshore and Polar Engineering Conference*. 17−22 June. Stavanger, Norway, 361-368.
27. Farid, M. (2014). *Motion of Three Offshore Structures Due to the Effect of Hydrodynamic Interaction*. Bachelor of Engineering Thesis. Universiti Teknologi Malaysia, Skudai, Johor, Malaysia.
28. Feng, Q. (2009). Contact dynamics of two floating cable-connected bodies. *Ocean Engineering*. 36 (9–10), 681-690.
29. Fikri, M., Jaswar, Mufti, F.M, Agustin, Maimun, A., Sanusi and Siow, C. L. (2012). Study on Stability of Floating Liquefied Natural Gas (LNG). Proceedings of the 6th Asia Pacific Workshop on Marine Hydrodynamics. Pg. 364-369.
30. Finnegan, W., and Goggins, J. (2012). Numerical simulation of linear water waves and wave–structure interaction. *Ocean Engineering*. 43 (0), 23-31.
31. Fitzgerald, J., and Bergdahl, L. (2007). Including Mooring in the Assessment of a Generic Offshore Wave Energy Converter: A Frequency Domain Approach. *Marine Structures.* 21 (1), 23-46.
32. Frigaard, P., Høgedal, M., and Christensen, M. (1993). *Wave Generation Theory*. Aalborg: Hydraulics & Coastal Engineering Laboratory, Department of Civil Engineering, Aalborg University.
33. Harnois V., Weller, S. D., Johanning, L., Thies, P. R., Marc, L. B., Dominique, L. R., Veronique, S., and Jeremy, O. (2015). Numerical model validation for mooring systems: Method and application for wave energy converters. *Renewable Energy*. 75, 869-887.
34. Hassan Abyn, Adi Maimun, Jaswar, M. Rafiqul Islam, Allan Magee, Behnam Bodaghi, Mohamad Pauzi, Siow; C. L. and M. Mobassher Tofa (2014). Hydrodynamic interaction of floating structure in regular waves. Jurnal Teknologi (Sciences and Engineering). 66(2), 91-96.
35. Hassan Abyn, Adi Maimun, M. Rafiqul Islam, Allan Magee, Jaswar, Behnam Bodaghi, Mohamad Pauzi and Siow, C. L. (2014). Effect of mesh number on accuracy of semi-submersible motion prediction. Jurnal Teknologi (Sciences and Engineering). 66(2), 67-72. Abyn, H., Maimun. A., Jaswar, M. Rafiqul Islam, Siow, C. L. and Behnam Bodaghi

(2014). TLP motion effect on semi-submersible motion. Proceedings of the Annual Offshore Technology Conference. 538-548.

36. Heavens, O. S., and Ditchburn, R. W. (1991). *Insight into Optics*. Chichester: Wiley & Sons.
37. Herbich, J. B., Ansari, K. A., Chakrabarti, S. K., Demirbilek, Z., Fenton, J. D., Isobe, M., Kim, M. H., Panchang, V. G., Randall, R. E., Triantafyllou, M. S., Webster, W. C. and Xu, B (1999). In Developments in Offshore Engineering. Houston, America: Gulf Professional Publishing.
38. Hess, J. L., Smith, A. M. O. (1964). Calculation of Nonlifting Potential Flow about Arbitrary 3D Bodies. Journal of Ship Research.
39. Heurtier, J. M. (2001). Coupled Dynamic Response of Moored FPSO with Risers. *Proceedings of the Eleventh International Offshore and Polar Engineering Conference*. 17-22 June. Stavanger, Norway, 319 - 326.
40. Hong, S. Y., Kim, J. H., Cho, S. K., Choi, Y. R., Kim, Y. S. (2005). Numerical and experimental study on hydrodynamic interaction of side-by-side moored multiple vessels. Ocean Engineering, 32(7), 783-801.
41. Inoue, Y., and Ali, M. T. (2003). A Numerical Investigation on the Behaviour of Multiple Floating Bodies of Arbitrary Arrangements in Regular Waves. *Proceedings of The Thirteenth (2003) International Offshore and Polar Engineering Conference*. 25-30 May. Honolulu, Hawaii, USA, 558-562.
42. International Towing Tank Conference, ITTC (2002). 7.5-02, 07-02.1. Kgs. Lyngby, Denmark: International Towing Tank Conference.
43. Ioannis, K. C. (2011). Three dimensional wave scattering by arrays of elliptical and circular cylinders.Ocean Engineering, Vol. 38(13), pp. 1480-1494.
44. J. Koto, Moh Hafidz Efendy, Amirrudin Bin Yaacob, Construction -Ship and Offshore Structure-, Ocean & Aerospace Research Institute, Indonesia.
45. Jaswar and Siow, C. L. (2013). Concept of Gap Distance in Motion Interaction between Multiple Floating Bodies. Journal of Ocean, Mechanical and Aerospace -Science and Engineering-, 2,13-19.
46. Jaswar, Amin, A., Agustin, Maimun, A., Munirah, Mufti, F.M., Jonathan and Siow, C. L. (2012). Study on Powering of Podded Propulsion VLCC. Proceedings of the 6th Asia Pacific Workshop on Marine Hydrodynamics. Pg. 499-504.

47. Jaswar, Hashim, M. H., Abd. Khair Junaidi and Siow, C. L. (2013). Axial Force of Offshore Pipeline. The International Conference on Marine Safety and Environment. 12-November- 2013. Johor Bahru, Malaysia.
48. Jaswar, Prayetno, E., Kader, A. S. A. and Siow, C. L. (2013). Wing-In-Ground for Rescue Operation in Kepulauan Riau. The International Conference on Marine Safety and Environment. 12-November-2013. Johor Bahru, Malaysia.
49. Jaswar, Rashid, H A., Abd Khair Junaidi and Siow, C. L. (2013). Expansion of Deep Water Subsea Pipeline. The International Conference on Marine Safety and Environment. 12- November-2013. Johor Bahru, Malaysia.
50. Jaswar, Razak, M. K. R. A. and Siow, C. L. (2013). Vortex-Induced Vibration of Riser. The International Conference on Marine Safety and Environment. 12-November-2013. Johor Bahru, Malaysia.
51. Jaswar, Sanusi, Siow, C. L. and Azaniza Wati (2013). Optimization of Rounded-Shape Floating LNG Supply Chain Efficiency with Simulation Modeling. The 12th International Conference on System Science and Simulation in Engineering. 23-April-2013. Morioka, Japan,26-33.
52. Jaswar, Siow, C. L. and Efi Afrizal (2013). Fluid Flow Characteristic around Round-Shaped FPSO. The 12th Asian International Conference on Fluid Machinery, 25-September-2013. Yogyakarta, Indonesia, 1-12.
53. Jaswar, Siow, C. L., Maimun, A. and Soares, C. G. (2014). Estimation of Electrical-Wave Power in Merang Shore, Terengganu, Malaysia. Jurnal Teknologi (Sciences & Engineering). 66(2), 9–14.
54. Jaswar, Tiau, K.U., Hassan Abyn and Siow, C.L. (2014). Stability of mobile floating harbor container crane. Jurnal Teknologi (Sciences and Engineering). 66(2), 133-139.
55. Journee, J. M. J and Massie, W. W. (2001). Offshore Hydromechanics. (1st ed.). Delf University of Technology.
56. Kagawa, Y., Tsuchiya, T., Fujioka, K., and Takeuchi, M. (1999). Discrete Huygens' Model Approach To Sound Wave Propagation—Reverberation In A Room, Sound Source Identification And Tomography In Time Reversal. *Journal of Sound and Vibration*. 225, 61-78.
57. Kagemoto, H., and Yue, K. P. (1987). Wave-Induced Motions of Multiple Floating Bodies. *Journal of The Society of Naval Architects of Japan*. 161, 152-158.

58. Kashiwagi M., Takagi, K., Yoshida, N., Murai, M., and Higo, Y (2003). Practical Floating Body Fluid Dynamic Study: Mathematic Calculation Method on Oscillation Motion Problem. Tokyo, Japan: Seizando-Shoten Publishing Co. Ltd. (柏木 正, 高木 建, 吉田 尚史, 村井 基彦, と 肥後 靖。(2003)。*実践浮体の流体力学前編-動揺問題の数値計算法*。東京都, 日本：成山堂書店)
59. Kashiwagi, M. (2000). Hydrodynamic Interactions Among A Great Number Of Columns Supporting A Very Large Flexible Structure. *Journal of Fluids and Structures*. 14 (7), 1013-1034.
60. Kashiwagi, M. (2008). 3-D Calculation for Multiple Floating Bodies in Proximity Using Wave Interaction Theory. *International Journal of Offshore and Polar Engineering*. 18 (1), 14–20.
61. Kashiwagi, M. and Q.-q.Shi. (2010). Pressure distribution computed by wave-interaction theory for adjacent multiple bodies. Journal of Hydrodynamics, Ser. B, 22(5, Supplement 1): p. 526-531.
62. Kashiwagi, M., and Shi, Q. Q. (2010). Pressure distribution computed by wave-interaction theory for adjacent multiple bodies. *Journal of Hydrodynamics, Ser. B.* **22** (5-1), 526-531.
63. Kashiwagi, M., Endo, K., and Yamaguchi, H. (2005). Wave drift forces and moments on two ships arranged side by side in waves. *Ocean Engineering*. 32 (5-6), 529-555.
64. Kim, M. S., and Ha, M. K. (2002). Prediction of Motion Responses between Two Offshore Floating Structures in Waves. *Journal of Ship and Ocean Technology*. 6 (3), 13- 25.
65. Kodan, N. (1984). The motions of adjacent floating structures in oblique waves. Proc. of Third Offshore Mechanics and Arctic Engineering OMAE, New Orleans.
66. Koo, B. J., and Kim, M.H. (2005). Hydrodynamic interactions and relative motions of two floating platforms with mooring lines in side-by-side offloading operation. *Applied Ocean Research*. 27 (6), 292-310.
67. Koto, J., Siow, C. L., Khairuddin, N. M., Afrizal, Abyn, H. and Soares, C. G. (2014). Comparison of floating structures motion prediction between diffraction, diffraction-viscous and diffraction-Morison methods. The 2nd International Conference on Maritime Technology and Engineering.
68. Kvittem, M. I., Bachynski, E. E. and Moan, T. (2012). Effect of Hydrodynamic modeling in Fully Coupled Simulations of a Semi-Submersible Wind Turbine. *Energy Procedia*. 24.

69. Lamport, W. B., and Josefsson, P. M. (2008). The Next Generation Of Round Fit-For-Purpose Hull Form FPSOS Offers Advantages Over Traditional Ship-Shaped Hull Forms. *2008 DeepGulf Conference*. 9-11 December. New Orleans, Louisiana, USA, 1-9.
70. Liu, S. and Papanikolaou, A. (2012). On Nonlinear Simulation Method and Tools for Evaluating the Performance of Ships and Offshore Structures in Wave. *Journal of Applied athematics*. 2012 (2012).
71. Loken, A. E. (1981). Hydrodynamic interaction between several floating bodies of arbitrary form in waves. *Proc. of Int'l Symposium on Hydrodynamics in Ocean Engineering*. 24-28 August. NIT, Trondheim, Vol. 2,745-779.
72. Lu, L., Teng, B., Sun, L., and Chen, B. (2011). Modelling of multi-bodies in close proximity under water waves—Fluid forces on floating bodies. *Ocean Engineering*. 38(13), 1403-1416.
73. Matos, V. L. F., Simos, A. N., and Sphaier, S. H. (2011). Second-order resonant heave, roll and pitch motions of a deep-draft semi-submersible: Theoretical and experimental results. Ocean Engineering. 38(17–18), 2227-2243.
74. Mavrakos, S. A. (2004). Hydrodynamic coefficients in heave of two concentric surface-piercing truncated circular cylinders. *Applied Ocean Research*. 26 (3-4), 84-97.
75. McIver, P. (2002). Wave interaction with arrays of structures. *Applied Ocean Research.* 24 (3), 121-126.
76. Menon, B and V ienneau, J. (1992). SHIPMO Seakeeping Predictions and Correlations. *The Twenty-Third American Towing Tank Conference*. 11-12 June. New Orleans, Louisiana, United States, 55-63.
77. Montasir, O. A., Yenduri, A., and Kurian, V. J. (2015). Effect of Mooring Line Configuration on the Dynamic Response of Truss Spar Platforms. *Ocean Engineering.* 96, 161-172.
78. Muhammad Farid Abdul Halim and Jaswar Koto (2014). Hydrodynamic Interaction of Three Floating Structures. Journal of Ocean, Mechanical and Aerospace Science and Engineering. Vol.8, 1-11.
79. Nallayarasu, S., and Prasad, P. S. (2012). Hydrodynamic response of spar and semi-submersible interlinked by a rigid yoke – Part I: regular waves. *Journal of Ships and Offshore Structure.* 7 (3), 297-309.
80. Newman, J. N. (1984). An expansion of the oscillatory source potential. *Applied Ocean Research.* 6 (2), 116-117.

81. Newman, J. N. (1986). Distributions of sources and normal dipoles over a quadrilateral panel. *Journal of Engineering Mathematics.* 20, 113 – 126.
82. Niedziela, J. (2008). *Bessel Functions and Their Applications.* University of Tennessee, Knoxville.
83. NMRI, 2016: Model Ship KVLCC2M retrieved March, 2, 2016 from https://www.nmri.go.jp/institutes/fluid_performance_evaluation/cfd_rd/cfdws05/gothenburg2000/KVLCC/kvlcc_g&c.htm.
84. Noblesse, F. (1982). The Green function in the theory of radiation and diffraction of regular water waves by a body. *Journal of Engineering Mathematics*. 16 (2), 137-169.
85. Offshore Technology, The Price of Nigerian Oil http://www.offshore-technology.com/features/feature1975/feature1975-2.html
86. Ohkusu, M. (1974). Hydrodynamic Force on Multiple Cylinders in Waves. *International Symposium on the Dynamics of Marine Vehicles and Structures in Waves.* 1-5 April. London, UK, 107-112.
87. Ohkusu, M. (1998). Validation of Theoretical Methods for Ship Motions by Means of Experiment. *Twenty-Second Symposium on Naval Hydrodynamics*. 9-14 August. Washington, D.C., USA, 341-358.
88. Ohkusu, M., (1974). Ship motions in vicinity of a structure. Proc. of International Conference on Behavior of Offshore Structure.NIT, Trondheim.
89. Perwitasari, R. N. (2010). *Hydrodynamic Interaction and Mooring Analysis for Offloading between FPSO and LNG Shuttle Tanker*. Master of Engineering Thesis. Norwegian University of Sciences and Technologi, Norway.
90. Renato, S. T. d. C., Lenzi, A., and Cordioli, J. A. (2015). Time domain representation of frequency-dependent surface impedance using finite impulse response filters in discrete Huygens' modeling. *Applied Acoustics.* 96, 180-190,
91. Sannasiraj, S. A., Sundaravadivelu, R., and Sundar, V. (2001). Diffraction–radiation of multiple floating structures in directional waves. *Ocean Engineering*. 28 (2), 201-234.
92. Saven Marine, 2016a: Piranema Spirit retrieved March, 2, 2016 from http://www.sevanmarine.com/projects/floating-production?id=14:piranema-spirit&catid=41.
93. Saven Marine, 2016b: Sevan 1000 FPSO for Goliat retrieved March, 2, 2016 from http://www.sevanmarine.com/projects/floating-production?id=582:sevan-1000-fpso-for-goliat&catid=41.

94. SBS, http://www.sbs-international.com/business-areas/floating-production-systems/
95. Shen, Z-r., Ye, H-x, and Wan, D-c. (2014). URANS simulations of ship motion responses in long-crest irregular waves. *Journal of Hydrodynamics*. 26 (3), 436-446.
96. Siddorn, P. and Taylor, R. E. (2008). Diffraction and independent radiation by an array of floating cylinders. *Ocean Engineering*. 35 (13), 1289-1303.
97. SIMMAN, 2014: Geometry and Conditions of KVLCC2 retrieved March, 2, 2016 from http://simman2014.dk/ship-data/moeri-kvlcc2-tanker/geometry-and-conditions-moeri-kvlcc2-tanker/.
98. Siow, C. L, Jaswar Koto, Hassan Abyn, N.M Khairuddin. (2014). Linearized Morison Drag for Improvement Heave Response of Semi-Submersible by Diffraction Potential. Journal of Ocean, Mechanical and Aerospace Science and Engineering. Vol.6, 8-16.
99. Siow, C. L. (2013). Design Study of High Performance Steam Propulsion System for LNG Carrier. Journal of Ocean, Mechanical and Aerospace -Science and Engineering-. 1, 1-7.
100. Siow, C. L., Abby Hassan, and Jaswar (2013). Semi-Submersible's Response Prediction by Diffraction Potential Method. The International Conference on Marine Safety and Environment.
101. Siow, C. L., Jaswar and Efi Afrizal (2014). Computational fluid dynamic using parallel loop of multi-cores processor. Applied Mechanics and Materials. 493, 80-85.
102. Siow, C. L., Jaswar Koto and Hassan Abyn (2014). Semi-Submersible Heave Response Study Using Diffraction Potential Theory with Viscous Damping Correction. Journal of Ocean, Mechanical and Aerospace -Science and Engineering-.5, 23-29.
103. Siow, C. L., Jaswar Koto and Khairuddin, N. M. (2014). Study on Model Scale Rounded-Shape FPSO's Mooring Lines. Journal of Ocean, Mechanical and Aerospace -Science and Engineering-. 12, 1-4.
104. Siow, C. L., Jaswar Koto, Hassan Abby and Khairuddin, N. M. (2014). Prediction of Semi-Submersible's Motion Response by Using Diffraction Potential Theory and Heave Viscous Damping Correction, Jurnal Teknologi (Sciences & Engineering). 69:7, 127–133.
105. Siow, C. L., Jaswar Koto, Hassan Abyn and Khairuddin. N. M. (2014). Linearized Morison Drag for Improvement Heave Response of Semi-Submersible by Diffraction Potential. Journal of Ocean, Mechanical and Aerospace -Science and Engineering-. 6, 8-16.Jaswar Koto and Siow. C. L. (2014). Experimental Study of Gap Distance between

Floating Structures in Tandem Arrangement. Journal of Ocean, Mechanical and Aerospace -Science and Engineering-. 9, 1-8.

106. Siow, C. L., Jaswar, Afrizal, E., Abyn, H., Maimun, A. and Pauzi, M. (2013). Comparative of Hydrodynamic Effect between Double Bodies to Single Body in Tank. The 8th International Conference on Numerical Analysis in Engineering. Pekanbaru, Indonesia.

107. Siow, C. L., Koto, J., Hassan Abyn and Adi Maimun (2013). Gap distance Analysis of floating structures in tandem arrangement. Developments in Maritime Transportation and Exploitation of Sea Resources - Proceedings of IMAM 2013, 15th International Congress of the International Maritime Association of the Mediterranean. 255-263.

108. Siow, C. L., Koto, J., Pauzi, M., Yasukawa, H., Matsuda, A. and Terada, D. (2015). Prediction of Motion Responses of Ship Shape Floating Structure using Diffraction Potential. Journal of Ocean, Mechanical and Aerospace -Science and Engineering-. 20, 1-5.

109. Siow, C. L., Koto, J., Pauzi, M., Yasukawa, H., Matsuda, A. and Terada, D. (2015). Prediction of Motion Responses of Rounded-Shape FPSO using Diffraction Potential. Journal of Subsea and Offshore-Science and Engineering-. 2, 12-15.

110. Siow, C. L., Koto, J., Yasukawa, H., Matsuda, A., Terada, D. and Soares, C. G. (2015). Theoretical Review on Prediction of Motion Response using Diffraction Potential and Morison. Journal of Ocean, Mechanical and Aerospace -Science and Engineering-. 18, 8-13.

111. Siow, C. L., Koto, J., Yasukawa, H., Matsuda, A., Terada, D., Soares, C. G., Incecik, A., and Pauzi, M. A. G. (2015), Mooring effect on wave frequency response of round shape FPSO. *Jurnal Teknologi*. 74(5), 59-68.

112. Siow, C. L., Koto, J., Yasukawa, H., Matsuda, A., Terada, D., Soares, C. G., Atilla Incecik and Pauzi, M. A. G. (2015). Mooring effect on wave frequency response of round shape FPSO. Jurnal Teknologi. 74(5), 59-68.

113. Siow, C. L., Koto, J., Yasukawa, H., Matsuda, A., Terada, D., Soares, C. G., Atilla Incecik, Pauzi, M. and Maimun, A. (2015). Experimental Study on Effect of Mooring on Motion Response of Rounded-Shape FPSO Model. Journal of Ocean, Mechanical and Aerospace -Science and Engineering-. 19, 1-7.

114. Siow, C. L., Koto, J., Yasukawa, H., Matsuda, A., Terada, D., Soares, C. G., Muhamad Zameri bin Mat Samad and Priyanto, A., (2015). Wave Induce Motion of Round Shaped FPSO. Journal of Subsea and Offshore-Science and Engineering-. 1, 9-17.

115. Siow, C. L., Koto, J., Yasukawa, H., Matsuda, A., Terada, D., Soares, C. G. and Zameri, M. (2014). Experiment Study on Hydrodynamics Characteristic of Rounded-Shape FPSO. The 1st Conference on Ocean, Mechanical and Aerospace-Science and Engineering-.

116. Siow, C.L., Koto, J., Abyn, H. &Maimum, A. (2013). Gap distance analysis of floating structures in tandem arrangement. Developments in Maritime Transportation and Exploitation of Sea Resources. Taylor & Francis Group, London. P. 255-263.

117. Siow, C.L., Jaswar, Afrizal, E., Abyn, H., Adi, M., Pauzi, M. (2013). Comparative of Hydrodynamic Effect between Double Bodies to Single Body in Tank.The 8th International Conference On Numerical Analysis In Engineering.Pekanbaru, Indonesia

118. Sjöbris, C. (2012). *Decommissioning of SPM buoy*. Master of Science Thesis. Chalmers University of Technology, Gothenburg, Sweden.

119. Soares, C. G., Fonseca, N. and Pascoal, R. (2005). Experimental and Numerical Study of the Motions of a Turret Moored FPSO in Waves. *Journal of Offshore Mechanics and Arctic Engineering*. 127(3), 197-204.

120. Söylemez, M. (1995). Motion tests of a twin-hulled semi-submersible. Ocean Engineering, 22(6), 643-660.

121. Spyros A. M. (2004). Hydrodynamic coefficients in heave of two concentric surface-piercing truncated circular cylinders.Applied Ocean Research, Vol. 26 (3-4), pp. 84-97.

122. Srinivasan, N., Singh, S., Chakrabarti, S., Sundaravadivelu, R., and Kanotra, R. (2008). Design of Non-Ship-Shape FPSO for Sakhalin-V Deepwater. *SPE Russion Oil and Gas Technical Conference and Exhibition*. 28-30 October. Moscow, Russia.

123. Sun, Y. W., and Kang, H. G. (2012). Application of CLEAR-VOF method to wave and flow simulations. *Water Science and Engineering*. 5 (1), 67-78.

124. Tajali, Z., and Shafieefar, M. (2011). Hydrodynamic analysis of multi-body floating piers under wave action. *Ocean Engineering*. 38 (17–18), 1925-1933.

125. Tiau, K. U., Jaswar, Hassan Abyn and Siow, C. L. (2012). Study On Mobile Floating Harbor Concept. Proceedings of The 6th Asia Pacific Workshop on Marine Hydrodynamics. Pg. 202- 206.

126. Van Oortmerssen, G. (1979). Hydrodynamic interaction between two structures of floating in waves. Proc. of BOSS ‘79. Second International Conference on Behavior of Offshore Structures, London.

127. Wang, C. Z., Wu, G. X., and Khoo, B. C. (2011). Fully nonlinear simulation of resonant motion of liquid confined between floating structures. *Computers and Fluids*. 44 (1), 89-101.

128. Wang, T. Y., Zhang, J., and Liu, J. K. (2012). Concept Design of a New Non-Ship-Shaped FPSO. *Applied Mechanics and Materials*. 170-173, 2222-2227.

129. Wu, S., Murray, J. J., Virk, G. S. (1997). The motions and internal forces of a moored semi-submersible in regular waves.Ocean Engineering, 24(7), 593-603.

130. Yan, S., Ma, Q. W., and Cheng, X. M. (2011). Fully Nonlinear Hydrodynamic Interaction Between Two 3D Floating Structures in Close Proximity. *International Journal of Offshore and Polar Engineering*. 21 (3), 178–185.

131. Yılmaz, O. (2004). An iterative procedure for the diffraction of water waves by multiple cylinders. *Ocean Engineering*. 31 (11–12), 1437-1446.

132. Yilmaz, O., Incecik, A. (1996). Extreme motion response analysis of moored semi-submersibles.Ocean Engineering, 23(6), 497-517.

133. Yong, L., Baudic, S., Poranski, P., Wichers, J., Stansberg., C. T., and Ormberg, H. (2004). Deepstar Study on Predicting FPSO Responses. *Offshore Technology Conference*. 3-6 May. Houston, Texas, USA, 1-15.

134. Yu, R. (1995). *Dynamic Response of a Floating Dock in Regular and Irregular Waves*. Master of Engineering Thesis. Memorial University of Newfoundland, Newfoundland, Canada.

135. Yus-Farid, M. (2015). *Numerical Simulation Dynamic Characteristic of X Round-Shaped FPSO*. Bachelor of Engineering Thesis. Universiti Teknologi Malaysia, Skudai, Johor, Malaysia.

136. Zhao, W. H., Yang, J. M., Hu, Z. Q., and Wei, Y. F. (2011). Recent developments on the hydrodynamics of floating liquid natural gas (FLNG). *Ocean Engineering*. 38 (14–15), 1555-1567.

137. Zhao, W.H,Yang, J.M, andHu, Z.Q. (2012).Hydrodynamic interaction between FLNG vessel and LNG carrier in side by side configuration. Journal of Hydrodynamics.Ser. B, Vol. 24, Issue 5, Pages 648-657.

138. Zhou, X. C., Wang, D. J., and Chwang, A. T. (1996). Hydrodynamic Interaction between Two Vertical Cylinders in Water Waves. *Applied Mathematics and Mechanics*. 18 (10), 927-940.

139. Zhu, H. R., Zhu, R. C., and Miao, G. P. (2008). A Time Domain Investigation on the Hydrodynamic Resonance Phenomena of 3-D Multiple Floating Structures. *Journal of Hydrodynamics, Ser. B.* 20 (5), 611-616.

140. Zhu, R. C., Miao, G. P., and Zhu, H. R. (2006). The radiation problem of multiple structures with small gaps in between. *Journal of Hydrodynamics, Ser. B.* 18 (5), 520-526.

Appendix A

SOLUTION ON CALCULATE LENGTH OF WAVE CREST

Assuming that the length of wave crest can be represented by a quadratic equation *n* as $S_{c,n}$. Then the length of the wave crest can be calculated by integrate the equation (A-1).

$$S_{c,n} = \int_{x_{\psi,n}}^{x_{\psi,n+1}} \sqrt{1 + \left(\frac{dy}{dx}\right)^2}\, dx \qquad (A-1)$$

Where,

$$\frac{dy}{dx} = 2a_n + b_n \qquad (A-2)$$

$$S_{c,n} = \int_{x_{\psi,n}}^{x_{\psi,n+1}} \sqrt{1 + (2a_n + b_n)^2}\, dx \qquad (A-3)$$

Let,

$$2a_n x + b_n = \tan u \qquad (A-4)$$

$$x = \frac{\tan u}{2a_n} - \frac{b_n}{2a_n} \qquad (A-5)$$

$$dx = \frac{1}{2a_n} \sec^2 u \; du \qquad (A-6)$$

$$u = \tan^{-1}(2a_n x + b_n) \qquad (A-7)$$

Insert equation (A-4) and equation (A-6) into equation (A-3),

$$S_{c,n} = \int_{x_{\psi,n}}^{x_{\psi,n+1}} \sqrt{1 + \tan^2 u}\; \frac{1}{2a_n} \sec^2 u \; du \qquad (A-8)$$

$$S_{c,n} = \frac{1}{2a_n}\int_{x_{\psi,n}}^{x_{\psi,n+1}} \sqrt{1+\tan^2 u}\ \sec^2 u\ du \qquad (A-9)$$

Where the trigonometry identity said that $1+\tan^2 u = \sec^2 u$, then

$$S_{c,n} = \frac{1}{2a_n}\int_{x_{\psi,n}}^{x_{\psi,n+1}} \sqrt{\sec^2 u}\ \sec^2 u\ du$$

$$= \frac{1}{2a_n}\int_{x_{\psi,n}}^{x_{\psi,n+1}} \sec^3 u\ du \qquad (A-10)$$

Solving the equation (A-10) obtained that

$$S_{c,n} = \frac{1}{2a_n}\left[\frac{\sec u \cdot \tan u}{2} + \frac{\ln|\sec u + \tan u|}{2}\right]\Bigg|_{x_{\psi,n}}^{x_{\psi,n+1}} \qquad (A-11)$$

Insert equation (A-7) into equation (A-11), then

$$S_{c,n} = \frac{1}{2a_n}\left[\frac{\sec(\tan^{-1}(2a_n x+b_n))\cdot\tan(\tan^{-1}(2a_n x+b_n))}{2} + \frac{\ln|\sec(\tan^{-1}(2a_n x+b_n))+\tan(\tan^{-1}(2a_n x+b_n))|}{2}\right]\Bigg|_{x_{\psi,n}}^{x_{\psi,n+1}} \qquad (A-12)$$

Based on the trigonometry rule,

$$\tan(\tan^{-1}(2a_n x+b_n)) = 2a_n x+b_n \qquad (A-13)$$

$$\sec(\tan^{-1}(2a_n x+b_n)) = \sqrt{1+(2a_n+b_n)^2} \qquad (A-14)$$

Insert equation (A-13) and equation (A-14) into equation (A-12), then

$$S_{c,n} = \frac{1}{2a_n}\left[\frac{(2a_n+b_n)\sqrt{1+(2a_n+b_n)^2}}{2} + \frac{\ln\left|\sqrt{1+(2a_n+b_n)^2}+(2a_n+b_n)\right|}{2}\right]\Bigg|_{x_{\psi,n}}^{x_{\psi,n+1}} \qquad (A-15)$$

Where, from the equation (A-1) to equation (A-15), $S_{c,n}$ is the length of the wave crest represent by the quadratic equation n, $x_{\psi,n}$ is the X-coordinate of the wave crest, a_n and $b_n$is the coefficient of the quadratic equation which represent the wave crest.

Appendix B

INTERFACE OF SELF-DEVELOPED SOFTWARE

The interface of the self-developed programming code is shown in the following figures.

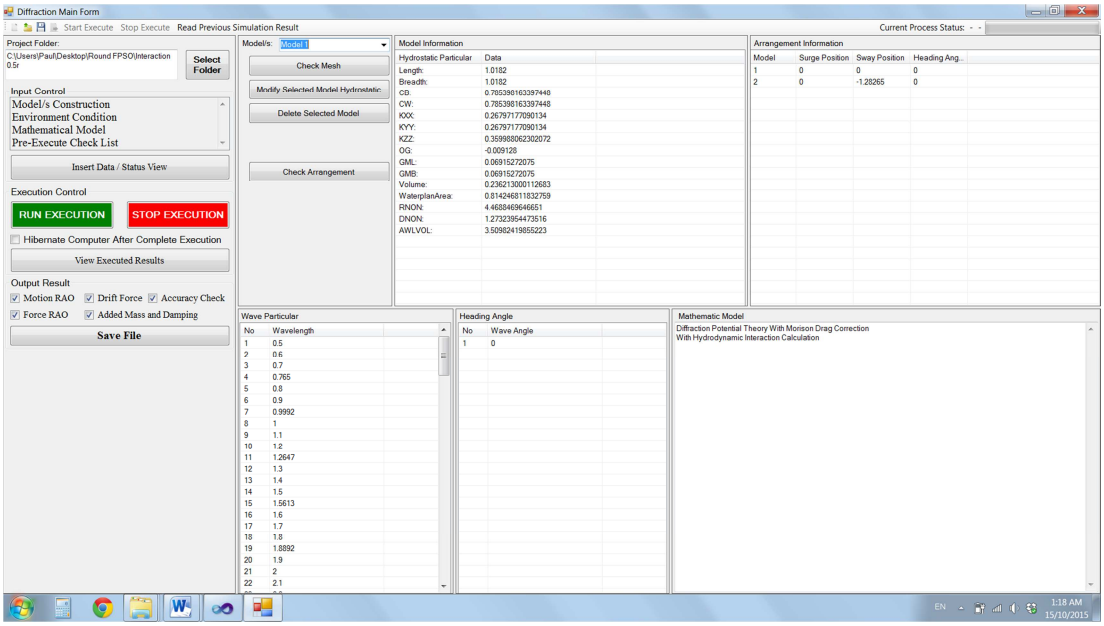

Figure B-1 The main frame of the self-developed software

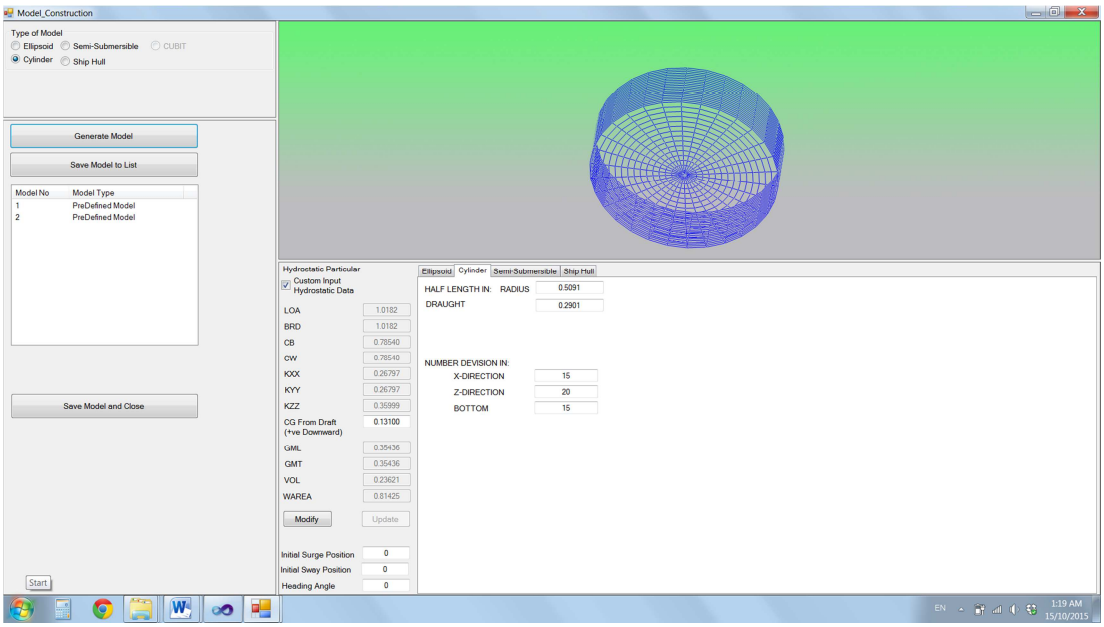

Figure B-2 The interface of the self-developed software designed for model construction

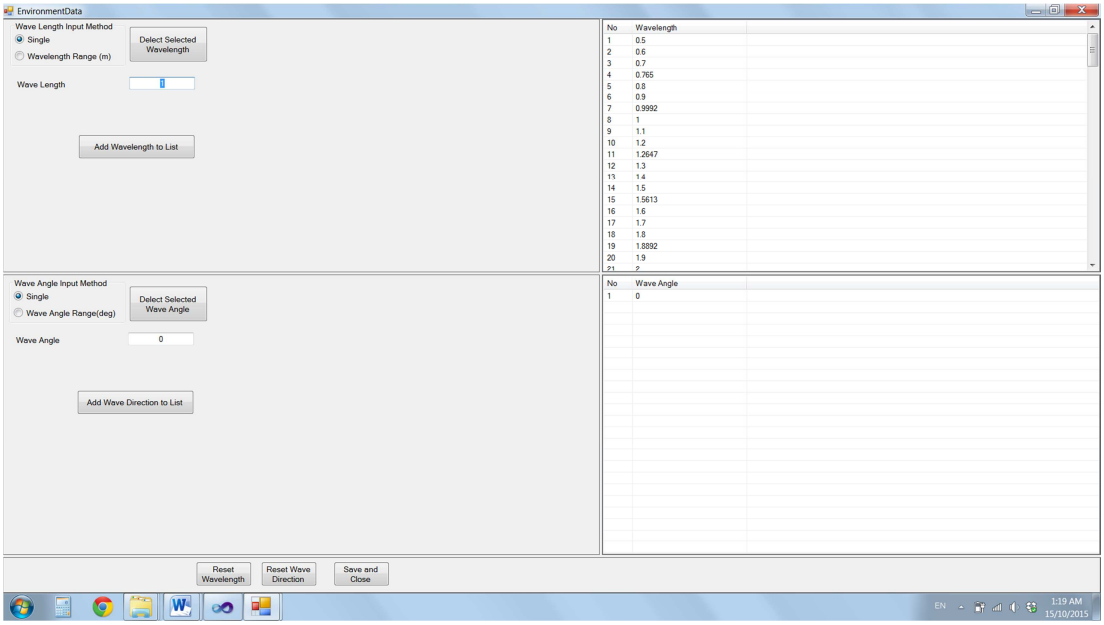

Figure B-3 The interface of the self-developed software designed for insert environment data

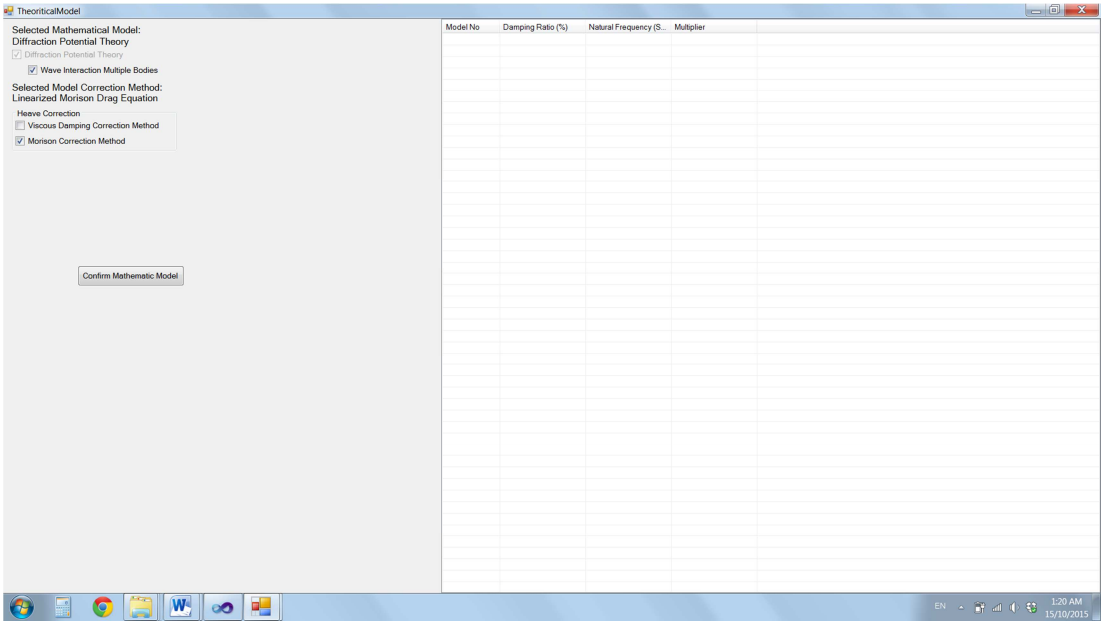

Figure B-4 The interface of the self-developed software designed for user to select the basic theory used for calculation. The interface also allows the user to insert the extra damping coefficient for the calculation

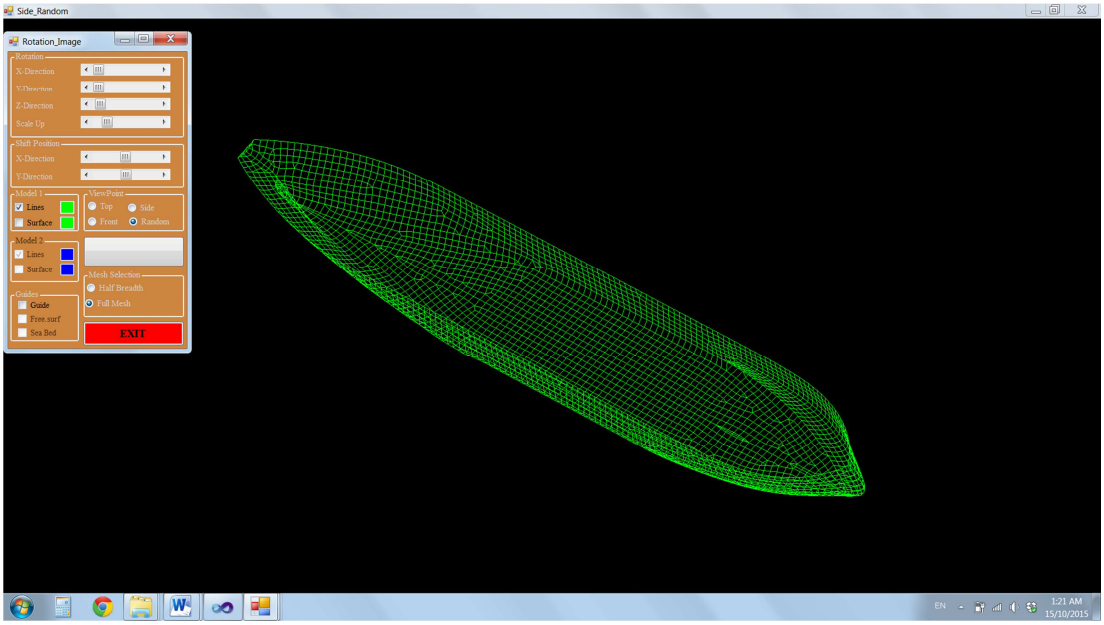

Figure B-5 The interface of the self-developed software designed present the meshes constructed by the software

Appendix C

MESH OF THE FLOATING STRUCTURE GENERATED BY ANSYS AQWA

The mesh of the Round Shape FLNG generated by ANSYS AQWA used for execution is showed in Figure C-1. The mesh of the KVLCC2 tanker ship generated by ANSYS AQWA used for execution is showed in Figure C-2.

To predict the interaction between Round Shape FLNG with KVLCC2 tanker, both the selected model were arranged close to each other. The Figure C-3 shows the meshes for both structures used in execute the motion response of floating structure when both structures are interacting between each other.

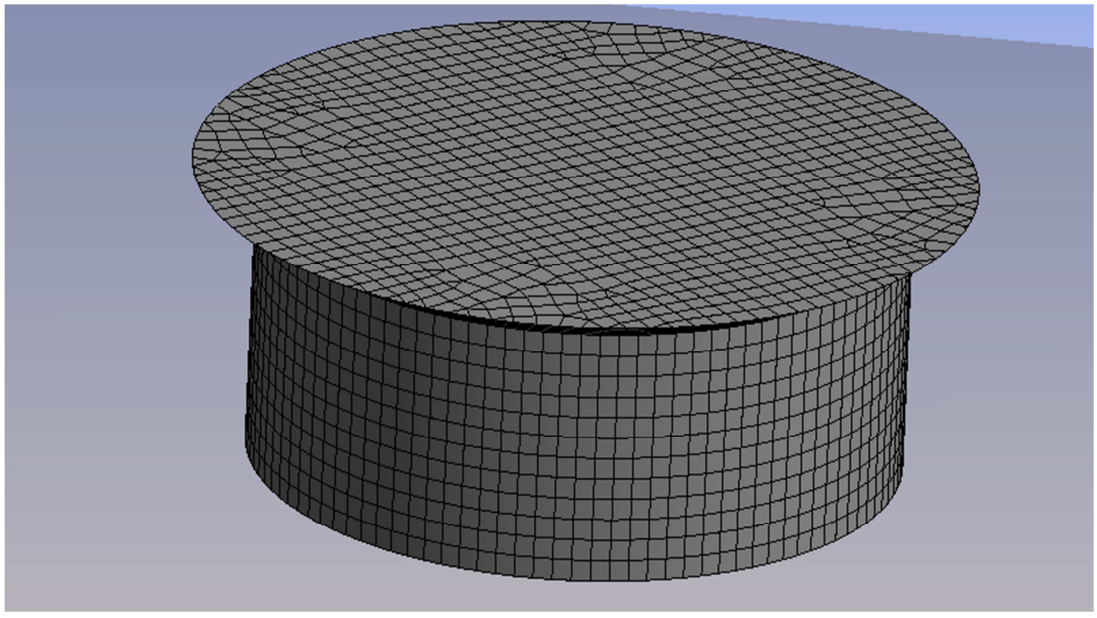

Figure C-1 The meshes for the Round Shape FLNG constructed by ANSYS AQWA.

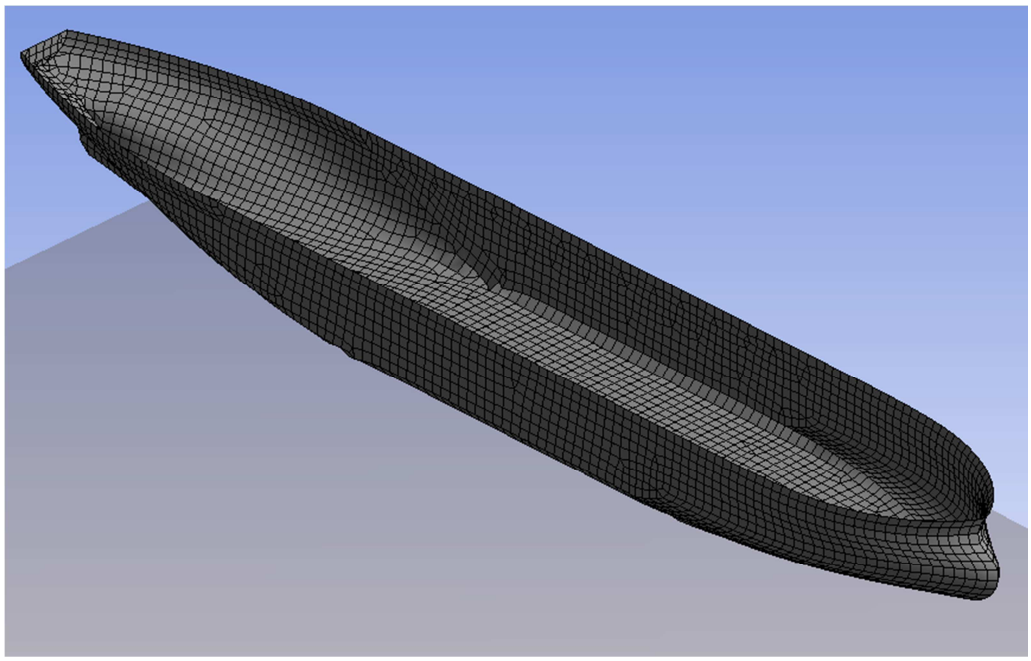

Figure C-2 The meshes for the KVLCC2 Tanker Ship constructed by ANSYS AQWA

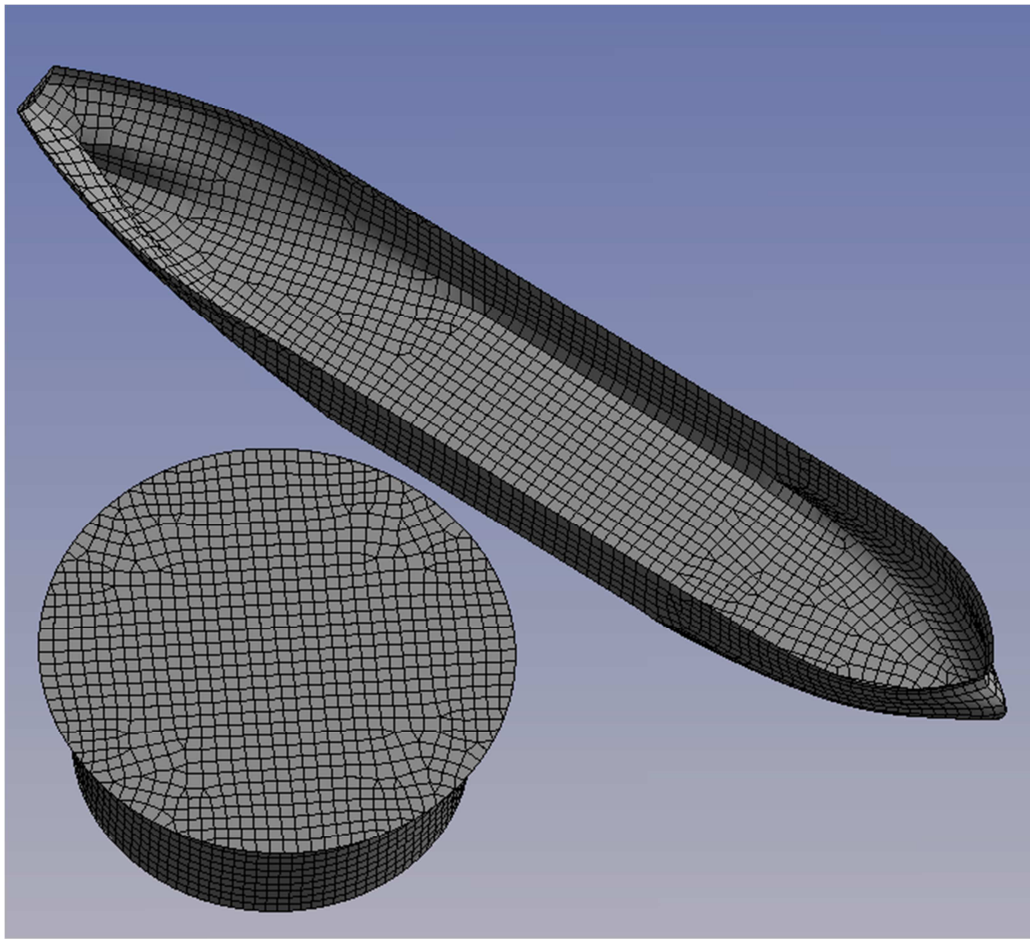

Figure C-3 The meshes for the both the Round Shape FLNG and KVLCC2 Tanker Ship constructed by ANSYS AQWA for predict the motion interaction effect

Appendix D

PHOTO OF MODEL EXPERIMENT

The photos for the model experiment are presented as follow:

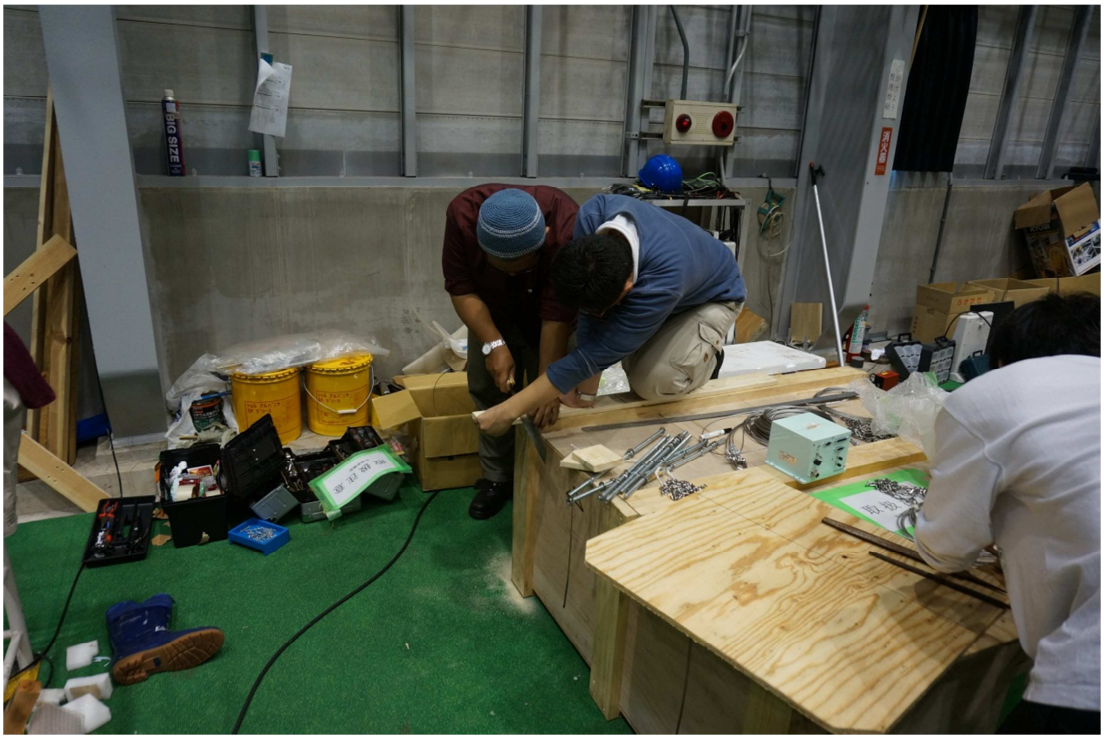

Figure D-1 Model preparation

Figure D-2 Model preparation

Figure D-3 Model installation

Figure D-4 Model installation

Figure D-5 Motion data recording

Appendix E

SAMPLES CALCULATION PROCEDURE TO PREDICT MOTION NATURAL FREQUENCY

The motion natural frequency of the round shape FLNG is predicted by using simple mathematical equation and decay experiment. Three samples of calculation are presented in this appendix. The three samples are the process to calculate natural frequency for surge motion, heave motion and pitch motion.

To calculate the surge natural frequency, the mooring force is required to estimate first. The restoring force for surge motion is contributed from the attached mooring line. So the mooring force is the main parameter to determine the natural frequency for surge motion. Besides, the natural frequency of other horizontal plane motion such as sway motion and yaw motion also calculate using the similar process to calculate the surge natural frequency in this research.

The surge restoring force mooring force is able to calculate after the amount mooring force able to generate by the mooring cables are known. The amount of mooring force generated by the designed round shape FLNG mooring system to avoid the FLNG experience large surge motion is presented in the Figure E-1. The calculation process to estimate the surge natural frequency is presented as follow.

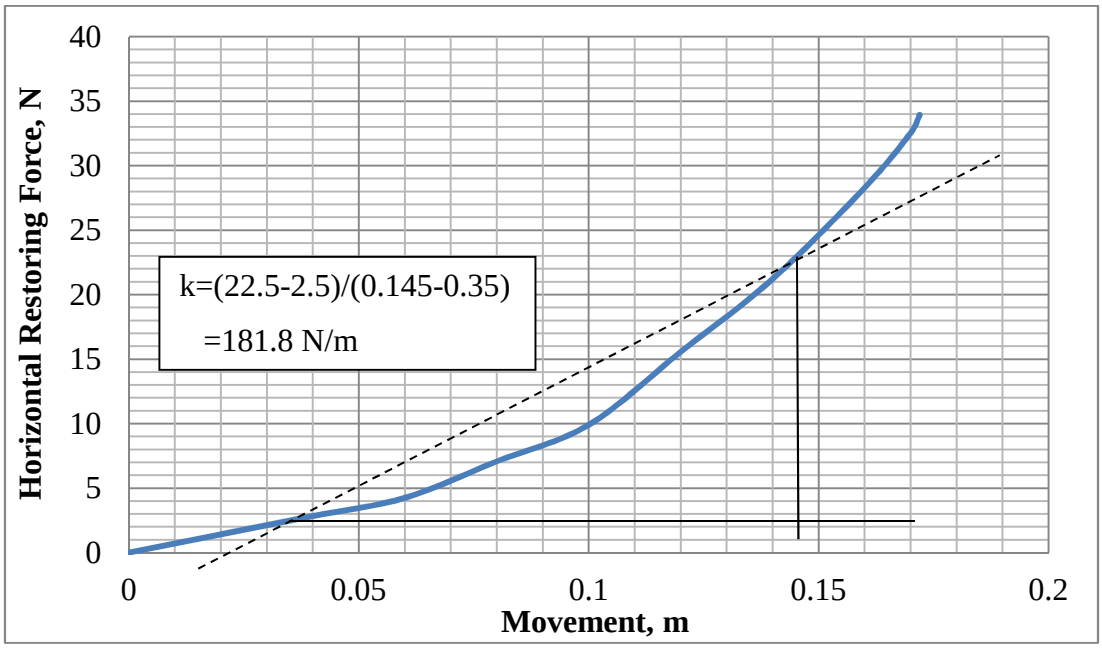

Figure E-1 FLNG surge restoring force due to mooring effect

Mass, $\Delta_{FLNG} = \rho\nabla$

$$= 1000 \cdot 0.2361 = 236.1\ kg$$

Surge Added Mass, $A_{11} = \rho\pi R^2 D$

$$= 1000 \cdot \pi \cdot 0.509^2 \cdot 0.2901 = 236.1kg$$

Surge Restoring Force, $C_1 = \dfrac{(22.5 - 2.5)/9.81}{0.145 - 0.35} = 18.53kg/m$

Surge natural period, $T_1 = 2\pi\sqrt{\dfrac{\Delta + A_{11}}{C_1}}$

$$= 2\pi\sqrt{\frac{236.1 + 236.1}{18.53}} = 32\ sec$$

Surge natural frequency $= \dfrac{1}{T_1}$

$$= \frac{1}{32} = 0.03125\ Hz$$

The heave restoring force is contributed from the hydrostatic term. In this research, the heave natural frequency is calculated direction using the equation 7.2. The parameters involved in calculate the heave natural period are shown in Table E-1 and the sample calculated to obtain the heave natural frequency of this round shape FLNG is presented as follow.

Table E-1: Parameters used to calculate heave natural frequency

Diameter of FLNG	1.0182	m
Water plane area, Aw	0.81425	m^2
Volume, ∇	0.2361	m^3
Mass, Δ	236.1	kg
Added Mass, A_{33}	212.49	kg
Density, ρ	1000	kg/m^3
Gravity Acceleration, g	9.80665	m/s

Heave restoring force, $C_3 = \rho g \text{Aw} = 7985.06\ N.m$

Heave natural period, $T_3 = 2\pi\sqrt{\dfrac{\Delta + A_{33}}{C_3}} = 1.489\ s$

Heave natural frequency $= \dfrac{1}{T_3} = 0.6716\ Hz$

The roll natural period is estimate from the decay experiment. The similar process is used to obtain the pitch natural period. The recorded roll decay time series data is presented in Figure E-2 and the parameters used to estimate the roll natural frequency and the radius of gyration of this round shape FLNG is shown in Table E-2. The calculation process to obtain the roll natural frequency is as follow.

Table E-2 : Parameters used to calculate roll natural frequency

Diameter of FLNG	1.0182	m
GM_T	0.0691	m
Volume, ∇	0.2361	m^3
Mass, Δ	236.1	kg
Added Mass, A_{44}	7.53	kg. m^2
Density, ρ	1000	kg/m^3
Gravity Acceleration, g	9.80665	m/s

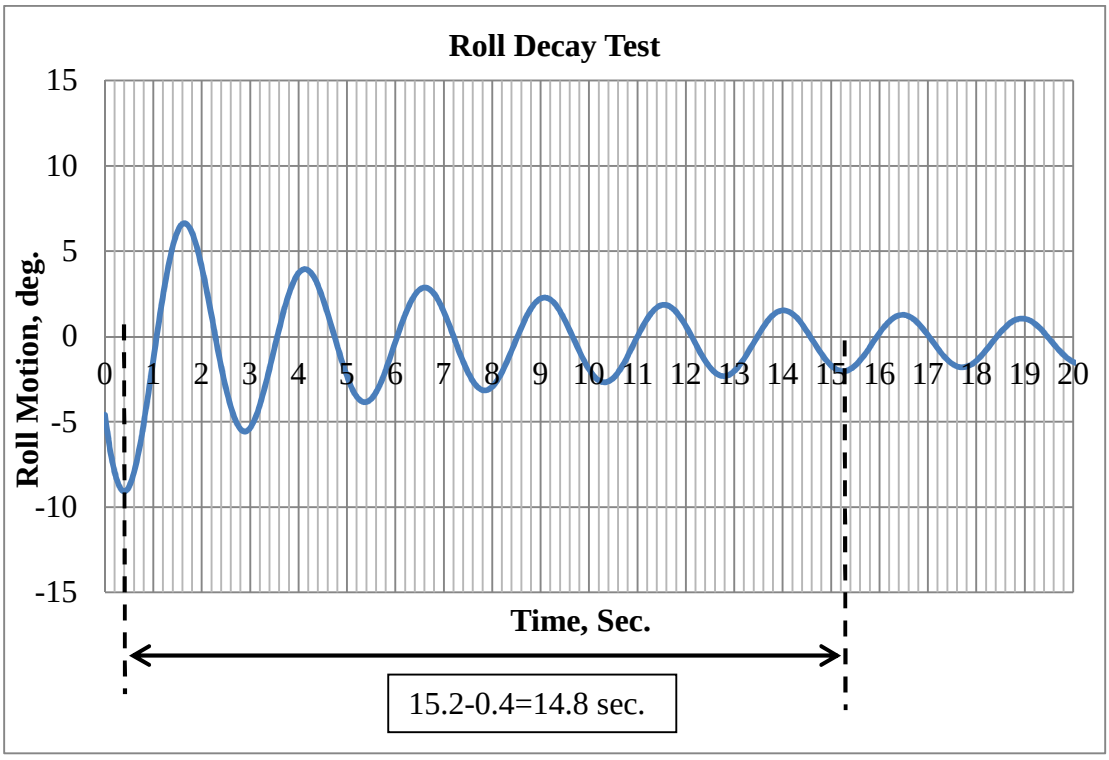

Figure E-2 Round shape FLNG's Roll decay result

Average natural period of roll, $T_4 = \frac{(15.2 - 0.4)}{6} = 2.47\ s$

Roll natural frequency $= \frac{1}{T_4} = 0.4049\ Hz$

Roll restoring force, $C_4 = \rho g \nabla\ GM_t = 160.0\ N.m$

Roll natural frequency, $W_{n,4} = \frac{2\pi}{T_4} = 2.547\ rad/s$

Moment of inertia, $I_{yy} = \frac{C_4}{w_{n,4}^2} - A_{44} = 17.13\ kg.m^2$

Radius of Gyration, $k_{yy} = \sqrt{\frac{I_{yy}}{\rho \nabla}} = 0.269\ m^2$

Appendix F

MOTION MEASUREMENT SOFTWARE FOR MODEL EXPERIMENT

The 6 DoF motion of round shape FLNG are measured by theodolite camera and gyroscope. The programming software is used to process the signal from the measurement devices so the motion data of the FLNG is obtained from experiment. As mentioned in chapter 7, the linear motion of the FLNG is measured by theodolite camera, the theodolite camera able to obtain the distance of optical marker from the camera, vertical angle and horizontal angle between the optical marker and the camera. The software to measure the linear motion of the FLNG using the data measure by theodolite camera is provided by the laboratory. The interface of the software is shown in the Figure F-1 and the sample data output by the measurement software are shown in Figure F-2 to Figure F-4. As provided by the laboratory, the mathematical equations to calculate the position of the FLNG in wave dynamic tank are presented from equation to equation.

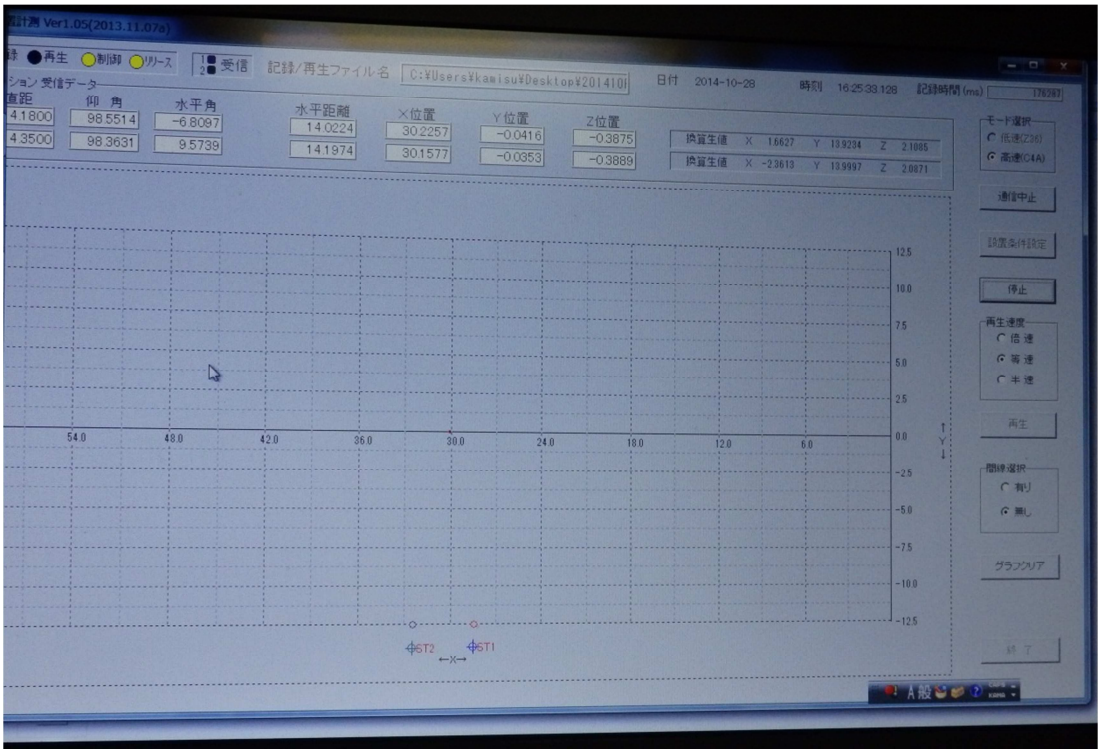

Figure F-1 Interface of the software to process the data from theodolite camera

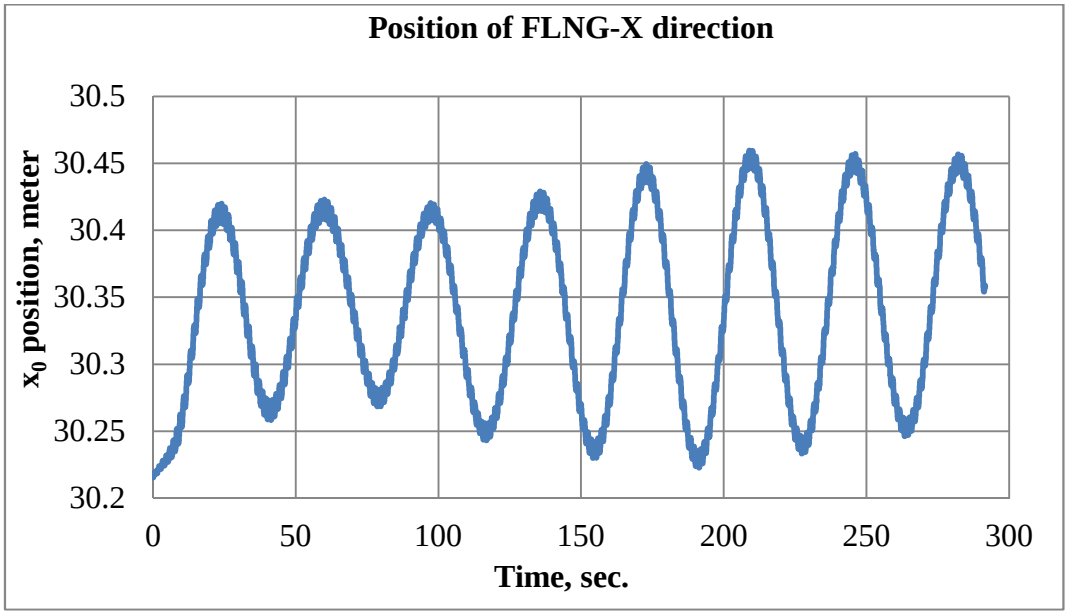

Figure F-2 Position of round shape FLNG in X-direction measured from theodolite camera in head sea single structure motion experiment test with wavelength 2.27 meters

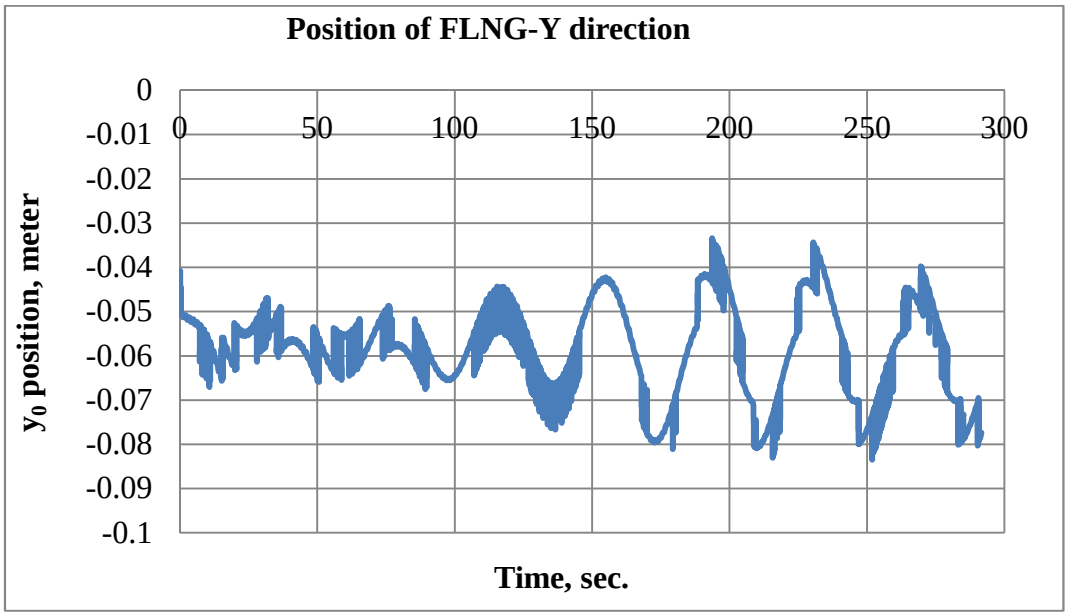

Figure F-3 Position of round shape FLNG in Y-direction measured from theodolite camera in head sea single structure motion experiment test with wavelength 2.27 meters

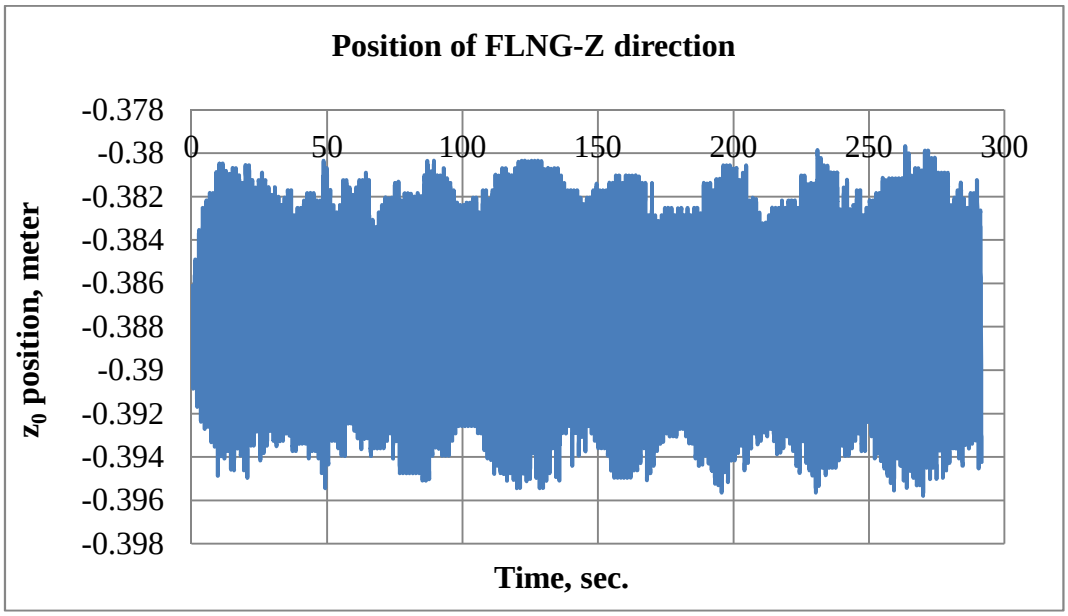

Figure F-4 Position of round shape FLNG in Z-direction measured from theodolite camera in head sea single structure motion experiment test with wavelength 2.27 meters

The position of optical marker can be known if the position of the theodolite camera, the distance between theodolite camera and optical marker, horizontal angle between theodolite camera and optical marker and vertical angle between theodolite camera and optical marker is knows. Since the required information is able to provide by the theodolite camera, therefore the position of the optical marker can be calculated by the mathematical model presented in this appendix.

Let the initial X, Y and Z position of the theodolite camera from the zero offset labeled as X_T, Y_T and Z_T. The distance between theodolite camera and optical marker is labeled as $l_{TO}\ (t)$, the horizontal angle between theodolite camera and optical marker is labeled as $\theta_{H,TO}\ (t)$ and the vertical angle between theodolite camera and optical marker is labeled as $\theta_{V,TO}\ (t)$. The relationship between the variables can be presented as in Figure F-5.

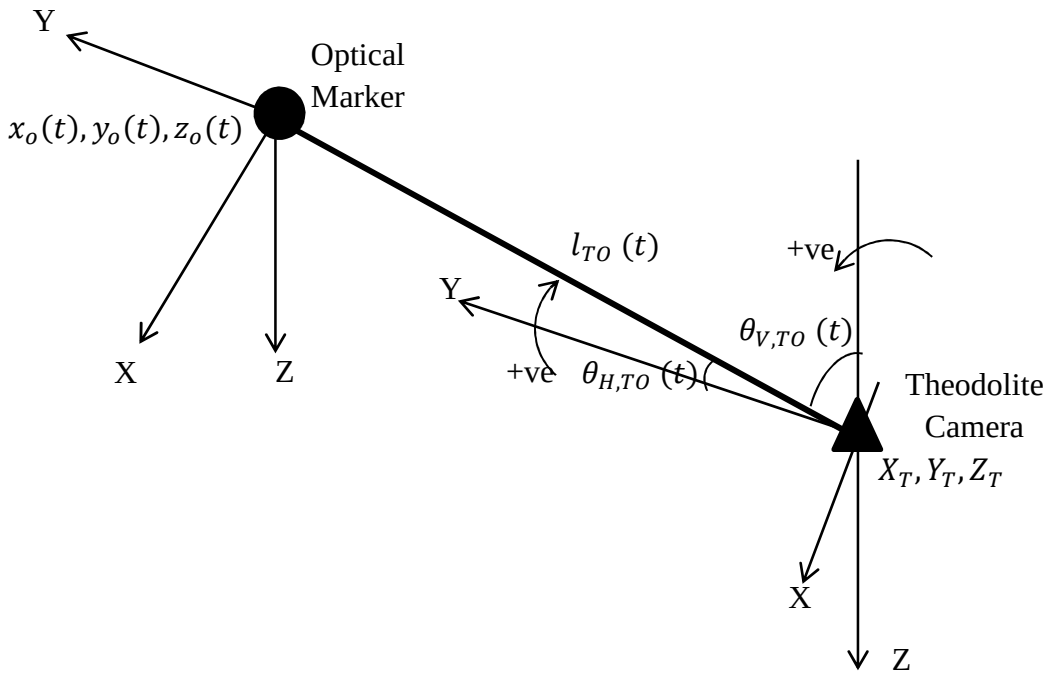

Figure F-5 Relationship between the position of the theodolite camera with the optical marker

Let the position of the optical marker in X, Y and Z position labeled as $x_o(t), y_o(t)$ and $z_o(t)$. Then, the mathematic equation to relate the position between theodolite camera with the optical marker can be shown as follow.

$$x_o(t) = X_T - l_{TO}\ (t) \sin\left(\theta_{V,TO}\ (t)\right) \sin\left(\theta_{H,TO}\ (t)\right) \qquad (F-1)$$

$$y_o(t) = X_T + l_{TO}\ (t) \sin\left(\theta_{V,TO}\ (t)\right) \cos\left(\theta_{H,TO}\ (t)\right) \qquad (F-2)$$

$$z(t) = X_T - l_{TO}\ (t) \cos\left(\theta_{V,TO}\ (t)\right) \qquad (F-3)$$

On the other hand, the rotation motion of the round shape FLNG is able to measure directly by the gyroscope. The gyroscope is connecting to the computer via Bluetooth system to transfer the data so the measured data can be saved in the connected computer. The

interface of the software to process the data from the gyroscope is shows in Figure F-6 and the rotational motion data measured by the gyroscope are shown in Figure F-7 to Figure F-9.

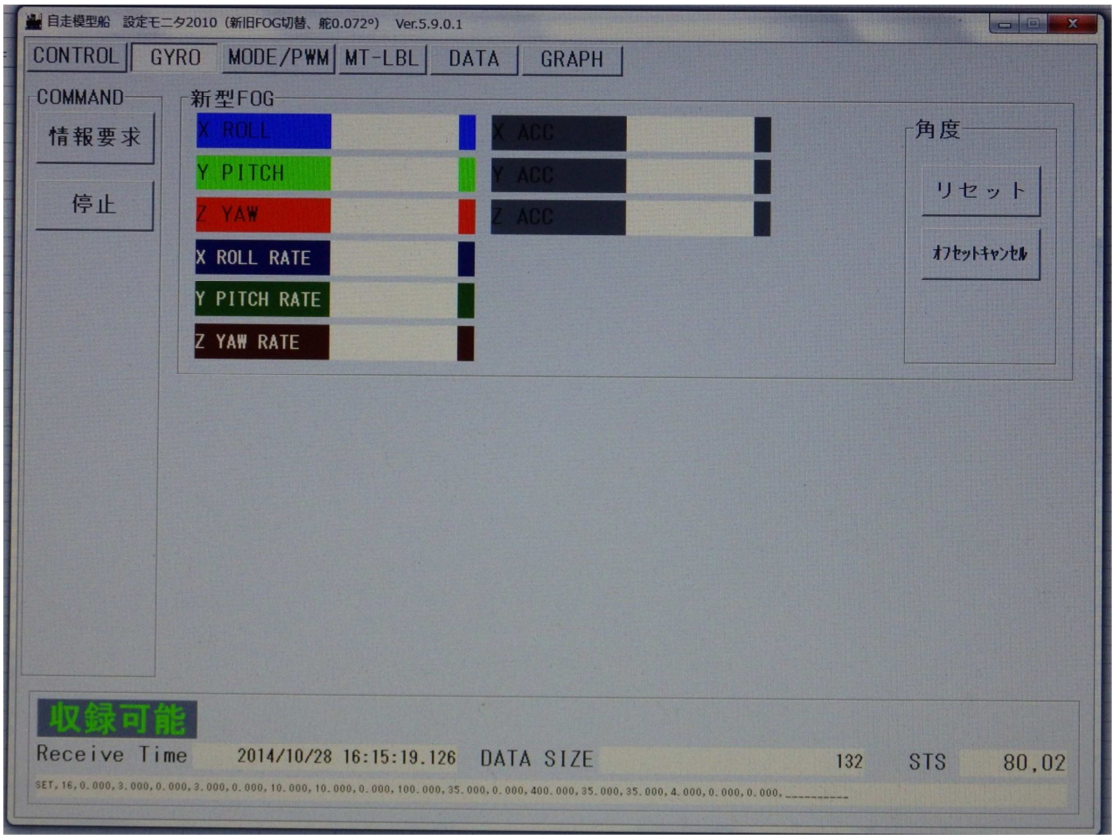

Figure F-6 Interface of the software to process the data from gyroscope

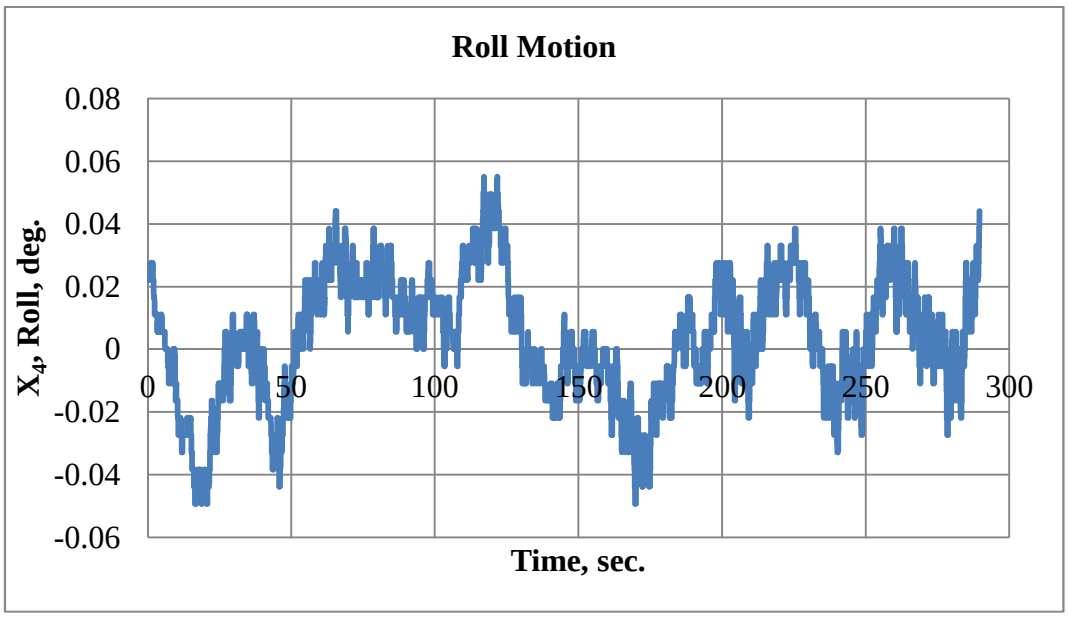

Figure F-7 Roll motion of round shape FLNG measured by gyroscope in head sea single structure motion experiment test with wavelength 2.27 meters

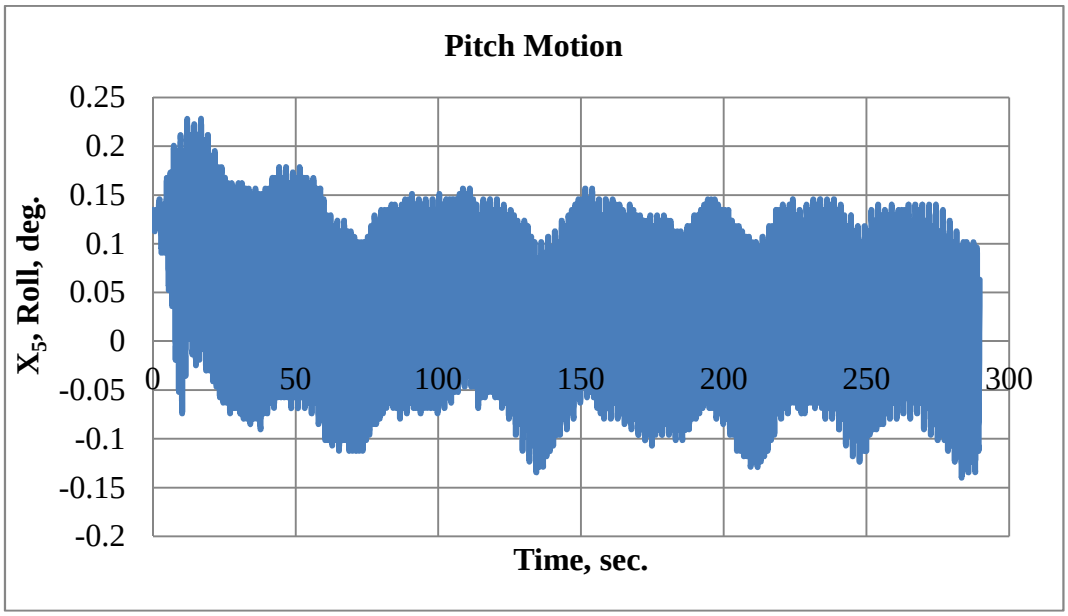

Figure F-8 Pitch motion of round shape FLNG measured by gyroscope in head sea single structure motion experiment test with wavelength 2.27 meters

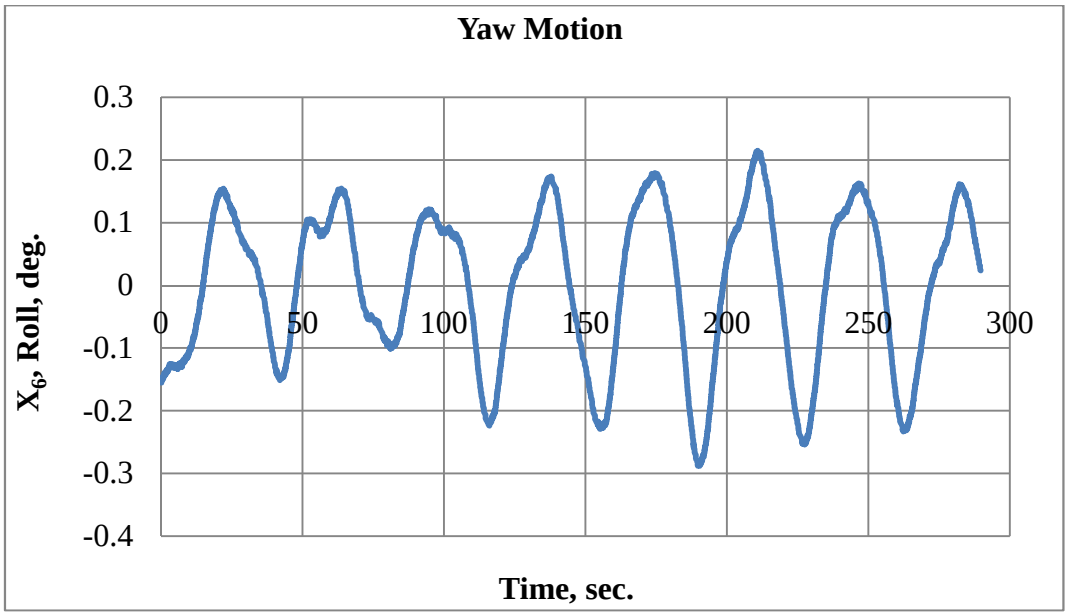

Figure F-9: Yaw motion of round shape FLNG measured by gyroscope in head sea single structure motion experiment test with wavelength 2.27 meters

Autobiographies

Jaswar Koto was born on October, 1970. He is a descendant of the Prophet Rasullullah S.A.W through Husein R.A. He is currently a professor on offshore engineering and president at Ocean and Aerospace Research Institute, Indonesia.

He is currently president of International Society of Ocean, Mechanical & Aerospace for scientist and engineers. He has been invited as a visiting professor and guest lecturers more than 16 times and has received several international awards. He actively supervises PhD, Master and Bachelor Students. He has published more than 200 papers, 13 books on ship and offshore engineering, has created 10 simulation software and has invented 11 theories such as Ice-Ship, Benefit-Cost-Risk, DSM, helicopter blade and hydrodynamic.

He received his bachelor degree in 1994 from Institut Teknologi Sepuluh Nopember (ITS), Indonesia, and then continued further studies in Curtin University of Technology and Notre Dame University. In 2003 he has completed his PhD with “2.5 Years PhD Academic Award” form Aerospace and Marine Engineering, Osaka Prefecture University, Japan.

Since 1994, he has started his researches on subsea pipeline structure analysis, corrosion on subsea pipeline due to Carbon Monoxide, hydrodynamic analysis of AUV in Perth, Australia. He joined Research and Development Institute, Sumitomo Heavy Industries -Marine Engineering-, Japan. In 2005, he joined ExxonMobil for LNG EPCI projects. He has a contract with Mechanical Engineering and also appointed as head of High Performance Computing, CICT, Universiti Teknologi Malaysia.

Dr. Siow Chee Loon was born on November 1987. He is a lecturer on Naval Architecture and Offshore Engineering, Mechanical Engineering, Universiti Teknologi. He received his bachelor degree from Universiti Teknologi Malaysia. He received his PhD from Mechanical Engineering, Universiti Teknologi Malaysia under supervision Prof. Koto Universiti Teknologi Malaysia and Prof.Soares, Technical University of Lisbon, Portugal. He published

papers more than 20 papers. He received several academic awards.

Dr Adi Maimun obtained his B.Sc in Naval Architecture from the University of Strathclyde, Glasgow in 1983. He joined Universiti Teknologi Malaysia (UTM) as a tutor the same year. He later return to Strathclyde University for his Masters and Ph.D. in Marine Technology and obtained his degrees in 1985 and 1993 respectively

Dr Adi Maimun is currently serving as Professor of Naval Architecture at the Dept. of Aeronautics, Automotive and Ocean Engineering, Faculty of Mechanical Engineering. He was Head of Marine Laboratory (1986-1989), Head of Panel for Marine Technology (1999-2000), Head of Department for Marine Technology (2000-2007) and the Deputy Dean (Development) for the Faculty of Mechanical Engineering (2007-2011). Head of Marine Hydrodynamics Research Group, UTM (2010-present).

Dr Adi Maimun specializes mainly in the field of Marine Vehicles/Structures Dynamics using CFD, AIS, Time domain simulations and experimental work. He had taught, conducted research and consultancy work in the said field and had published over 70 papers in conferences and journals.

Dr. Adi Maimun is currently a Fellow Member of the Royal Institution of Naval Architects (UK) and a Chartered Engineer (UK). He had served as committee member for number years for the Malaysia Joint Branch (MJB) of Royal Institution of Naval Architects (RINA) and Institute of Marine Engineers Science and Technology (IMarEST). He is currently the Chairman (2015-2016) for RINA-IMarEST MJB (Southern Chapter). In the international field he had served in the International committee board for the conferences of MARTEC (since 2002), APHYDRO (since 2002) and OMAE (2008). Local organizing chairman for MARTEC 2004 and APHYDRO 2010. Malaysia Correspondent member for International Ship and Offshore Structures Congress (ISSC) (2015-2016).

Published by

Ocean & Aerospace Research Institute, Indonesia
Pekanbaru-Riau, INDONESIA
http://isomase.org/OCAri/Home.php

Edited by

Mechanical-Offshore Engineering,
Universiti Teknologi Malaysia,
MALAYSIA
http://fkm.utm.my/

Supported by

International Society of Ocean, Mechanical & Aerospace - scientists & engineers –
D/A: Resty Menara Hotel
Jalan Sisingamangaraja No. 89 (28282),
Pekanbaru-Riau INDONESIA
http://www.isomase.org/

Deep Water & Offshore
Indonesian Oil and Gas Community,
INDONESIA

Hydrodynamic 20092016013